Experimental Investigation of Transition over a NACA 0018 Airfoil at a Low Reynolds Number

by

Michael S. H. Boutilier

A thesis
presented to the University of Waterloo
in fulfillment of the
thesis requirement for the degree of
Master of Applied Science
in
Mechanical Engineering

Waterloo, Ontario, Canada, 2011

© Michael S. H. Boutilier 2011

I hereby declare that I am the sole author of this thesis. This is a true copy of the thesis, including any required final revisions, as accepted by my examiners.

I understand that my thesis may be made electronically available to the public.

Abstract

Shear layer development over a NACA 0018 airfoil at a chord Reynolds number of 100,000 was investigated experimentally. The effects of experimental setup and analysis tools on the results were also examined.

The sensitivity of linear stability predictions for measured separated shear layer velocity profiles to both the analysis approach and experimental data scatter was evaluated. Analysis approaches that are relatively insensitive to experimental data scatter were identified. Stability predictions were shown to be more sensitive to the analysis approach than to experimental data scatter, with differences in the predicted maximum disturbance growth rate and corresponding frequency of approximately 35% between approaches.

A parametric study on the effects of experimental setup on low Reynolds number airfoil experiments was completed. It was found that measured lift forces and vortex shedding frequencies were affected by the end plate configuration. It was concluded that the ratio of end plate spacing to projected model height should be at least seven, consistent with the guideline for circular cylinders. Measurements before and after test section wall streamlining revealed errors in lift coefficients due to blockage as high as 9% and errors in the wake vortex shedding frequency of 3.5%.

Shear layer development over the model was investigated in detail. Flow visualization images linked an observed asymmetry in wake velocity profiles to pronounced vortex roll-up below the wake centerline. Linear stability predictions based on the mean hot-wire profiles were found to agree with measured disturbance growth rates, wave numbers, and streamwise velocity fluctuation profiles. Embedded surface pressure sensors were shown to provide reasonable estimates of disturbance growth rate, wave number, and convection speed for conditions at which a separation bubble formed on the airfoil surface. Convection speeds of between 30 and 50% of the edge velocity were measured, consistent with phase speed estimates from linear stability theory.

Acknowledgements

I would like to thank my supervisor, Professor Serhiy Yarusevych, for providing guidance and sharing his insight at every stage of this investigation. His experience with experimental techniques was invaluable in the planning and troubleshooting phases of this project.

I am grateful to Ryan Gerakopulos for developing the airfoil model used in these experiments. His expertise in mechanical design and meticulous care in developing the embedded pressure sensor array has ensured the reliability of measurements presented in this thesis.

I would also like to thank the other students in my research group, Sina Kheirkhah, Christopher Morton, and Holly Neatby, who were always willing to discuss ideas and results with me. Holly's help with renovations to experimental hardware is particularly appreciated.

Laboratory staff members Jim Merli, Neil Griffett, and Jason Benninger, provided me continual support with hardware designs and modifications. I would specifically like to acknowledge the contributions of Neil, who designed and built the Scanivalve mechanical multiplexer control circuit, and Jason, who manufactured the end plates for the airfoil model.

Financial support for this work was provided by the Natural Sciences and Engineering Research Council of Canada and the Ontario Graduate Scholarship Program.

Table of Contents

List of Tables **xiii**

List of Figures **xix**

Nomenclature **xxi**

1 Introduction **1**

2 Background **5**

2.1 Low Reynolds Number Airfoil Operation 5

2.1.1 Structure of Transitional Separation Bubbles 9

2.2 Stability Theory 12

2.2.1 Stability of Separated Shear Layers 14

2.2.2 Approaches to Linear Stability Analysis of Measured Separated Shear Layer Profiles 16

2.3 Influence of Experimental Setup 17

2.3.1 End Plates on Aerodynamic Models 17

2.3.2 Test Section Wall Interference 19

2.3.3 Hot-Wire Measurements in Separation Bubbles 21

2.4 Surface Pressure Measurements with Embedded Sensors 23

3 Experimental Methodology **25**

3.1 Experimental Setup 25

3.1.1 NACA 0018 Airfoil Model 27

3.1.2 End Plate Design 29

3.2 Measurement Techniques 29

3.2.1 Static Pressure Measurements 30

3.2.2 Velocity Measurements 30

3.2.3 Microphone Measurements 31
3.3 Wall Adaptation 33
3.4 Flow Visualization 35

4 Sensitivity of Linear Stability Analysis of Separated Shear Layers 37
4.1 Numerical Methods 38
4.2 Rayleigh Equation Solutions using Experimental Profiles Directly 40
4.3 Rayleigh Equation Solutions for Curve Fits to Experimental Profiles 45
4.4 Solutions to the Orr-Sommerfeld Equation for Experimental Profiles 53

5 Effect of Experimental Setup on Flow Development 63
5.1 End Plate Configuration 63
5.2 Blockage 73
5.3 Intrusive Techniques 82
5.3.1 Influence of the Hot-Wire Probe and Traverse 82
5.3.2 Effect of Opening the Wind Tunnel Door 86

6 Boundary Layer Development 87
6.1 Flow Visualization 87
6.2 Boundary Layer Measurements 96
6.3 Instability of the Laminar Separated Shear Layers 117

7 Conclusions 133
7.1 Sensitivity of Linear Stability Analysis 133
7.2 Effect of Experimental Setup 135
7.3 Separated Shear Layer Development 136

8 Recommendations 139

PERMISSIONS 143

REFERENCES 147

APPENDICES 161

A Experimental Uncertainty 163
A.1 Uncertainty in Experimental Setup 163
A.2 Hot-Wire Uncertainty 165
A.3 Uncertainty in Static Pressure Measurements 169

A.4 Microphone Measurement Uncertainty 172
A.5 Uncertainty in SLW Configuration 173

B End Plate Design 175
B.1 End Plate Drawings 176

C Scanivalve Control System 183

D Wall Adaptation Strategy 189
D.1 Estimating the Imaginary Velocity Field 191
  D.1.1 Potential Flow Estimate 192
D.2 Determining Wall Contours 193

E Additional WAS Results 195

F LST Solvers 199
F.1 PWL Method 199
F.2 RK Integration 200
  F.2.1 An Alternative to the Rayleigh Equation for Inviscid LST 201
  F.2.2 Compound Matrix Method 203
F.3 FD Formulation 204
F.4 Chebyshev Collocation Formulation 204
F.5 Companion Matrix Method 207

G Intrusiveness of Flow Visualization 209

List of Tables

4.1 Comparison of measured growth rate spectrum to Rayleigh equation predictions using various solution methods directly on experimental profiles 45
4.2 Definitions of velocity profile curve fits 46
4.3 Curve fit residuals and error parameters for Rayleigh equation solutions on one hundred discrete profiles, created by imposing data scatter on the simulated profile from Eqs. 4.1 and 4.2 with $\Delta y/\delta^* = 5.6 \times 10^{-2}$ 49
4.4 Average and maximum error in the frequency of maximum disturbance growth rate predictions from Fig. 4.7 53
4.5 Error parameters for stability analysis of one hundred discrete profiles, created by imposing data scatter on the simulated profile from Eqs. 4.1 and 4.2 with $\Delta y/\delta^* = 5.6 \times 10^{-2}$ 58

5.1 Blockage ratio, B, for various angles of attack with and without end plates installed 73
5.2 Strouhal number variation with wall configuration for $AOA = 15°$ and $b/c = 2.0$ 81

6.1 Characteristic parameters of profiles used in linear stability calculations . . 118
6.2 Summary of flow development in the separation bubble 125

A.1 Summary of measurement uncertainty estimates 164

C.1 Description of labels in Fig. C.1 184
C.2 Description of terminal wires in Fig. C.2 185

List of Figures

2.1 Illustration of low Reynolds number airfoil flow regimes 6
2.2 Reynolds number and angle of attack dependence of separation and reattachment locations for a NACA 0018 airfoil 7
2.3 Time averaged transitional separation bubble model 9

3.1 University of Waterloo adaptive-wall wind tunnel 26
3.2 Airfoil model with end plates and end caps installed 28
3.3 Definition of coordinate systems 28
3.4 Hot-wire positioning traverse 32
3.5 Illustration of the WAS concept 33
3.6 Sketch of the smoke-wire flow visualization setup 36

4.1 Comparison of Rayleigh equation eigenvalue spectrum predictions for the simulated profile, computed using various solution methods directly on discrete profiles 41
4.2 Comparison of Rayleigh equation streamwise velocity fluctuation profile predictions at $\omega\delta^*/U_e = 1.17$ for the simulated profile of $\Delta y/\delta^* = 5.6 \times 10^{-2}$, computed using various solution methods directly on discrete profiles . . . 42
4.3 Second standard deviation bands of Rayleigh equation growth rate and wave number predictions computed using various solution methods directly on one hundred simulated discrete profiles with $\Delta y/\delta^* = 5.6 \times 10^{-2}$ and imposed data scatter 43
4.4 Eigenvalue spectrum of the Rayleigh equation using various curve fits to the simulated velocity profile of Eqs. 4.1 and 4.2 with $\Delta y/\delta^* = 5.6 \times 10^{-2}$ . . . 47
4.5 Variability in Rayleigh equation eigenvalue spectra for various curve fit forms used in the analysis 50
4.6 Streamwise velocity fluctuation profile predictions of the Rayleigh equation at $\omega\delta^*/U_e = 1.17$, using curve fits on the simulated velocity profile 51

4.7 Computed Rayleigh equation growth rate spectra of various measured separated shear layer profiles 52
4.8 Eigenvalue spectra of the Orr-Sommerfeld and Rayleigh equations for the profile fit of Eqs. 4.1 and 4.2, compared to measurements 54
4.9 Mean velocity profile and streamwise velocity fluctuation amplitude profiles of the Rayleigh and Orr-Sommerfeld equations 55
4.10 Eigenvalue spectrum of the Orr-Sommerfeld equation using various forms of curve fits to the simulated velocity profile of Eqs. 4.1 and 4.2 with $\Delta y/\delta^* = 5.6 \times 10^{-2}$ 56
4.11 Variability of the Orr-Sommerfeld equation eigenvalue spectra for various curve fit forms due to profile data scatter 57
4.12 Streamwise velocity fluctuation profile predictions of the Orr-Sommerfeld equation at $\omega\delta^*/U_e = 1.17$, using curve fits on the simulated velocity profile from Eqs. 4.1 and 4.2 with $\Delta y/\delta^* = 5.6 \times 10^{-2}$ 59
4.13 Comparison of growth rate spectrum measurements to LST predictions for published measurements on a NACA 0025 airfoil 60

5.1 Streamwise distributions of surface pressure for the various end plate configurations 65
5.2 Variation in lift coefficient computed from the measured pressure distributions for the various end plate configurations 66
5.3 Upper surface spanwise pressure distributions for the various end plate configurations 68
5.4 Energy spectra of surface pressure fluctuations for various end plate configurations 69
5.5 Energy spectra of vertical velocity at $X/c = 2.7$ with various end plate configurations 70
5.6 Variation of ASW wall pressure distribution with end plate configuration for $AOA = 10^\circ$ 72
5.7 ASW contour and SLW contours for each angle of attack tested, with end plates installed at $b/c = 2.0$ 74
5.8 Wall pressure distributions in the GSW, ASW, and SLW configurations . . 75
5.9 Streamwise distributions of surface pressure for various wall configurations with end plates installed at $b/c = 2.0$ 77
5.10 Variation in lift coefficient computed from the measured pressure distributions for the various end plate configurations 78
5.11 Energy spectra of pressure fluctuations for various wall configurations . . . 80

5.12 Model surface pressure distributions with the hot-wire probe at various positions . . . 83
5.13 Energy spectra of surface pressure fluctuations with end plates installed at $b/c = 2.0$ and the hot-wire probe at various positions . . . 85

6.1 Smoke-wire flow visualization for $AOA = 0°$ . . . 88
6.2 Smoke-wire flow visualization for $AOA = 5°$ . . . 88
6.3 Smoke-wire flow visualization for $AOA = 10°$ . . . 89
6.4 Smoke-wire flow visualization for $AOA = 15°$ . . . 89
6.5 Wake profiles of mean velocity and RMS velocity measured at $X/c = 0.95$ with a normal hot-wire probe for $AOA = 10°$ and $Re_c = 10^5$ . . . 90
6.6 Boundary layer smoke-wire flow visualization and measured profiles for $AOA = 0°$ . . . 92
6.7 Boundary layer smoke-wire flow visualization and measured profiles for $AOA = 5°$ . . . 93
6.8 Boundary layer smoke-wire flow visualization and measured profiles for $AOA = 10°$ . . . 94
6.9 Boundary layer smoke-wire flow visualization and measured profiles for $AOA = 15°$ . . . 95
6.10 Model surface pressure distributions and associated estimates of separation, transition, and reattachment locations . . . 97
6.11 Boundary layer profiles of mean and RMS velocity for $AOA = 0°$ . . . 99
6.12 Boundary layer profiles of mean and RMS velocity for $AOA = 5°$ . . . 100
6.13 Boundary layer profiles of mean and RMS velocity for $AOA = 10°$ . . . 101
6.14 Boundary layer profiles of mean and RMS velocity for $AOA = 15°$ . . . 102
6.15 Boundary layer profiles in and around the separation bubble showing mean and RMS velocity for $AOA = 10°$ . . . 103
6.16 Estimated regions of reverse flow on the upper surface . . . 106
6.17 Estimated zero mean velocity contour and boundary layer thickness parameters for $AOA = 0$, 5, and 10° . . . 107
6.18 Estimated zero mean velocity contour and boundary layer thickness parameters for $AOA = 15°$ . . . 108
6.19 Streamwise development of RMS streamwise velocity, at $y = \delta^*$, and RMS surface pressure fluctuations, compared to locations of mean separation, transition, and reattachment . . . 110
6.20 Spectra of streamwise velocity fluctuations and surface pressure fluctuations for $AOA = 0°$ . . . 113

6.21 Spectra of streamwise velocity fluctuations and surface pressure fluctuations for $AOA = 5^\circ$ . . . 114
6.22 Spectra of streamwise velocity fluctuations and surface pressure fluctuations for $AOA = 10^\circ$ . . . 115
6.23 Spectra of streamwise velocity fluctuations and surface pressure fluctuations for $AOA = 15^\circ$ . . . 116
6.24 Measured velocity profiles and corresponding fits used in linear stability calculations . . . 119
6.25 Growth rate spectra from hot-wire measurements and surface pressure measurements compared to predictions of the Rayleigh equation and the Orr-Sommerfeld equation . . . 121
6.26 Percentage difference in the maximum disturbance growth rate prediction between viscous and inviscid linear stability analyses from several separated shear layer experiments . . . 122
6.27 Wave number spectra measured and computed from the Rayleigh equation and the Orr-Sommerfeld equation . . . 123
6.28 Comparison of measured convection speeds and computed phase speeds at the dominant frequencies of disturbance amplification . . . 126
6.29 Comparison of convection speed and phase speed measurements from various studies . . . 127
6.30 Streamwise velocity fluctuation amplitude profiles measured and computed from the Rayleigh and Orr-Sommerfeld equations for $AOA = 0^\circ$ . . . 128
6.31 Streamwise velocity fluctuation amplitude profiles measured and computed from the Rayleigh and Orr-Sommerfeld equations for $AOA = 5^\circ$ . . . 128
6.32 Streamwise velocity fluctuation amplitude profiles measured and computed from the Rayleigh and Orr-Sommerfeld equations for $AOA = 10^\circ$ . . . 129
6.33 Streamwise velocity fluctuation amplitude profiles measured and computed from the Rayleigh and Orr-Sommerfeld equations for $AOA = 15^\circ$ . . . 129
6.34 Streamwise velocity fluctuation phase shift profiles computed for the measured velocity profiles from the Orr-Sommerfeld equation . . . 131

C.1 Scanivalve mechanical multiplexer system pneumatic and electrical connection routing diagram . . . 185
C.2 Scanivalve mechanical multiplexer system control circuit . . . 186

D.1 Sketch of sources and sinks approximation for potential flow calculation . . . 192

E.1 Streamwise distributions of model surface pressure in the SLW configuration with only end caps installed 196
E.2 SLW contours with and without end plates installed and using the original and potential flow imaginary velocity field estimation methods 197
E.3 Wall pressure distributions with and without end plates installed and using the original and potential flow imaginary velocity field estimation methods 198

F.1 Convergence rate and variability due to data scatter for the alternative RK method applied directly to discrete velocity profile data 202

G.1 Response of mean surface pressure near the suction peak to opening the wind tunnel door for fifteen seconds 210
G.2 Time evolution of normalized energy spectra of pressure fluctuations measured with embedded microphones, with the wind tunnel door open for the time between the dashed lines 211

Nomenclature

AOA	angle of attack
$\mathbf{a}$	vector of a_j components
a_j	parameters to be determined in curve fit or potential flow calculations
$a_{k,j}$	curve fit parameters
a_n	strength of the n^{th} source in the potential flow model
B	model blockage ratio, computed as the quotient of projected model area, and the projected end plate area if they are installed, onto a streamwise normal plane, to the test section cross sectional area in the geometrically straight wall configuratio
b	spanwise distance between the end plates
C_k	coefficient matrix
$C_{k_{m,n}}$	(m,n) component of the C_k matrix
C_L	sectional lift coefficient, $C_L = L/q_\infty$
C_p	model pressure coefficient, $C_p = (P - P_\infty)/q_\infty$
$C_{p,w}$	wall pressure coefficient, $C_{p,w} = (P_w - P_\infty)/q_\infty$
$CPLF$	coupling factor in wall adaptation calculations
c	chord length
c_r	disturbance phase speed, $c_r = \omega\alpha_r / \left(\alpha_r^2 + \alpha_i^2\right)$
d	model height projected onto a flow normal plane
E_{pp}	normalized energy spectrum of surface pressure fluctuations
E_{vv}	normalized energy spectrum of vertical velocity component
F	function used in curve fit definitions
f	frequency
f^{peak}	frequency of maximum disturbance growth rate
G	function used in curve fit definitions
H	boundary layer thickness shape factor, $H = \delta^*/\theta$
h	streamline offset in potential flow model
I	identity matrix, with the same dimensions as C_0

i	imaginary unit, $i = \sqrt{-1}$
j	an index
k	an index
L	lift force per unit span
L_{DS}	length of the domain downstream of the test section included in the potential flow model
L_{TS}	length of the test section
L_{US}	length of the domain upstream of the test section included in the potential flow model
N	number of measurement locations
n	an index
P	mean surface pressure at a location on the model surface
P_w	mean surface pressure at a location on the test section wall
P_∞	free-stream static pressure
p	fluctuating component of pressure
$\tilde{p}$	root-mean-square surface pressure
p_m	m^{th} discrete point on the boundary contour in the potential flow model
q_∞	free-stream dynamic pressure, $q_\infty = \frac{1}{2}\rho U_\infty^2$
R	least squares residuals for fits on profiles with data scatter, normalized by the number of data points and the edge velocity, and expressed as a percentage
R_0	least squares residuals for fits on profiles without data scatter, normalized by the number of data points and the edge velocity, and expressed as a percentage
Re_c	chord Reynolds number, $Re_c = U_\infty c/\nu$
Re_x	Reynolds number based on the distance from the leading edge, $Re_x = U_\infty x/\nu$
Re_{δ^*}	Reynolds number based on edge velocity and displacement thickness, $Re_{\delta^*} = U_e\delta^*/\nu$
SF	scaling factor in wall adaptation calculations
Sp	smoothing parameter
St	Strouhal number based on projected model height and free-stream velocity, $St = fd/U_\infty$
T_n	n^{th} Chebyshev polynomial
t	time elapsed since data acquisition began
U	time averaged streamwise component of velocity
U_c	convection speed of pressure fluctuations
U_e	edge velocity

U_I	velocity along the boundary contour from the imaginary flow field in wall adaptation calculations
U_I^{new}	final computed value of U_I for the current iteration of the wall adaptation algorithm
$U_I^{new,c}$	intermediate value of U_I for the current iteration of the wall adaptation algorithm, after coupling is accounted for
$U_I^{new,s}$	intermediate value of U_I for the current iteration of the wall adaptation algorithm, after scaling is applied
U_I^{old}	U_I computed in the previous iteration of the wall adaptation algorithm
U_i	velocity at the mean profile inflection point
U_k	U value of the k^{th} discrete velocity profile location
U''_k	the finite difference approximation of the second derivative of the measured velocity profile at y_k
$U''_{\max}$	maximum magnitude of U'' from a curve fit to U data
U_n	velocity, U, at y_n
U'_n	dU/dy on the n^{th} piecewise linear velocity profile curve segment
U_R	velocity along the boundary contour from the real flow field in wall adaptation calculations
U_R^{old}	U_R measured in the previous iteration of the wall adaptation algorithm
U''_{RMS}	root-mean-square data scatter in second derivative of a measured velocity profile, defined by Eq. 4.3
U_∞	free-stream velocity
u	streamwise component of velocity fluctuations
$\tilde{u}$	root-mean-square of the streamwise velocity component
$\|u\|$	amplitude of streamwise velocity fluctuations at a particular y location
$\|u\|_k$	streamwise velocity fluctuation amplitude profile for the k^{th} velocity profile with data scatter
v	vertical component of velocity fluctuations
v_m	vertical component velocity fluctuations at y_m
v_w	computed velocity through the boundary contour in the wall adaptation algorithm
X	distance measured from the model axle in the streamwise direction
X_0	X location of the source of strength a_0 in the potential flow model
X_m	X coordinate of p_m in the potential flow model
X_n	X coordinate of the source of strength a_n in the potential flow model
X_p	X location of the hot-wire probe
X_{vo}	X location of the virtual origin of the wind tunnel wall turbulent boundary

x	distance from the leading edge of the airfoil model measured along the chord
$\check{x}$	integration variable in v_w calculation
x_p	x location of the hot-wire probe
x_R	x location of mean flow reattachment
x_S	x location of separation
x_T	x location of transition
Y	vertical distance from the model axle
Y_m	Y coordinate of p_m in the potential flow model
Y_p	Y location of the hot-wire probe
y	distance from the model surface
$\hat{y}$	transformed y coordinate system onto the Chebyshev polynomial domain, $\hat{y} = 2y/y_{\max} - 1$
y_k	y value of the k^{th} discrete velocity profile location
y_m	y location of the m^{th} profile point
$\hat{y}_m$	value of $\hat{y}$ at the m^{th} discrete profile point
$y_{\max}$	maximum y location included in stability calculations
y_n	y value at the connection point between piecewise linear velocity profile segments n and $n+1$
z	spanwise distance from the model mid-span plane towards the Lexan end plate side
α	complex disturbance wave number, $\alpha = \alpha_r + i\alpha_i$
α_i	disturbance attenuation rate
α_i^{peak}	negative of the maximum value of $-\alpha_i$
$\overline{\alpha_i^{\text{peak}}}$	average value of $\alpha_{i,k}^{\text{peak}}$ over the one hundred simulated profiles with data scatter
$\alpha_{i,k}$	growth rate spectrum predicted for the k^{th} velocity profile with data scatter
$\alpha_{i,k}^{\text{peak}}$	negative of the maximum value of $-\alpha_{i,k}$
α_r	disturbance wave number
α_r^{peak}	value of α_r corresponding to α_i^{peak}
Γ	notational vorticity in the wall adaptation calculations
γ	shear layer profile angle, defined as $\gamma = \arctan\left(dy/dU\right)$ at the mean profile inflection point
ΔY	vertical displacement of an adjustable wall from the geometrically straight wall configuration
Δy	discrete velocity profile point spacing
$\Delta\left(\frac{dY}{dX}\right)$	change in the wall slope computed in the wall adaptation calculations

δ_0	non-zero y location at which $U/U_\infty = 0$
δ_e	edge thickness, i.e., the y location at which $U = U_e$
δ^*	boundary layer displacement thickness on the model, $\delta^* = \int_0^{\delta_e}(1-U/U_e)\text{dy}$
δ^*_w	boundary layer displacement thickness on the test section walls, $\delta^*_w = \int_0^{\infty}(1-U/U_\infty)\text{dy}$
$\overline{\varepsilon}_\alpha$	average percentage error in the maximum disturbance growth rate over one hundred simulated profiles with data scatter, as defined by Eq. 4.4
ε_ν	percentage difference in the maximum disturbance growth rate prediction between viscous and inviscid linear stability analyses
$\overline{\varepsilon}_\Sigma$	average percentage integrated growth rate spectrum error, based on one hundred simulated profiles with data scatter, as defined by Eq. 4.6
ε_ω	percentage error in the frequency of the maximum disturbance growth rate
$\overline{\varepsilon}_\omega$	average percentage error in the frequency of maximum disturbance growth rate, based on one hundred simulated profiles with data scatter, as defined in Eq. 4.5
η	non-dimensional vertical coordinate, $\eta = y/a_1$
Θ_m	variables in the compound matrix method calculations
θ	boundary layer momentum thickness, $\theta = \int_0^{\delta_e} U/U_e(1-U/U_e)\text{dy}$
λ	disturbance wave length
ν	kinematic viscosity
ξ	transform parameter used in Chebyshev collocation method derivation, $\xi = 2/y_{\text{max}}$
ρ	density of air in the test section
ϕ	modal streamwise velocity fluctuation phase, shifted to a maximum along the profile of 2π rad
χ	variable grouping in compound matrix method derivation, $\chi = \sqrt{\alpha^2 + i\alpha Re_{\delta^*}(1-\omega/\alpha)/(U_e\delta^*)}$
ω	angular frequency of disturbance
ω_i	imaginary part of ω, corresponding to the temporal amplification rate of disturbances
$\overline{\omega^{\text{peak}}}$	average value of ω_k^{peak} over the one hundred simulated profiles with data scatter
ω_k^{peak}	value of ω corresponding to $\alpha_{i,k}^{\text{peak}}$
ω_{max}	maximum angular frequency for which disturbances are unstable in the averaged growth rate spectrum

Chapter 1

Introduction

Various engineering systems, including unmanned aerial vehicles and small wind turbines, employ airfoils operating in the chord Reynolds number range from 10^4 to 5×10^5 (Refs. [1–4]). The aerodynamic performance of such airfoils is often a concern because of the low lift and high drag generated at low Reynolds numbers [4]. Airfoil geometry optimization as well as passive and active flow control systems are being explored to improve the performance of devices using low Reynolds number airfoils [5, 6]. Each of these techniques requires a detailed understanding of flow development, which is being provided by continuing experimental and computational studies.

Laminar boundary layer separation is the main impediment to low Reynolds number airfoil performance [7]. In contrast to airfoil operation at higher Reynolds numbers, at low Reynolds numbers the boundary layer on the upper surface often remains laminar downstream of the point of minimum surface pressure, where an adverse pressure gradient opposes the oncoming flow [8]. As a result, laminar boundary layer separation is common. The laminar separated shear layer is highly unstable, leading to turbulent transition shortly downstream of the separation point. At sufficiently low Reynolds numbers or high angles of attack, the turbulent separated shear layer remains detached, leaving the airfoil in a stalled state and resulting in very poor aerodynamic performance [1]. At higher Reynolds numbers or lower angles of attack, the turbulent flow reattaches to form a turbulent boundary layer on the aft portion of the airfoil, significantly improving aerodynamic performance. Studies on performance improvement therefore generally focus on controlling the separated flow region [5]. Such work relies on knowledge of flow development in the separated region.

The focus of this experimental investigation is transition in the laminar separated shear layer that forms over an airfoil operating at a low Reynolds number. The feasibility of using an embedded pressure sensor array to measure disturbance development is also of interest. Before proceeding to acquire detailed measurements of flow development, various aspects of the experimental setup and analysis tools will be investigated to ensure the reliability of the results.

Previous studies have demonstrated that low Reynolds number airfoil experiments are sensitive to the experimental setup [3, 9, 10]. These investigations have mainly focused on the effect of free-stream turbulence on flow development. Other aspects of the experimental setup that are known to affect flow development include end plate design and position [11–14], test section wall interference [15–20], and intrusive equipment such as hot-wire probes [21]. The effects of these factors have been studied for circular cylinders, and the conclusions of such studies are used as general guidelines for other model geometries [14–16, 21]. However, the applicability of these guidelines for low Reynolds number experiments on two-dimensional airfoils has not been thoroughly assessed. The strong influence of the separated flow region on measured aerodynamic performance and the sensitivity of this region to experimental conditions makes such an assessment valuable.

Experimental and computational studies on transition in separation bubbles often compare results to predictions of linear stability theory (LST) to provide insight into the mechanisms governing the initial stage of transition, assess the validity of this stability model, or evaluate the predictions of transition models [22–32]. However, it has been shown that for separated shear layer velocity profiles, such solutions are sensitive to the method of analysis [33, 34]. Experimental data scatter also contributes to the uncertainty in such calculations. This uncertainty should be estimated before drawing conclusions from linear stability predictions.

With confidence in the experimental setup and analysis tools established, detailed measurements of flow development over the model will be completed. An embedded surface pressure sensor array will be used for some of these measurements, and will be evaluated based on its capabilities for measuring flow development over airfoils. Surface pressure sensor arrays can provide simultaneous measurements at high sample rates and multiple spatial locations, in significantly less time than is required for detailed velocity measurements over the model surface. This may be an acceptable compromise in parametric studies in which more detailed information than lift and drag coefficients is desired but for which full flow field mapping is not required. Surface pressure sensor arrays also have potential for in-flight flow diagnostics as a method to monitor sources of aerodynamic noise or performance variation, and could be used as an active feedback method for flow control systems [35]. Gerakopulos [35] developed a NACA 0018 airfoil model with an embedded pressure sensor array to explore the feasibility of such a system for real-time flow diagnostics. Part of the present investigation will extend this work, focusing on the potential for pressure sensor arrays to measure disturbance development over the airfoil. Detailed measurements of flow development, complemented by theoretical stability predictions, will be used to validate the results.

The purpose of this investigation is to gain insight into shear layer development over low Reynolds number airfoils through a detailed experimental study on a NACA 0018 airfoil model. Uncertainty due to the experimental setup and stability analysis tools affect the reliability of these results, and will therefore be examined prior to completing detailed measurements. The objectives of this thesis are further subdivided below:

1. Conduct a sensitivity analysis on approaches to performing spatial linear stability analysis on measured separated shear layer velocity profiles, in order to,
    (a) identify systematic approaches to the analysis which are relatively insensitive to velocity profile data scatter,
    (b) estimate the uncertainty in such calculations, and
    (c) evaluate the importance of including viscous effects in the analysis;
2. Assess the influence of experimental setup on flow development, specifically considering,
    (a) the effect of end caps and end plates as well as the effect of end plate spacing,
    (b) the effect of test section blockage, and
    (c) the effect of the hot-wire probe, traversing mechanism, and the smoke-wire flow visualization technique;
3. Investigate flow development over the airfoil at various angles of attack in detail, including an assessment of the feasibility of using an embedded surface pressure sensor array to measure transition characteristics in the separated shear layer.

Chapter 2

Background

The main focus of this thesis is airfoil operation at low Reynolds numbers, with particular attention to the process of transition in the separated shear layer that develops in this Reynolds number regime. General findings on this topic from previous studies are discussed below. The present investigation also considers the sensitivity of linear stability analysis, a common tool used in experimental separation bubble research, and the effect of various aspects of the experimental setup on such experiments. These topics are also discussed. Finally, a brief review of embedded surface pressure sensor measurement techniques is provided.

2.1 Low Reynolds Number Airfoil Operation

Airfoils operating at low chord Reynolds numbers (i.e., $10^4 \lesssim Re_c \lesssim 5\times10^5$) are susceptible to laminar boundary layer separation as a result of an adverse pressure gradient acting on the flow [1, 2]. The laminar separated shear layer is sensitive to free-stream disturbances and will generally transition to turbulent flow shortly downstream of the separation point. Depending on the flow conditions, the turbulent shear layer can remain separated or reattach to form a turbulent boundary layer. Airfoil operation at low Reynolds numbers is typically categorized based on whether boundary layer reattachment occurs, because this is a major factor contributing to aerodynamic performance [9]. Important features of both low Reynolds number airfoil flow regimes are illustrated in Fig. 2.1.

For flow conditions at which turbulent transition on the suction side is followed by boundary layer reattachment, a closed region of recirculating flow, called a separation bubble, is formed. Depending on its size and location, a separation bubble can either reduce lift compared to that produced in fully turbulent flow over the airfoil by reducing

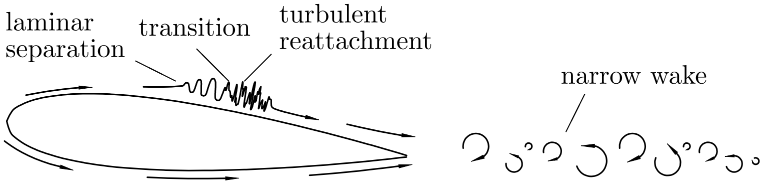

(a) separation followed by reattachment

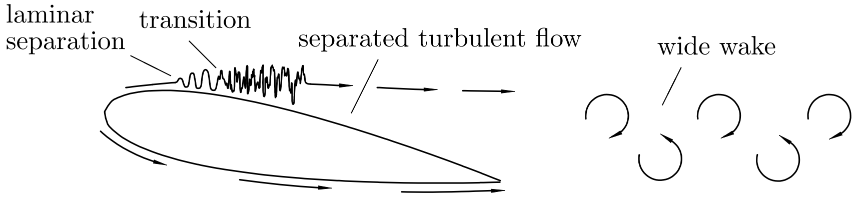

(b) separation without reattachment

Figure 2.1: Illustration of low Reynolds number airfoil flow regimes.

the maximum suction pressure [36, 37], or can increase lift by creating a region of higher suction in the vicinity of the separation bubble [30]. The reattached turbulent boundary layer downstream of the separation bubble will generally be thicker than would result from attached boundary layer transition, increasing pressure drag and possibly resulting in earlier turbulent boundary layer separation [38]. Although the thicker boundary layer reduces skin friction drag, the net effect is typically an increase in total drag [30]. When shear layer transition is not followed by reattachment, the airfoil is left in a stalled state, resulting in poor aerodynamic performance [8]. At low Reynolds numbers, airfoils can stall at relatively low angles of attack.

Detailed information about aerodynamic performance and flow development over low Reynolds number airfoils are important in the design of lifting surfaces and flow control systems for this flow regime. A detailed aerodynamic characterization for the NACA 0018 airfoil model used in this thesis is presented in Ref. [39]. Consistent with the general trends for other airfoils at low Reynolds numbers [8], it was found that as the angle of attack is increased at a constant Reynolds number, the separation bubble moves upstream and decreases in length; above a critical angle of attack, the turbulent shear layer fails to reattach [39]. Increasing the Reynolds number at a fixed angle of attack has a less significant effect on the separation location, but reduces the separation bubble length; below a critical value of Reynolds number, the separated shear layer fails to reattach.

These trends can be observed in Fig. 2.2, which presents data for the NACA 0018 airfoil model used in the present investigation.

For each Reynolds number, there is a critical angle of attack at which a small increase in angle will cause an abrupt change between flow regimes of separation with reattachment and separation without reattachment [1, 2]. A similar abrupt change can be observed at a constant angle of attack by decreasing the Reynolds number below a critical value. This phenomenon was first noted by Gaster [40] for the separated flow region over a flat plate with an imposed pressure gradient. Gaster [40] referred to the dramatic increase in separation bubble length or the complete loss of boundary layer reattachment, following a small change in experimental parameters, as bubble bursting.

Applying low Reynolds number airfoil performance data in design can be an issue due to several factors. Experiments on airfoils at low Reynolds numbers are very sensitive to the angle of attack, Reynolds number, and free-stream turbulence [3]. Furthermore, these experiments typically involve very low forces and pressures, which are difficult to measure

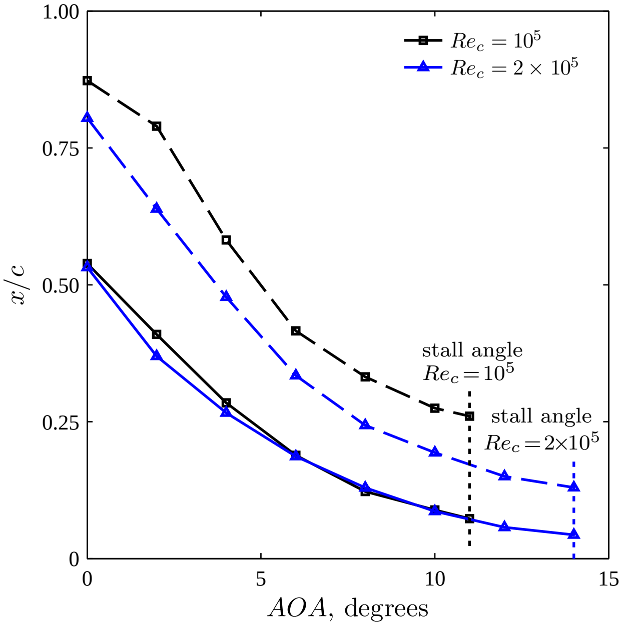

Figure 2.2: Reynolds number and angle of attack dependence of separation (solid lines) and reattachment (dashed lines) locations for a NACA 0018 airfoil. Markers identify measured data points from Gerakopulos et al. [39] and the present investigation.

accurately [3]. Some of these issues are discussed further in Section 2.3. Hysteresis in aerodynamic forces with angle of attack and Reynolds number is another concern [9,10,41]. Hysteresis in airfoil performance at low Reynolds numbers refers to the dependence of boundary layer reattachment, and as a result, airfoil lift and drag coefficients at a particular Reynolds number and angle of attack, on whether these parameters were approached from higher or lower values. This dependence is an important factor in stall recovery. Hysteresis was measured to extend over angles of attack of more than 10° by Mueller [9] for a Lissaman 7769 airfoil at $Re_c = 1.5 \times 10^5$ and by Marchman [10] for a Wortmann FX63-137 airfoil at $Re_c = 2 \times 10^5$. By increasing the free-stream turbulence intensity from 0.07% to 0.28% by means of screens and flow restrictors, Mueller [9] was able to reduce the extent of hysteresis and eventually eliminate it. This change in turbulence intensity also had the effect of increasing the maximum lift coefficient by 3%. The implication of the significant effect of turbulence intensity on hysteresis is that the extent of the hysteresis loop will be affected by the facility in which measurements are performed. Other considerations for micro air vehicle design include the low aspect ratio wing sections required in certain applications [42], the significant variation in atmospheric turbulence intensity [43, 44], as well as gusts and lulls on the order of the flight speed [45].

The relatively poor aerodynamic performance and wide variation in operating conditions for airfoils at low Reynolds numbers makes the use of flow control systems attractive. An example of a simple passive flow control method is to install standard vortex generators near the leading edge of the airfoil to establish a turbulent boundary layer. This can improve aerodynamic performance for some flow conditions, but can cause an undesirable increase of skin friction drag by replacing the laminar boundary layer upstream of the separation point with a turbulent one [46]. Furthermore, such vortex generators have the disadvantage of not being adaptable as flow conditions change. Various other techniques have been considered for low Reynolds number airfoil flow control. Typically these methods seek to move the separation point farther downstream or accelerate the transition process [5]. Methods of separation control include wall suction, to reduce the boundary layer thickness [5]; use of plasma actuators, which generate a body force in the flow to maintain an attached boundary layer [47]; and specific geometry design to optimize performance at low Reynolds numbers, as in the design of the SD 7003 airfoil [5, 48]. Acoustic excitation [5, 22, 49] and oscillating piezoceramic actuators [46] have shown promise in controlling transition in separation bubbles. Both of these methods create disturbances at particular frequencies and locations, accelerating natural shear layer transition. It has been demonstrated that such approaches can induce turbulent reattachment in flows that would otherwise remain separated, significantly improving aerodynamic performance [22, 50]. In a numerical simulation of flow over a NACA 0012 airfoil at $AOA = 5°$ and $Re_c = 5 \times 10^4$, for which a separation bubble formed without forced excitation, Jones et al. [30] predicted that although lift was decreased through forcing at a particular frequency, an increase in the lift to drag ratio of 23% could be achieved. Such transition control methods have the potential to adapt to flow conditions to provide optimal control, and require very little energy input [51]. To realize this potential, active feedback methods are required and are an area of recent interest [35, 51].

2.1.1 Structure of Transitional Separation Bubbles

A model for time averaged transitional separation bubbles was proposed by Horton [36], and is presented in Fig. 2.3. On an airfoil at a low Reynolds number, the boundary layer on the upper surface remains laminar into the adverse pressure gradient region downstream of the suction peak. At some location in this region, the laminar boundary layer separates. The separated shear layer is more sensitive to small disturbances than the attached boundary layer upstream, and as a result, transition to turbulence commonly occurs in this region. Enhanced momentum transfer in the turbulent separated shear layer can lead to boundary layer reattachment downstream.

Through comparisons with velocity profile measurements in shear layers over low Reynolds number airfoils, it has been found that the locations of mean

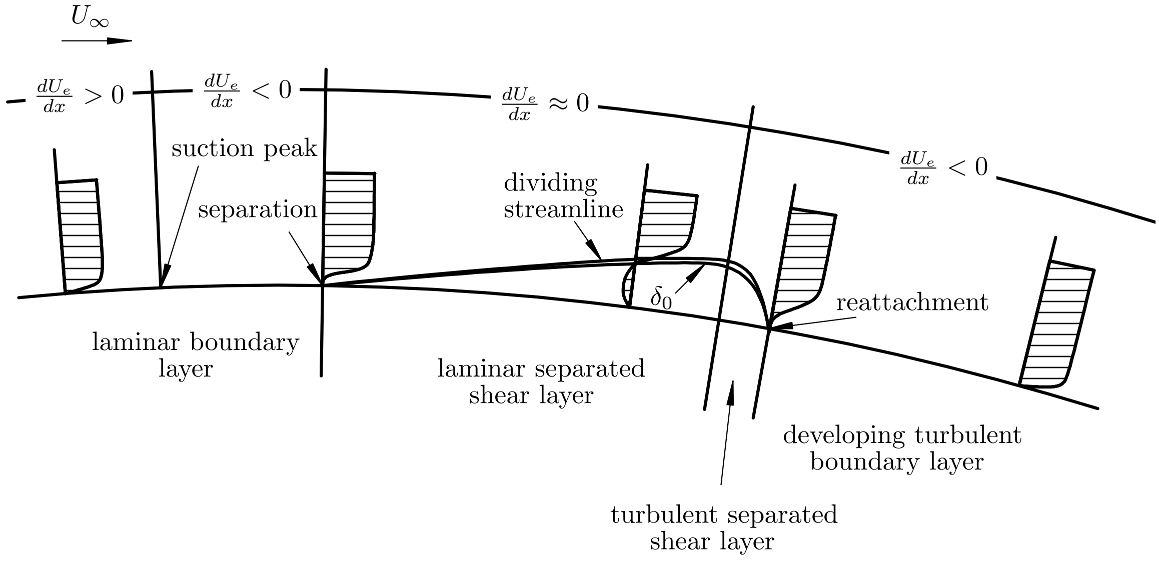
U_∞
$\frac{dU_e}{dx} > 0$
$\frac{dU_e}{dx} < 0$
$\frac{dU_e}{dx} \approx 0$
$\frac{dU_e}{dx} < 0$
suction peak
separation
dividing streamline
δ_0
reattachment
laminar boundary layer
laminar separated shear layer
developing turbulent boundary layer
turbulent separated shear layer

Figure 2.3: Time averaged transitional separation bubble model.

separation, transition, and reattachment can be approximated based on surface pressure distributions [8, 52, 53]. Tani [52] noted the existence of a mean surface pressure plateau between the separation and transition locations, which has zero slope for most conditions [38]. The separation and transition locations can be estimated as the start and end of this region, respectively. Downstream of the transition location, rapid pressure recovery occurs. The mean reattachment point can be estimated as the location where the rate of this pressure recovery slows, typically to the rate that would be observed in inviscid or fully turbulent flow over the geometry [8]. It has also been found that the point identified as the approximate transition location generally has the maximum boundary layer displacement thickness [53]. Boundary layer momentum thickness has been found to remain nearly constant upstream of the transition location, then abruptly change to have a positive slope downstream [53].

Laminar-to-turbulent transition in the separated shear layer is initiated by the amplification of background disturbances in the pressure and velocity fields within a band of unstable frequencies [54]. As disturbances grow, they begin to interact. This can lead to a secondary amplification of disturbances centered around subharmonics of the primary frequency of disturbance amplification. Disturbance interactions eventually cause the disturbance amplification rates to diminish to zero.

In the late stages of transition, shear layer roll-up has been observed in the separation bubbles over flat plates and airfoils in direct numerical simulations [30–32, 51, 55–57] and experiments [23, 37, 58, 59]. The vortex passing frequency has been shown to correspond to the central frequency of primary disturbance growth. Early numerical studies on separation bubbles over flat plates showed that vortex roll-up resulted from a Kelvin-Helmholtz instability of the separated shear layer [55]. This has been supported qualitatively by the observation of Kelvin's cat's eye vortex patterns in separation bubble experiments on a flat plate by Watmuff [23] and on an SD 7003 airfoil by Burgmann & Schröder [37]. Such patterns are common to free shear layers for which transition is governed by a Kelvin-Helmholtz instability mechanism [60].

Near the mean reattachment point, other coherent structures are observed. However, studies of unsteady flow development near the mean reattachment location have shown significant variations in flow phenomena with surface geometry and operating conditions. Under certain conditions, the reattachment process is relatively steady, with rapid breakdown to turbulence not accompanied by the shedding of large scale spanwise vortical structures [32]. In other cases, turbulent shear layer reattachment is an unsteady phenomenon, due to the shedding of large scale structures into the turbulent boundary layer. This unsteadiness is observed in direct numerical simulations [55] and flow visualization experiments [53] as a variation in the separation bubble height and length with time, and is referred to as bubble flapping.

Pauley et al. [55], based on a direct numerical simulation of the separation bubble over a flat plate, concluded that bubble flapping resulted from the shedding of roll-up vortices from the bubble. Other numerical studies on flat plates and airfoils have found that, even when the background disturbances are too small for convective instability to cause shear layer roll-up, separation bubble vortex shedding persists at a frequency that does not necessarily correspond to the dominant frequency of the Kelvin-Helmholtz instability [30, 31, 51, 56]. This difference between the shear layer instability frequency and the bubble shedding frequency has been observed experimentally in a transitional separation bubble forming behind a backward facing step [24]. Various explanations for the occurrence of separation bubble flapping at frequencies other than that of the primary disturbance amplification have been proposed. Based on a direct numerical simulation of flow over a NACA 0012 airfoil at $AOA = 5^\circ$ and $Re_c = 5 \times 10^4$, Jones et al. [30] suggest that bubble shedding can be self-sustained through an absolute instability of the shed vortices to three-dimensional disturbances. They later proposed that wave packets, which have developed though disturbance amplification in the separated shear layer, can undergo acoustic scattering at the trailing edge of the airfoil and induce higher initial disturbance amplitudes in the separated shear layer [31]. The upstream disturbance environment in the shear layer has a particular frequency character determined by a frequency-dependent receptivity of the shear layer at the leading edge, providing a possible explanation for why bubble shedding was observed at a frequency of almost one-third of the central instability frequency. Marxen & Rist [56], based on a direct numerical simulation of the separation bubble on a flat plate, suggest that bubble shedding could be a transient effect of varying levels of free-stream disturbances. They explain that the free-stream disturbance level affects the transition location, and hence, the separation bubble height and length. The separation bubble shape influences the upstream pressure distribution imposed on the shear layer by the external irrotational flow, and as a result, the location of boundary layer separation. Each of these factors also influence the dominant shear layer instability frequency and disturbance amplification rates. Through this viscous-inviscid interaction, the flow takes time to adjust to changes in the free-stream disturbance level. Bubble flapping could therefore be caused by the constantly varying free-stream disturbance field observed in actual flows, which would result in continuous changes in the bubble shape. In other studies, it has been suggested that the observed self-sustained bubble shedding in numerical simulations could be a result of insufficient solution convergence [51].

Recent experimental studies have examined bubble shedding and coherent structures forming near the mean reattachment point in separation bubbles. For the separation bubble forming on a flat plate with an imposed pressure gradient, Watmuff [23] observed the center of shed vortices moving away from the surface into the higher speed free stream, causing the formation of detached vortex loops with legs pointing upstream and towards the surface. Burgmann et al. [58] did not observe such structures in the separation bubble of an SD 7003 airfoil at $Re_c = 2 \times 10^4$ and $AOA = 4^\circ$, leading them to conclude that surface curvature has a significant effect on coherent structure development in the transition region. They instead identified several common vortical structures which emerged through the transition process, and further verified the existence of these structure at other Reynolds numbers and incidence angles [37, 58, 59]. Vortex shedding from the separation bubble was identified and, in some cycles, vortex pairing was observed, as is commonly seen in free shear layer transition [60]. Spanwise vortices shed from the separation bubble were observed to fragment into vortices with spanwise lengths on the order of $0.1c$. It was speculated that this fragmentation resulted from the variation in vorticity across the span. These fragmented vortices were observed to develop a c-shaped structure, with legs directed downstream and away from the surface. It was explained that momentum transfer from the free stream towards the wall due to vortex circulation causes deceleration of the vortex center, deforming the spanwise vortices into c-shaped vortex structures. These structures had no spanwise regularity and were found to interact with each other. At a chord Reynolds number of 6×10^4, the increased free-stream fluid entrainment caused the c-vortices to split at the center, creating counter-rotating screwdriver vortices with greatest strength in the streamwise direction [59]. Screwdriver vortices were seen to interact and form Λ-shaped structures [37], though distinct from the regular Λ-vortex pattern typically observed in boundary layer transition [24, 61–63]. Just downstream of the mean reattachment location, the large scale vortex structures burst, ejecting fluid away from the wall. Rapid breakdown to small scale turbulence was observed just downstream of vortex bursting.

2.2 Stability Theory

Stability theory has provided many tools to help understand the onset of transition in separated shear layers [64]. This section reviews some basic concepts of stability theory and outlines some of the results obtained for transitional separation bubbles.

Linear stability theory (LST) provides a model for the amplification of small amplitude disturbances in a laminar flow [33, 65–67]. This model is derived from the Navier-Stokes equations under various simplifying assumptions. Velocity components are separated into a mean base flow and time dependent fluctuation terms. The mean base flow is assumed to be parallel. It is further assumed that the velocity fluctuations can be decomposed into normal modes across a frequency spectrum. This is done by assuming that each disturbance component develops as a traveling wave and that separate modes do not interact. Finally, it is assumed that the disturbance amplitude is small, so that products of fluctuations in the equations can be neglected. This leads to the Orr-Sommerfeld equation [61]:

$$(U - \omega/\alpha)\left(v'' - \alpha^2 v\right) - U'' v = -\frac{iU_e \delta^*}{\alpha Re_{\delta^*}}\left(v'''' - 2\alpha^2 v'' + \alpha^4 v\right), \tag{2.1}$$

where primes indicate differentiation with respect to y. For a separated shear layer, no-slip and impermeability conditions are enforced on the velocity fluctuation components at the wall. Furthermore, disturbances are assumed to decay to zero far from the wall [61]. These conditions are expressed as,

$$v(0) = v(\infty) = v'(0) = v'(\infty) = 0. \tag{2.2}$$

Equations 2.1 and 2.2 form an eigenvalue problem with v as the eigenfunction [33,65–67]. Non-trivial solutions can only be obtained for certain combinations of α and ω. The problem can be solved by specifying one of these parameters and finding solutions for the other. When α is selected, and set to a real value, the solution corresponds to temporal amplification, with disturbance growth occurring for positive values of ω_i. This type of disturbance growth therefore corresponds to an absolute instability. When ω is selected, and set to a real value, spatial disturbance amplification rates are computed, with negative values of α_i identifying disturbance growth. This formulation corresponds to convective instabilities.

Viscosity, present in Eq. 2.1 through the Reynolds number, can have a stabilizing or destabilizing effect on laminar flows [65]. For laminar boundary layers, no disturbance amplification is predicted from Eqs. 2.1 and 2.2 in the limit of zero viscosity; however, flow instability is predicted for finite Reynolds numbers [65]. For such flows, viscosity has a strong destabilizing effect. In contrast, free shear layers show maximum amplification in the limit of zero viscosity, with lower growth rates predicted when viscous effects are accounted for [60,67]. Early linear stability calculations only considered the inviscid limit to simplify the problem [65,66,68]. The simplified governing equation is referred to as the Rayleigh equation [66]:

$$v'' - \left(\frac{U''}{U - \omega/\alpha} + \alpha^2\right) v = 0. \tag{2.3}$$

Since this equation is second order, only two boundary conditions can be imposed. Typically, vertical velocity fluctuations are assumed to be zero at the wall and in the free stream [66]:

$$v(0) = v(\infty) = 0. \tag{2.4}$$

The Rayleigh inflection point theorem states that it is a necessary, but not a sufficient condition, that a velocity profile exhibiting inviscid temporal instability, have an inflection point [33]. Fjørtoft's theorem further specifies that a necessary, but not a sufficient condition, for a flow to be susceptible to inviscid temporal instability is that $U''(U - U_i) < 0$ somewhere on the profile [33]. Although these theorems do not have viscous or spatial equivalents, the importance of the base profile inflection point on inviscid stability is commonly used to distinguish inviscid instability from purely viscous mechanisms [60, 67].

LST is the most commonly applied stability analysis tool employed to understand measured transitional separation bubble development [22, 24–27, 29–32]. More advanced stability analysis tools, such as secondary stability analysis and the parabolized stability equations (PSE), have been applied in theoretical and numerical studies on transitional separation bubble development [31, 64, 69–72].

Secondary stability analysis was developed to explain the spanwise periodicity, exemplified by Λ-vortex structures, observed shortly downstream of the initial onset of instability in attached boundary layer transition [61, 73]. This theory is similar to LST, except the laminar base flow is modulated by the time varying instability waves computed from the primary analysis, with amplitudes estimated from the free-stream disturbance levels [67]. Similar to LST, a modal decomposition is assumed and non-linear fluctuation terms are neglected [61, 74]. Secondary stability theory is considered a pseudo-non-linear model because the modulated mean profile is taken into account [67].

The PSE are derived from the Navier-Stokes equations by separating the flow into mean and fluctuating components [66, 67, 75, 76]. Fluctuations are decomposed into normal modes, with a spatially dependent wave number. It is assumed that downstream disturbance growth does not affect upstream development. The amplitude of fluctuations are assumed to vary much more gradually in the streamwise direction than in the vertical direction, simplifying the governing equations to a parabolic system [67]. These assumptions inherently limit the applicability of the PSE to convectively unstable flows [75]. As compared to LST, the PSE allow non-linear terms to be included, a non-parallel base flow to be analyzed, and upstream disturbance growth to be accounted for [75]. Furthermore, background turbulence character can be modeled through the inclusion of forcing terms in the system of equations. However, solution of the PSE requires two component base velocity profiles, not available from normal hot-wire measurements.

2.2.1 Stability of Separated Shear Layers

The stability of laminar separation bubbles was first examined by applying LST to analytical velocity profiles selected to resemble separation bubble profiles [34, 77–79]. It was found that the spatial growth rate spectrum was roughly bounded between those for the Blasius boundary layer and a free shear layer, with a higher central frequency and corresponding growth rate associated with the free shear layer [24, 78]. With increasing boundary layer shape factor, the shear layer thickens and the stability spectrum approaches that of a free shear layer. As the shape factor decreases, viscous effects become stronger and the growth rate spectrum approaches that of an attached boundary layer [24]. Thus, inviscid stability analysis can provide accurate predictions for thick separation bubbles, but viscous effects need to be accounted for in thinner bubbles [34]. Computed LST growth rate spectra for approximate separation bubble profiles were used in various transition location prediction algorithms [78, 80]. These predictions often apply the e^N method, in which the growth rate is integrated in the streamwise direction, and transition is predicted where the amplitude of disturbances have increased by a factor selected based on experimental data [63]. Recent experimental and numerical investigations of transition in separation bubbles show that these approaches can accurately predict the transition location [28]. Dovgal et al. [34] demonstrated that, for a particular family of approximate separation bubble profiles, the linear growth of disturbances at the dominant frequency of instability had maximum growth in the streamwise direction. Experiments on a separation bubble on a flat plate by Lang et al. [25], in which disturbances with spanwise periodicity were imposed, showed that two-dimensional growth dominated oblique wave development, supporting the theoretical predictions of Dovgal et al. [34]. From experimental measurements on separation bubbles forming behind backward facing steps, Dovgal et al. [34] concluded that non-linear disturbance growth is not observed until disturbance amplitudes reach approximately 1% of the free-stream velocity. Based on a comparison of the results of a two-dimensional direct numerical simulation with linear stability analysis predictions, Pauley et al. [55] and Lin & Pauley [57] concluded that an inviscid instability mechanism dominated transition in the separation bubble on a flat plate.

Spatial linear stability analysis assumes convective instability of the flow. A number of theoretical investigation have examined this assumption and concluded that, for separated shear layers with maximum reverse flow speeds exceeding roughly 15 to 30% of the free-stream velocity, the laminar shear layer can become absolutely unstable [64, 70, 71]. Rist et al. [54] compared instability growth in the separation bubble on a flat plate computed from direct numerical simulation, LST predictions, and secondary stability analysis. Consistent with the work of Dovgal et al. [34], they found that once primary instability caused disturbances to reach amplitudes on the order of 1% of the free-stream speed, non-linear development caused the growth of harmonic and subharmonic modes, which were reasonably predicted by secondary stability analysis up to the saturation point of linear growth. In contrast to attached boundary layer instability, in which secondary amplification rates of ten times that of primary disturbance growth are predicted, they found secondary amplification rates in the separated shear layer to be only twice that of primary growth. As such, the secondary instability of separated shear layers is less significant than that of attached boundary layers, and can be difficult to detect. Based on direct numerical simulation results, Rist et al. [54] determined that, at the streamwise location where primary growth saturates, the growth of three-dimensional disturbances through secondary instability is reduced significantly. Furthermore, up to this point, the linear stability predictions accuracy matched the simulation prediction of disturbance growth at the fundamental frequency.

Theofilis et al. [64] compared predictions of LST, solutions to the PSE, and results from a direct numerical simulation of a separation bubble on a flat plate. They found that the PSE solutions very closely matched direct numerical simulation results, and that LST provided accurate predictions of primary disturbance growth. This suggests that non-parallel flow effects do not significantly contribute to disturbance growth in separation bubbles [30, 64].

2.2.2 Approaches to Linear Stability Analysis of Measured Separated Shear Layer Profiles

Beyond a purely theoretical study of separation bubble transition, LST has been applied to understand measured separation bubble transition in a number of investigations of flow over flat plates and low Reynolds number airfoils [22–32]. Despite neglecting three-dimensional and non-linear interactions [54,73] as well as non-parallel flow effects [31,81], LST has been shown to provide meaningful predictions for measured separation bubbles [24]. Linear theory has been shown to accurately predict the two-dimensional fundamental growth up to non-linear saturation [54]. Furthermore, a number of investigations have linked linear Kelvin-Helmholtz wave growth to observed modal disturbance profiles, shear layer roll-up, and separation bubble shedding [22–26, 37, 55]. When applied to normal hot-wire measurements, linear stability analysis has a distinct advantage over more advanced models, in that it only requires a single component velocity profile for the calculations.

Spatial linear stability analysis has been applied to measured separated shear layer velocity profiles by Nishioka et al. [22] and Lang et al. [25] for flat plates and by LeBlanc et al. [27] and Yarusevych et al. [26, 29] for airfoils operating at low Reynolds numbers. In each of these investigations, the measured velocity profile was processed differently for use in linear stability calculations. Nishioka et al. [22] devised a logistic series curve fit which accurately matched the measured data. Yarusevych et al. [26,29] applied smoothing spline fits to their velocity data. LeBlanc et al. [27] fit a modified reverse flow Falkner-Skan profile to their data in order to estimate the boundary layer thickness shape factor, then completed the stability calculations using the unmodified reverse flow Falkner-Skan profile corresponding to that shape factor. Lang et al. [25] approximated the second derivative of the velocity profile directly from high spatial resolution experimental data and used the data in the stability analysis without curve fitting. Other profile forms have been employed in numerical studies of separation bubble stability. These include piecewise sinusoidal functions [77], modified hyperbolic tangent and exponential forms [34, 79], cubic spline fits [30, 31], as well as other modified reverse flow Falkner-Skan profiles [70].

Drazin & Reid [33] have noted that linear stability predictions for boundary layer profiles at separation depend on the specific functional form of the velocity profile used in the analysis. Furthermore, Dovgal et al. [34] compared stability predictions for reverse flow Falkner-Skan profiles to similar modified hyperbolic tangent profiles and concluded that LST eigenvalue spectra for separated shear layers are sensitive to the exact shape of the profile. They warned that this could be important if experimental data is to be compared to stability calculations. The wide variation in stability analysis approaches employed for measured and computed separation bubble profiles warrants further examination of the sensitivity of linear stability calculations to the method of analysis.

2.3 Influence of Experimental Setup

Experimental investigations of airfoil operation at low Reynolds numbers are challenging, in part because of the high sensitivity of the flow to free-stream disturbances and those generated by the experimental setup [3]. This can cause differences in measured aerodynamic forces for matching flow parameters in different facilities [3]. In some experiments, changes in the zero-lift angle of attack were observed with changing Reynolds number [10]. Elements of the experimental setup that are known to influence flow development are expected to have a pronounced effect on low Reynolds number airfoil experiments due to the inherent sensitivity of this type of flow. The influence of three aspects of the experimental setup will be assessed in this thesis: end plates, test section walls, and intrusive measurement equipment. Background information on each of these factors are provided in this section.

2.3.1 End Plates on Aerodynamic Models

End plates are commonly installed on aerodynamic models to mitigate three-dimensional end effects [14]. A number of studies have been conducted to devise guidelines for end plate design and spacing to produce flow near the center-span plane similar to that over a wide-span model [11–14, 82]. Early parametric studies of end plate dimensions and position focused specifically on the use of end plates on circular cylinder models; however, the findings of these investigations have been applied as guidelines for other geometries [14]. It was found that, for models with a spanwise length to diameter ratio of thirty or greater, mean and fluctuating forces, as well as the mean base pressure measured on the center-span plane, are representative of a wide-span model without end plates present [13,83]. For cylinder models of lower length to diameter ratios, end plates are required to establish flow conditions representative of a wide-span model on the center-span plane and should extend at least 2.5 cylinder diameters upstream of the model and 4.5 diameters downstream [11]. The streamwise extent of the end plates should not appreciably exceed this recommendation to limit boundary layer growth on the end plates and reduce the influence of this growth on model wake development [12]. Fox & West [13] concluded that a minimum spacing of seven cylinder diameters between the two end plates is required to obtain a base pressure coefficient on the center-span plane matching that on a wide-span model. This spacing is consistent with that determined by Szepessy & Bearman [84] based on measurements of fluctuating lift and vortex shedding frequency.

Experimental studies on flow development over non-circular geometries have similarly found that improved mean spanwise uniformity can be achieved by installing end plates on these models [85]. Kubo et al. [14] studied the effect of end plate design on drag force and base pressure on circular cylinders, flat plates, and rectangular cylinders of various dimensions. Similar to the recommendations for a circular cylinder [11], they found that the end plate diameter should be at least 8.5 times the height of the model projected onto a streamwise normal plane [14]. Kubo et al. [14] recommend that the end plates extend at least 4.28 model heights downstream, consistent with the value recommended for a circular cylinder [82]. This estimate was derived from Kármán's theory of vortex streets based on the conclusion that the end plates should extend downstream of the model to the end of the vortex formation region to prevent the high suction in this region from entraining momentum from fluid passing between the end plate and the test section wall [14]. For a circular cylinder, it was found that rectangular end plates produce flow on the center-span plane most representative of that over a wide-span model [11]. However, results for a square cylinder indicate that the orientation of rectangular end plates can affect surface pressure distributions on non-circular models [82].

End plates have been used in a number of experimental studies on airfoils operating at low Reynolds numbers [42,86–88]. Reported end plate dimensions for such experiments appear to roughly follow the guidelines established for other geometries, as described above [86–88]. A comparison of low Reynolds number lift coefficient measurements on Wortmann FX63-137 airfoil models showed that consistent results could be obtained between different facilities with different end plate mounting designs, model aspect ratios, and measurement techniques [10]. However, this comparison revealed that differences between measured lift coefficients could result if small gaps exist between the model and the end plates [10]. Force balance measurements are sometimes conducted with gaps between the model and end plates, isolating the model from the end plates so as to remove the end plate drag from the measurement [10, 15]. Particularly for wing models with spanwise variation in cross section, force balance measurements are common. Pelletier & Mueller [86] investigated the effects of end plates on force balance measurements on a two-dimensional Eppler 61 airfoil model at chord Reynolds numbers between 4×10^4 and 10^5. They demonstrated that because corner flows developing at the junction between the end plate and the model can extend over a significant spanwise length at low Reynolds numbers, the measured lift forces can be reduced by as much as 30% due to secondary flows developing with end plates installed. They showed that the effect of corner flows can be significantly reduced by measuring aerodynamic force over a central span section of the airfoil. Further investigation is required to determine how end plates affect separation bubble characteristics and laminar-to-turbulent transition in two-dimensional low Reynolds number airfoil experiments.

2.3.2 Test Section Wall Interference

Wall interference is another aspect of experimental setup which is known to influence experimental results [16]. Wall interference includes solid blockage, wake blockage, boundary layer blockage, streamline displacement by the test section walls, as well as wall and model boundary layer interaction [15, 20]. Blockage effects are the only consequences of wall interference considered in this investigation. Solid blockage results from the partial obstruction of the of the test section at the model location, and causes an increase in the effective free-stream velocity over the model. Boundary layer blockage accounts for the increase in free-stream velocity in the wind tunnel due to boundary layer growth on the test section walls. Without a model present, the pressure decreases nearly linearly along the length of the test section due to boundary layer growth [15]. This pressure gradient induces a force on any model tested in the facility. Wake blockage identifies the effect of test section confinement on wake development behind the model [20]. Conservation of mass flow rate through the test section requires the mass flow rate in the free stream to increase where there is a velocity deficit in the wake. This leads to a higher free-stream speed in the confined test section than would be observed in an unconfined flow field. Wake blockage can also limit wake growth. Generally, blockage increases measured drag coefficients, increases wake vortex shedding frequencies, and reduces model surface pressure coefficients [89–92].

For solid area blockage ratios of less than 0.5% of the cross sectional area of the test section, blockage effects are generally negligible [20, 93]. Constraints on model instrumentation and wind tunnel dimensions often result in models of higher blockage ratios, commonly between 1 and 10% [15]. For such higher blockage ratios, various data correction methods exist to compensate for blockage [15, 17, 18]. These tools range from simple correction factors incorporating correlations based on measurements or theory to more sophisticated techniques that combine measured wall pressures with potential flow approximations [15]. However, aerodynamic forces on airfoils operating at low Reynolds numbers are strongly linked to the characteristics of the separated flow region which develops over the airfoil surface, and which is sensitive to the free-stream environment [9]. If wall interference influences the separated flow region development, size, or location, simple post-test data correction tools may not accurately correct measured aerodynamic forces. Furthermore, if wall interference alters the transition process, qualitative results from studies on this phenomenon could be affected.

Performing experiments in specialized test sections is an alternative to post-test data correction. Various test sections have been designed for this purpose [16, 19, 20]. The objective in each of these test section designs is to produce a section of flow in the wind tunnel that better resembles that in an unconfined and infinite flow field. Relatively simple examples are facilities with fixed-wall, diverging test sections and ones in which boundary layer suction is applied [15]. Ventilated test section are a common design for industrial wind tunnels [20]. Such facilities incorporate slots or perforations to allow some flow through the test section boundaries. This approach is a compromise between the high blockage created by closed test sections and the excessive flow expansion in open test sections. More accurate data can be obtained, and higher blockage ratio models can be tested, in facilities with two adjustable walls. In such facilities, two of the test section walls can be contoured to reduce interference [19]. This idea has been extended in the design of three-dimensional adaptive test section facilities, employing eight segmented adjustable wall sections or deformable rubber tube test sections [19]. From data obtained in such facilities, it has been concluded that the effects of blockage on aerodynamic data from three-dimensional models could be achieved with much simpler two adaptive-wall test sections [16]. Adaptive slotted test sections combine ventilated and adaptive-wall test section concepts [20]. In these facilities, closed longitudinal slots with adjustable depth are installed along all four walls of the test section. This provides a simple way to adjust the test section cross sectional area in the streamwise direction, and allows adjustment on all test section walls for three-dimensional adaptation [20].

The experimental facility used in the present investigation was a two adaptive-wall test section wind tunnel. Various algorithms have been developed for streamlining test sections with two adaptive walls [94]. Two efficient methods commonly employed in wall adaptation experiments are the FLEXWALL strategy [95] and the Wall Adaptation Strategy (WAS) [94, 96]. In both strategies, the flow is divided into a real flow field in the test section and imaginary flow fields elsewhere. Both strategies aim to determine wall contours for which the measured pressure distribution along the wall matches that of the imaginary potential flow field along the boundary. In a flow bounded by only the upper and lower walls, and for which the walls are sufficiently removed from the rotational flow created by the model, this flow field would resemble unbounded flow development. In practice, factors including finite test section length, boundary layer displacement from the side walls of the test section, interaction of the model and the side wall boundary layers, and experimental uncertainty, can cause discrepancies between the flow with streamlined walls and that in an unbounded flow field. In the FLEXWALL strategy, the measured wall pressure distributions are used to compute the imaginary potential flow fields [95]. The walls are adjusted and the calculations repeated, until the computed imaginary flow field satisfies the impermeability condition at the wall. In the WAS, the imaginary potential flow field is computed based on the known boundary contour coordinates, and the computed pressure distribution along this boundary is compared to the measured pressure distribution [16, 91, 94, 96]. The walls are adjusted until these distributions match. Russo et al. [90] showed that measurements of pressure distributions and aerodynamic forces on a NACA 0012 airfoil model at a Mach number of 0.4 obtained after applying each of these two strategies were in agreement. In a recent study by Goodyer & Saquib [91], it was shown that the WAS could be used to correct cylinder drag coefficients at up to 50% blockage, and wake vortex shedding Strouhal numbers at up to 85% blockage.

2.3.3 Hot-Wire Measurements in Separation Bubbles

Hot-wire measurements are often used in the study of separation bubbles on wind tunnel models because they provide high spatial resolution measurements, high frequency response, and require only a relatively simple setup [22, 23, 26–29, 97]. However, this measurement technique has several deficiencies. Of particular concern to low Reynolds number airfoil experiments are the low speed measurement errors inherent to hot-wire data and the influence of the intrusive probe and support equipment on flow development. It should be noted that Laser Doppler anemometry and particle image velocimetry techniques also suffer from low speed measurement errors near model surfaces [98].

Low speed and near surface hot-wire measurements can be affected by rectification error [99], low speed calibration errors [23], error due to high mean vertical flow speed [99], and enhanced conductive heat transfer to the model surface [100–102]. Rectification error in hot-wire measurements results from the inability of the probe to resolve the flow direction [99]. For mean flow speeds near zero, this leads to a higher mean speed measurement and lower root-mean-square (RMS) speed measurement than in the physical flow. Normal hot-wire probes are also unable to distinguish between flow in the streamwise and vertical directions. At locations of high vertical speed, the mean vertical velocity component increases the measured mean velocity and causes a higher contribution of the vertical velocity fluctuations to the measured RMS velocity. Hot-wire measurements near a solid surface can also be affected by enhanced conductive heat transfer across the thin fluid layer separating the high temperature wire element from the surface, causing an increase in the measured mean velocity [100–102]. Correction methods have been developed for conduction effects in attached boundary layers [100–102]; however, none of these corrections have been adopted as a standard procedure [99] and their validity for separated shear layer measurements has not been verified.

Research on more advanced hot-wire measurement techniques for separation bubbles has shown that various tools can improve measurement accuracy in the reverse flow region. Watmuff [23] demonstrated that by using a flying hot-wire technique as opposed to a stationary probe, measurement error due to signal rectification and vertical flow can be significantly reduced. Häggmark et al. [97] developed a measurement probe consisting of a hot-wire in between two resistance wires, positioned parallel and at the same elevation from the model. They showed that this probe could resolve the flow direction when used for a sufficiently high mean speed, but indicated that the probe could not be used near the separation point or for moderate to high turbulence intensities. They also indicated that the probe cannot be used to measure high frequency velocity fluctuations. Furthermore, both of these methods were used to measure the separation bubble on a flat plate and would be much more difficult to employ on an airfoil model, due to surface curvature.

Positioning a hot-wire probe near the surface of a model can distort the flow field [103], causing more significant measurement errors than due to low speed limitations of the sensor. Brendel & Mueller [53] have noted changes in flow development in separation bubbles over low Reynolds number airfoils due to the presence of a hot-wire probe. They note that these effects are small when the angle of the probe to the surface is kept below 10°. They further explored the errors due to probe positioning in the separation bubble of a low Reynolds number airfoil by comparing hot-wire and laser Doppler anemometer measurements on a Wortmann FX63-137 airfoil at $Re_c = 10^5$ and for angles of attack of -5 and 10°. They found that, for these flow conditions, the hot-wire probe did not significantly affect the measured profile in the laminar portion of the separation bubble. Discrepancies were observed between the transition and reattachment locations, and were attributed to hot-wire errors rather than changes in flow development. A similar assessment of the influence of a hot-wire probe on flow development for other airfoil geometries and angles of attack could provide further verification of these findings. In both of the cases examined by Brendel & Mueller [53], the separation bubble formed over the mid-to-aft chord portion of the airfoil. It is of interest to examine a case in which the separation bubble forms near the leading edge, because this occurs for flow conditions close to those at which the bubble bursts, and therefore, the flow is likely to be more sensitive to the experimental conditions. Investigating the effect of the hot-wire probe on disturbance development in the transition region is also of interest.

2.4 Surface Pressure Measurements with Embedded Sensors

Surface pressure measurements have been used to gain insight into flow development over various geometries. Willmarth [104] summarizes several investigations which have considered the pressure fluctuations on the surface beneath turbulent boundary layers to identify sources of noise and vibrations on aircraft. Theoretical work has shown that surface pressure fluctuations depend on velocity fluctuations throughout a region of the flow field, not just at a single point. Cross-power spectra of surface pressure signals have been used to evaluate the convection and decay of wall pressure fluctuations in the flow field. This work has also shown that the background sound field in testing facilities limits low frequency measurements with embedded pressure sensors. Paterson et al. [105] used arrays of five microphones embedded in the surface of NACA 0012 and NACA 0018 airfoil models to investigate sources of noise generation at chord Reynolds numbers between 4×10^5 and 3×10^6. They showed that the propagation speed of surface pressure fluctuations could be determined from a cross-correlation of microphone responses. They also showed that the microphone signals could be used to identify whether the boundary layer is laminar or turbulent, based on the relative magnitudes of pressure fluctuations in these regimes.

Surface pressure fluctuation measurements have been used in a number of studies on separation bubble development [106–112]. Separation bubbles forming over blunt splitter plates, splitter plates with fences, forward facing steps, backward facing steps, and in pipe expansion sections show similar trends [106–112]. Upstream of separation, RMS pressure fluctuations are typically very small. The RMS pressure begins to rise at the separation point, and continues to increase over the region of mean pressure recovery. A maximum is reached in the reattachment region, sightly upstream of the mean reattachment point, as the turbulent shear layer moves towards the wall. The magnitude of this peak can differ significantly between geometries [106, 107]. Streamwise pressure fluctuation amplitude development shows no characteristic feature at the mean reattachment location. The pressure fluctuation magnitude decays downstream of the RMS peak, as turbulent energy diffuses away from the wall [106].

Investigations into the separation bubble forming on blunt splitter plates [111], splitter plates with fences [107], forward facing steps [108], and backward facing steps [108–110] show that surface pressure data exhibit significant energy content at the frequency corresponding to spanwise vortical structures forming in the shear layer. In some experiments, a second lower energy peak is observed, typically at a frequency of between one-fifth and one-third that of the vortical structures, and is often attributed to bubble flapping [107, 109, 111]. Based on surface pressure fluctuation measurements in the separation bubble that formed behind a backward facing step, Driver et al. [109] suggested that the bubble flapping they observed, having an amplitude of 20% of the shear layer thickness, resulted from a disordered process of vortex roll-up and pairing in the shear layer. They further determined that the unsteadiness due to bubble flapping did not provide a significant contribution to the overall turbulence intensity measured using surface pressure sensors.

Convection speeds on the order of 50 to 60% of the free-stream velocity in separation bubbles on blunt face splitter plates [111] and backward facing steps [108] have been measured by analyzing cross-spectra and cross-correlations of measurements from pairs of embedded pressure sensors. Farabee & Casarella [108] determined that the surface pressure field was convected downstream in the separation bubble, despite the reverse flow near the wall. Lee & Sung [110] computed the frequency wave number energy spectrum for the pressure fluctuations on the surface beneath a separation bubble behind a backward facing step using data from an array of thirty-two microphones. They identified a ridge in the spectrum corresponding to the downstream convection speed determined by Farabee & Casarella [108]. Hudy et al. [107] performed a similar analysis on surface pressure measurements from an array of eighty microphones beneath the separation bubble formed behind a fence on a splitter plate. They identified a second ridge in the upstream section of the separation bubble, with an upstream convection speed of approximately 20% of the free-stream speed. They suggested that the upstream convection of disturbances indicates that an absolute instability may be responsible for bubble flapping on this geometry.

The experimental model used in the present investigation was designed by Gerakopulos [35] to investigate the feasibility of embedded pressure sensor arrays for real-time measurements of flow development over low Reynolds number airfoils. Gerakopulos [35] concluded that measurements from embedded pressure sensors below the separation bubble on a low Reynolds number airfoil agree qualitatively with those obtained in the separation bubbles formed on other geometries [35]; the development of disturbance fluctuations contained a characteristic maximum just upstream of the reattachment location, a frequency band of amplified disturbances could be identified, and surface pressure fluctuation convective speeds were approximately 50% of the edge velocity. It was further noted that when separation occurs without subsequent reattachment, surface pressure fluctuations have significantly lower amplitudes than when a separation bubble forms, and that the RMS surface pressure distributions do not exhibit a characteristic maximum along the streamwise coordinate.

Chapter 3

Experimental Methodology

This investigation is concerned with the process of transition in the separated shear layer over an airfoil at a low Reynolds number and with the influence of specific aspects of the experimental setup on low Reynolds number airfoil experiments. Flow conditions to be examined in detail were selected to (1) allow observation of both separation bubble formation and flow transition without turbulent reattachment, (2) have as high a free-stream dynamic pressure as possible to reduce measurement uncertainty, while not being so high as to make smoke-wire flow visualization infeasible, (3) provide a wide range of separation bubble dimensions, and (4) produce a relatively wide range of moderate blockage ratios. Based on the surface pressure distributions on this model for a wide range of flow conditions, presented in Ref. [39], a chord Reynolds number of 10^5 and angles of attack of 0, 5, 10, and 15° were selected for this study.

This chapter describes the experiment, measurement and flow visualization techniques, as well as the wall streamlining algorithm. The uncertainties in experimental conditions and measured parameters are discussed and quantified in Appendix A.

3.1 Experimental Setup

Experiments were preformed in an adaptive-wall, open-return, suction-type wind tunnel at the University of Waterloo. A diagram of the wind tunnel is provided in Fig. 3.1. A section of aluminum honeycomb and four steel screens were installed upstream of the contraction section during recent flow conditioning upgrades [92]. The contraction section has an area contraction ratio of 9.55. For the experiments presented in this thesis, flow uniformity at the streamwise location of the model was within ±0.6% and the maximum free-stream turbulence intensity was less than 0.3%.

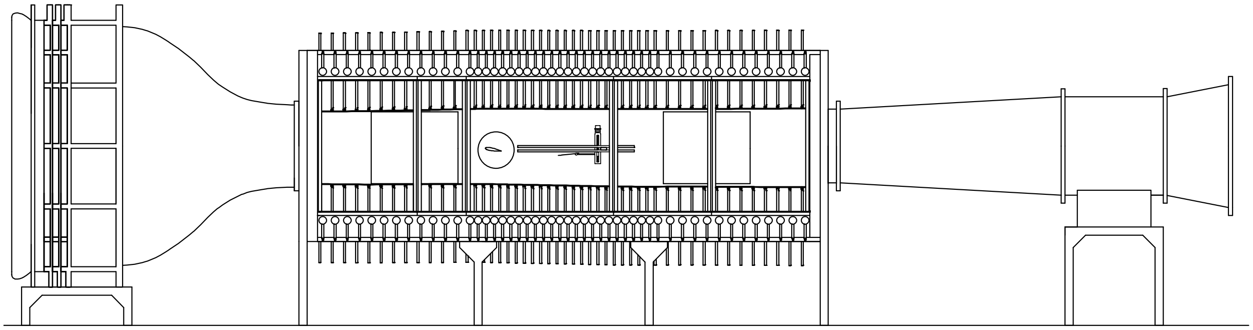

Figure 3.1: University of Waterloo adaptive-wall wind tunnel.

The test section has two rigid side walls and adjustable top and bottom walls that can be contoured along their entire 6.0 m lengths using 48 rack and pinion type jacks attached to each wall. The jacks have a finer spacing of 100 mm over a 2.25 m section around the model than in the rest of the test section, where the jack spacing is 150 mm. This design allows for more refined adjustment of wall contours around the model, where flow streamline curvature can be significant. The linear resolution of the scales for setting the jacks is 0.1 mm, and the uncertainty in setting the jacks is estimated to be less than 1 mm [113]. Inflatable rubber seals lining the edges of the adjustable walls and in contact with the rigid side walls were charged with air at a pressure of 150 kPa during experiments, as recommended by Sumner [113], to prevent air leakage into the wind tunnel through these interfaces. For the purpose of flow visualization, one of the rigid side walls is made of particle board painted a matte black, whereas the other is made of clear cast acrylic [92].

Measurements are presented for geometrically straight wall (GSW), aerodynamically straight wall (ASW), and streamlined wall (SLW) configurations. In the GSW configuration, the walls are straight and parallel. The test section has a width of 0.61 m and a height of 0.89 m in this configuration. In the ASW configuration, the wall contours are set to compensate for boundary layer growth on the test section walls, producing a constant flow speed along the central streamwise axis of an empty test section at the desired chord Reynolds number. The SLW configuration is the final adapted configuration, which mitigates solid and wake blockage for a particular geometry and set of flow conditions, producing a region of flow that closely matches that expected in an unbounded flow field.

Static pressure measurements on the adjustable walls, required for wall adaptation, were performed using seventy static pressure taps installed on both the top and bottom walls. The spacing between pressure taps is 50 mm over a 2.25 m section near the model and 150 mm elsewhere, providing higher resolution where significant pressure variation is expected [92]. Static pressure taps are 1 mm in diameter and were drilled normal to the wall. Each static pressure tap is connected to a Scanivalve mechanical multiplexer by 1.6 mm diameter flexible tubing.

In wall adaptation studies, the definition of free-stream velocity is important because the free-stream speed in an empty test section at the model location for a fixed fan voltage will change when the wall contours are adjusted. Appropriately defining the free-stream speed ensures that a comparison of measurements in different wall configurations are meaningful and that the converged wall shapes apply to the correct chord Reynolds number. In the present investigation, the free-stream velocity was set based on the static pressure difference measured across the inlet contraction section; by this procedure, the mass flow rate through the wind tunnel is fixed, independent of the wall configuration and angle of attack, for a given value of the pressure difference across the contraction section [98]. The free-stream velocity was set for experiments in the ASW, SLW, and intermediate wall configurations in the wall streamlining procedure, based on the pressure difference across the contraction section required to obtain the desired chord Reynolds number in an empty test section set in the ASW configuration. The free-stream speed in the GSW configuration was set to obtain the desired chord Reynolds number at the model location in an empty test section with the walls set in the GSW configuration. Setting the free-stream speed in this way allows the results for the GSW, ASW, and SLW configurations to be compared to quantify the error due to blockage expected for measurements in a fixed-wall test section. The pressure difference across the contraction section was measured based on the average pressure from three static pressure taps of 1 mm diameter located on the top and the two side walls of the contraction section on the large and small area sides. The pressure taps were connected by 1.6 mm flexible tubing to an inclined manometer with a resolution of 1.25 Pa. Free-stream speed was determined from the pressure difference across the contraction section using a measured relationship between the pressure difference across the contraction and the free-stream speed at the model location. The total uncertainty in setting the free-stream velocity was estimated to be less than 2.5%.

3.1.1 NACA 0018 Airfoil Model

Experiments were performed on a NACA 0018 airfoil model with a 200 mm chord length and a 600 mm span. A diagram of the model is provided in Fig. 3.2. The aluminum model was polished by the procedure described by Gerakopulos [35] to ensure a smooth and uniform surface finish, and was subsequently anodized. A total of ninety-five static pressure taps of 0.4 mm diameter were distributed along the model surface. Sixty-five pressure taps were distributed along the airfoil chord on the center-span plane and the remainder formed three spanwise rows on the upper surface of the airfoil at streamwise locations of $x/c = 0.15$, 0.30, and 0.60. The static pressure taps were connected to Scanivalve mechanical multiplexers by 0.8 mm diameter flexible tubing. Surface pressure fluctuation measurements were obtained using twenty-five microphones installed below the upper surface of the airfoil under 0.8 mm diameter holes. Twenty-two microphones were distributed along the chord and four formed a spanwise row. Further details on the model construction and instrumentation, as well as technical drawings, can be found in Ref. [35].

The angle of attack of the model was set using a digital protractor with an angular

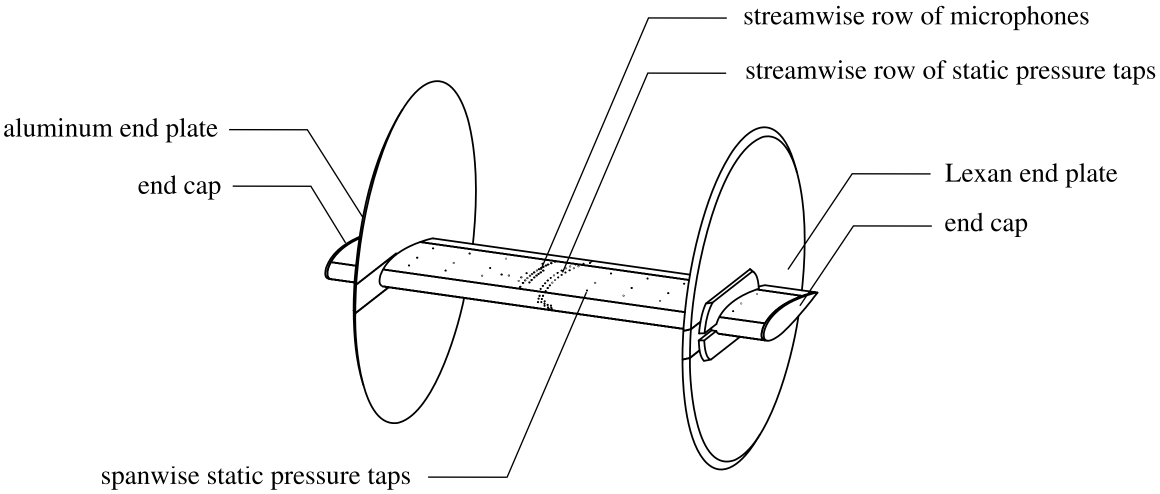
streamwise row of microphones
streamwise row of static pressure taps
aluminum end plate
end cap
Lexan end plate
end cap
spanwise static pressure taps

Figure 3.2: Airfoil model with end plates and end caps installed.

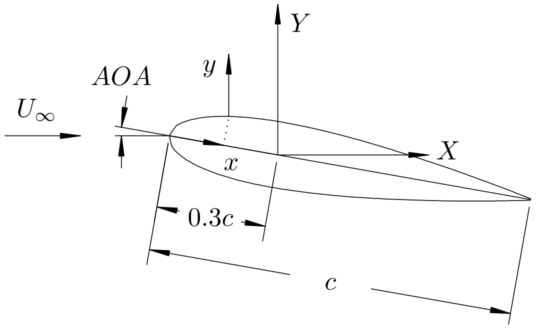
Y
y
AOA
U_∞
X
x
$0.3c$
c

Figure 3.3: Definition of coordinate systems.

resolution of 0.1°. The model axis of rotation was located $0.3c$ downstream of the leading edge and $10c$ downstream of the contraction. This provides a more than sufficient length of the adaptive test section upstream and downstream of the model for wall adaptation studies [89, 114].

The two coordinate systems used in data presentation throughout this thesis are defined with respect to the airfoil model in Fig. 3.3.

3.1.2 End Plate Design

End caps and end plates were used in different configurations for these experiments. The end caps are rubber inserts which follow the airfoil profile and fill the 5 mm gaps between the model and the side walls. The end plates were designed based on the recommendations of several prior studies [11–14, 82] and the designs used in other low Reynolds number airfoil investigations [42, 86–88]. The end plate design is illustrated in Fig. 3.2. Circular end plates extending 90 mm upstream of the leading edge and 160 mm downstream of the trailing edge were selected. For the purpose of flow visualization, one end plate is made of clear Lexan and the other of aluminum painted a matte black. The outer circumference of each end plate has a sharp 30° edge (Fig. 3.2). At zero angle of attack, the end plates add an additional 1.1% blockage to the model. As illustrated in Fig. 3.2, the end plates are designed to clamp onto the airfoil as opposed to the model axle. This allowed the same airfoil model to be used in a study on the effect of the spanwise spacing between end plates, and ensured that the model aspect ratio, b/c, could be varied without changing the solid blockage ratio, B. Further details on the end plate design considerations as well as technical drawings are provided in Appendix B.

3.2 Measurement Techniques

Three quantitative measurement techniques were employed in this investigation: static pressure measurements using digital pressure transducers, velocity measurements using hot-wire sensors, and surface pressure fluctuation measurements using microphones embedded in the upper surface of the model. Measurement procedures are described in this section, with a more detailed discussion of measurement uncertainty provided in Appendix A.

3.2.1 Static Pressure Measurements

For all differential static pressure measurements, the reference pressure was that measured at a wall pressure tap upstream of the adaptive section. Wall and model static pressure taps were connected through four Scanivalve mechanical multiplexers to a Lucas Schaevitz P3061-2WD pressure transducer. Pneumatic and electrical connection schematics for this system are provided in Appendix C. The mechanical Scanivalve system was renovated and installed to replace the Scanivalve digital pressure scanners (ZOC33 modules) which have been used in recent experiments conducted in this facility [35, 92]. The system was installed to reduce the overall uncertainty in static pressure measurements by (1) employing a transducer with a narrower operating range and a lower absolute uncertainty, (2) performing measurements at each location using the same sensor, to reduce the compounded uncertainty in computed differences due to calibration and zero pressure voltage offset uncertainty, and (3) reducing the zero pressure voltage offset variation with temperature over the duration of an experiment. These refinements were necessary for the relatively low wall pressures to be measured in the present investigation compared to other recent experiments in the adaptive-wall wind tunnel at the University of Waterloo [35,92].

The Lucas Schaevitz P3061-2WD pressure transducer had a full scale range of 500 Pa and provided a ±5 V output which was measured using a National Instruments PCI-6259 data acquisition card. The pressure transducer was calibrated against two inclined manometers. For pressures of less than 62.5 Pa, a manometer with a resolution of 1.25 Pa was used, whereas for higher pressures, a manometer with a resolution of 2.5 Pa was used. Voltage measurements were adjusted by the difference between the calibration zero pressure voltage offset and that measured before each experiment to compensate for changes in the voltage response with ambient temperature [98]. A sixty second delay between switching to the first pressure tap and acquiring pressure data ensured sufficient time for the line pressure to stabilize. Subsequent changes between static pressure taps were followed by a thirty second delay. These times were determined to be sufficient based on 200 s samples of each pressure tap on the model and walls in the sequence of a standard measurement routine. Based on the calculations summarized in Appendix A, the uncertainty in static pressure measurements is estimated to be less than 1.6% of the dynamic pressure.

3.2.2 Velocity Measurements

Velocity measurements were preformed in the shear layer on the upper surface of the airfoil and in the airfoil wake. Near surface measurements were performed using a Dantec 55P15 normal boundary layer type hot-wire probe, angled at 7° to the model surface, in accordance with the recommendations of Brendel & Mueller [53]. Wake measurements were preformed using a Dantec 55P61 cross-wire probe. All hot-wire sensors were operated by Dantec 56C17 constant temperature anemometer bridges. Hot-wire bridge output voltages were digitized using National Instruments PCI-4472 and PCI-6259 data acquisition cards for boundary layer and wake measurements, respectively.

Hot-wire sensors were calibrated using a Pitot-static tube positioned at the same streamwise location, upstream of the model and 10 mm from each hot-wire probe. An inclined manometer with a minor division of 1.25 Pa was used to measure the pressure difference between the stagnation and static ports on the Pitot-static tube. A fifth order polynomial fit to the voltage response of the hot-wire was used to interpolate velocity data between calibration points [115]. Based on the method employed by Watmuff [23] for hot-wire measurements in a separation bubble, the zero velocity voltage used in the calibration was taken as the absolute minimum voltage measured over the sample duration with the wind tunnel off.

An automated three-axis traversing mechanism, described in Ref. [116] and illustrated in Fig. 3.4, was used to position the hot-wire probe in the flow, with an estimated uncertainty in traverse movements of ±0.05 mm. The hot-wire probe extended 500 mm upstream of the traverse. The traversing mechanism produced a blockage of about 4.5% of the nominal test section area.

For boundary layer measurements, the distance between the hot-wire probe and the model surface was determined optically using a Nikon D300 camera equipped with a Nikon SB-600 speedlight and a Nikon UV-Nikkor 105 mm f/4.5 macro lens. The uncertainty in probe positioning is estimated to be less than ±0.05 mm.

Boundary layer profile measurements were acquired at a sample rate of 5000 Hz for twenty-six seconds, with a four second delay before measuring after changing the probe position. Velocity measurements for boundary layer and wake velocity energy spectra were acquired at 5000 Hz for 420 s. Wake spectra were measured at $X/c = 2.7$ at the Y/c location of highest turbulence intensity, as determined from measured wake profiles not presented in this thesis. Based on the discussion in Appendix A, the uncertainty in hot-wire measurements was estimated to be less than 5%.

3.2.3 Microphone Measurements

Surface pressure fluctuations were measured using an array of embedded microphones, designed and tested by Gerakopulos [35]. Details on the microphone array design, technical drawings, calibration procedures, and microphone frequency response curves are available in Ref. [35]. Important features of the microphone array are summarized here.

The microphone array consists of twenty-five embedded Panasonic WM-62C omnidirectional back electret condenser microphones, distributed as shown in Fig. 3.2. The

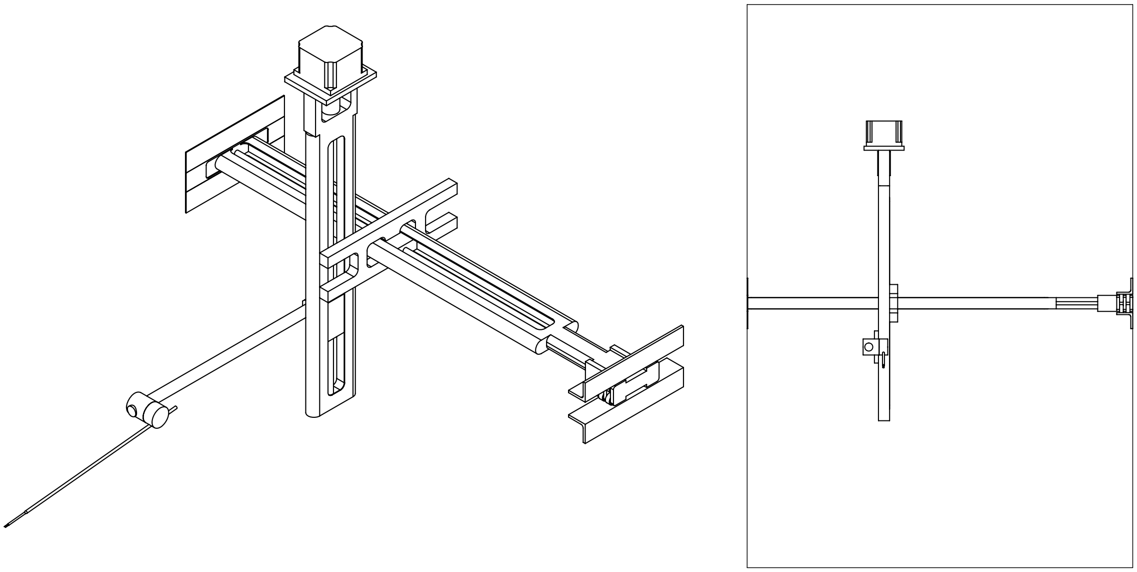

(a) (b)

Figure 3.4: Hot-wire positioning traverse: (a) isometric view and (b) view from upstream with GSW test section boundaries outlined.

microphones were installed below and concentric with 0.8 mm diameter holes in the upper surface of the airfoil, in contact with the inner surface of the 1 mm thick airfoil skin. The hole diameter was selected to ensure that the Helmholtz resonance frequency was well above the frequency range of pressure fluctuations observed during experiments on this model [35].

Output voltage signals from each microphone were amplified by Linear Technology low-noise and high-speed precision dual operational amplifiers (LT 1120). The voltage signal was carried to the data acquisition system by a 1 m Belden RG-178 coaxial cable and a 5 m Belden RG-174 mini-coaxial cable, connected by snap fit subminiature-B connectors. Simultaneous acquisition of up to eight voltage signals is accomplished using a 24 bit National Instruments PCI-4472 data acquisition card.

Before installation in the airfoil model, each microphone was calibrated in an anechoic chamber designed and built by McPhee [117]. The resulting frequency response and sensitivity constants are provided by Gerakopulos [35]. A nearly constant voltage response with frequency was obtained between 100 Hz and 2 kHz, defining the usable range of the microphone array. Surface pressure spectra and RMS pressure were obtained from microphone measurements acquired at 40 kHz for twenty-six seconds, and low-pass filtered below 2.5 kHz.

3.3 Wall Adaptation

Wall streamlining was performed to mitigate blockage effects on measurements of shear layer development over the airfoil model. Furthermore, measurements in the GSW, ASW, and SLW configurations were compared to assess the influence of blockage on low Reynolds number airfoil experiments. Wall streamlining was performed using the Wall Adaptation Strategy (WAS) of Judd et al. [96]. The WAS is an iterative procedure by which wall contours are determined that provide measured wall pressure distributions matching those obtained from inviscid flow solutions over the boundary contours. A MATLAB program was developed to perform WAS calculations for this facility, and has been used for wall streamlining calculations in this investigation. The WAS is outlined in this section, and details are provided in Appendix D.

Figure 3.5 illustrates the basic concept of the WAS. In the WAS, the flow field is divided into three sections by boundary contours. The boundary contours are defined as the wall contours, offset by the difference between the ASW and GSW wall displacements. The section of flow between the top and bottom boundary contours is the real flow field,

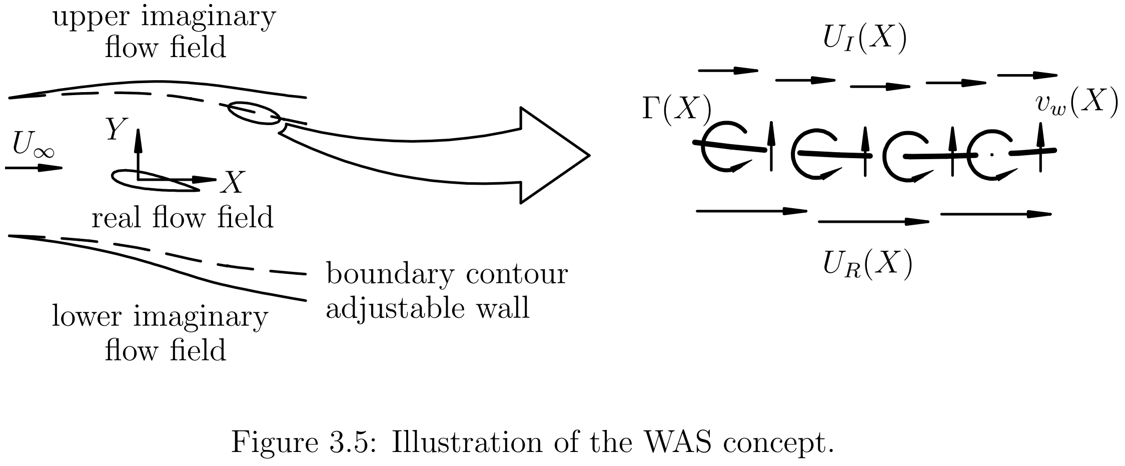

Figure 3.5: Illustration of the WAS concept.

and can be measured experimentally. Outside of the boundary contours are the upper and lower imaginary flow fields, which are the potential flow solutions for flow over the boundary contours. If the top and bottom walls are sufficiently removed from rotational flow created by the model, and thin boundary layer approximations apply to the top and bottom test section wall boundary layers, then when the imaginary and real flow fields match along the boundary contours, the real flow field approximates that in an unbounded flow. Differences between the flow field in the test section and that which would occur under unconfined conditions may still result from the finite test section length, streamline displacement by the side walls, and differences between the actual and computed wall displacement thickness due to model induced pressure gradients.

In the present investigation, the test section was set in the ASW configuration for the first iteration of the WAS. ASW contours were computed assuming $1/7^{\text{th}}$ power law turbulent boundary layer growth from a virtual origin determined from boundary layer measurements in Ref. [113]. The validity of this virtual origin and $1/7^{\text{th}}$ power law boundary layer growth, for a chord Reynolds number of 10^5, were verified by measuring eight boundary layer profiles on the side walls. In order to achieve a constant free-stream velocity in an empty test section, the ASW wall displacements need to accommodate the total effective flow area reduction caused by boundary layer growth on all four test section walls. This is accomplished by adjusting computed displacement thicknesses by a measured scaling factor to compensate for side wall boundary layer growth. For the test section configuration used in the present investigation, this scaling factor was determined by Sumner [113], and recently verified by Bishop [92], to be 2.72.

At the start of each iteration of the WAS, the static pressure taps distributed along the center-span of the top and bottom walls are used to measure the pressure distribution along the boundary contour. Continuity is established between the measured flow field and the imaginary flow fields by imposing imaginary distributed vorticity sources along the boundary contours (Fig. 3.5). This creates vertical velocity components through the boundary contours. The SLW configuration can therefore be equivalently defined as the wall shape for which the imaginary and real pressure distributions along the boundary contour match, the vorticity distribution becomes zero, or the vertical velocity through the boundary contour becomes zero.

At each streamwise location, the change in wall contour is determined by a small wall slope approximation to eliminate the vertical velocity component at each location along the boundary contour. Because estimated wall movements do not account for changes in the real flow field created by the movement of the opposite wall, wall movements tend to overshoot the SLW contours due to a one-dimensional continuity effect on the free-stream speed [94]. To prevent algorithm divergence, wall movements are adjusted by an empirically selected scaling factor, taken to be 0.8 based on the recommendations of Wolf &

Goodyer [94]. The effect that moving one wall has on the real flow field over the other wall is partially compensated for by an empirically selected coupling factor, which transfers a portion of the movement of each wall onto the other. Based on a parametric study discussed by Wolf & Goodyer [94], which explored the effect of the coupling factor on the WAS convergence rate, a coupling factor of 0.35 was selected for the present investigation.

Imaginary flow field estimates for the new wall contours can be determined by potential flow solutions for flow over the boundary contours. In this investigation, the imaginary flow field was determined from potential flow theory by modeling each boundary contour as one side of a symmetric body with a uniform flow upstream [91, 118]. The imaginary flow field was computed by finding the strengths of a series of potential flow sources, distributed along the centerline of the body, such that a streamline coinciding with the boundary contour was produced by superposition of the flow fields created by each source.

A third order polynomial spline for the wall shape over a 1 m section at the downstream end of the test section is used to produce a smooth transition between the computed wall shapes and the fixed wall diffuser section. The walls are then set to the computed contours, wall pressure measurements are acquired, and the next set of wall contours are computed. Various convergence criteria can be used to decide when the SLW configuration is determined to within the experimental uncertainty [19]. In this investigation, the wall shapes were considered to be converged once that predicted wall movements were less than the uncertainty in setting the wall shapes, i.e., less than 1 mm.

The original formulation of the WAS employed an approximate method to determine the imaginary flow field, instead of a potential flow solution, in order to improve the speed of wall contour iterations [96]. This approximate method is described in Appendix D. Since previous studies in this facility employed the original method for computing the imaginary velocity along the boundary contour [92, 113], converged wall shapes were compared from both methods to ensure the reliability of the results. As discussed in Appendix E, differences between the SLW configurations determined from the original velocity field estimation method and potential flow calculations were on the order of the uncertainty in setting the wall contours.

3.4 Flow Visualization

Smoke-wire flow visualization was used to gain insight into the overall flow field development. The smoke-wire flow visualization setup was designed based on the recommendations of Yarusevych et al. [119]. A sketch of the setup is presented in Fig. 3.6. It consisted of a 0.1 mm diameter 304 stainless steel wire suspended at a spanwise location approximately 50 mm towards the acrylic side wall from the center-span plane and 50 mm

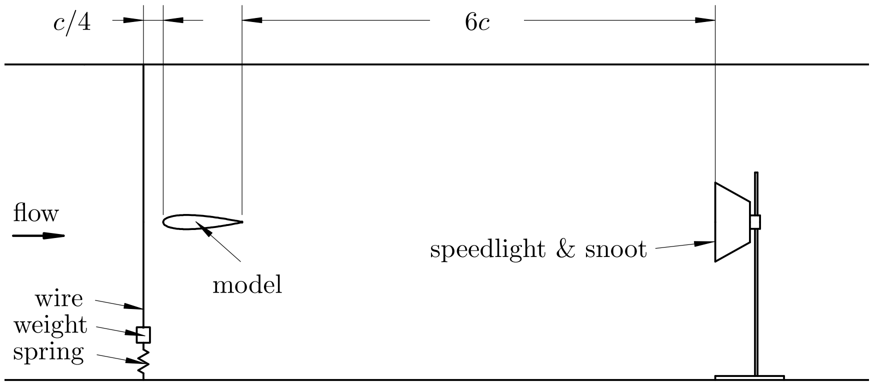

Figure 3.6: Sketch of the smoke-wire flow visualization setup (not to scale).

upstream of the leading edge of the airfoil at zero angle of attack. One end of the wire was rigidly fixed to the upper wall of the wind tunnel while the other end was attached to a weight and a spring. The weight and spring were used to maintain tension and reduce spanwise oscillations of the wire. A 70% glycol in water mixture was selected as the smoke generating fluid, following a comparison of various smoke fluids, including motor oils, model train smoke fluid, baby oil, and other glycol in water mixtures. This fluid was applied to the wire with a Q-tip, and a variable alternating current transformer was used to apply approximately 85 V across the 0.7 m long wire to evaporate the fluid and generate smoke. The smoke was illuminated with a Nikon SB-600 speedlight, positioned as shown in Fig 3.6. A specially designed snoot was installed on the speedlight to reduce illumination of the particle board wall and glare on the acrylic wall.

Flow visualization photographs were obtained using a Nikon D300 digital camera with a Nikon 18-70 mm f/3.5-4.5 Nikkor AF-S DX lens. The camera was operated in an eight frame-per-second continuous shooting mode. A Cactus PT-04 radio frequency trigger and receiver pair was wired together and used to synchronize the off-camera flash to the shutter.

Chapter 4

Sensitivity of Linear Stability Analysis of Separated Shear Layers

In this chapter, the sensitivity of spatial linear stability analysis of measured separated shear layer profiles is explored. Linear stability analysis involves numerically solving the Orr-Sommerfeld equation (Eq. 2.1) or the Rayleigh equation (Eq. 2.3) for a particular base velocity profile, $U(y)$. When the velocity profile is determined from experimental data, the approach to processing that profile for use in stability calculations can affect the results. In this investigation, two general categories of approaches are considered: (1) directly using experimental data in the differential equation and (2) solving the differential equation for a curve fit to experimental data. When the measured profile is directly used in the stability equation, the numerical solution method can affect the results due to the relatively low spatial resolution of measured profiles. For this reason, the sensitivity of solutions obtained by various numerical methods are compared for cases in which stability analysis is performed directly on the measured velocity profile. When the velocity profile used in the stability calculations is obtained by curve fitting experimental data, the spatial resolution of the profile can be increased indefinitely to obtain a grid independent solution. For such an approach, any reliable numerical solution method will yield the same result for a given curve fit. However, the solution obtained can be sensitive to both the type of curve fit employed and experimental data scatter [34]. Both of these sensitivities will be explored for approaches in which a curve fit is applied to the measured velocity profile.

The following methodology is employed to compare the stability predictions obtained using the various numerical solution methods and velocity profile processing approaches. First, a simulated velocity profile is analyzed to isolate the effects of experimental data scatter from variability in stability predictions due to the choice of profile processing approach and solution method. For this purpose, a curve fit determined by Nishioka et al. [22] for a velocity profile measured in the separated shear layer that formed over a flat plate airfoil at $AOA = 8°$ and $x/c = 0.027$ is selected. The profile is defined as follows [22]:

$$\frac{U}{U_\infty} = 1 - \frac{G(y)}{G(0)}, \tag{4.1}$$

where,

$$G(y) = \frac{-0.260}{1 + e^{2(y+0.2)}} + \frac{1.692}{\left[1 + 0.2e^{5.5(y-1.8)}\right]^5} + \frac{0.405}{\left[1 + 0.2e^{8(y-1.8)}\right]^5} + \frac{0.183}{\left[1 + 0.2e^{2(y-3.2)}\right]^{0.125}}. \tag{4.2}$$

The shape of this profile is common to separated shear layers forming over airfoils operating at low Reynolds numbers [23,25–27,33,97]. The curve fit was selected by Nishioka et al. [22] to facilitate inviscid stability analysis and accurately represents the measured velocity profile [22]. Discrete data points on this curve fit, with a constant $\Delta y/\delta^*$ spacing are used to simulate a measured velocity profile without data scatter. Grid independent solutions to the Rayleigh and Orr-Sommerfeld equations for this curve fit were obtained, and are referred to as reference solutions in subsequent discussion.

The second basis for comparison of the stability predictions obtained using various solution methods and velocity profile processing approaches is the susceptibility of these predictions to the velocity profile data scatter inherent in experimental measurements. To model data scatter, Gaussian noise with a second standard deviation of 2.5% of the free-stream velocity is imposed on the simulated velocity profile described above. This level of data scatter was found to approximate an upper bound on the data scatter observed in the separated shear layer measurements from Refs. [23], [25], [26], [27], [33], and [97].

Finally, the solution methods and velocity profile processing approaches are evaluated based on stability predictions for measured separated shear layer profiles presented in previous studies.

The above methodology is applied separately in Sections 4.2, 4.3, and 4.4 for respectively solving the Rayleigh equation directly using experimental data, the Rayleigh equation using a curve fit to experimental data, and the Orr-Sommerfeld equation.

4.1 Numerical Methods

Several numerical methods are available to solve Eq. 2.3. Three methods are considered in this investigation for use when experimental data is analyzed without curve fitting:

1. a finite difference (FD) method,
2. a piecewise linear velocity profile approximation (PWL) method, and

3. a Runge-Kutta (RK) integration method.

In the FD method, the derivatives in Eq. 2.3 are approximated using second order central difference formulas, leading to an algebraic eigenvalue problem for each disturbance frequency [33,120]; the resulting system of equations can be solved using a linear companion matrix method [120, 121]. In the PWL method, the velocity profile in Eq. 2.3 is approximated as a set of linear segments; enforcing continuity of the pressure field and the wall-normal velocity field leads to an algebraic eigenvalue problem for each disturbance frequency, which can be solved using a root-finding algorithm [33, 66, 67]. In the RK method, Eq. 2.3 is written as an equivalent system of first order differential equations. For each disturbance frequency, the equations are numerically integrated from the free stream to the wall; the eigenvalue is determined by a shooting procedure to satisfy the boundary condition at the wall [33,66,67]. Both second order and fourth order RK formulations were considered in this investigation. For a velocity profile of sufficiently high spatial resolution, each of the above solution methods converge to the same eigenvalue spectrum. However, these solution methods will be compared based on their predictions for the relatively low spatial resolution typical of measured separated shear layer profiles.

Each of the methods described above has specific advantages. The FD method can be used to solve for the eigenvalues directly, without applying a shooting method, avoiding numerical sensitivity to the initial value selected in the root-finding procedure. The PWL method does not require the calculation of U'', which is advantageous because experimental data scatter is compounded in computing U''. The RK method is more efficient than the FD method when high spectral resolution is desired, and is less sensitive to the initial eigenvalue estimates used in the shooting procedure than the PWL method.

The RK method can be applied to different equivalent first order systems derived from the Rayleigh equation. Two formulations are considered here, one in terms of vertical and streamwise velocity fluctuations and the other in terms of vertical velocity and pressure fluctuations. Unless otherwise specified, the RK method will refer to the more common approach, in which integration is performed to obtain the vertical and streamwise velocity fluctuation profiles [122]. In this formulation, the second derivative of the base velocity profile is required, and is computed using a second order central difference approximation for the interior points, and first order forward and backward difference formulas at the lower and upper domain boundaries, respectively. Since experimental data scatter is amplified in computing U'', it has been suggested that the alternative system of first order equations for vertical velocity and pressure fluctuations, which does not contain a U'' term, could provide solutions less sensitive to experimental data scatter [123]. The performance of an RK method using this alternative formulation is discussed briefly in Section 4.2, with supporting results and discussion presented in Appendix F.

When curve fitting is employed to obtain a high spatial resolution base velocity profile, each of the solution methods will provide effectively the same grid independent results. Only fourth order RK integration of the vertical and streamwise velocity fluctuation equations is employed when the Rayleigh equation is solved for a curve fit to the experimental data. This method is considered to provide numerically exact solutions to the Rayleigh equation [120].

For reasons explained in Section 4.4, only approaches employing curve fitting of the base velocity profile have been considered for solving the Orr-Sommerfeld equation. The Orr-Sommerfeld equation is solved in two steps. First, the solution is computed using a Chebyshev collocation method [66] with a linear companion matrix method to determine the eigenvalues [120]. Higher resolution is then achieved by using the eigenvalue spectrum computed from the Chebyshev collocation method to initiate the shooting procedure in a compound matrix method solution employing fourth order Runge-Kutta integration [67].

MATLAB solvers for the Rayleigh and Orr-Sommerfeld equations were written based on each of the solution methods discussed above, and used to generate the stability predictions presented in this thesis. Further details on each of the solution methods are provided in Appendix F.

4.2 Rayleigh Equation Solutions using Experimental Profiles Directly

The FD, PWL, and RK methods, applied directly to discrete velocity data, are first compared based on their predictions for a profile without experimental data scatter. For this purpose, a simulated discrete velocity profile generated from the continuous profile of Eqs. 4.1 and 4.2 was considered. The growth rate spectrum predictions for velocity profiles of various spatial resolutions are presented in Fig. 4.1. It should be noted that, for the profile of Nishioka et al. [22], a data point spacing of $\Delta y/\delta^* = 5.6 \times 10^{-2}$ corresponds to $\Delta y = 0.1$ mm, which is a relatively high spatial resolution for separated shear layer measurements [22,23,26,27,54,97]. Figure 4.1 shows that all three solution methods provide similar eigenvalue predictions at each level of data density, and that they each converge to the reference solution for a sufficiently high spatial resolution. With a profile point spacing of $\Delta y/\delta^* = 5.6 \times 10^{-2}$, the maximum disturbance growth rate and corresponding frequency are predicted to within 4% of the reference solution.

For disturbance frequencies at which the eigenvalue is accurately predicted, the three solution methods applied to a discrete velocity profile with a point spacing of $\Delta y/\delta^* = 5.6 \times 10^{-2}$ provide accurate estimates of the streamwise velocity fluctuation profiles. This

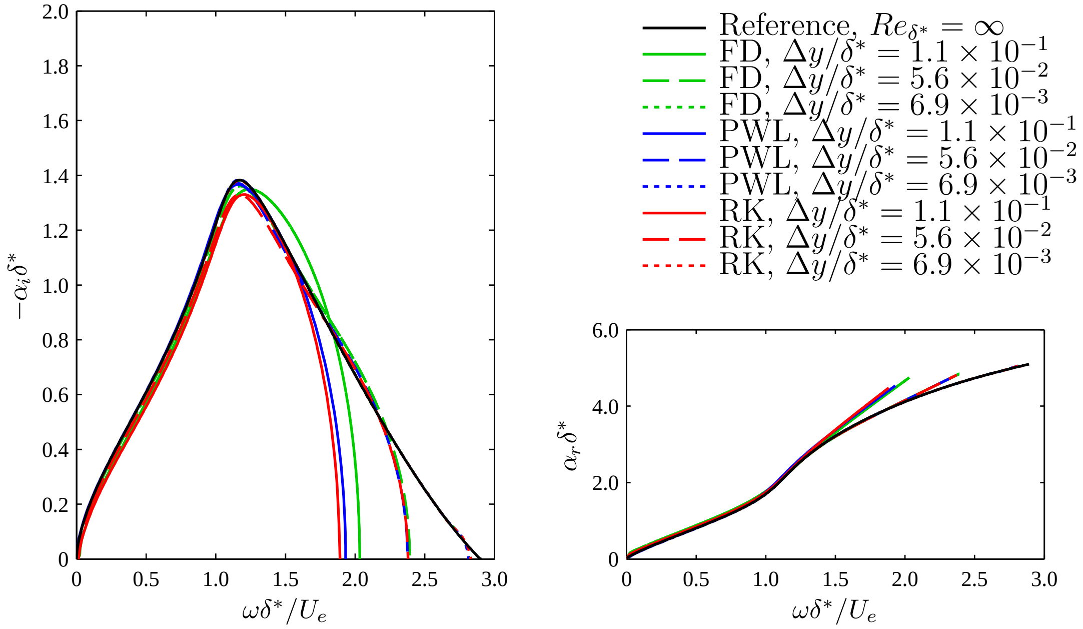

(a) (b)

Figure 4.1: Comparison of Rayleigh equation eigenvalue spectrum predictions for the simulated profile, computed using various solution methods directly on discrete profiles.

is illustrated by the streamwise velocity fluctuation amplitude and phase profile plots shown in Figs. 4.2b and 4.2c. The profiles pertain to the predicted frequency of maximum disturbance growth rate from the reference solution ($\omega\delta^*/U_e = 1.17$). Figure 4.2 shows that, as compared to the PWL method, the FD and second order RK methods more accurately predict the fluctuation amplitude and phase, particularly in the range $0.75 \lesssim y/\delta^* \lesssim 1.25$. The results presented in Figs. 4.1 and 4.2 demonstrate that the three solution methods applied directly to the simulated velocity data without data scatter and with sufficiently high spatial resolution provide predictions similar to the reference solution.

In practice, experimental data scatter contaminates measured velocity profiles. The effect of velocity profile data scatter on stability predictions is modeled by imposing Gaussian noise with a second standard deviation of 2.5% of the free-stream velocity on the simulated velocity profile with a point spacing of $\Delta y/\delta^* = 5.6 \times 10^{-2}$. One hundred profiles were generated in this way and stability analysis was subsequently performed directly on each profile. The impact of the simulated data scatter on the stability spectrum is depicted in Fig. 4.3. The FD, PWL, and RK methods show the greatest spectral deviation due to

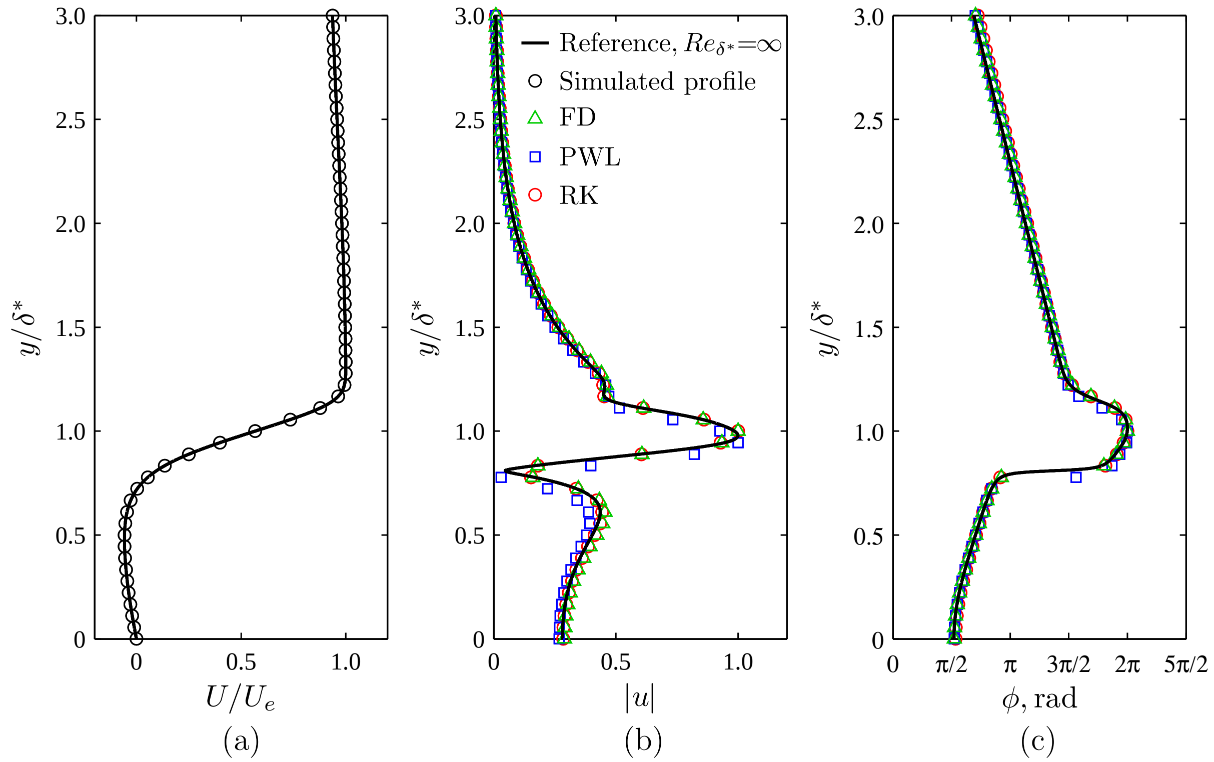

Figure 4.2: Comparison of Rayleigh equation streamwise velocity fluctuation profile predictions at $\omega\delta^*/U_e = 1.17$ for the simulated profile of $\Delta y/\delta^* = 5.6 \times 10^{-2}$, computed using various solution methods directly on discrete profiles. Presented are the (a) mean velocity profile curve fit of Nishioka et al. [22], (b) streamwise velocity fluctuation amplitude, and (c) streamwise velocity fluctuation phase.

data scatter for $\omega\delta^*/U_e \gtrsim 1.0$. For all three solution methods, the maximum disturbance growth rate and corresponding frequency are predicted to within 7.5% and 15% bands, respectively.

A few notes on the performance of other numerical methods for solving the Rayleigh equation should be made before continuing to examine the accuracy of the FD, PWL, and RK methods. The Chebyshev collocation method is a common and accurate tool used to solve the Rayleigh equation [66, 120, 121, 124–131]. For numerical accuracy, collocation points are usually selected as the locations of maxima and minima of the highest order Chebyshev polynomial used in the expansion [132]. However, experimental velocity profiles are typically acquired with a regular point spacing, and therefore do not match to these

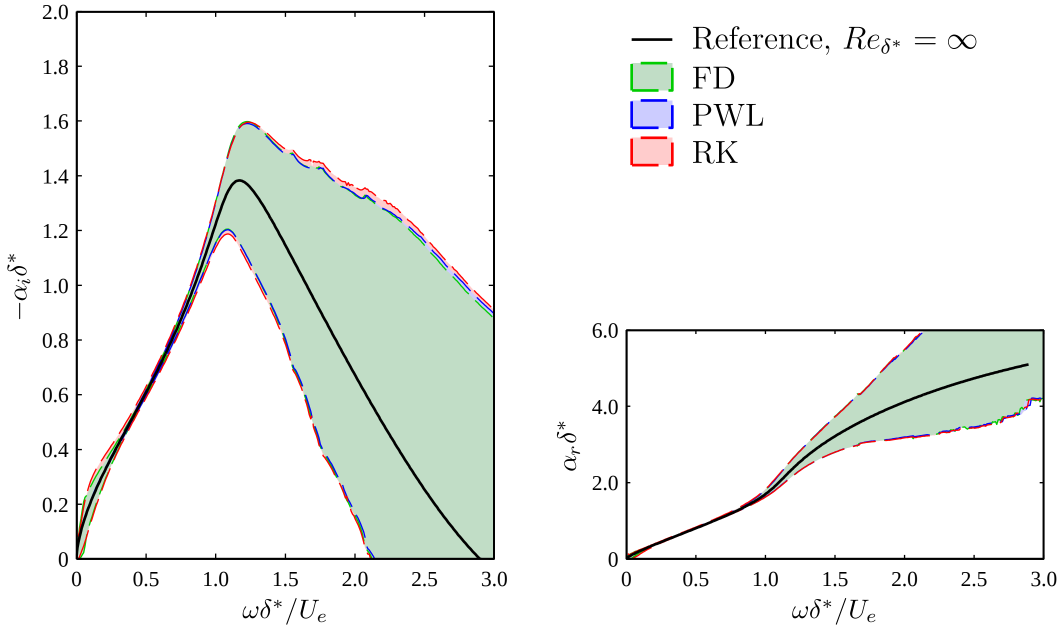

(a) (b)

Figure 4.3: Second standard deviation bands of Rayleigh equation growth rate predictions computed using various solution methods directly on one hundred simulated discrete profiles with $\Delta y/\delta^* = 5.6 \times 10^{-2}$ and imposed data scatter.

collocation points. As such, this approach has not been considered. An alternative formulation of the RK method, in which the Rayleigh equation is reduced to an equivalent system of equations for the vertical velocity fluctuations and the pressure fluctuations was evaluated based on convergence with velocity profile spatial resolution and sensitivity to data scatter. The results are presented in Appendix F. It was found that this method requires higher velocity profile spatial resolution than the other methods considered to obtain a growth rate spectrum with reasonable high frequency behavior. Finally, when performing the analysis directly on discrete velocity profiles, it was found that using a fourth order RK method instead of a second order method unnecessarily limits the usefulness of the results by providing 50% lower spatial resolution in the streamwise velocity fluctuation profiles.

Although the results in Fig. 4.3 suggest that reasonable stability predictions can be obtained using discrete velocity data with a spatial resolution and level of data scatter typical of experimental measurements, the methods need to be further evaluated using actual experimental velocity profiles. The results of the stability analyses performed on ten measured separated shear layer profiles from various studies are summarized in Table 4.1. In this table, data scatter has been quantified by U''_{RMS}, defined as,

$$U''_{RMS} = \sqrt{\sum_{k=1}^{N} \frac{\left[U''(y_k) - U''_k\right]^2}{\left(U''_{\max}\right)^2 N}}, \tag{4.3}$$

to reflect the sensitivity of U'' to data scatter and the significance of U'' in Eq. 2.3. In Eq. 4.3, U'' is determined from a Dini et al. [79] fit, defined in Section 4.3, $U''_{\max}$ is the maximum magnitude of U'', and U''_k is the finite difference approximation of the second derivative of the measured velocity profile at y_k. It should be noted that the velocity profile data were extracted from published figures, and that this process has contributed to the data scatter in the analyzed profiles. For comparison of Table 4.1 and Fig. 4.3, note that the one hundred simulated data scatter profiles have a mean U''_{RMS} value of 0.27 with a standard deviation of 0.04.

The results presented in Table 4.1 suggest that velocity profiles with relatively low data scatter, such as those from Lang et al. [25] and LeBlanc et al. [27], provide reasonable growth rate spectrum predictions for all frequencies including that of the maximum disturbance growth rate. With higher levels of data scatter, as in the profiles of Yarusevych et al. [26] for $Re_c = 1.5 \times 10^5$, reasonable predictions of the frequency of maximum disturbance growth rate were obtained, however, the growth rate spectra exhibit extraneous behavior at frequencies beyond the spectral peak. Two forms of extraneous spectral behavior were observed: a leveling off of the growth rate at high frequencies before steeply falling to zero, and continuously increasing growth rates at high frequencies. At even higher levels of data scatter, the extraneous behavior extended to frequencies below that of the expected growth rate peak, preventing a peak from being identified. It should be noted that although the frequency of the dominant disturbances are predicted to within 30% for some data sets (Table 4.1), the deviation in the predicted growth rate exceeded 100% in some cases. This amount of deviation between measured growth rates and predictions of stability analysis on measured separated shear layer profiles is observed in Ref. [26], in which it is speculated that the level of discrepancy could be reduced by performing viscous analysis instead.

The results presented here indicate that the FD, PWL, and second order RK methods can provide accurate predictions of the frequency corresponding to the maximum disturbance amplification when velocity profile data with relatively low data scatter are available. However, as velocity profile data scatter increases, the reliability of stability

Table 4.1: Comparison of measured growth rate spectrum to Rayleigh equation predictions using various solution methods directly on experimental profiles. The – symbol indicates that the solution had no spectral peak.

experiment	U''_{RMS}	ε_ω FD	ε_ω PWL	ε_ω RK	extraneous behavior?
Häggmark et al. [97], flat plate, $Re_x = 3.92 \times 10^5$	0.64	37	37	–	yes
Lang et al. [25], flat plate, $x = 300$ mm	0.09	1	1	1	no
LeBlanc et al. [27], Liebeck LA2573A, $Re_c = 2.35 \times 10^5$, $AOA = 4°$, $x/c = 0.371$	0.09	4	4	5	no
Watmuff [23], flat plate, $Re_x = 3.42 \times 10^5$	0.13	26	27	20	no
Yarusevych et al. [26], NACA 0025, $Re_c = 10^5$, $AOA = 0°$, $x/c = 0.44$	0.35	–	–	–	yes
Yarusevych et al. [26], NACA 0025, $Re_c = 10^5$, $AOA = 5°$, $x/c = 0.37$	0.19	12	12	8	yes
Yarusevych et al. [26], NACA 0025, $Re_c = 10^5$, $AOA = 10°$, $x/c = 0.25$	0.25	–	–	–	yes
Yarusevych et al. [26], NACA 0025, $Re_c = 1.5 \times 10^5$, $AOA = 0°$, $x/c = 0.62$	0.11	26	25	25	yes
Yarusevych et al. [26], NACA 0025, $Re_c = 1.5 \times 10^5$, $AOA = 5°$, $x/c = 0.44$	0.16	15	13	16	yes
Yarusevych et al. [26], NACA 0025, $Re_c = 1.5 \times 10^5$, $AOA = 10°$, $x/c = 0.22$	0.20	2	2	6	yes

predictions deteriorates. For velocity profiles with relatively high levels of data scatter, velocity profile curve fitting may be employed to mitigate the effects of data scatter.

4.3 Rayleigh Equation Solutions for Curve Fits to Experimental Profiles

In this section, the sensitivity of inviscid spatial linear stability predictions for curve fits to the measured base velocity profile is considered. Since it has been established that, for a velocity profile with sufficient spatial resolution, solutions obtained using the FD, PWL, and RK methods match, only the fourth order RK method will be employed in this section.

The curve fits considered in this investigation are summarized in Table 4.2 and include common generic curve fit forms [133] as well as functional forms used in previous studies to approximate separated shear layer profiles [22, 27, 34, 67, 77–79]. The parameters a_j and

Table 4.2: Definitions of velocity profile curve fits.

curve fit	definition
cubic spline [133]	piecewise cubic polynomial, U, with continuous U' and U''
Dini et al. [79] fit	$\frac{U}{U_e} = \frac{1-a_1}{2}\left[1 + \tanh\left(\frac{y-a_2}{a_3}\right)\right]$
Dovgal et al. [34] fit	$\frac{U}{U_e} = \frac{\tanh[a_1(y-a_2)]+\tanh(a_1 a_2)}{1+\tanh(a_1 a_2)} + a_3 \frac{y}{a_2} \exp\left[-1.5\left(\frac{y}{a_2}\right)^2 + 0.5\right]$
Falkner-Skan fit [61]	$\frac{U}{U_e} = F'(\eta)$ where F is given by $F''' + FF'' + a_2(1 - F'^2) = 0$ subject to $F(0) = F'(0) = 0$ and $F'(\infty) = 1$
Green [77] fit	$\frac{U}{U_e} = \begin{bmatrix} 1-2a_3, & 0 \leq y < a_1 \\ 1-a_3\left[1+\cos\left(\pi\frac{y-a_1}{a_2}\right)\right], & a_1 \leq y < a_2 \\ 1, & a_2 \leq y \end{bmatrix}$
LeBlanc et al. [27] fit	$\frac{U}{U_e} = \begin{bmatrix} a_3 F'(\eta), & F' < 0 \\ F'(\eta), & 0 \geq F' \end{bmatrix}$ where F is given by $F''' + FF'' + a_2(1 - F'^2) = 0$ subject to $F(0) = F'(0) = 0$ and $F'(\infty) = 1$
logistic series fit [22]	$\frac{U}{U_e} = 1 - \frac{G(y)}{G(0)}$ where $G(y) = \sum_{k=1}^{4}\left[\frac{a_{k,1}}{1+a_{k,2}\exp[a_{k,3}(y+a_{k,4})]}\right]^{a_{k,5}}$
piecewise cubic Hermite polynomial [133]	piecewise cubic Hermite polynomial, U, for which U' at the interval end points are approximated by finite difference formulas
sine series [133]	$\sum_{k=1}^{3} a_{k,1} \sin\left(a_{k,2} y + a_{k,3}\right)$
smoothing spline [133]	piecewise cubic polynomial, U, that minimizes $Sp \sum_k \left[U_k - U\left(y_k\right)\right]^2 + (1 - Sp) \int \lvert U'' \rvert^2 dy$

$a_{k,j}$ in the curve fit definitions were determined for each discrete profile using a numerical least squares residual optimization procedure.

The sensitivity of stability predictions to the choice of velocity profile curve fit is first established independent of the effect of velocity profile data scatter. This was accomplished by completing inviscid spatial linear stability analysis using each of the curve fits identified in Table 4.2 to approximate the base velocity profile of Eqs. 4.1 and 4.2 with a point spacing of $\Delta y/\delta^* = 5.6 \times 10^{-2}$ and without imposed data scatter. Figure 4.4 shows the growth rate and wave number spectra obtained using each of the fits except the smoothing spline. Despite all fits closely approximating the simulated velocity data ($R_0 < 0.4$), there is significant variation in the corresponding stability predictions. Specifically, the maximum disturbance growth rate predictions vary within a band of 30% of the value predicted by the reference solution, and the corresponding frequency similarly varies within a band of 15%. Note that since the simulated velocity data used here were generated from another curve fit, i.e., from Eqs. 4.1 and 4.2, the close agreement of a given spectrum with that from the reference solution should not be used as a performance measure for the corresponding

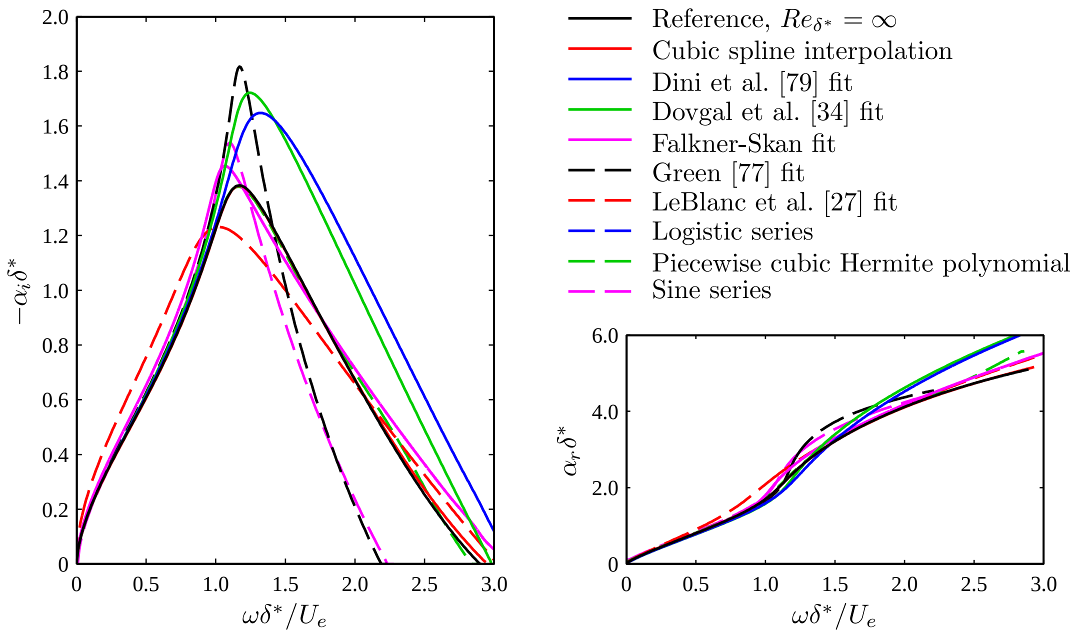

(a) (b)

Figure 4.4: Eigenvalue spectrum of the Rayleigh equation using various curve fits to the simulated velocity profile of Eqs. 4.1 and 4.2 with $\Delta y/\delta^* = 5.6 \times 10^{-2}$.

fit; only the relative difference between the spectra pertaining to different curve fits is significant.

Growth rate spectrum predictions computed using a smoothing spline fit to the velocity profile data were found to be sensitive to the choice of smoothing parameter. This was determined by performing stability analysis on smoothing spline fits to six velocity profiles presented by Yarusevych et al. [26]. The optimum value of the smoothing parameter, i.e., that resulting in the most accurate estimate of the experimentally measured frequency of maximum disturbance growth rate, varied by more than 20% between these six profiles. Furthermore, over the range of smoothing parameters for which a reasonable fit to the velocity profile was obtained ($R_0 \lesssim 1$), the predicted frequency of maximum disturbance amplification was found to vary by up to 50% for a given mean profile. Thus, it was concluded that performing stability analysis on a smoothing spline fit to measured velocity profile data may yield stability predictions that depend on the subjectively chosen smoothing parameter. As such, smoothing spline fits should be avoided when performing stability analysis on experimental data.

The susceptibility of stability predictions to experimental data scatter is critical in selecting a curve fitting method for approximating a measured velocity profile. The sensitivity of LST predictions to velocity profile data scatter was evaluated using the simulated discrete velocity profile of Eqs. 4.1 and 4.2 with $\Delta y/\delta^* = 5.6 \times 10^{-2}$ and imposing Gaussian data scatter with a second standard deviation of 2.5% of the free-stream velocity. One hundred discrete profiles were generated in this way. Each of the curve fits considered (Table 4.2) were applied to the generated profiles, and stability analysis was subsequently performed on these profile fits. Table 4.3 summarizes the results, presenting five measures to evaluate the stability predictions obtained with each curve fit. Note that an over-bar on a parameter signifies an average over the one hundred data sets, and that the superscript "peak" designates the quantity as corresponding to the maximum disturbance growth rate. The least squares residual without data scatter, R_0, and the average least squares residual over all one hundred profiles with data scatter, $\overline{R}$, are normalized by the number of data points and the edge velocity, and are expressed as percentages. They quantify the agreement between the curve fits and the discrete data points. The average error in the maximum disturbance growth rate quantifies the deviation in the magnitude of the spectral peak, and is defined as follows:

$$\overline{\varepsilon}_\alpha = \frac{1}{100} \sum_{k=1}^{100} \left| \frac{\overline{\alpha_i^{\text{peak}}} - \alpha_{i,k}^{\text{peak}}}{\overline{\alpha_i^{\text{peak}}}} \right| \times 100\%. \tag{4.4}$$

Similarly, the average error in the frequency corresponding to the maximum disturbance growth rate is defined as,

$$\overline{\varepsilon}_\omega = \frac{1}{100} \sum_{k=1}^{100} \left| \frac{\overline{\omega^{\text{peak}}} - \omega_k^{\text{peak}}}{\overline{\omega^{\text{peak}}}} \right| \times 100\%. \tag{4.5}$$

The integrated growth rate error quantifies the deviation in the growth rate predictions across the spectrum, not just at the peak. It is computed from,

$$\overline{\varepsilon}_\Sigma = \frac{1}{100} \sum_{k=1}^{100} \frac{\int_0^{\omega_{\max}} |\overline{\alpha_i} - \alpha_{i,k}| \, d\omega}{\int_0^{\omega_{\max}} |\overline{\alpha_i}| \, d\omega} \times 100\%, \tag{4.6}$$

in which $\omega_{\max}$ is the maximum frequency for which disturbances are unstable in the averaged growth rate spectrum.

The results presented in Table 4.3 show that the predictions of stability analysis performed on curve fits that pass closest to the velocity profile data points, i.e., on curve

Table 4.3: Curve fit residuals and error parameters for Rayleigh equation solutions on one hundred discrete profiles, created by imposing data scatter on the simulated profile from Eqs. 4.1 and 4.2 with $\Delta y/\delta^* = 5.6 \times 10^{-2}$.

curve fit	R_0	$\overline{R}$	$\overline{\varepsilon}_\omega$	$\overline{\varepsilon}_\alpha$	$\overline{\varepsilon}_\Sigma$
cubic spline	0	0	5.6	4.5	28.0
Dini et al. [79] fit	0.029	0.039	1.8	1.3	3.5
Dovgal et al. [34] fit	0.016	0.025	1.9	1.6	3.8
Green [77] fit	0.026	0.035	2.5	1.3	3.9
LeBlanc et al. [27] fit	0.0026	0.012	2.1	1.7	4.0
logistic series	0.00041	0.018	17.7	16.4	25.2
piecewise cubic Hermite polynomial	0	0	7.5	6.0	35.4
reverse flow Falkner-Skan fit	0.078	0.085	3.4	3.1	8.9
sine series	0.017	0.044	10.5	4.1	13.7
smoothing spline, $Sp = 0.99$	0.35	0.36	1.4	0.6	1.6
smoothing spline, $Sp = 0.999$	0.037	0.044	2.6	0.9	3.1
smoothing spline, $Sp = 0.9999$	0.0016	0.0067	3.4	1.9	7.7
smoothing spline, $Sp = 0.99999$	0.000040	0.0019	5.0	3.4	21.1

fits with the lowest average least squares residuals, are the most susceptible to velocity profile data scatter. Specifically, the cubic spline, logistic series, piecewise cubic Hermite polynomial, sine series, and smoothing splines with relatively high values of the smoothing parameter ($Sp \gtrsim 0.99999$ in this case) have the lowest least squares residuals but result in integrated growth rate spectrum error values greater than 10%. All of the error measures for the stability predictions obtained using the Dini et al. [79] fit, Dovgal et al. [34] fit, Green [77] fit, LeBlanc et al. [27] fit, and the reverse flow Falkner-Skan fit, are less than 10%, while the fits still match the velocity profile well ($\overline{R} \leq 0.40$). Thus, these five curve fits are expected to provide the lowest variability due to data scatter in the velocity profile measurements and will therefore be the focus of the remainder of this section.

Variability in the growth rate spectrum due to data scatter in the simulated velocity profile is illustrated in Fig. 4.5 for the five curve fits identified as providing stability predictions with low sensitivity to velocity profile data scatter. Shaded regions in the figure outline second standard deviation bands for the one hundred simulated velocity profiles with data scatter. Each band gives an indication of the extent of variability that can be expected by repeating the analysis with that curve fit on successive velocity profile measurements for the same flow conditions. A comparison of the results in Figs. 4.4 and 4.5 suggests that, for the five curve fits identified, there is greater variability in the growth rate spectrum predictions due to the choice of curve fit type (Fig. 4.4) than due to data scatter when applying a specific curve fit (Fig. 4.5).

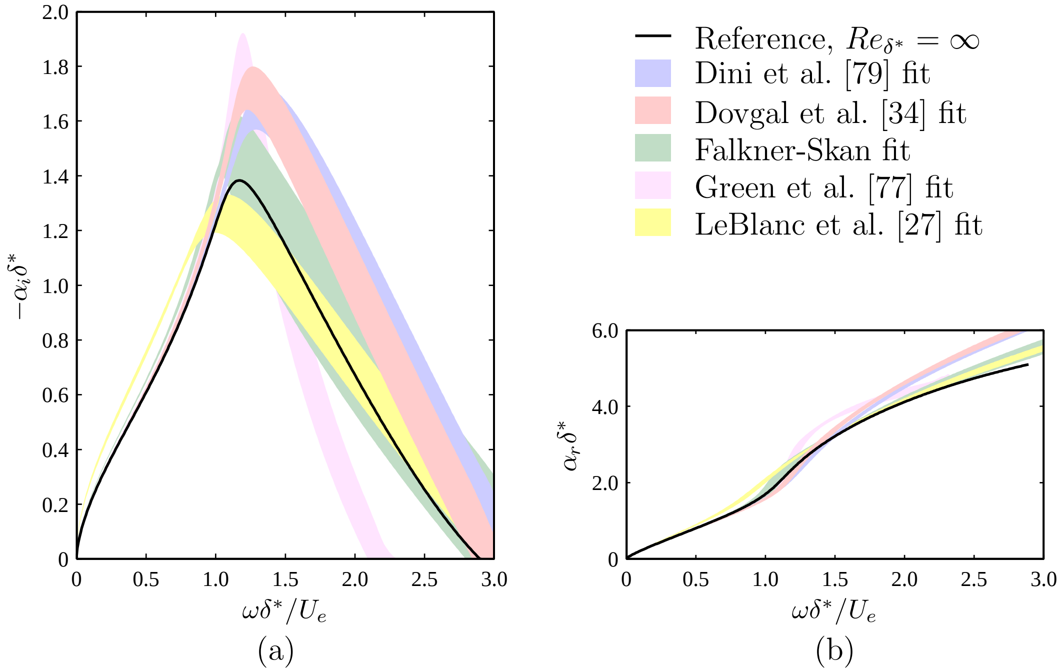

Figure 4.5: Variability in Rayleigh equation eigenvalue spectra for various curve fit forms used in the analysis. Bands show the second standard deviation of growth rate predictions based on the analysis of one hundred simulated discrete profiles with $\Delta y/\delta^* = 5.6 \times 10^{-2}$ and imposed data scatter.

It should be noted that, if estimating the streamwise velocity fluctuation profiles using linear stability analysis is of particular importance in a given study, fits with discontinuities in the base velocity profile should be avoided. The Green [77] and LeBlanc et al. [27] fits have such discontinuities. Figure 4.6 shows streamwise velocity fluctuation profiles obtained from stability analysis using the five curve fits to the simulated velocity profile from Eqs. 4.1 and 4.2 with $\Delta y/\delta^* = 5.6 \times 10^{-2}$ and without data scatter. The results reveal discontinuities in velocity fluctuation profiles for the Green [77] and LeBlanc et al. [27] fits at the locations of discontinuities in the slopes of their respective base profile fits. Specifically, in Figs. 4.6b and 4.6c this occurs at $y/\delta^* \approx 0.74$ for the LeBlanc et al. [27] fit and at $y/\delta^* \approx 0.69$ and 1.24 for the Green [77] fit. Despite producing discontinuities in the streamwise velocity fluctuation profiles, the Green [77] and LeBlanc et al. [27] curve fits result in reasonable growth rate spectrum predictions and have low susceptibility to data scatter. For these reasons, the Green [77] and LeBlanc et al. [27] fits will be further

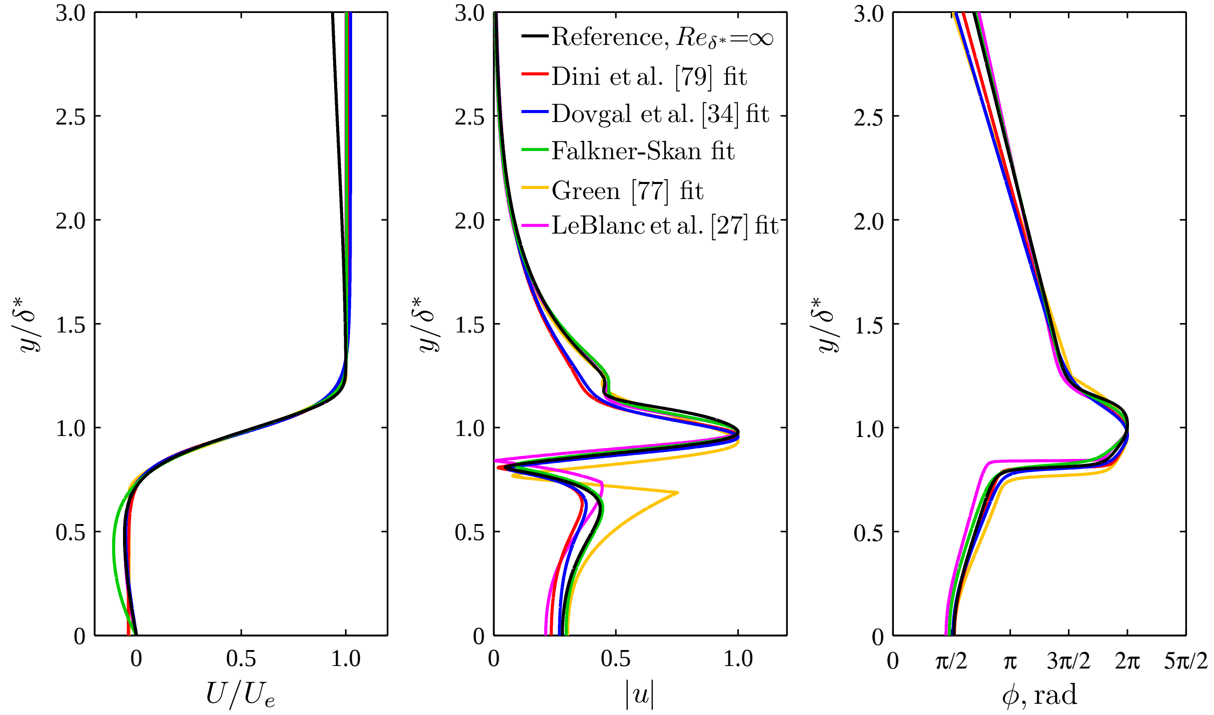

(a) (b) (c)

Figure 4.6: Streamwise velocity fluctuation profile predictions of the Rayleigh equation at $\omega\delta^*/U_e = 1.17$, using curve fits on the simulated velocity profile from Eqs. 4.1 and 4.2 with $\Delta y/\delta^* = 5.6 \times 10^{-2}$. Presented are the (a) curve fits to the mean velocity profile, (b) velocity fluctuation amplitude, and (c) velocity fluctuation phase.

evaluated along with the reverse flow Falkner-Skan, Dini et al. [79], and Dovgal et al. [34] fits by comparing their stability predictions for measured separated shear layer profiles.

Stability analysis was performed on ten published separated shear layer profiles using each of the five curve fits shown to provide stability predictions with relatively low susceptibility to data scatter. The obtained growth rate spectra are plotted in Fig. 4.7. The results suggest that no single fit is consistently able to produce the best estimate of the measured frequency of maximum disturbance growth rate for the ten profiles analyzed. Moreover, the frequency estimates obtained for two different fits can deviate by up to 35% for the same measured profile. The deviations between the predicted frequencies of maximum disturbance growth rate and those measured experimentally are quantified in Table 4.4. For each curve fit, the average error and the maximum error are tabulated. The

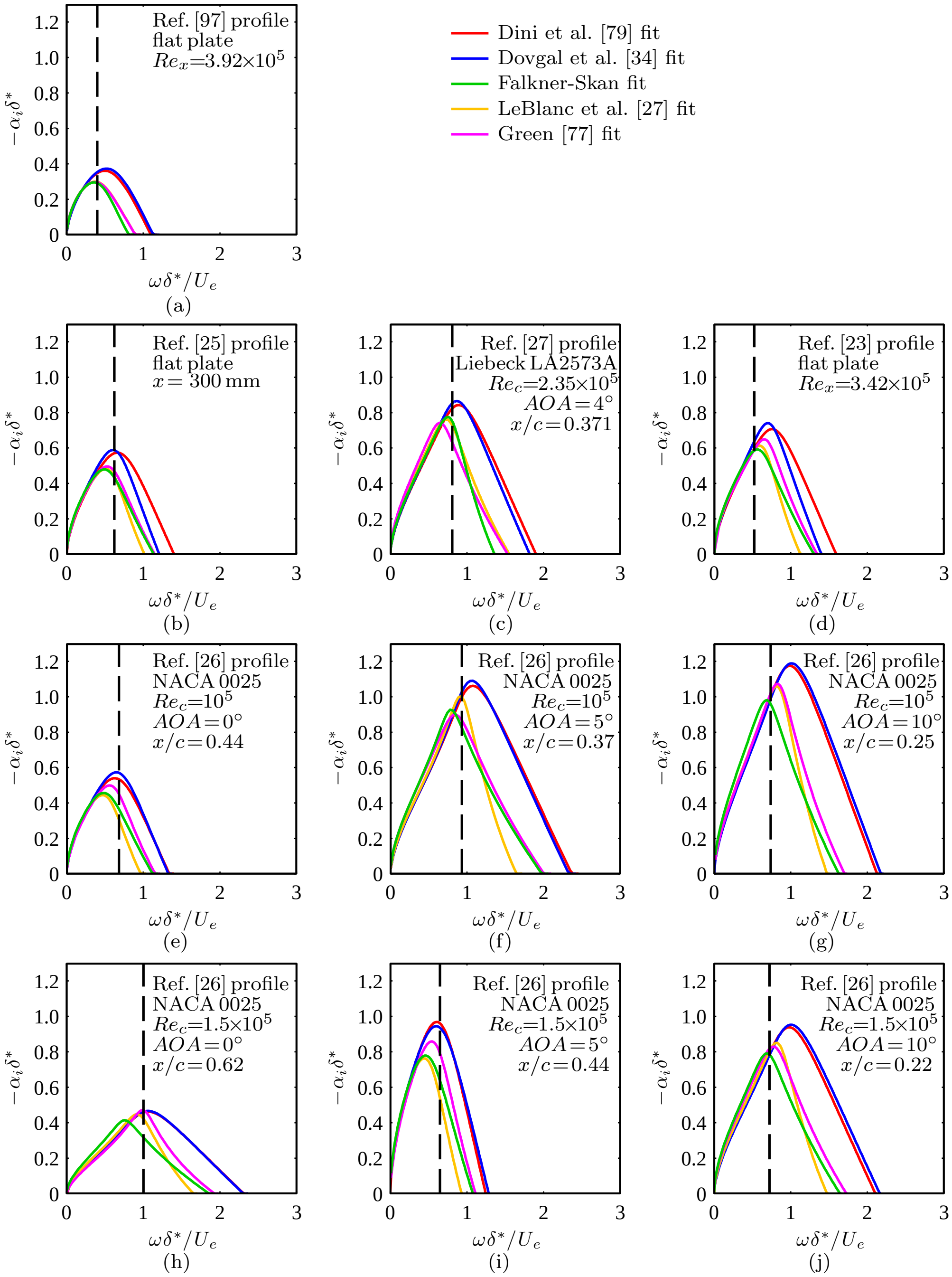

Figure 4.7: Computed Rayleigh equation growth rate spectra of various measured separated shear layer profiles. Dashed lines indicate the measured frequency of maximum energy content. Values of U_e and δ^* were estimated using the LeBlanc et al. [27] fit.

Table 4.4: Average and maximum error in the frequency of maximum disturbance growth rate predictions from Fig. 4.7.

curve fit	average error	maximum error
Dini et al. [79]	19%	44%
Dovgal et al. [34]	18%	39%
Flakner-Skan fit	16%	30%
Green [77] fit	14%	32%
LeBlanc et al. [27] fit	12%	25%

results show that the LeBlanc et al. [27] fit provides the lowest average and maximum errors in the characteristic frequency predicted for the ten measured velocity profiles considered. However, the LeBlanc et al. [27] fit was only the best predictor of the frequency of maximum disturbance growth rate for three out of the ten profiles analyzed. For the experimental profiles analyzed, the reverse flow Falkner-Skan, Green [77], and LeBlanc et al. [27] curve fits performed better on the average than the Dini et al. [79] and Dovgal et al. [34] fits, as indicated by the data in Table 4.4. However, Figs. 4.7b, e, and i show that there are cases in which using either the Dini et al. [79] or Dovgal et al. [34] curve fits provide more accurate predictions of the frequency of maximum disturbance growth rate compared to those obtained using other fits. The results presented in this section give an indication of the level of uncertainty in the predictions of inviscid spatial linear stability analysis when curve fits are applied to measured velocity profiles.

4.4 Solutions to the Orr-Sommerfeld Equation for Experimental Profiles

Inviscid spatial linear stability analysis of measured separated shear layer profiles often provides reasonable estimates of the frequency of maximum disturbance growth rate, but over-predicts the magnitude of the growth rate spectrum [22,26,29]. Including viscosity in the analysis has the effect of reducing the disturbance amplification rate, and may improve the estimates. The sensitivity of solutions to the Orr-Sommerfeld equation for measured separated shear layers to experimental data scatter and the velocity profile processing approach are examined in this section.

Figure 4.8 compares the eigenvalue spectra of the Rayleigh and Orr-Sommerfeld equations for the reference profile of Eqs. 4.1 and 4.2 to the measured spectrum. Based on the eigenvalue spectrum, viscosity acts only to damp disturbance amplification, preserving

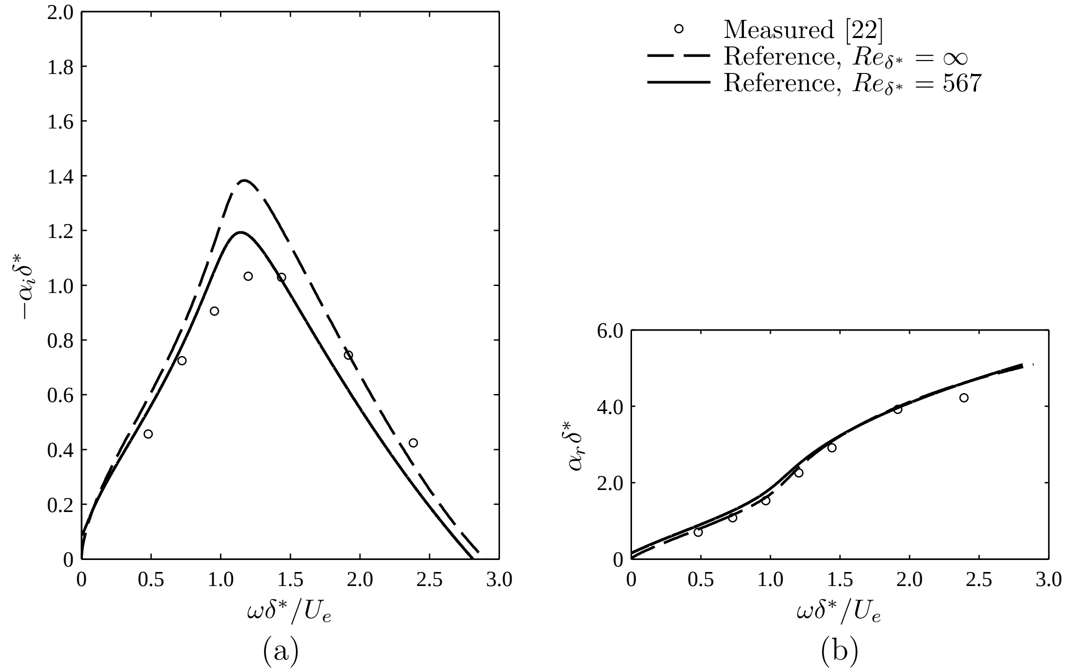

Figure 4.8: Eigenvalue spectra of the Orr-Sommerfeld and Rayleigh equations for the profile fit of Eqs. 4.1 and 4.2, compared to measurements of Nishioka et al. [22].

the shape of the inviscid growth rate spectrum and approximate frequency of maximum disturbance growth rate. Minor changes are observed in the wave number spectrum. Including viscosity in the linear stability predictions reduces the difference between the predicted and measured maximum disturbance growth rate by about 50%, but reduces the agreement between measurements and predictions at higher frequencies ($\omega\delta^*/U_e \gtrsim 1.5$).

Figure 4.9 compares the measured streamwise velocity fluctuation profiles at two frequencies to those predicted by the Rayleigh and Orr-Sommerfeld equations. The viscous and inviscid profile predictions show similar characteristic fluctuation profiles, with a dominant peak occurring at approximately the location of the mean velocity profile inflection point. This is in contrast to a fluctuation profile with a single peak near the wall predicted for viscous Tollmien-Schlichting wave growth in attached boundary layers [61]. The most significant difference between the Rayleigh and Orr-Sommerfeld equation predictions of the velocity fluctuation profiles is that the Orr-Sommerfeld equation solution satisfies the no-slip condition at the wall. However, this does not have a significant effect on the profile at distances from the wall that could be measured with the hot-wire

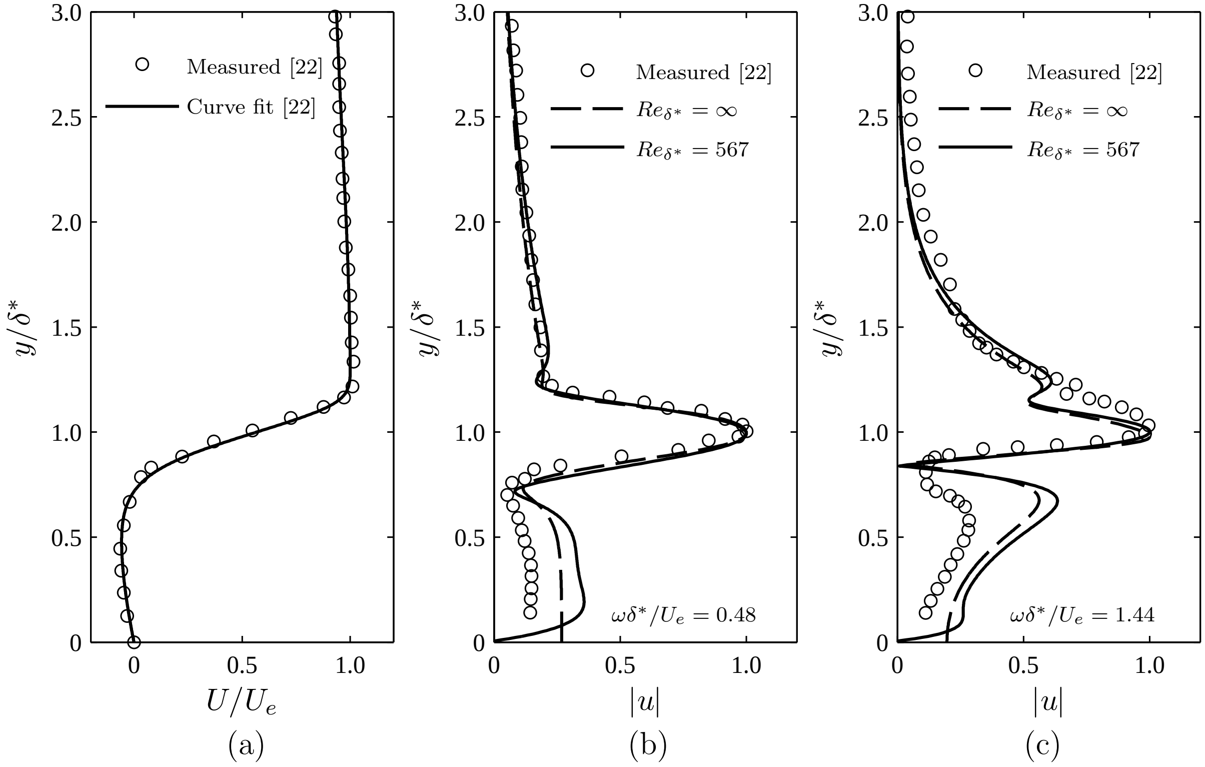

(a) (b) (c)

Figure 4.9: Mean velocity profile, (a), and streamwise velocity fluctuation amplitude profiles, (b) and (c), of the Rayleigh and Orr-Sommerfeld equations, for the profile fit of Eqs. 4.1 and 4.2.

probe ($y/\delta^* \gtrsim 0.1$ for this profiles). Furthermore, including viscous effects in the predictions does not reduce the discrepancy between the measured and predicted velocity fluctuation profiles. The similarity between the viscous and inviscid predictions in Figs. 4.8 and 4.9, illustrate the dominance of an inviscid instability mechanism in the laminar separated shear layer.

Several of the conclusions drawn from the previous sections on the sensitivity of inviscid spatial linear stability analysis of measured separated shear layer velocity profiles can be extended to Orr-Sommerfeld equation solutions for such profiles. First, when the analysis is to be performed on wind tunnel measurements of separated shear layers on low Reynolds number airfoils, the data scatter and spatial resolution commonly available are not sufficient to provide confidence in the results. Therefore, only methods employing curve fitting will be considered for solving the Orr-Sommerfeld equation based on experimental data. Second, curve fits which closely follow data scatter in measured profiles will be most sensitive to experimental data scatter. Curve fits for which Rayleigh equation solutions were found to be sensitive to experimental data scatter are therefore excluded in this section. To demonstrate that the level of variability in the growth rate spectrum predictions due to the choice of velocity profile curve fit is similar for the Orr-Sommerfeld equation as for the Rayleigh equation, the eigenvalue spectrum of the Orr-Sommerfeld equation for each curve fit on the simulated velocity profile of Eqs. 4.1 and 4.2 with a point spacing of $\Delta y/\delta^* = 5.6 \times 10^{-2}$ were computed and are presented in Fig. 4.10. Comparing Figs. 4.4 and 4.10, it can be seen that the eigenvalue spectra of the Rayleigh and Orr-Sommerfeld equations are similar for each fit, with the Orr-Sommerfeld equation growth rate spectrum for each fit being of lower magnitude than the corresponding Rayleigh equation spectrum. Third, due to the presence of derivatives of the mean velocity profile in both the Rayleigh and Orr-Sommerfeld equations, profile fits with discontinuous derivatives will have discontinuities in the predicted streamwise velocity fluctuation profiles. For this reason, the Green [77]

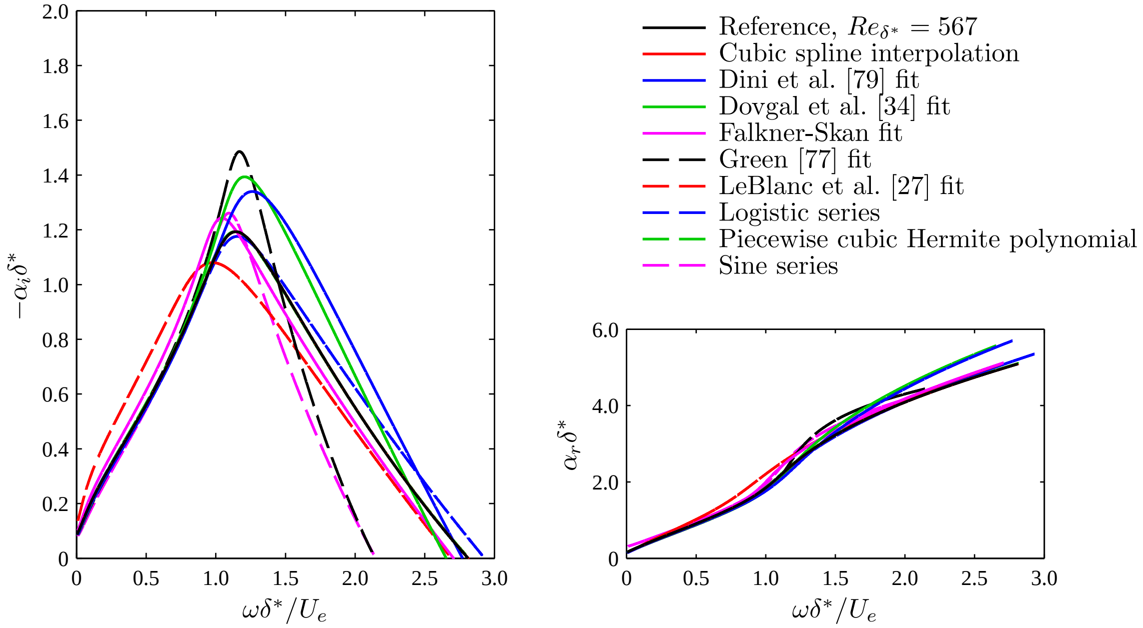

(a) (b)

Figure 4.10: Eigenvalue spectrum of the Orr-Sommerfeld equation using various forms of curve fits to the simulated velocity profile of Eqs. 4.1 and 4.2 with $\Delta y/\delta^* = 5.6 \times 10^{-2}$.

and LeBlanc et al. [27] fits will not be considered further for Orr-Sommerfeld equation solutions. Thus, only the Dini et al. [79], Dovgal et al. [34], and Falkner-Skan fits will be considered for base velocity profile representations when solving the Orr-Sommerfeld equation for measured separated shear layer profiles.

Variability to velocity profile data scatter was again assessed based on one hundred simulated velocity profiles with data scatter by imposing Gaussian noise on the simulated velocity profile of Eqs. 4.1 and 4.2 with a profile point spacing of $\Delta y/\delta^* = 5.6\times10^{-2}$. Second standard deviation bands of the resulting eigenvalue spectra are presented in Fig. 4.11, with corresponding error measures presented in Table 4.5. A comparison of Figs. 4.5 and 4.11 shows that, as was found for Rayleigh equation solutions, the Falkner-Skan fit provides the highest variability in the growth rate spectrum of the Orr-Sommerfeld equation out of the three profile fits considered. Furthermore, the compounded variability in the results due to the choice of curve fit and data scatter appears to be smaller for Orr-Sommerfeld equation

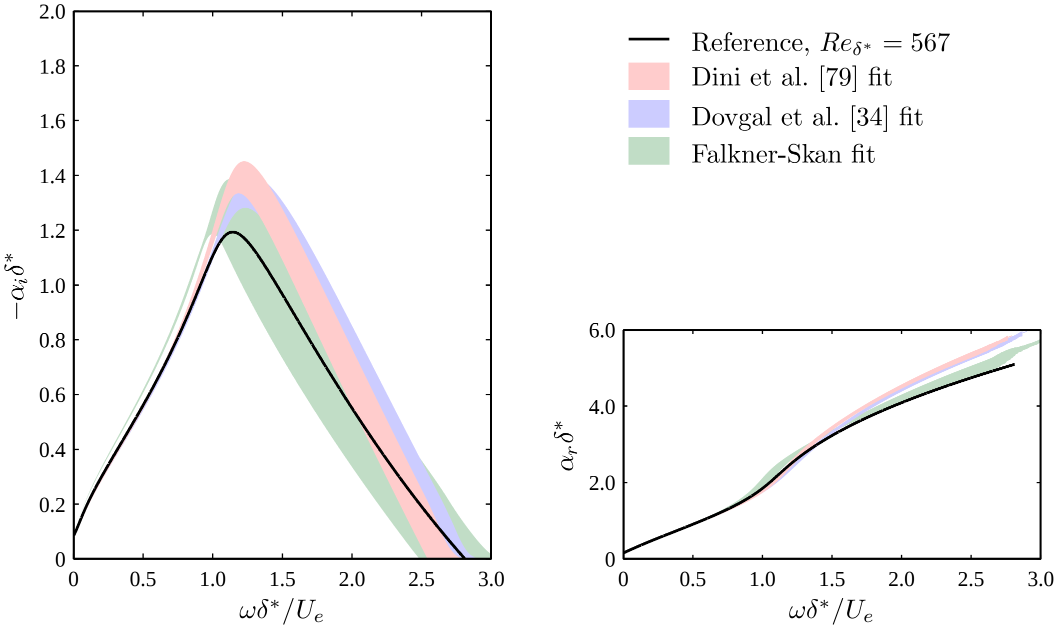

(a) (b)

Figure 4.11: Variability in Orr-Sommerfeld equation eigenvalue spectra for various curve fit forms used in the analysis. Bands show the second standard deviation of growth rate predictions based on the analysis of one hundred simulated discrete profiles with $\Delta y/\delta^* = 5.6\times10^{-2}$ and imposed data scatter.

predictions, as indicated by the greater overlap of the three bands in Fig. 4.11 compared to those in Fig. 4.5. Comparing Tables 4.3 and 4.5, it can be concluded that the relative error measures for the Orr-Sommerfeld equation solutions are marginally lower than those of the Rayleigh equation solutions. This suggests that including viscosity in the stability analysis not only improves the accuracy of the growth rate predictions but also reduces the sensitivity of the analysis to data scatter.

Streamwise velocity fluctuation profiles computed using the three curve fits to the simulated velocity profile of Eqs. 4.1 and 4.2 with a point spacing of $\Delta y/\delta^* = 5.6 \times 10^{-2}$ and no imposed data scatter are presented in Fig. 4.12. By comparing Figs. 4.6 and 4.12, it can be concluded that satisfying the no-slip condition at the wall reduces the difference between predictions from different curve fits near the wall ($y/\delta^* \lesssim 0.75$). However, the upper peak near $y/\delta^* \approx 1.25$ is still more prominent for the Falkner-Skan fit than for the Dini et al. [79] and Dovgal et al. [34] fits. Phase shift profiles show a lower level of disagreement between the three fits.

Figure 4.12a shows that the Falkner-Skan, Dini et al. [79], and Dovgal et al. [34] fits produce very different mean profile curvatures in the reverse flow region near the wall. Most notably, the Dovgal et al. [34] fit follows the measured curvature well, whereas the Dini et al. [79] fit approaches a constant value and does not satisfy the mean flow no-slip condition at the wall. Despite this difference, Fig. 4.10 shows that, as was found for Rayleigh equation solutions, the eigenvalue spectrum of the Orr-Sommerfeld equation for the Dini et al. [79] and Dovgal et al. [34] fits are very similar. Furthermore, the streamwise velocity fluctuation profiles from these fits and the Falkner-Skan fit are very similar. It may be expected that the additional boundary conditions imposed in the Orr-Sommerfeld equation solution will cause the curvature of the profile near the wall to have a more significant effect on the results than in solutions to the Rayleigh equation. However, velocity profile curvature in the reverse flow region had no significant effect on the stability predictions, indicating that measurement error in the reverse flow region, inherent to near wall velocity measurements,

Table 4.5: Error parameters for stability analysis of one hundred discrete profiles, created by imposing data scatter on the simulated profile from Eqs. 4.1 and 4.2 with $\Delta y/\delta^* = 5.6 \times 10^{-2}$.

curve fit	$\overline{\varepsilon}_\omega$	$\overline{\varepsilon}_\alpha$	$\overline{\varepsilon}_\Sigma$
Dini et al. [79] fit	1.7	1.1	3.1
Dovgal et al. [34] fit	1.7	1.3	3.4
reverse flow Falkner-Skan fit	3.4	2.9	7.8

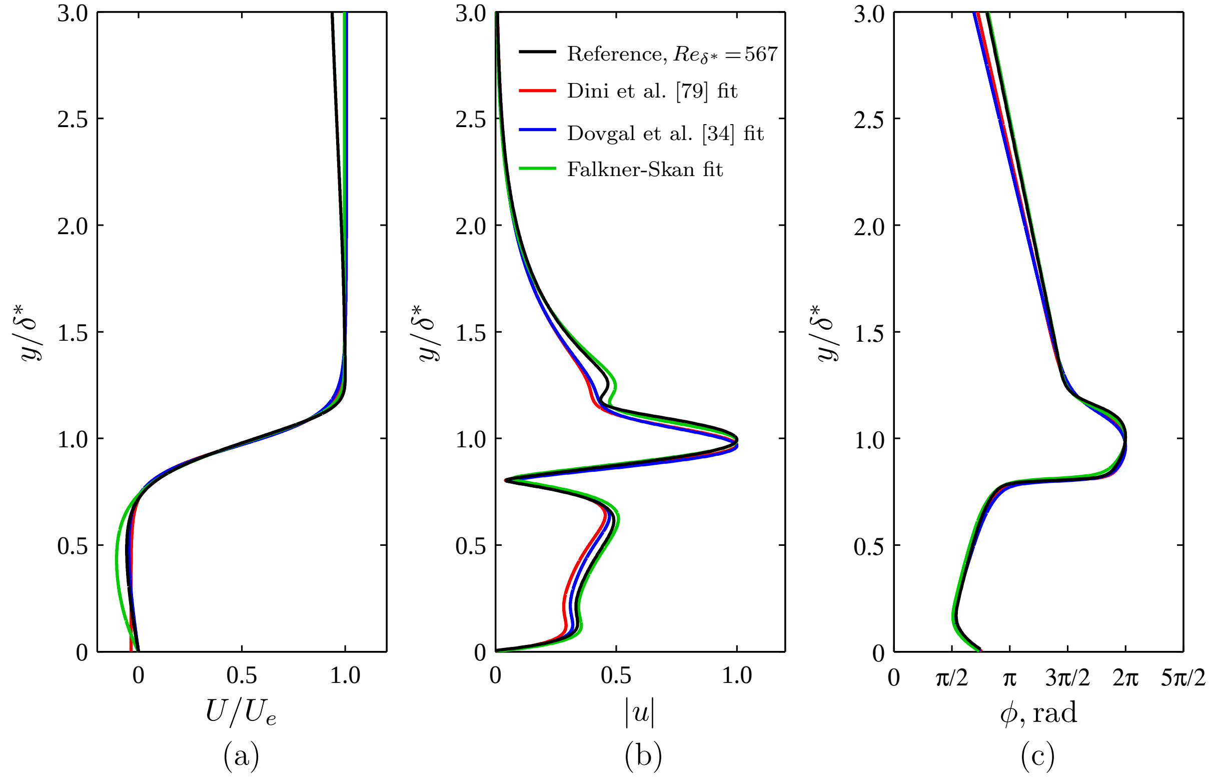

Figure 4.12: Streamwise velocity fluctuation profile predictions of the Orr-Sommerfeld equation at $\omega\delta^*/U_e = 1.17$, using curve fits on the simulated velocity profile from Eqs. 4.1 and 4.2 with $\Delta y/\delta^* = 5.6 \times 10^{-2}$. Presented are the (a) curve fits to the mean velocity profile, (b) velocity fluctuation amplitude, and (c) velocity fluctuation phase.

will not have a significant effect on linear stability predictions for measured separated shear layer profiles.

Stability predictions based on Dini et al. [79], Dovgal et al. [34], and Falkner-Skan curve fits were further evaluated by comparing predictions for six measured separated shear layer profiles over a NACA 0025 airfoil from Yarusevych et al. [26] to measured growth rate spectra. Figure 4.13 presents growth rate spectra of the Orr-Sommerfeld and Rayleigh equations for each of these profiles. In contrast to the results in Fig. 4.8, based on measurements from Nishioka et al. [22], the results in Fig. 4.13 show no significant improvement in the predictions of linear stability analysis compared to measured growth rates when viscosity is included in the analysis. Whereas the results in Fig. 4.8 show

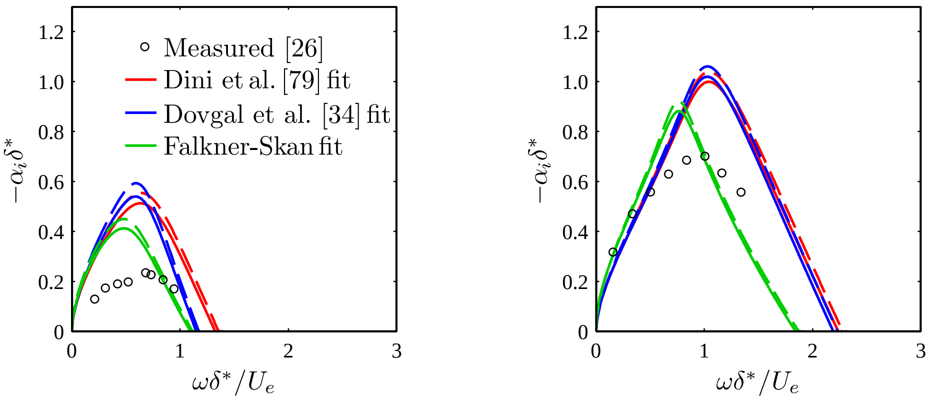

(a) $Re_c = 10^5, AOA = 0°, x/c = 0.44$ (b) $Re_c = 1.5 \times 10^5, AOA = 0°, x/c = 0.62$

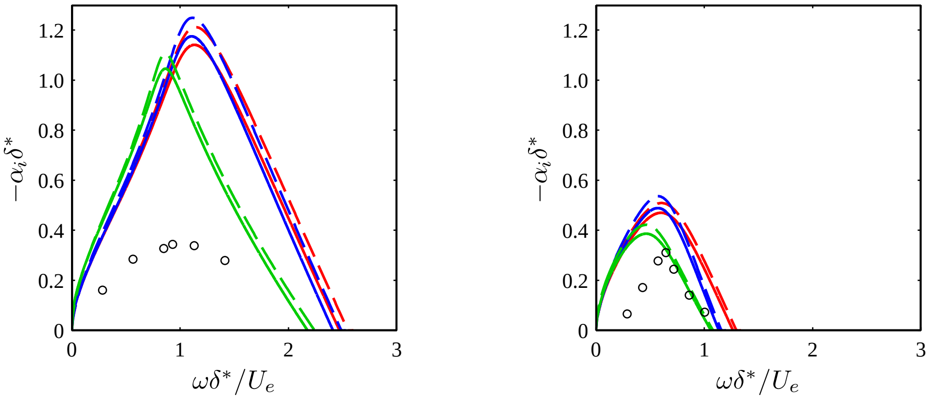

(c) $Re_c = 10^5, AOA = 5°, x/c = 0.37$ (d) $Re_c = 1.5 \times 10^5, AOA = 5°, x/c = 0.44$

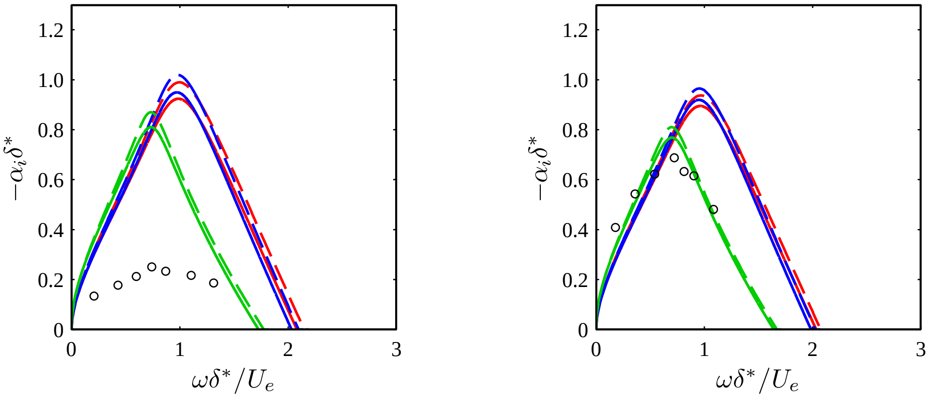

(e) $Re_c = 10^5, AOA = 10°, x/c = 0.25$ (f) $Re_c = 1.5 \times 10^5, AOA = 10°, x/c = 0.22$

Figure 4.13: Comparison of growth rate spectrum measurements to LST predictions for published measurements on a NACA 0025 airfoil. Rayleigh and Orr-Sommerfeld equation solutions are indicated by dashed and solid curves, respectively.

that including viscosity in the analysis can reduce the discrepancy between predicted and measured maximum amplification rates by 50%, Fig. 4.13 shows improvements of only 5 to 20%. As was found for Rayleigh equation solutions, no single fit provided the most accurate prediction of the maximum disturbance growth rate for all of the measured profiles examined.

Experimental uncertainty in growth rate measurements and simplifications of LST may contribute to the differences between the measured and computed growth rate spectra in Figs. 4.8 and 4.13 that remain after viscosity is included in the calculations. Experimental uncertainty in the measured growth rates can be significant, as discussed in Appendix A. This is likely the most significant factor contributing to the observed discrepancies. Simplifications of LST may also contribute. However, a comparison of direct numerical simulation, a PSE solution, and LST predictions by Theofilis et al. [64] for disturbance growth in the separation bubble on a flat plate, indicated a difference of about 10% between the linear stability predictions and the other two data sets. This is a much smaller discrepancy than observed in Fig. 4.13 between measured growth rate spectra and linear stability predictions.

From this investigation into the sensitivity of linear stability analysis of measured separated shear layer profiles, it can be concluded that, for data typical of hot-wire measurements of separated shear layer velocity profiles over low Reynolds number airfoils, curve fitting is required before completing stability calculations. For this purpose, the Falkner-Skan, Dini et al. [79], and Dovgal et al. [34] fits provide relatively low variability to profile data scatter and yield streamwise velocity fluctuation profiles without discontinuities. The relative variability between curve fits can be greater than the variability of a particular curve fit to data scatter, and no one fit consistently provided the most accurate prediction of the frequency of maximum disturbance growth rate compared to that measured experimentally. Therefore, the analyst should consider the uncertainty induced by the choice of curve fitting method on the conclusions drawn from the analysis. No changes were observed in the general trends of the eigenvalue spectrum or velocity fluctuation profiles when viscosity was included in the analysis; however, including viscosity reduced the predicted disturbance growth rates and also reduced the sensitivity of stability predictions to velocity profile data scatter. The apparent sensitivity of spatial linear stability analysis of measured separated shear layer profiles to experimental data scatter and velocity profile processing approach should be considered when drawing conclusions from such an analysis.

Chapter 5

Effect of Experimental Setup on Flow Development

This chapter focuses on the effects that three elements of the experimental setup have on flow development: end plates, test section walls, and intrusive equipment. The effect of each element will be evaluated from measurements of static pressure distributions, model surface pressure fluctuations, and energy spectra of velocity fluctuations in the airfoil wake. Static pressure distributions along the chord are used to determine the effect of each element of the experimental setup on lift and locations of flow separation, transition, and reattachment. Similar pressure measurements along three spanwise rows of pressure taps are used to assess mean flow two-dimensionality. Spectral analysis of measurements from microphones embedded in the airfoil surface below the separated flow region are compared to determine how disturbance amplification in the transitioning flow is affected by the experimental setup. Energy spectra of velocity fluctuations are used to evaluate the effect of experimental setup on wake vortex shedding characteristics.

5.1 End Plate Configuration

In this section, the effects of end plates on flow development are examined by comparing measurements obtained with different end plate configurations. Seven configurations were considered: neither end caps nor end plates installed (free ends), only end caps installed, and end caps and end plates installed with five different spanwise end plate spacing distances in the range $0.5 \leq b/c \leq 2.5$. Boundary layer measurements on the side walls of the wind tunnel at the location of the airfoil model showed that the boundary layer thickness is approximately $0.26c$. Thus, the inward side of each end plate is just outside of the side wall boundary layer for a spanwise end plate spacing of $b/c = 2.5$. All data presented in this section were obtained with the wind tunnel walls set in the ASW configuration for an empty test section at $Re_c = 10^5$.

Surface pressure distributions measured for the various end plate configurations are presented in Fig. 5.1. The distributions for $AOA = 0$, 5, and 10° are typical for conditions at which a separation bubble forms [1,8]. The mean pressure on the upper surface decreases rapidly up to a suction peak near the leading edge. At a location downstream of the suction peak, the rate of pressure recovery decreases significantly, creating a pressure plateau in the model surface pressure distribution. The beginning and end of this pressure plateau mark the locations of laminar boundary layer separation and separated shear layer transition, respectively [8,52]. Rapid surface pressure recovery is observed up to the mean reattachment location, downstream of which pressure recovery continues at a reduced rate [8]. The surface pressure distributions for $AOA = 15°$ are typical for conditions at which laminar boundary layer separation occurs without subsequent reattachment: the upper surface pressure distribution is nearly flat over most of the chord, with the exception of a low magnitude suction peak just downstream of the leading edge.

For $AOA = 0$, 5, and 10°, relatively minor differences are observed between surface pressure distributions obtained for a model with free ends and those obtained with only end caps installed. However, for $AOA = 15°$, at which the airfoil is stalled, installing end caps causes a noticeable increase in the suction pressure over the upper surface of the model. Installing end plates produces a more substantial change in the surface pressure distributions for each angle of attack. Installing end plates at $b/c = 2.5$ causes an increase in the suction pressure on the upper surface. Further increases occur as the end plate spacing is reduced to $b/c = 1.5$. This change can be observed in the inset plots of the suction peaks and the pressure plateaus in Fig. 5.1. Decreasing the end plate spacing below $b/c = 1.5$ results in a reduction in magnitude of the suction peak and pressure plateau, for angles of attack other than zero. For $AOA = 5$ and 10°, the transition location moves upstream by approximately 4% of the chord for $b/c = 0.5$ compared to all other configurations with and without end plates installed. At $AOA = 15°$ (Fig. 5.1d), for which the airfoil is stalled, changing the end plate configuration causes a shift of up to 0.15 in the value of the surface pressure coefficient in the relatively constant surface pressure region downstream of the separation point. Based on the lower surface pressure distributions in Fig. 5.1 for $AOA = 5$ and 10°, it can be concluded that flow development over the lower surface of the model is less sensitive than that over the upper surface to the use of end plates and their spacing; appreciable changes in the lower surface pressure distribution from that measured in the free ends configuration are only observed for the lowest end plate spacing considered ($b/c = 0.5$).

Lift coefficients, computed from the measured pressure distributions, are presented

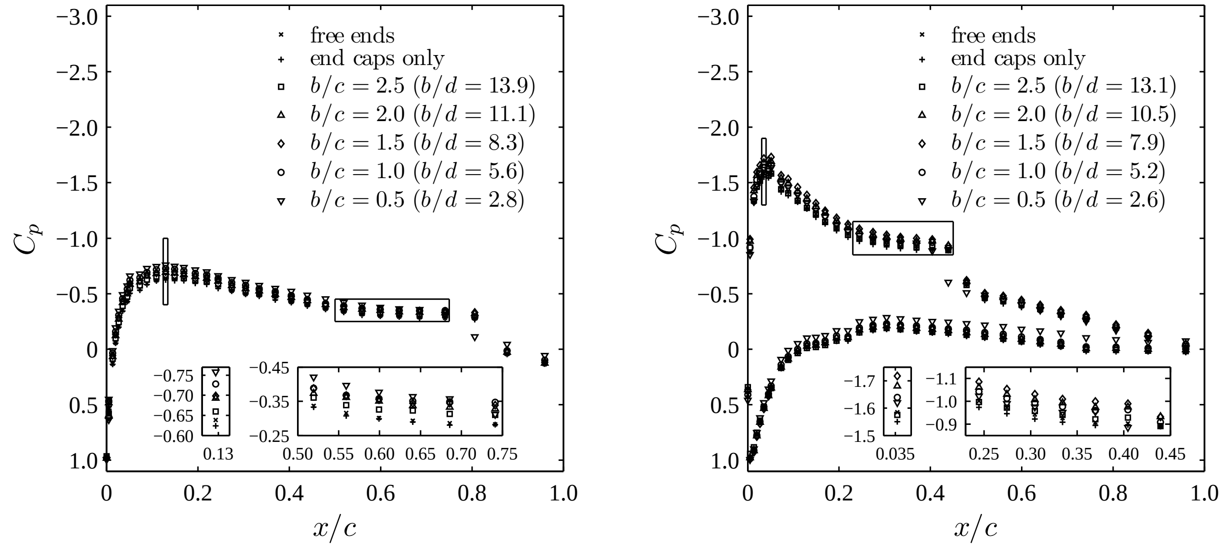

(a) $AOA = 0°$

(b) $AOA = 5°$

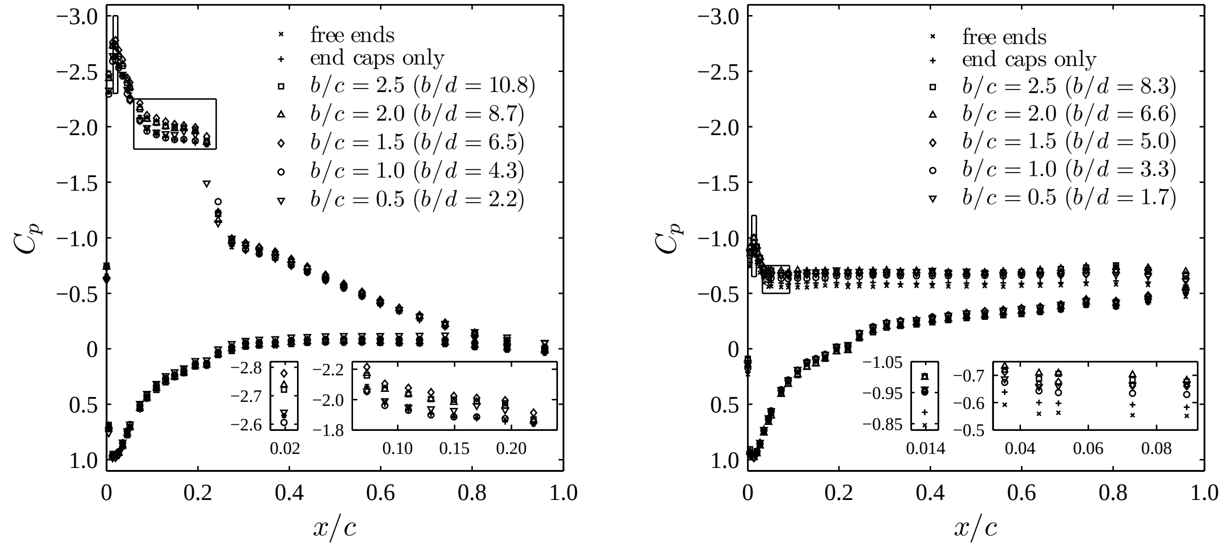

(c) $AOA = 10°$

(d) $AOA = 15°$

Figure 5.1: Streamwise distributions of surface pressure for the various end plate configurations. In plot (a), for clarity, only the upper surface pressure distribution is plotted. Solid lines indicate portions of the graph magnified in the inset plots.

in Fig. 5.2. Changing the end plate configuration causes changes in the measured lift coefficient by as much as 11% of the maximum lift coefficient at this Reynolds number. Lift increases when end plates are installed and is least sensitive to end plate spacings for $b/c \gtrsim 1.5$. Lift coefficients change more significantly with end plate spacing for $b/c \lesssim 1.5$. The non-zero lift coefficients observed for $AOA = 0°$ with end plates installed suggest that the end plates are changing the effective aerodynamic zero angle of attack. Previous low Reynolds number airfoil investigations have similarly observed that the zero-lift angle is sensitive to flow conditions [10]. In the present investigation, the effect of the end plate configuration on the stall angle was also investigated. Installing end plates at $b/c = 2.0$ was found to increase the stall angle by approximately 1° compared to the end caps only configuration.

The results in Figs. 5.1 and 5.2 show that the end plate configuration influences mean flow development on the center-span plane, and as a result, the lift coefficient computed from pressure measurements on this plane. The extent to which the flow is affected at other locations on the span is assessed on the basis of spanwise surface pressure distributions

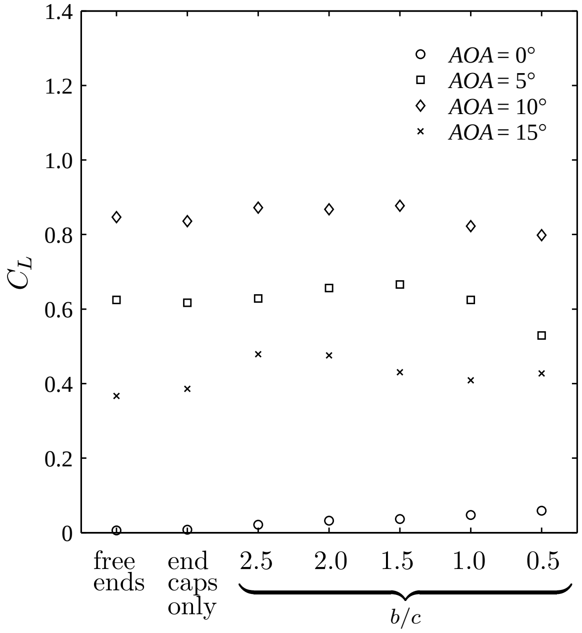

Figure 5.2: Variation in lift coefficient computed from the measured pressure distributions for the various end plate configurations. Measurements were repeatable to within the marker size.

measured at $x/c = 0.15$, 0.30, and 0.60. These distributions are presented in Fig. 5.3. The results show that installing end caps has a minor effect on mean spanwise uniformity. In contrast, installing end plates improved spanwise uniformity considerably for each angle of attack considered. The end plate spacing does not have an appreciable effect on mean spanwise uniformity for spacings as low as $b/c = 1.0$, the lowest value for which there is more than one z/c static pressure tap location between the end plates on this airfoil model.

Since separated shear layer development governs the aerodynamic performance of low Reynolds number airfoils [1], it is of interest to assess how experimental setup affects laminar-to-turbulent transition in the shear layer. Gerakopulos [35] showed that embedded surface pressure sensors can be used to characterize shear layer development over this airfoil model at low Reynolds numbers. Such measurements are used here to assess the effects of end plates on transition in the separated shear layer. Figure 5.4 presents energy spectra of pressure fluctuations from measurements with microphones embedded in the airfoil surface at various streamwise locations in the transition region. Note that results for $b/c = 0.5$ are not included because an end plate obstructs the embedded microphones when installed at this spacing. For each angle of attack, at least one streamwise location shows a band of frequencies over which disturbances have been amplified with respect to the broadband background disturbance environment. The process of disturbance amplification leads to turbulent transition, influencing the size and location of the separation bubble and, consequently, the overall aerodynamic performance. In Fig. 5.4, it can be seen that at some x/c locations, the end plate configuration affects the magnitude of amplified disturbances in the separated shear layer. For example, as end plates are installed and moved closer together for $AOA = 5^\circ$, the broad spectral peaks around $f = 500$ Hz at $x/c = 0.32$ and 0.34 increase in magnitude. For $AOA = 10^\circ$ the broad peak around $f = 1000$ Hz is less affected by the end plate configuration than for $AOA = 5^\circ$. However, from a close examination of the peaks in the energy spectrum at $AOA = 10^\circ$ for $x/c = 0.15$ and 0.17, it can be seen that end plates reduce the spectral noise across the peak. One possible explanation for this is that the improved spanwise uniformity in mean surface pressure with the end plates installed also reduces the spanwise variation in the central frequency of disturbance amplification, improving the coherence of measured pressure fluctuations. Another possibility is that the end plates are reducing the contribution of side wall boundary layer noise to the background disturbances being amplified in the shear layer.

The effects of end plate configuration on wake vortex shedding characteristics were assessed based on energy spectra of the vertical velocity fluctuations measured at $X/c = 2.7$. Figure 5.5 presents the results for $AOA = 10$ and 15°, with the selected angles producing the most pronounced spectral peaks and representing conditions under which separation occurs with and without reattachment.

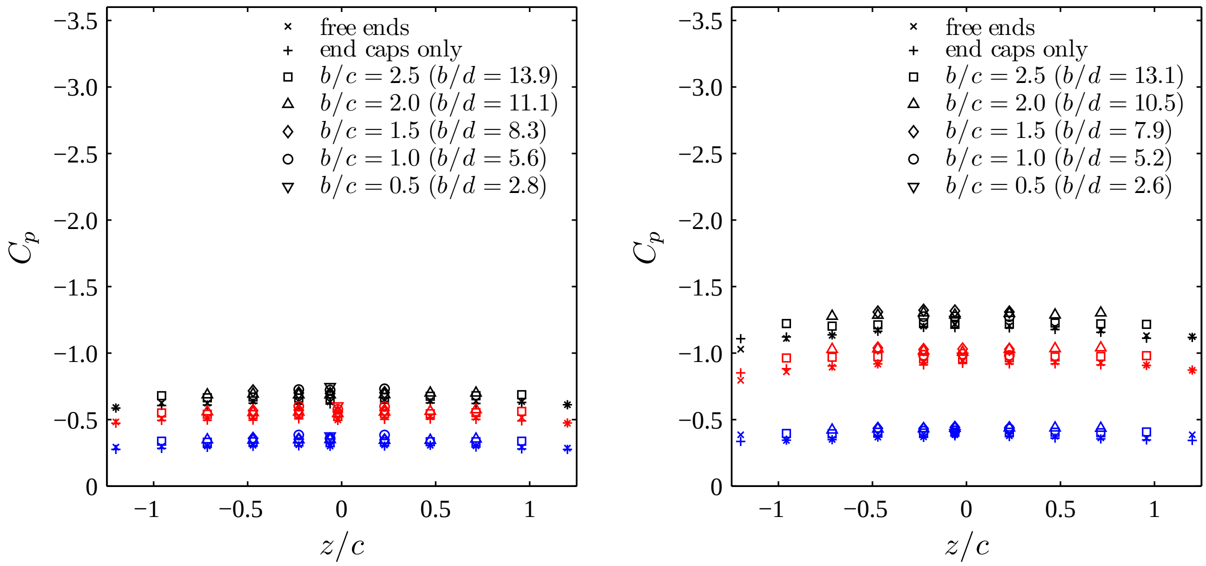

(a) $AOA = 0°$

(b) $AOA = 5°$

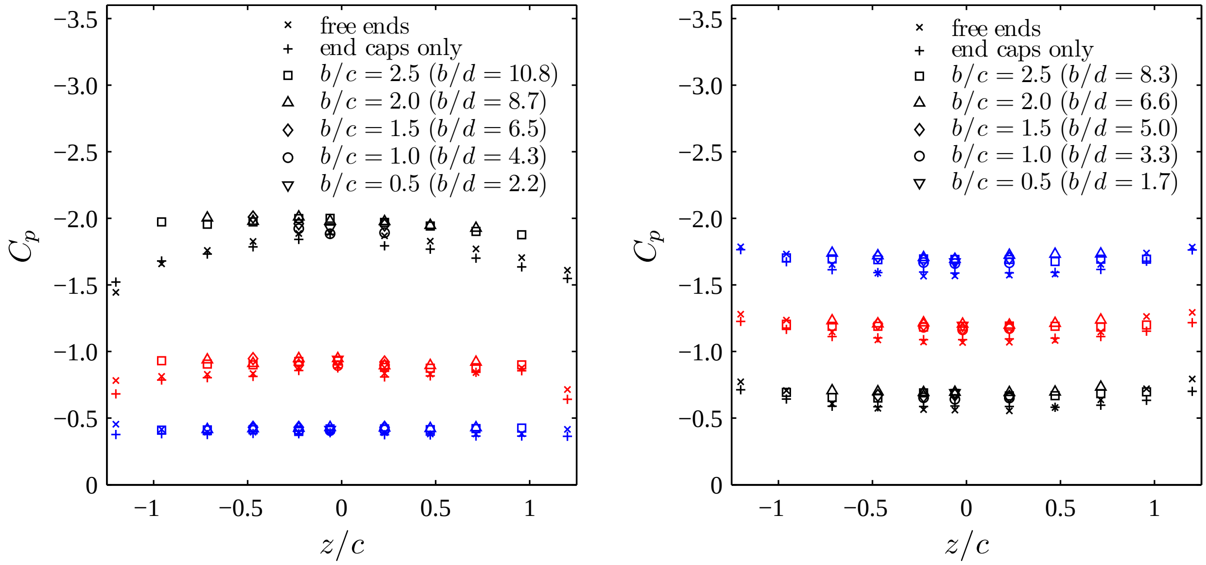

(c) $AOA = 10°$

(d) $AOA = 15°$

Figure 5.3: Upper surface spanwise pressure distributions for the various end plate configurations. Black, red, and blue markers show pressure coefficients at $x/c = 0.15$, 0.30, and 0.60, respectively. In plot (d), for clarity, C_p values for $x/c = 0.30$ and 0.60 are shifted by -0.5 and -1.0, respectively.

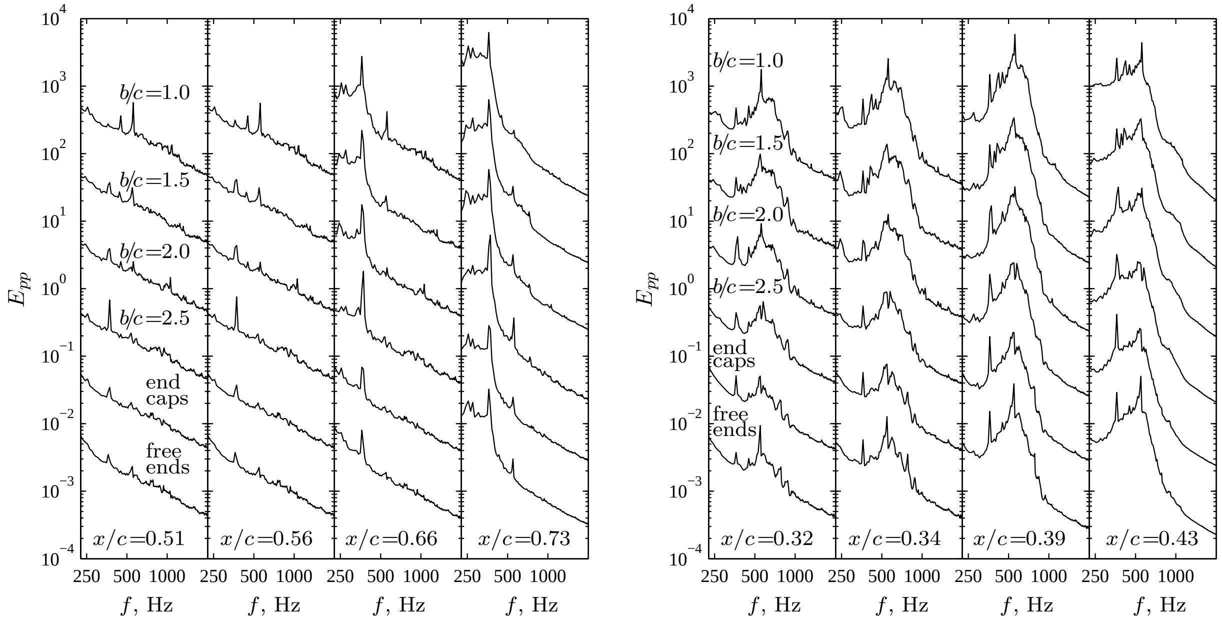

(a) $AOA = 0°$ (b) $AOA = 5°$

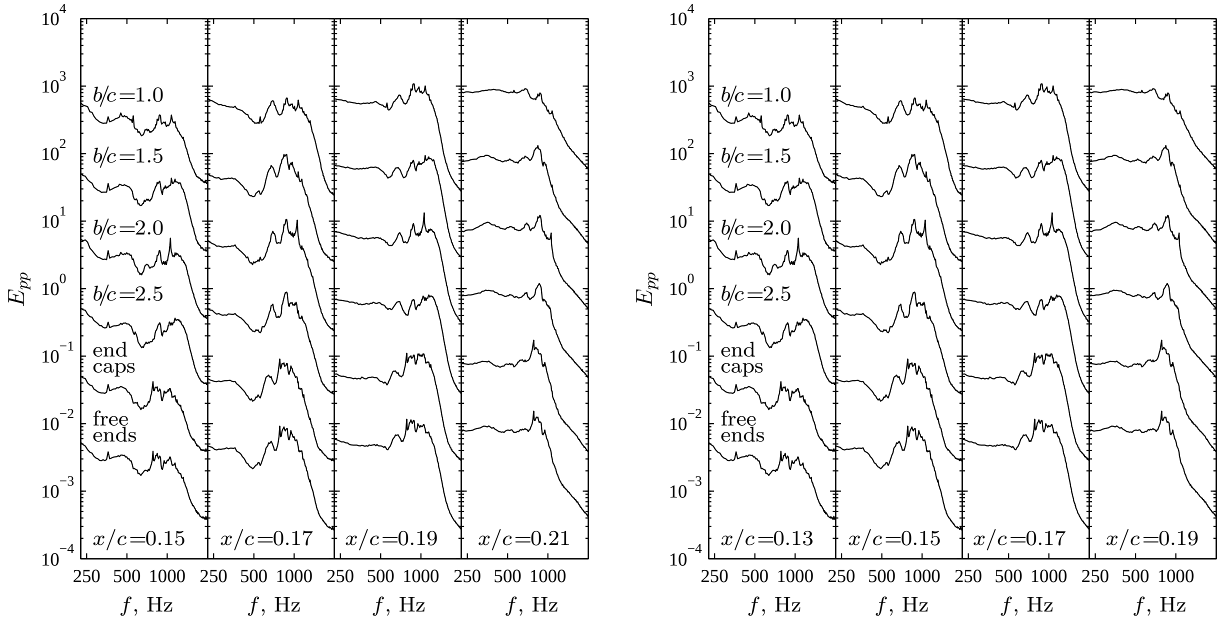

(c) $AOA = 10°$ (d) $AOA = 15°$

Figure 5.4: Energy spectra of surface pressure fluctuations for various end plate configurations. Note that, for clarity, successive spectra at a given x/c location and angle of attack are increased in magnitude by a factor of ten relative to the preceding spectrum.

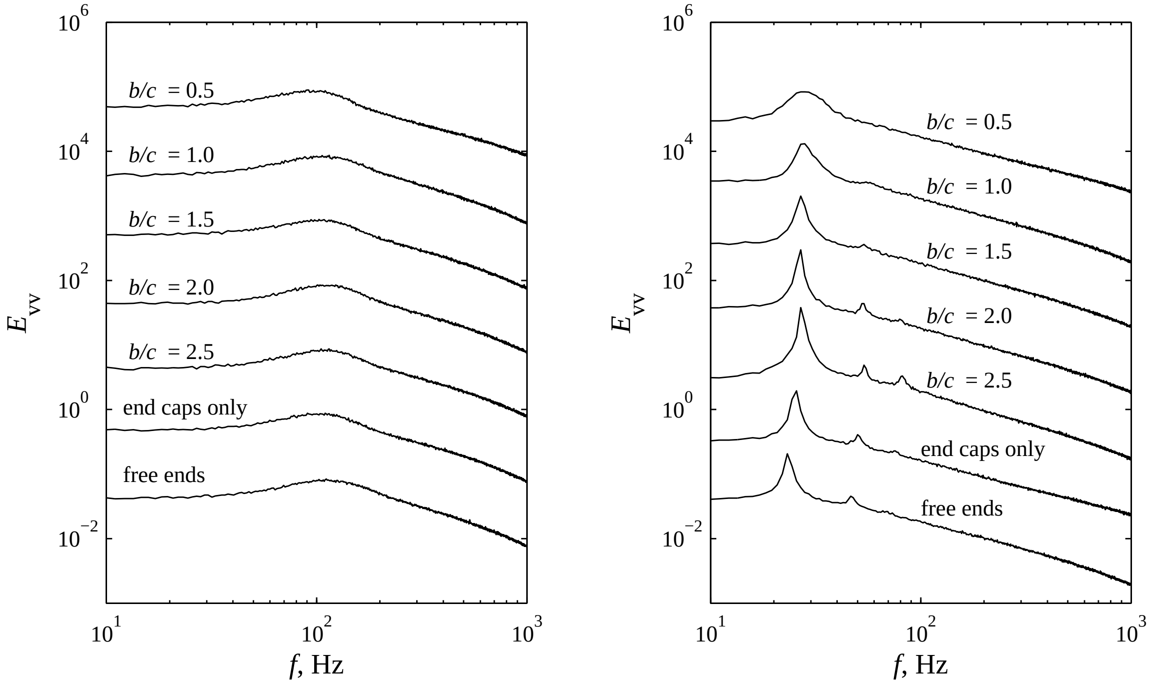

(a) $AOA = 10°$ (b) $AOA = 15°$

Figure 5.5: Energy spectra of vertical velocity at $X/c = 2.7$ with various end plate configurations. Note that, for clarity, successive spectra at a given angle of attack are increased in magnitude by a factor of ten relative to the preceding spectrum.

For $AOA = 15°$, separation occurs without subsequent reattachment, causing large scale wake vortex shedding, which is responsible for the strong peaks in the energy spectra in Fig. 5.5b. For the free ends configuration, this peak occurs at a frequency of approximately 23 Hz. Installing end caps causes this frequency to increase to 25 Hz. Installing end plates at $b/c = 2.5$ further increases the vortex shedding frequency to 27 Hz. This value is retained for all other end plate spacings considered. It should be noted that this shift in the wake vortex shedding frequency from 23 Hz to 27 Hz was also observed in energy spectra of pressure fluctuations measured using microphones embedded in the aft portion of the model. A similar increase in vortex shedding frequency on the center-span plane when end plates are installed can be observed in the results of Mair & Stansby [12] for a circular cylinder. In the present study, the vortex shedding frequency remains constant for all end plate spacings. This is consistent with the conclusion of West & Apelt [83], based on measurements on a circular cylinder, that the vortex shedding frequency does not vary with model aspect ratio at a constant blockage ratio. However, the fact that the measurements with free ends and with only end caps installed correspond to approximately the same solid blockage ratio, but result in different vortex shedding frequencies, indicates that the change in vortex shedding frequency is not only a result of the added blockage. It is speculated that end caps and end plates both reduce the volume of low momentum fluid transfered from the side wall boundary layer into the vortex formation region. Such momentum transfer could reduce the effective speed of flow structures and, consequently, the vortex shedding frequency. For end plate spacings of less than $b/c = 2.0$, the spectral peak broadens, suggesting that the end plates are affecting the coherence of spanwise vortical structures in the near wake.

For $AOA = 10^\circ$, laminar boundary layer separation is followed by turbulent boundary layer reattachment downstream, leading to a narrow wake with smaller and less coherent spanwise vortical structures being shed from the airfoil. As a result, the energy spectra in Fig. 5.5a have much broader peaks than those in Fig. 5.5b. For $AOA = 10^\circ$, the end plate configuration had no measurable effect on the central frequency of the spectral peak.

Fox & Wolf [13] concluded that, for a circular cylinder model without end plates installed, the ratio of spanwise width to diameter of the model must be greater than thirty to produce mean pressure distributions on the center-span plane representative of a wide-span model. Since no experimental data are available for a NACA 0018 airfoil model at $Re_c = 10^5$ and an aspect ratio of thirty or greater, it is not possible to verify that the results obtained with end plates installed are representative of flow over a wide-span model. However, the mean spanwise uniformity produced with end plates installed, and which is expected for flow over a wide-span model, suggests that end plates should be installed for measurements over airfoil models at low Reynolds numbers. Furthermore, the change in vortex shedding frequency seen in Fig. 5.5b when end plates are installed implies that end plates are required when performing measurements in the near wake of an airfoil at a low Reynolds number. The results in Fig. 5.5b also suggest that the end plate spacing should be greater than $b/d \approx 6.6$ ($b/c \approx 2.0$ for $AOA = 15^\circ$ on this model), to ensure that the end plates do not interfere with wake vortex shedding.

Figure 5.6 presents wall pressure distributions for $AOA = 10^\circ$ with the various end plate configurations. The free ends and end caps only configurations have blockage ratios of 5.2%, whereas the other configurations have blockage ratios, including the projected end plate area, of 6.3%. It can be seen that the end plate configuration affects the wall pressure distribution, suggesting that added blockage due to end plates is contributing to some of the measured changes in flow development discussed above.

The results presented in this section quantify the effects of end plates on flow development over an airfoil model at a low Reynolds number. End plates significantly improved mean spanwise flow uniformity compared to configurations without end plates

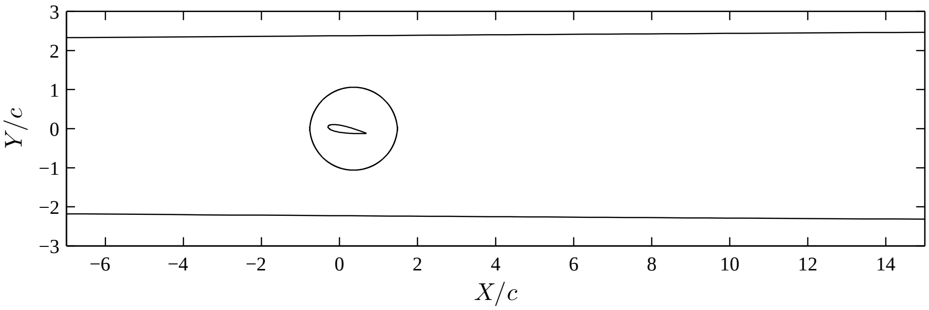

(a) model, end plates, and ASW contours

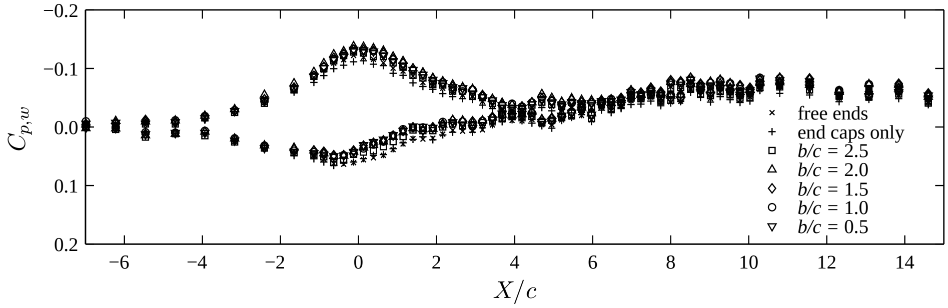

(b) wall pressure distributions

Figure 5.6: Variation of ASW wall pressure distribution with end plate configuration for $AOA = 10°$.

installed. Furthermore, it was shown that the end plate configuration can affect wake development and lift coefficients. The model aspect ratio could not be increased sufficiently to verify that, as was found for circular cylinder models [13], the sectional aerodynamic forces measured on a wide-span model would better match those measured with end plates installed at a large enough spacing. However, the results presented here are consistent with this finding. Based on the results of this section, it is concluded that end plates should be used in low Reynolds number airfoil experiments to reduce the mean spanwise non-uniformity of the flow. Consistent with the guidelines for circular cylinder models, it is recommended that the end plates have a spacing of $b/d \gtrsim 7$ and are positioned outside of the test section wall boundary layers. In the present investigation, an end plate spacing of $b/c = 2.0$ was selected to satisfy these conditions, and was shown to provide the lowest variation in lift coefficients and wake velocity energy spectra with end plate spacing.

5.2 Blockage

The effects of wind tunnel blockage were investigated by comparing measurements of flow development over the model before and after streamlining the wind tunnel walls. For the angles of attack and end plate configurations investigated, the solid blockage ratios, including end plate blockage, ranged from 4 to 8%. The blockage ratios for each configuration are listed in Table 5.1. Except where otherwise indicated, the measurements in this section were obtained with the end plates installed at $b/c = 2.0$. Appendix E provides similar data for measurements performed with only end caps installed.

Figure 5.7 presents ASW and SLW contours for the angles of attack investigated. In the GSW configuration, boundary layer blockage, solid blockage, and wake blockage influence flow development. Moving from GSW to ASW contours removes boundary layer blockage. The ASW contours show the effective change in test section area, at each streamwise location, required to maintain a constant free-stream speed along the streamwise axis in an empty test section. Moving from the ASW to SLW contours removes solid and wake blockage. The difference between the SLW and ASW contours are streamline displacements expected in an unconfined flow field at the distance of the walls from the model. For conditions at which boundary layer reattachment occurs, i.e., for $AOA = 0$, 5, and 10°, the upper SLW contour displacements increase with increasing angle of attack. This trend is expected because the blockage ratio increases with increasing angle of attack. For $AOA = 5$ and 10°, both the upper and lower SLW contours have positive displacements from the ASW contours, with the distance between the upper and lower walls at each location marginally greater than the distance between upper and lower ASW contours. This suggests that solid blockage is displacing streamlines near the upper and lower walls, without causing significant acceleration along these streamlines. Significantly different behavior is observed for $AOA = 15°$, at which the airfoil is stalled. As compared to the other angles of attack, the upper and lower walls are farther apart at the streamwise location of the model ($X/c = 0$) and the magnitudes of the SLW contour displacements from the ASW configuration are

Table 5.1: Blockage ratio, B, for various angles of attack with and without end plates installed.

AOA	without end plates	with end plates
0°	4.0%	5.1%
5°	4.3%	5.4%
10°	5.2%	6.3%
15°	6.8%	7.9%

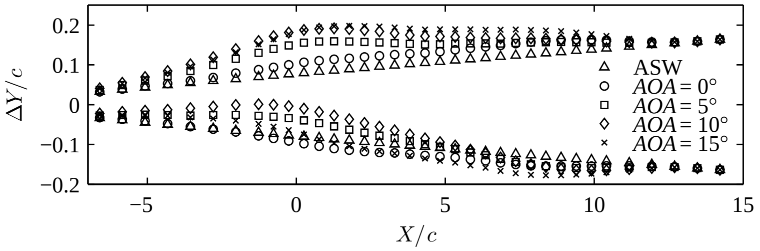

Figure 5.7: ASW contour and SLW contours for each angle of attack tested, with end plates installed at $b/c = 2.0$.

greater well downstream of the model ($X/c \gtrsim 5$). These differences in the streamline pattern near the walls for $AOA = 15°$ compared to the other angles reflect the significant changes in the flow field when the separation bubble bursts. Furthermore, the greater distances between the upper and lower SLW contours for $AOA = 15°$ indicate that the higher wake blockage produced by the stalled airfoil model is causing significantly higher acceleration of flow near the walls than for conditions at which a separation bubble forms over the airfoil.

Wall pressure distribution measurements were acquired in order to perform wall streamlining calculations. These data also provide insight into the overall flow field development and how blockage influences this development. Wall pressure distributions for the GSW, ASW, and SLW configurations are presented in Fig. 5.8. Since these pressure distributions are along streamlines on either side of the model, the area between the upper and lower wall pressure distributions represents the sectional lift force on the model. Only the upper wall pressure distribution is presented for $AOA = 0°$, because the upper and lower distributions nearly coincide for this angle. For $AOA = 5$, 10, and 15°, the asymmetry introduced into the flow by the airfoil results in higher speed flow near the upper wall than near the lower wall for $-3 \lesssim X/c \lesssim 5$. Upstream and downstream of this region, the differences between the upper and lower wall pressure distribution are small, but the GSW wall pressure distribution has a significant negative slope which quantifies free-stream acceleration due to blockage. This slope is reduced to almost zero in the ASW configuration, indicating that boundary layer blockage was primarily responsible for this acceleration. For angles of attack at which a separation bubble forms ($AOA = 0$, 5, and 10°), wall streamlining provides similar pressure distributions to those obtained in the ASW configuration. However, for each angle of attack the maximum suction pressure near $X/c = 0$ is lower in the SLW configuration. This is an indication of solid blockage mitigation

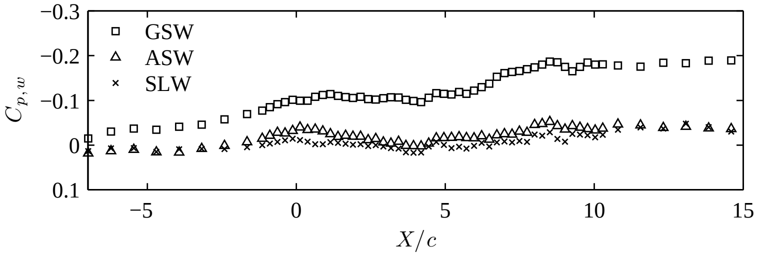

(a) $AOA = 0°$ $(B = 5.1\%)$

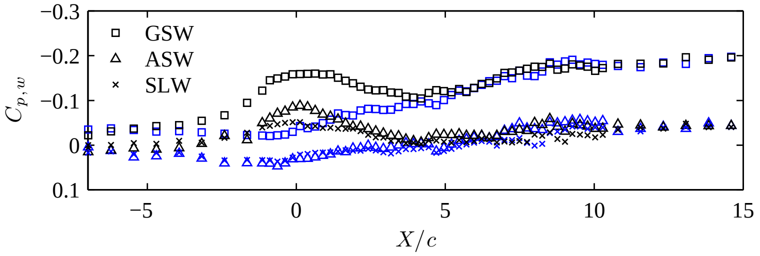

(b) $AOA = 5°$ $(B = 5.4\%)$

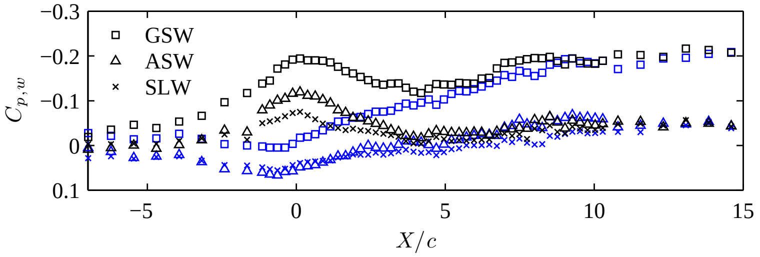

(c) $AOA = 10°$ $(B = 6.3\%)$

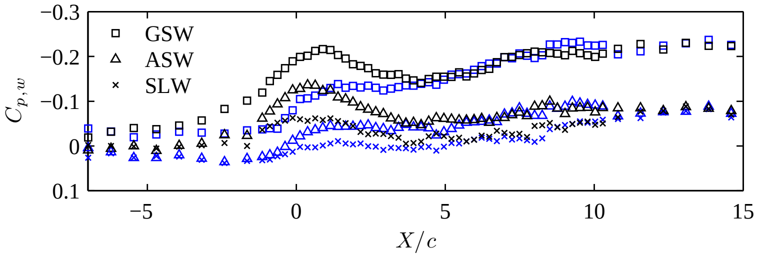

(d) $AOA = 15°$ $(B = 7.9\%)$

Figure 5.8: Upper (black) and lower (blue) wall pressure distributions in the GSW, ASW, and SLW configurations, with end plates installed at $b/c = 2.0$. For clarity, only the upper wall pressure distributions are shown in (a).

through wall streamlining; in the ASW configuration, a higher effective free-stream speed is measured than in the SLW configuration as a result of reduced cross sectional area at the streamwise location of the model. Downstream of the model, the ASW and SLW wall pressures have similar values for $AOA = 0$, 5, and 10°, suggesting that when the flow is attached near the trailing edge of the airfoil, the narrow wake that forms produces a low level of wake blockage. For $AOA = 15°$, at which the flow is separated at the trailing edge of the model and a wide wake is formed, the magnitudes of ASW configuration wall pressures are lower than the corresponding SLW configuration wall pressures. This indicates that wake blockage is causing a more significant acceleration of the free-stream flow over the model and in the wake when the airfoil is stalled. Note that, in each of the wall pressure distributions, differences between the upper and lower wall pressure coefficients on the order of 0.05 are observed near $X/c = 8$, corresponding to the location of the spanwise axis of the hot-wire traverse during these experiments.

The effect of blockage on mean flow development over the model is summarized through model surface pressure distributions in Fig. 5.9. For angles of attack at which a separation bubble forms, the length and position of the pressure plateau downstream of the suction peak does not change with wall configuration. This suggests that blockage has not affected the location or size of the separation bubble, to more than the spatial resolution of the static pressure taps. However, blockage causes a shift in the upper surface pressure distribution on the order of 10% of the dynamic pressure. This effect is more pronounced at higher angles of attack, due to the higher blockage ratios at higher angles. The greatest difference between the surface pressure distributions measured in the different wall configurations is observed for $AOA = 10°$ at $x/c \approx 0.24$, which is between the transition and reattachment points. This variation suggests that the transition and reattachment locations are affected by wall blockage, however, the changes are less than the spatial resolution of the static pressure taps.

The effect of blockage on measured lift coefficients is presented in Fig. 5.10a. Considering the data obtained with end plates installed at $b/c = 2.0$, it can be seen that the measured lift coefficients decrease as the walls are moved from GSW to ASW contours, and from ASW to SLW contours. The level of deviation between the measured GSW and SLW lift coefficient data increases with angle of attack, as expected from the higher solid blockage ratios at higher angles. Differences in the measured lift coefficients between the GSW and SLW configurations are as high as 9% of the maximum lift coefficient.

To separate the effects of end plates from the effects of blockage, wall streamlining was repeated with only end caps installed on the model. The resulting lift coefficients are plotted in Fig. 5.10a, with the corresponding surface pressure distributions, wall pressure distributions, and wall contours provided in Appendix E. The results show that, for conditions at which a separation bubble forms over the airfoil surface, i.e, for $AOA = 0$, 5,

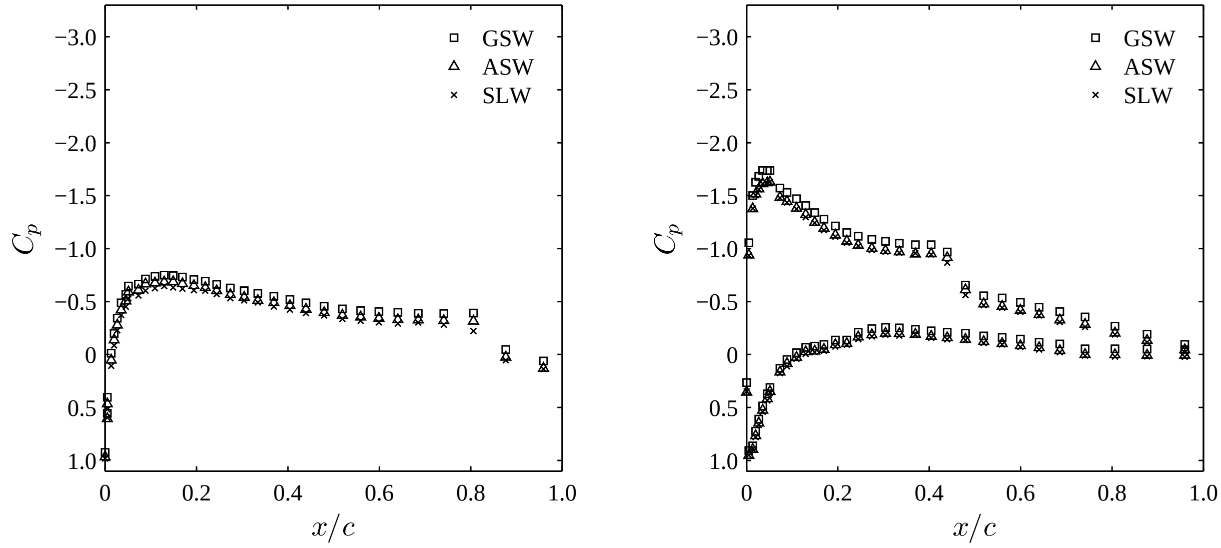

(a) $AOA = 0°$ (b) $AOA = 5°$

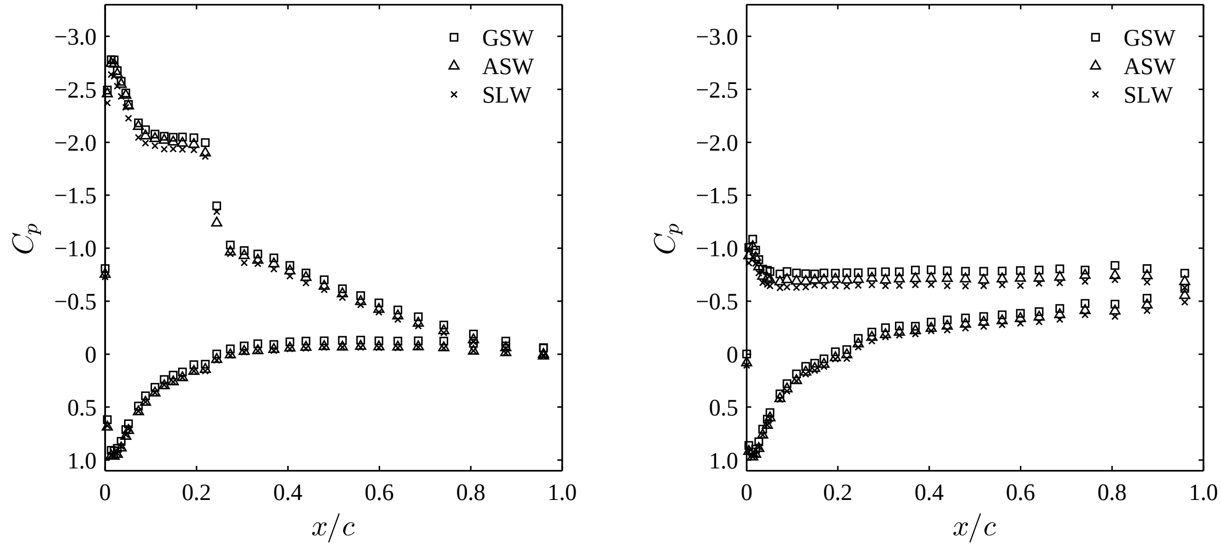

(c) $AOA = 10°$ (d) $AOA = 15°$

Figure 5.9: Streamwise distributions of surface pressure for various wall configurations with end plates installed at $b/c = 2.0$.

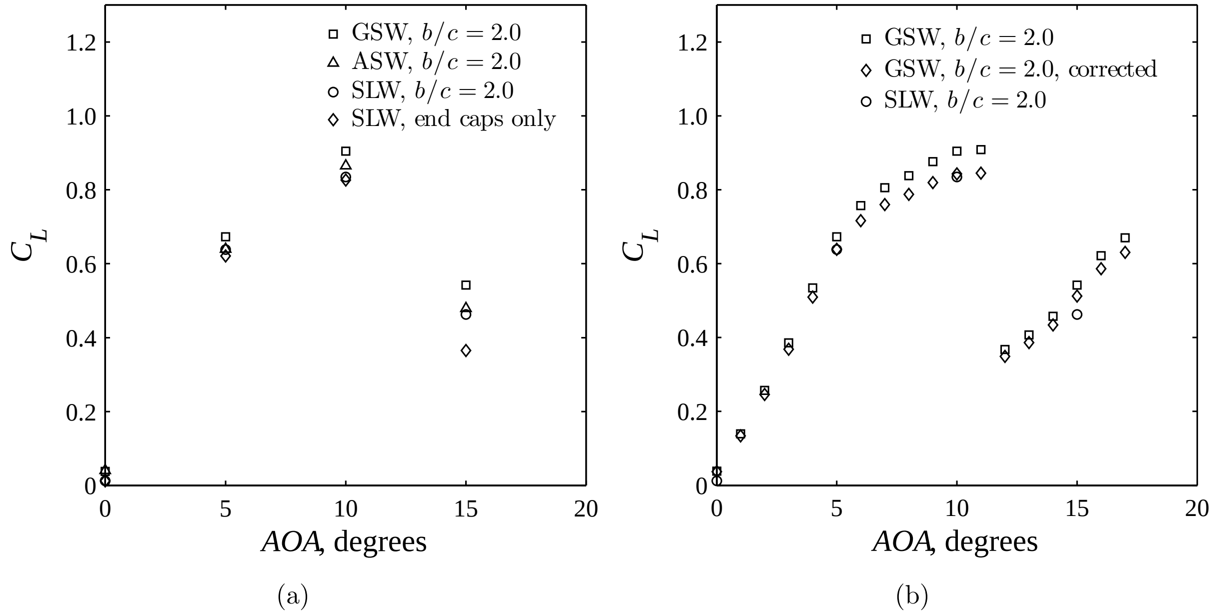

(a)

(b)

Figure 5.10: Variation in lift coefficient computed from the measured pressure distributions for the various end plate configurations: (a) comparison of GSW, ASW, and SLW configuration data and (b) comparison of corrected GSW data to SLW data.

and 10°, the measured lift coefficients in the SLW configuration with end plates installed at $b/c = 2.0$ and with only end caps installed agree to within the measurement repeatability, indicated by the marker size. This suggests that for angles of attack at which a separation bubble forms, the increased solid blockage created by using end plates with walls in the GSW or ASW configurations can bias lift coefficient measurements obtained from surface pressure distributions on the center-span plane. Significantly different behavior is observed for $AOA = 15°$. For this angle, the SLW lift coefficient with end plates installed at $b/c = 2.0$ and that with only end caps installed differ by approximately 11% of the maximum lift coefficient. This is a result of the lower suction pressure on the center-span plane without end plates installed, caused by the mean spanwise non-uniformity in surface pressures over a significant portion of the chord at $AOA = 15°$ (Fig. 5.3d). This finding suggests that, at post-stall angles of attack, the spanwise non-uniformity of the flow that exists without end plates installed causes greater error in the measured lift coefficients than that created by the added solid blockage when end plates are installed.

Aerodynamic forces measured in fixed-wall facilities are often adjusted to compensate for blockage effects [15]. It is, therefore, of interest to compare corrected lift coefficient data to measurements in the SLW configuration. Figure 5.10b compares measured lift data in the GSW configuration, the adjusted data obtained by applying the common blockage correction method described by Barlow et al. [15] for two-dimensional bodies spanning the test section, and measurements in the SLW configuration. The lift coefficient increases at an approximately constant rate with angle of attack for $0^\circ < AOA < 5^\circ$. The corresponding surface pressure distributions indicate that the separation bubble moves upstream with increasing angle of attack. For $5^\circ < AOA < 11^\circ$, the separation bubble forms sufficiently close to the leading edge to cause a significant reduction in the maximum suction pressure on the upper surface of the airfoil compared to flow development without separation. This results in the lower lift slope for $5^\circ < AOA < 11^\circ$ compared to $0^\circ < AOA < 5^\circ$. A significant reduction in lift occurs between $AOA = 11$ and 12°, indicating that the airfoil model has stalled. Applying the blockage correction formulas reduces the lift coefficients, with the most significant changes observed near the stall angle. The corrected lift coefficient data for $AOA = 5$ and 10° coincide with the SLW configuration measurements. This demonstrates that the simple blockage correction method can accurately correct lift coefficient data when a separation bubble forms on the airfoil surface. A difference between the corrected datum and the SLW configuration measurement is observed at $AOA = 0^\circ$, and is attributed to the sensitivity of the flow over airfoils at low Reynolds numbers near the zero-lift angle [10]. For $AOA = 15^\circ$, the correction method does not significantly reduce the difference between the GSW and SLW configuration measurements. This is a weakness of simple blockage correction methods, which do not adequately correct for bluff body wake blockage at blockage ratios above approximately 6% as a result of qualitative changes in model surface pressure distributions at higher blockage ratios [83, 134, 135].

The process of laminar-to-turbulent transition in the separated shear layer over the airfoil is of interest because it largely determines the overall airfoil performance. Energy spectra of model surface pressure fluctuations were used to assess the effect of blockage on the transition process, and are presented in Fig. 5.11. The results show that the central frequency and width of the spectral peaks, which are attributed to growing disturbances in the separated shear layer, do not change significantly as a result of wall streamlining. However, some variations are observed in the small peaks within the central band of amplified frequencies, for the different wall configurations. These changes indicate variations in the energy content at a particular location in the transitioning flow. This may be responsible for the minor dependence of the transition location on the wall configuration, observed in the mean surface pressure distributions (Fig. 5.9).

Changes in the wake vortex shedding frequency with wall configuration are presented in Table 5.2 for $AOA = 15^\circ$. Removing boundary layer blockage by moving from GSW contours to ASW contours reduces the Strouhal number for wake vortex shedding by about 0.002. This change is within the estimated uncertainty of ±0.002 in determining

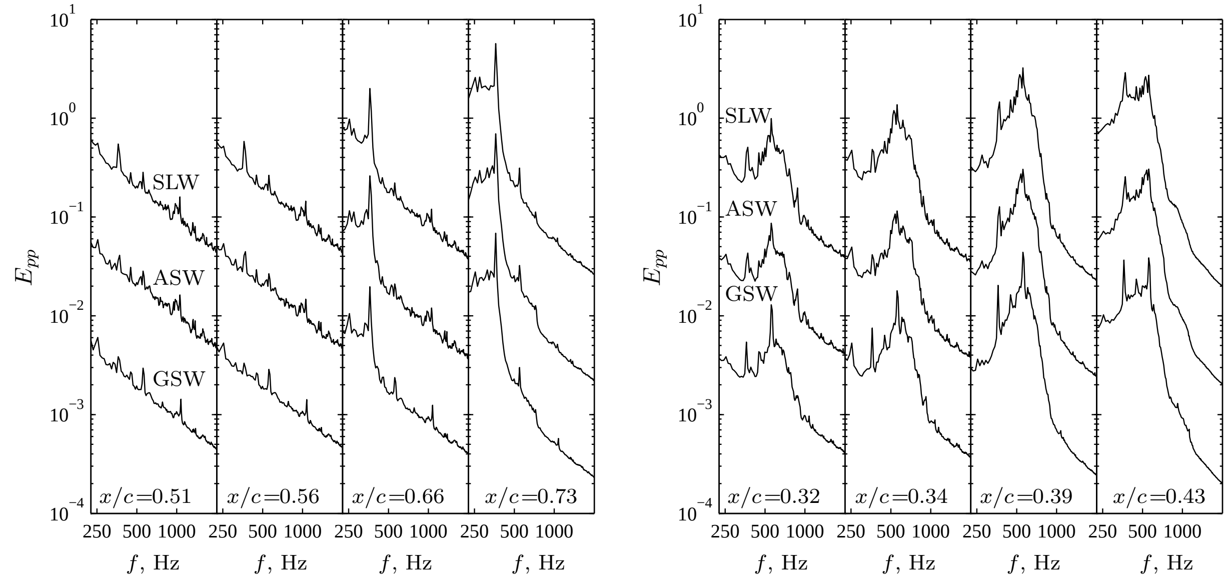

(a) $AOA = 0°$ (b) $AOA = 5°$

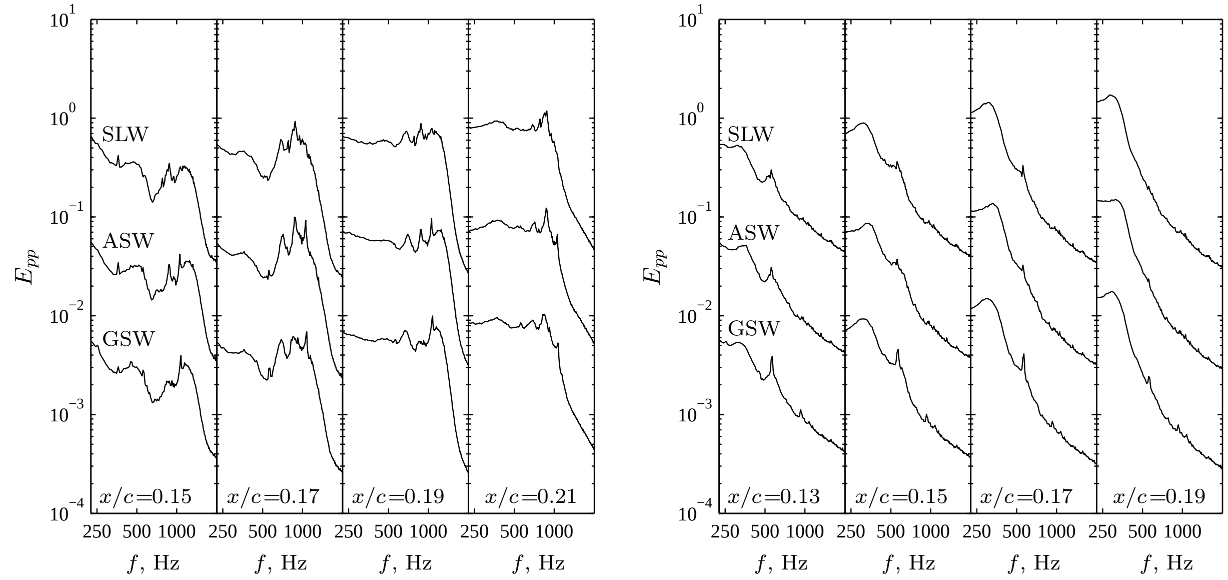

(c) $AOA = 10°$ (d) $AOA = 15°$

Figure 5.11: Energy spectra of surface pressure fluctuations for various wall configurations. Note that, for clarity, successive spectra at a given x/c location and angle of attack are increased in magnitude by a factor of ten relative to the preceding spectrum.

Table 5.2: Strouhal number variation with wall configuration for $AOA = 15°$ and $b/c = 2.0$.

configuration	St
GSW	0.208
ASW	0.206
SLW	0.201

the Strouhal number. Streamlining the walls changes the Strouhal number by about 0.005 from the ASW configuration. This is attributed to the reduced free-stream velocity in the wake when blockage is removed, resulting in a lower speed of vortex cores, and thus, a lower vortex passing frequency at the measurement location. Based on Fig. 5.8, it was concluded that the acceleration of the free stream downstream of the model for $AOA = 15°$ was primarily due to wake blockage, because differences between the ASW and SLW wall pressure distributions in the far wake were significant only for the post-stall angle of attack. This suggests that wake blockage is the most significant factor contributing to the observed 3.5% difference in measured wake vortex shedding frequency between the GSW and SLW configurations. The differences in measured wake vortex shedding frequency and wall pressures between the ASW and SLW configurations for $AOA = 15°$ indicate that solid and wake blockage should be taken into consideration for measurements in the wake of a stalled airfoil model under low Reynolds number conditions. It should be noted that changes in the wake vortex shedding frequency could not be resolved for conditions at which a separation bubble formed on the airfoil surface.

Based on this wall streamlining investigation, it was found that in low Reynolds number airfoil experiments with models of moderate blockage ratios ($4\% \lesssim B \lesssim 8\%$), test section blockage can cause measurable changes in sectional lift coefficients and wake vortex shedding frequencies. Blockage was found to cause an increase in the measured pressure distributions on the upper surface of the model, resulting in errors as high as 0.08 in the measured lift coefficients. Error increased with solid blockage ratio as the angle of attack was increased. It was shown that for conditions at which a separation bubble forms on the model surface, a simple correction method can be employed to accurately correct lift coefficient data. Test section blockage was found to cause a 3.5% increase in the the wake vortex shedding frequency behind the model at a post-stall angle of attack, suggesting that wall streamlining may be important in detailed studies on wake development under stalled conditions.

5.3 Intrusive Techniques

Positioning a hot-wire probe near the surface of a model can distort the flow field [21,103]. The extent to which the flow upstream of the probe is affected needs to be quantified in assessing the accuracy of near surface velocity measurements. This section considers the effect of a normal hot-wire probe, and the traverse used to position it, on flow development over an airfoil model at a low Reynolds number. The effect of opening and closing the wind tunnel door during operation is also discussed, since such intrusion is sometimes required to apply smoke generating fluid to a wire during smoke-wire flow visualization experiments.

5.3.1 Influence of the Hot-Wire Probe and Traverse

With end plates installed at $b/c = 2.0$, and the wind tunnel set in the appropriate SLW configuration, mean surface pressure distributions were measured with the hot-wire traverse at various positions in the spanwise plane of the static pressure taps. Measurements of surface pressure fluctuations were performed with the hot-wire probe at the same X-Y coordinates, in the spanwise plane of the embedded microphone array. As a baseline for comparison, measurements were first performed with the traverse positioned far downstream of the model, with the hot-wire probe tip at $X_p/c = 7$. The effect of the traverse was then assessed by repeating these measurements with the probe at $X_p/c = 0$ and $Y_p/c = 1$. Finally, the effect of the probe was investigated by repeating the measurements with a Dantec 55P15 hot-wire probe positioned at less than $0.005c$ from the surface, i.e., as close to the surface as possible without risking damage to the probe. These measurements were performed for three streamwise locations at each angle of attack to help identify regions where the hot-wire probe has the most significant effect on flow development. The resulting surface pressure distributions are presented in Fig. 5.12.

Figure 5.12 shows that moving the traverse upstream from $X_p/c = 7$ to $X_p/c = 0$ has a minor effect on the mean surface pressure distributions. The most significant changes occur for $AOA = 5$ and $10°$, for which shifts in the surface pressure of less than 5% of the dynamic pressure are observed in the pressure plateaus created by the separation bubbles.

The proximity of the probe to the surface of the airfoil has a measurable effect on upstream flow development only when the probe is positioned near the separation point. This is best illustrated by the × symbols in Fig. 5.12c. For this data set, the presence of the probe has eliminated the pressure plateau, indicating that the probe has caused attached boundary layer transition and prevented separation. Less significant changes occur in the pressure distributions upstream of the probe for $AOA = 0$ and $5°$, indicating that the flow is most sensitive to the proximity of the hot-wire probe for angles of attack just below the stall angle. Thus, near surface velocity profile measurements acquired with a hot-wire

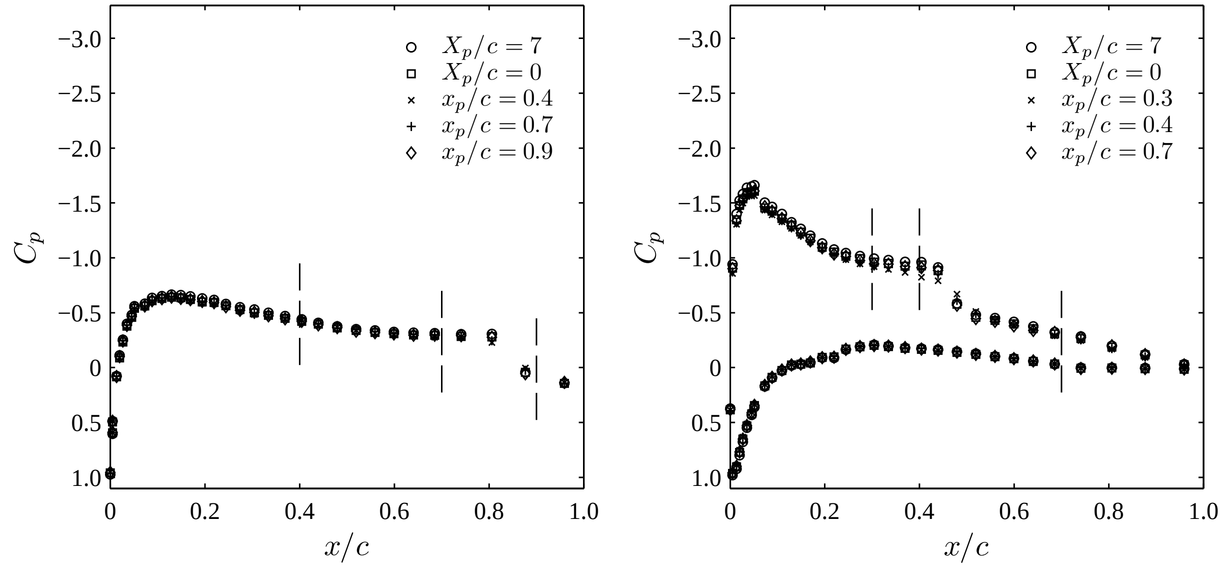

(a) $AOA = 0°$

(b) $AOA = 5°$

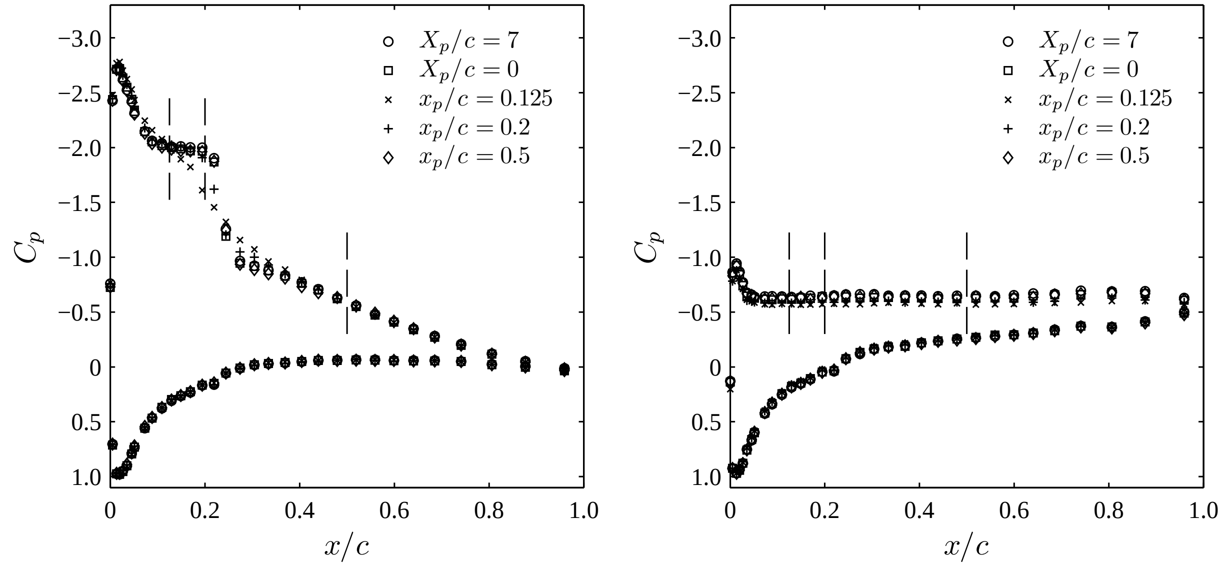

(c) $AOA = 10°$

(d) $AOA = 15°$

Figure 5.12: Model surface pressure distributions with the hot-wire probe at various positions. Legend entries identify the location of the probe tip, with X_p/c coordinates used when the probe is at $Y_p/c = 1$ and x_p/c coordinates used when the probe is within $0.005c$ of the upper surface of the model. Dashed lines identify x_p/c locations.

probe close to the measured separation point need to be carefully scrutinized for such flow conditions. For conditions at which reattachment occurs ($AOA = 0$, 5, and 10°) the pressure distribution sufficiently far downstream of the hot-wire probe appears unaffected by the proximity of the probe to the surface. However, the separated flow just downstream of the probe is affected, as exemplified by the $\times$ symbols in Fig. 5.12b. For the case of separated shear layer transition without subsequent reattachment, the $\times$ and $+$ symbols in Fig. 5.12d show that positioning the probe near the separation point increases the surface pressure by approximately 10% of the dynamic pressure in the nearly constant pressure region between $x/c \approx 0.05$ and $x/c \approx 0.9$. For all angles of attack considered, positioning the probe far downstream in the turbulent flow region ($\diamond$ symbols) appears to have no more effect on the flow development than moving the traverse from $X_p/c = 7$ to $X_p/c = 0$.

Spanwise surface pressure distributions were also measured for each angle of attack and probe position indicated in Fig. 5.12. No changes in spanwise uniformity due to probe position were observed.

Energy spectra from measurements with embedded microphones are presented in Fig. 5.13. For these measurements, the hot-wire probe was positioned in the spanwise plane of the embedded microphones. For each angle of attack, spectra at four streamwise locations are presented. At each streamwise location, a sequence of five spectra are plotted, which correspond to measurements with the hot-wire probe at each position considered. Moving the traverse towards the model from far downstream, with the probe far above the surface, i.e., moving from $X_p/c = 7$ to $X_p/c = 0$, does not have a significant effect on the energy spectra. However, differences are observed when the probe is positioned near the airfoil surface. For each angle of attack, there was one x_p/c probe position for which all of the x/c measurement locations were downstream of the hot-wire probe, i.e., $x_p/c = 0.4$ for $AOA = 0°$, $x_p/c = 0.3$ for $AOA = 5°$, $x_p/c = 0.125$ for $AOA = 10°$, and $x_p/c = 0.125$ for $AOA = 15°$. These measurements are severely affected by the presence of the hot-wire probe. However, measurements acquired just upstream of the hot-wire probe, e.g., those for $x_p/c = 0.4$ at $AOA = 5°$ and $x_p/c = 0.2$ at $AOA = 10°$, show only minor changes due to the presence of the hot-wire probe as compared to the baseline case with the probe at $X_p/c = 7$. Positioning the hot-wire probe in the turbulent boundary layer, i.e., positioning the probe at the highest value of x_p/c in Fig. 5.13 for $AOA = 0$, 5, and 10°, has no influence on upstream measurements. For the case of separation without reattachment ($AOA = 15°$), transition is less affected by the probe position than for cases at which turbulent boundary layer reattachment occurs.

The intrusion of the hot-wire probe had a measurable effect on flow development only when positioned near the separation point with the model near the stall angle. For most conditions, the mean surface pressure distributions and energy spectra of surface pressure fluctuations measured in the transitioning separated shear layer upstream of the hot-wire

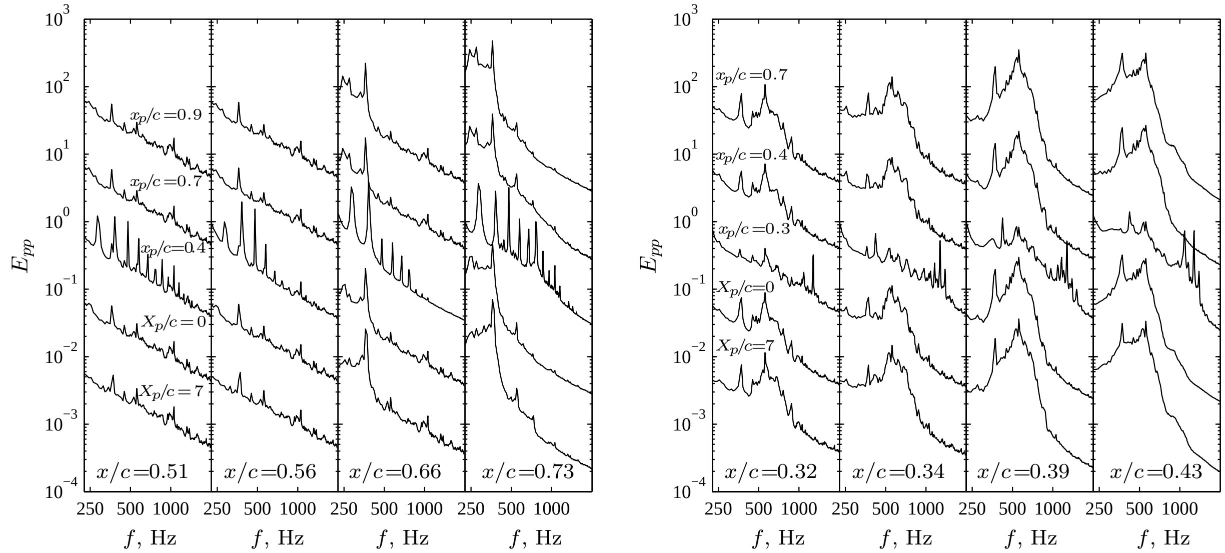

(a) $AOA = 0°$ (b) $AOA = 5°$

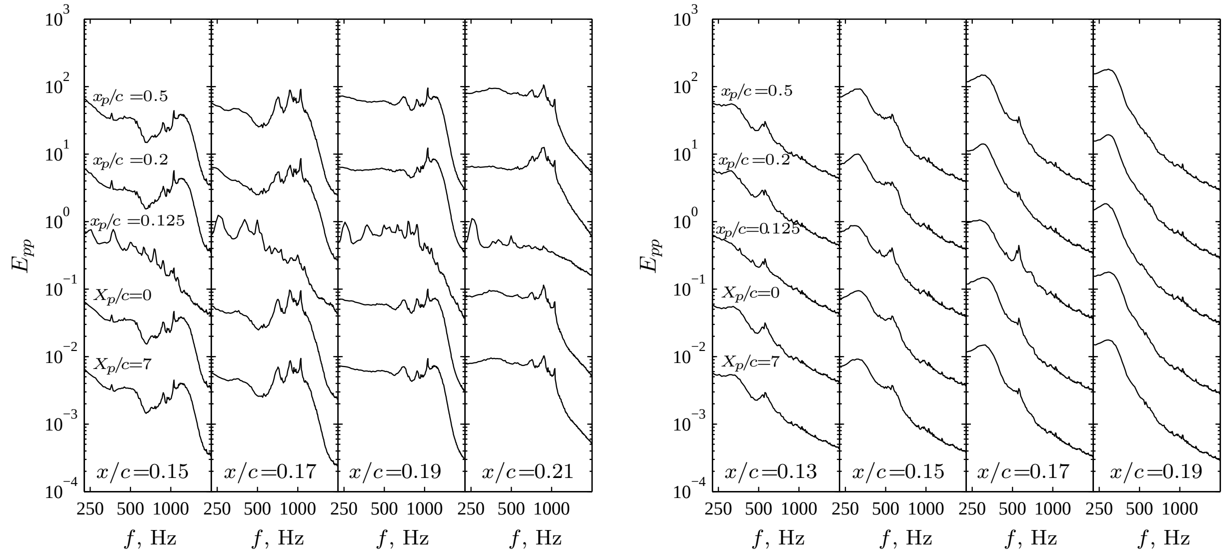

(c) $AOA = 10°$ (d) $AOA = 15°$

Figure 5.13: Energy spectra of surface pressure fluctuations with end plates installed at $b/c = 2.0$ and the hot-wire probe at various positions. Note that, for clarity, successive spectra at a given x/c location and angle of attack are increased in magnitude by a factor of ten relative to the preceding spectrum.

probe were unaffected by the presence of the probe. However, it was shown that positioning a hot-wire probe near the measured separation point for an angle of attack near the stall angle can cause attached boundary layer transition without separation, for conditions at which a transitional separation bubble would have otherwise formed.

5.3.2 Effect of Opening the Wind Tunnel Door

Smoke-wire flow visualization experiments, discussed in Chapter 6, required the wind tunnel door to be opened and closed while the tunnel was in operation. The effect of this intrusion on flow development after closing the door was assessed to ensure that the flow visualization images accurately reflect the measured flow development. Mean and fluctuating surface pressure measurements were used to evaluate the effect of opening the door. It was found that, within thirty seconds of closing the door, surface pressure spectra and the maximum suction pressure returned to the same conditions that existed prior to opening the door. Supporting results and discussion for this finding are presented in Appendix G.

Chapter 6

Boundary Layer Development

Shear layer development over the airfoil surface is examined in this chapter. The conclusions from Chapter 5 have been applied in the experiments of this chapter to improve the reliability of the results. Specifically, end caps were installed, end plates were positioned with a spacing of $b/c = 2.0$, the test section walls were set to the applicable SLW configuration for the angle of attack, and hot-wire measurements at locations where the probe affected flow development were identified.

6.1 Flow Visualization

Smoke-wire flow visualization was performed to provide qualitative insight into the overall flow field development. Flow visualization experiments incorporated a thirty second time delay between closing the wind tunnel door and acquiring images, as recommended in Section 5.3.2. End plates were removed for flow visualization experiments to improve smoke visibility.

Figures 6.1-6.4 present smoke-wire flow visualization images of the airfoil and near wake for various angles of attack. The end of the airfoil nearest to the camera is outlined in white, while streaklines occupy a plane near the center-span of the model. These images illustrate two distinctly different flow regimes, common to airfoil operation at low Reynolds numbers [1–3]. For AOA = 0, 5, and 10° (Figs. 6.1-6.3), the flow is attached near the trailing edge, resulting in streaklines near the airfoil surface that closely follow the surface curvature. A narrow wake forms behind the model with a centerline nearly parallel to the airfoil chord. Hot-wire measurements presented in Section 6.2 show that, for these angles of attack, a separation bubble forms on the airfoil surface. For $AOA = 15°$ (Fig. 6.4), boundary layer separation occurs near the leading edge without

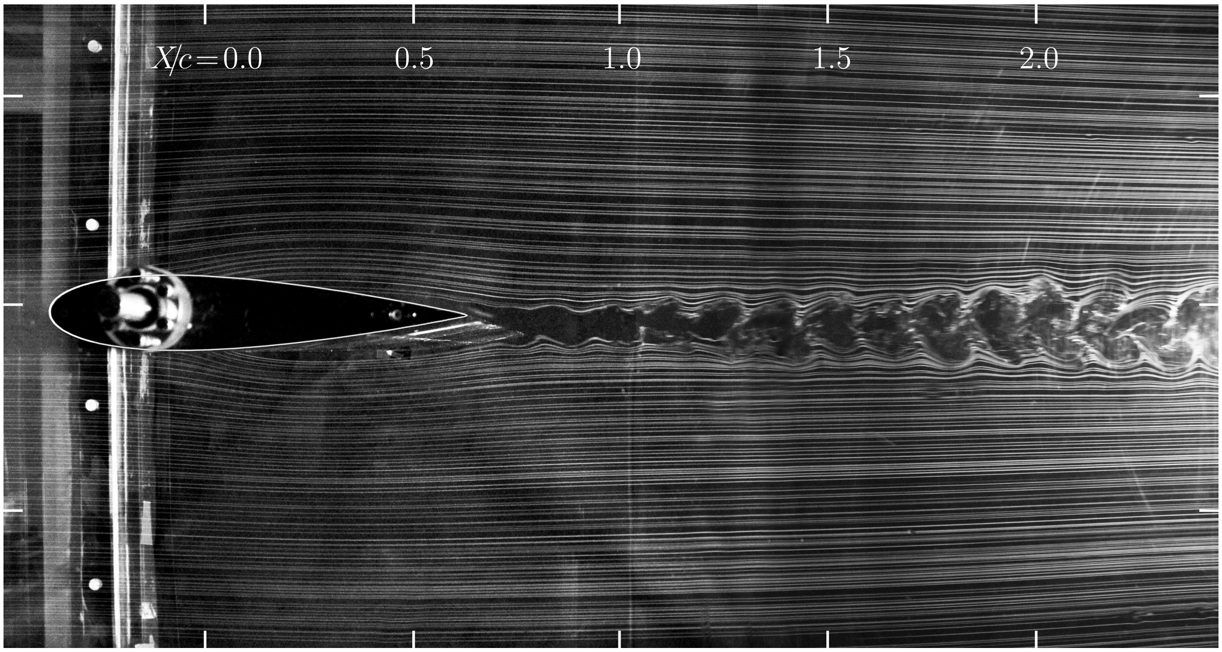
X/c = 0.0
0.5
1.0
1.5
2.0

Figure 6.1: Smoke-wire flow visualization for $AOA = 0°$.

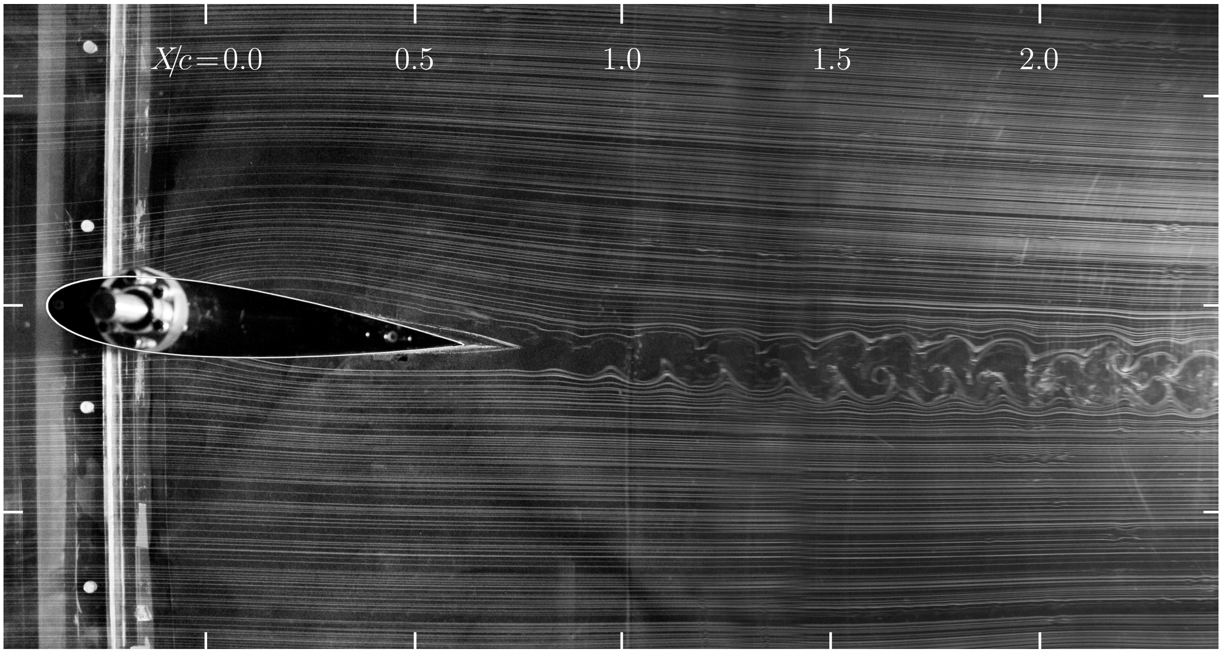
X/c = 0.0
0.5
1.0
1.5
2.0

Figure 6.2: Smoke-wire flow visualization for $AOA = 5°$.

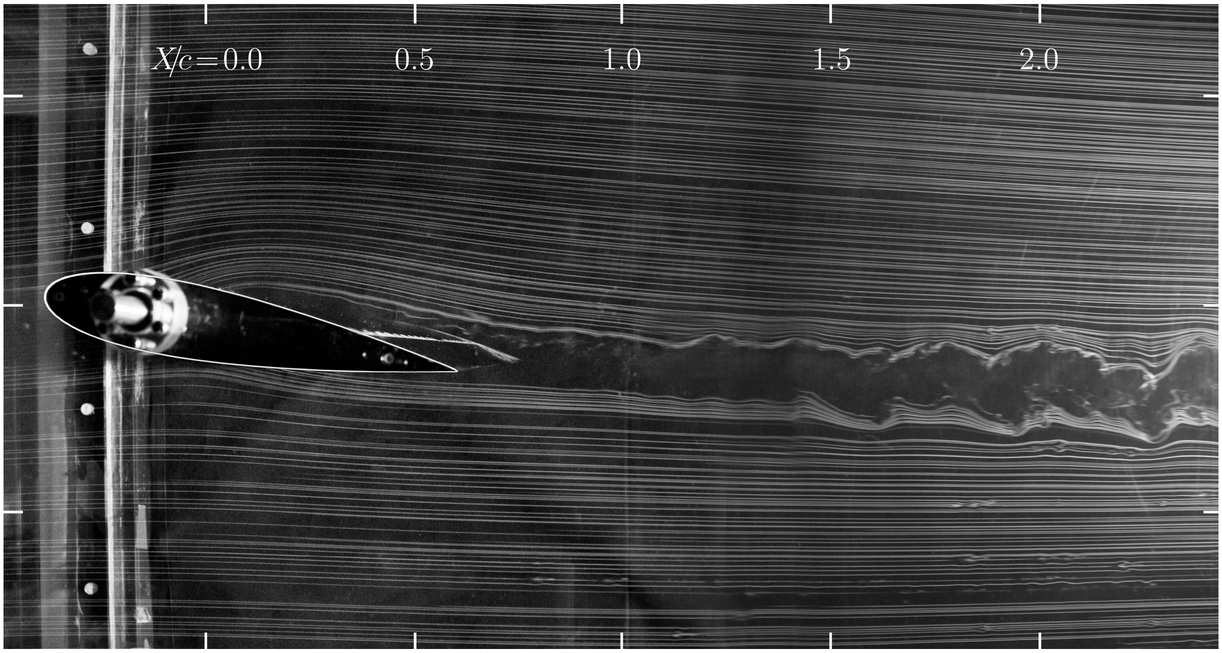
X/c = 0.0
0.5
1.0
1.5
2.0

Figure 6.3: Smoke-wire flow visualization for $AOA = 10°$.

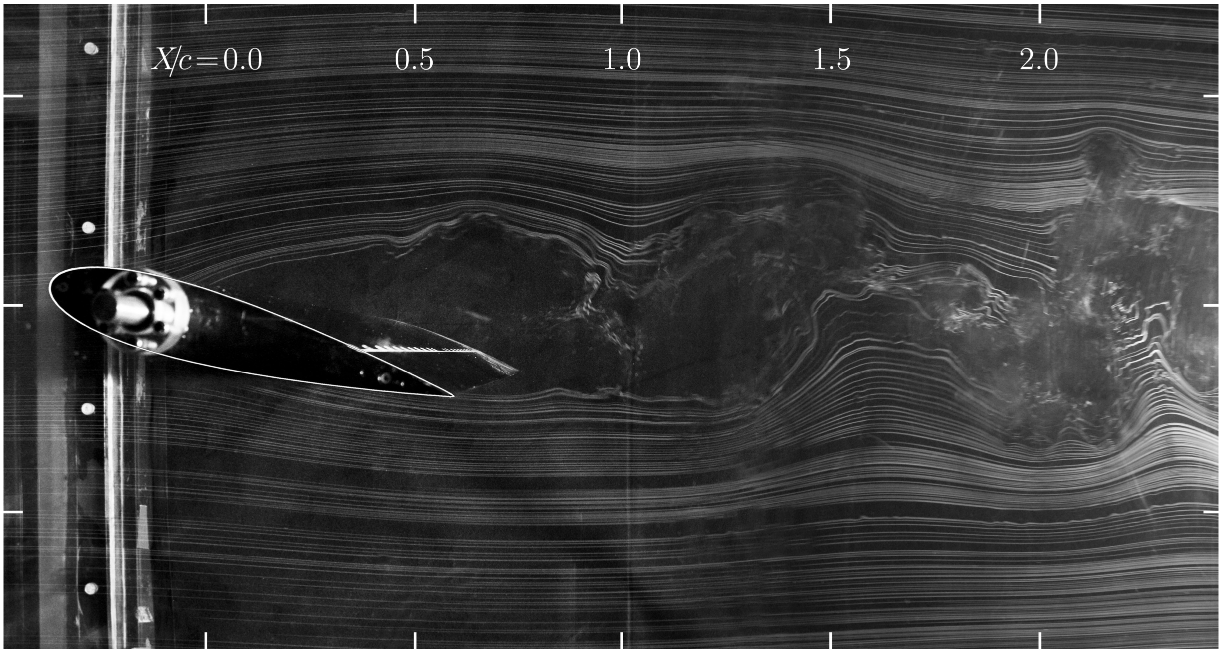
X/c = 0.0
0.5
1.0
1.5
2.0

Figure 6.4: Smoke-wire flow visualization for $AOA = 15°$.

reattaching farther downstream. As a result, a wider wake forms than at the lower angles considered.

Vortex shedding patterns can be seen in the wake of the airfoil for all angles of attack in Figs. 6.1-6.4, verifying that the dominant frequencies of the velocity fluctuations in the wake, identified from Fig. 5.5, are associated with vortex shedding. The larger and more clearly defined structures in Fig. 6.4 compared to Fig. 6.3 suggest greater coherence of wake structures at $AOA = 15°$ compared to $AOA = 10°$, agreeing with the trends noted for the velocity energy spectra in Fig. 5.5. Lower coherence of spanwise vortices when a separation bubble forms has also been noted for other flow conditions and airfoil geometries in prior low Reynolds number experiments [136, 137].

At non-zero angles of attack, the asymmetry in geometry causes wake vortices with positive and negative rotation to differ in shape. This may be responsible for the asymmetry in both the mean and RMS wake velocity profiles presented for this model in Ref. [137], and reproduced for $AOA = 10°$ and $Re_c = 10^5$ in Fig. 6.5. This behavior is clearly seen by comparing the streaklines on either side of the wake centerline in Fig. 6.2. The lower row of vortices, i.e., those with positive sign, show more defined roll-up. This may be the

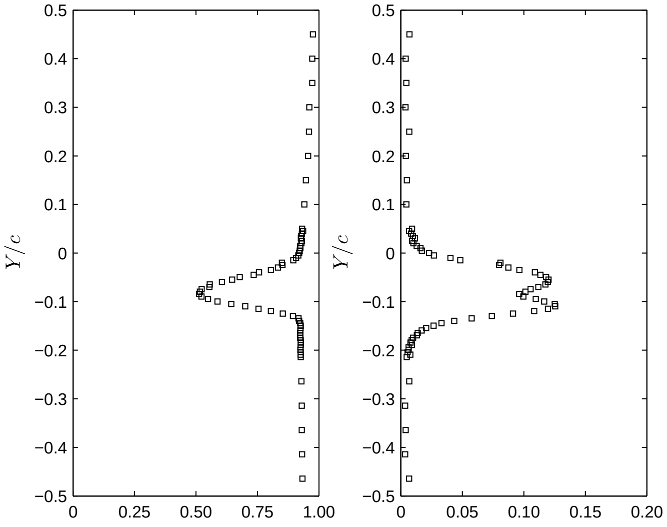

(a) (b)

Figure 6.5: Wake profiles of (a) mean velocity and (b) RMS velocity measured at $X/c = 0.95$ with a normal hot-wire probe for $AOA = 10°$, $Re_c = 10^5$, and in the GSW configuration. The data in this figure are reproduced from Ref. [137].

reason that the RMS wake velocity profile presented in Fig. 6.5b shows a more pronounced peak below the wake centerline than above it. A close examination of Fig. 6.5a reveals that the magnitude of $\partial U/\partial Y$ is higher at the shear layer core below the wake centerline than in the shear layer core above it. This indicates a higher mean vorticity of spanwise coherent structures below the wake centerline, and may be the reason that more defined peaks were observed in the wake velocity spectra computed from measurements along the shear layer core below the wake centerline than from measurements acquired in the shear layer core above the wake centerline.

The images in Figs. 6.1-6.4 can also be used to verify assumptions made in the end plate design and wall adaptation algorithm. Kubo et al. [14] concluded that end plates should be designed to extend downstream of the model to the end of the vortex formation region, so as to prevent the relatively high suction in this region from entraining fluid from the side wall boundary layer and affecting wake development. The end plate design developed for these experiments made use of an estimate of this length provided by Kubo et al. [14]. From the smoke-wire flow visualization images in Figs. 6.1-6.4, it was determined that, for each angle of attack, spanwise wake vortices being shed from the model form upstream of the trailing edges of the end plates, which extend $0.8c$ downstream of the trailing edge of the model. This confirms that the estimate used in the end plate design meets the end plate requirement suggested by Kubo et al. [14].

An assumption inherent in the wall adaptation algorithm used in these experiments is that a significant volume of irrotational flow separate the adjustable walls from the highly rotational flow created by the model. The smoke-wire flow visualization images in Figs. 6.1-6.4 show smooth streaklines away from the model and wake. The presence of the model induces mild curvature in the streaklines near the test section wall, however, the smooth streaklines away from the model and outside of the upper and lower wall boundary layers suggest that the flow rotationality in this region is negligible. These observations support the validity of the assumption of a sufficient volume of irrotational flow outside of the adjustable wall boundary layers.

The streakline patterns observed in Figs. 6.1-6.4 are consistent with the SLW configuration wall contours presented in Fig. 5.7. Near the top and bottom of each image, the shape of the streaklines agree qualitatively with the streamline patterns computed from the WAS. Specifically, the location of maximum streamline displacement predicted from the WAS calculations matches that in the flow visualization images, and the positive slope of the streamlines below and just upstream of the model at $AOA = 5$ and 10° are reflected in the images. Furthermore, the downward angle of the wall contours just downstream of the model for $AOA = 5$ and 10° are consistent with the negative slope of the wake centerline seen in Figs. 6.2 and 6.3.

Figures 6.6-6.9 present smoke-wire flow visualization images and measured mean

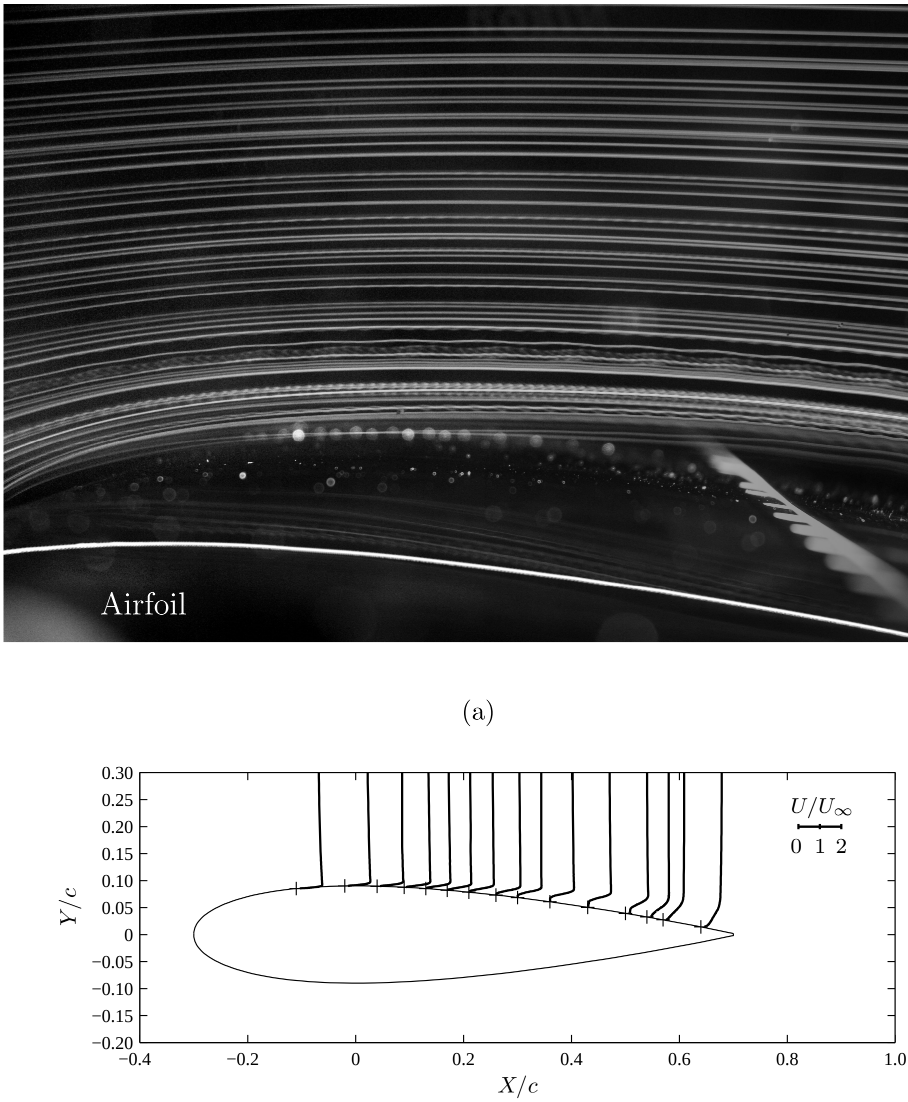

(a)

(b)

Figure 6.6: Boundary layer (a) smoke-wire flow visualization and (b) measured mean velocity profiles, for $AOA = 0^\circ$.

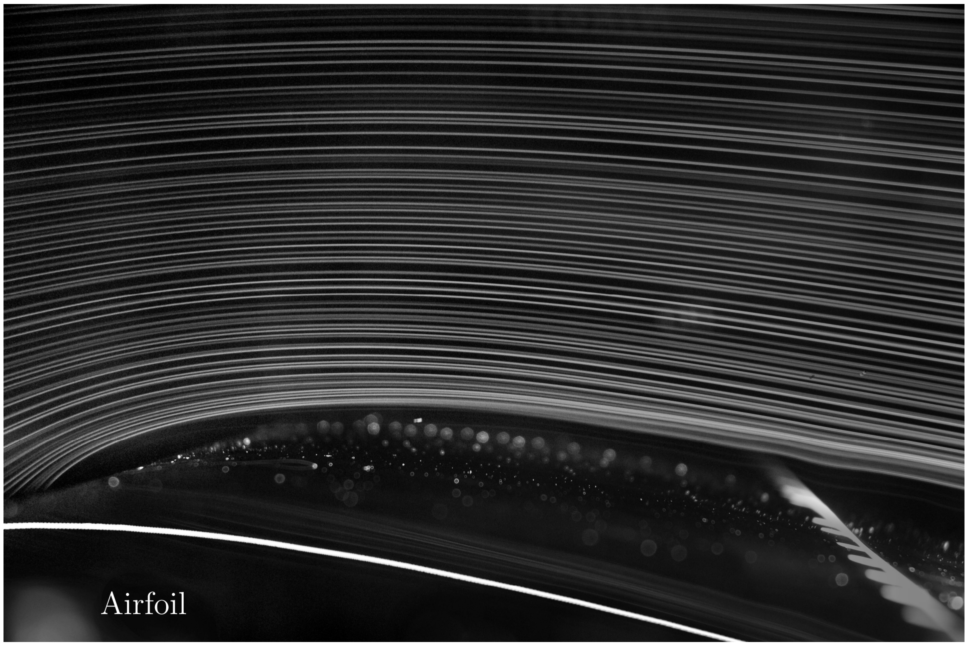

(a)

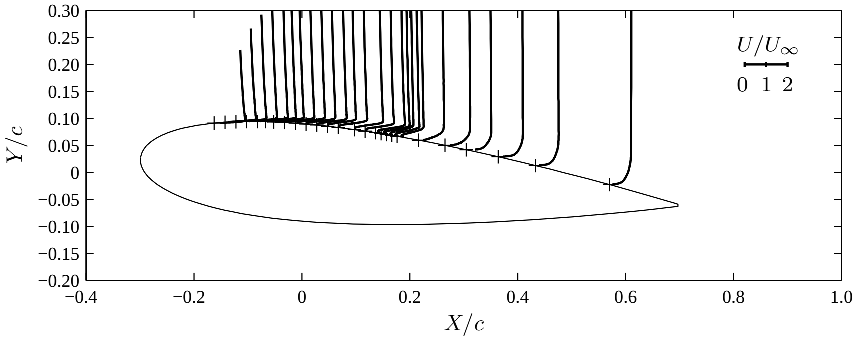

(b)

Figure 6.7: Boundary layer (a) smoke-wire flow visualization and (b) measured mean velocity profiles, for $AOA = 5°$.

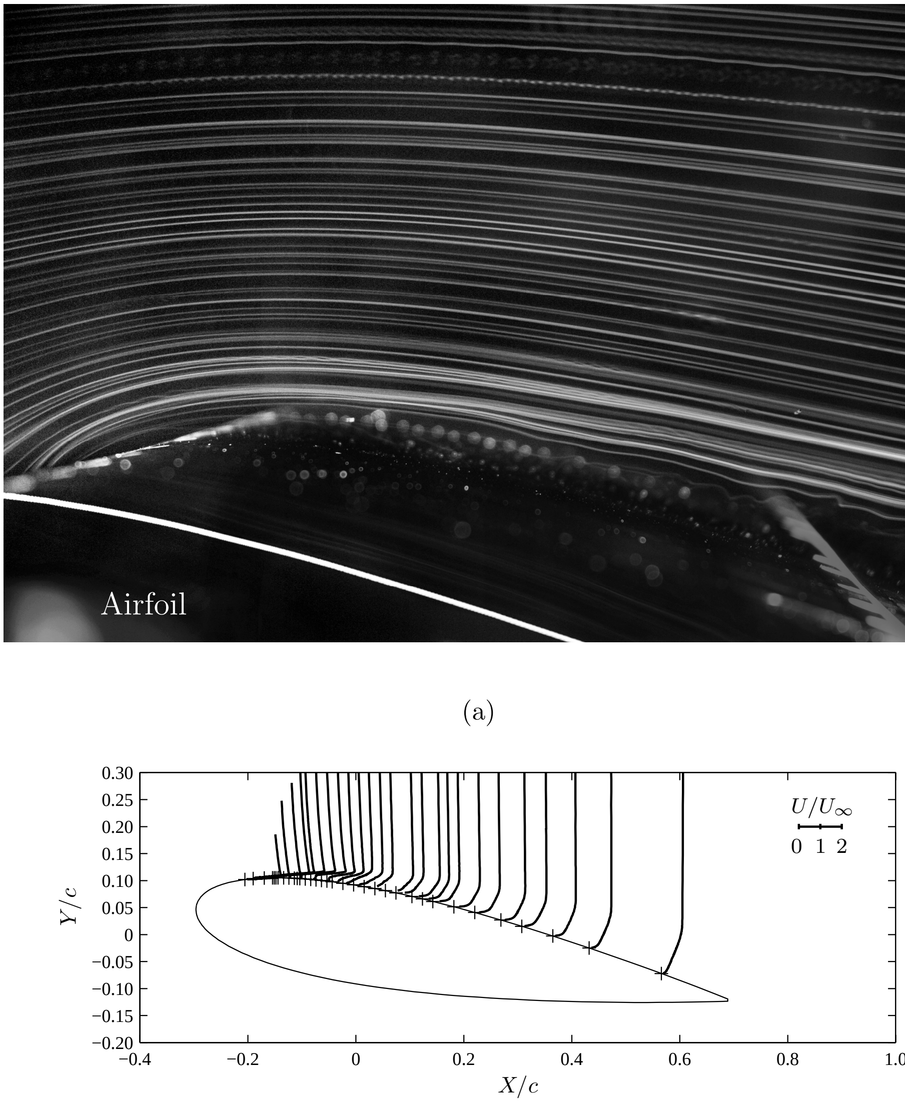

(a)

(b)

Figure 6.8: Boundary layer (a) smoke-wire flow visualization and (b) measured mean velocity profiles, for $AOA = 10°$.

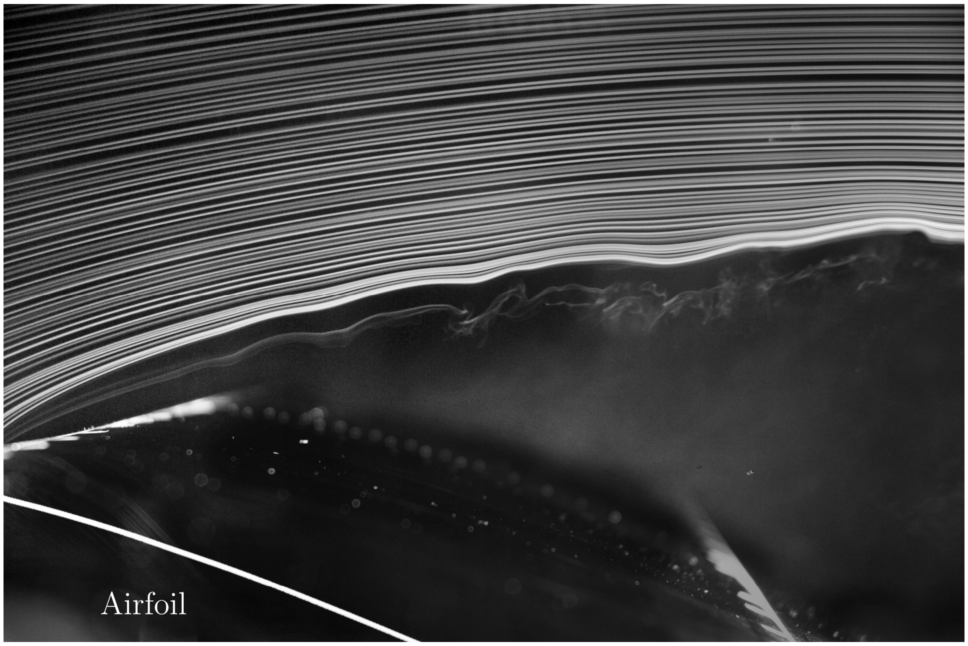

(a)

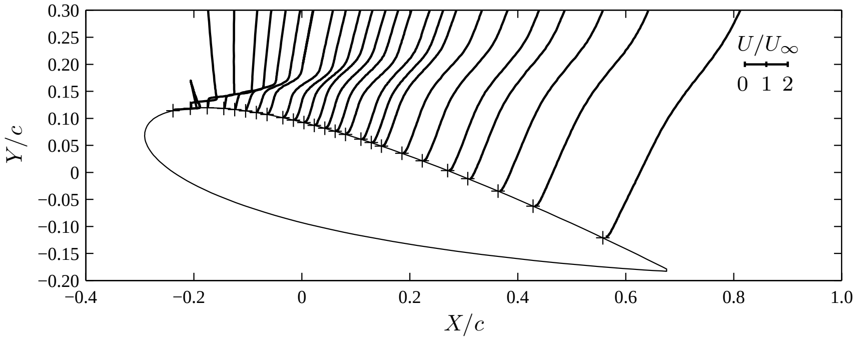

(b)

Figure 6.9: Boundary layer (a) smoke-wire flow visualization and (b) measured mean velocity profiles, for $AOA = 15°$.

velocity profiles over the upper surface of the airfoil. Note that, for AOA = 0, 5, and 10°, profile traverses were performed in the vertical direction, whereas for $AOA = 15°$, the boundary layer profiles were measured along paths normal to the airfoil surface. Only the profiles at $AOA = 15°$ could be measured along vectors normal to the surface, due to limitations on streamwise increments of the hot-wire traverse. The boundary layer profiles for AOA = 0, 5, and 10° show that the reverse flow region only extends to approximately $0.01c$ from the surface. As a result, the separation bubble is difficult to detect in the smoke-wire images.

For conditions at which boundary layer reattachment occurs (Figs. 6.6-6.8), the streaklines follow the airfoil curvature closely, suggesting that the parallel flow assumption of linear stability theory is valid for these flow conditions. However, for $AOA = 15°$ (Fig. 6.8), separation occurs close to the leading edge of the airfoil and the trajectory of the streaklines visible in the image form large angles with the surface.

For conditions at which boundary layer reattachment occurs, the boundary layer profiles show that the separation bubble moves upstream with increasing angle of attack; for $AOA = 0°$ the separation bubble is located near the trailing edge, for $AOA = 5°$ the separation bubble is at a mid-chord location, and for $AOA = 10°$ it is near the leading edge. Locations of separation and reattachment are difficult to identify from the smoke-wire images, due to the very thin shear layer at these locations. The separation bubble is tallest for $AOA = 0°$, and for this case, near the location of shear layer reattachment ($x_R/c \approx 0.9$), the streakline nearest to the airfoil surface steeply curves towards the model. The reattachment location could not be identified in the smoke-wire images for the thiner bubbles at AOA = 5 and 10°. However, streamwise oscillations in the streaklines near the airfoil surface can be observed in Figs. 6.7-6.9 downstream of the transition location, and are indicative of shear layer unsteadiness. Shear layer flapping may be a result of such unsteadiness, as has been observed in previous separation bubble experiments [53,107,109,111].

6.2 Boundary Layer Measurements

This section presents detailed measurements of flow development over the airfoil. Changes in flow development with angle of attack are summarized in the surface pressure distributions in Fig. 6.10. For conditions at which a separation bubble forms on the upper surface of the airfoil, locations of separation, transition, and reattachment were estimated from the mean surface pressure distributions, based on the method described by O'Meara & Mueller [8]. Figure 6.10 shows that, for conditions at which a separation bubble forms, as the angle of attack increases the maximum suction pressure on the upper surface increases,

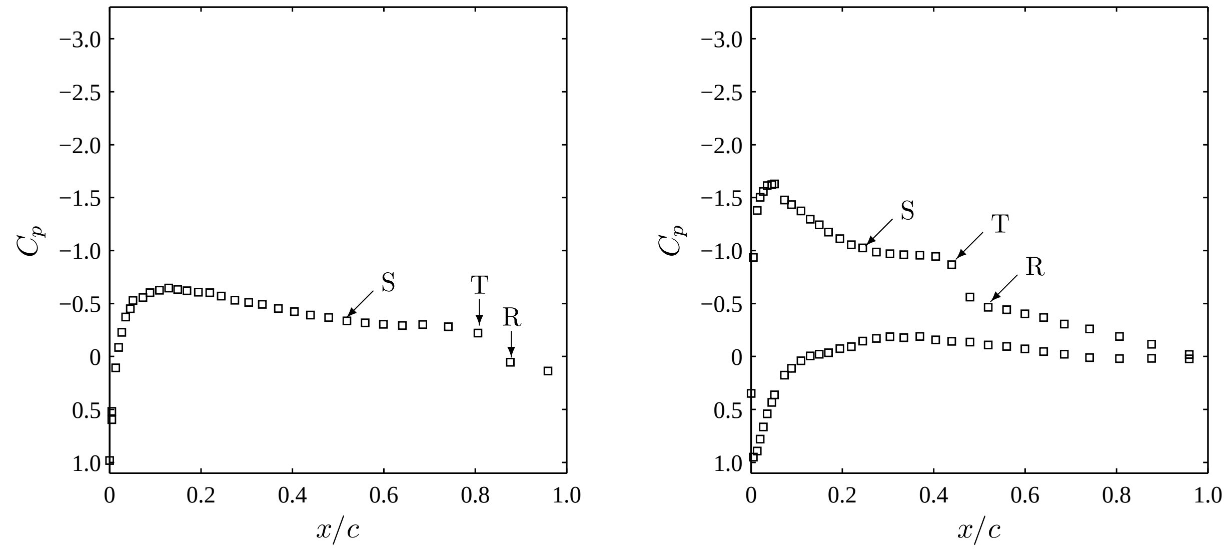

(a) $AOA = 0°$

(b) $AOA = 5°$

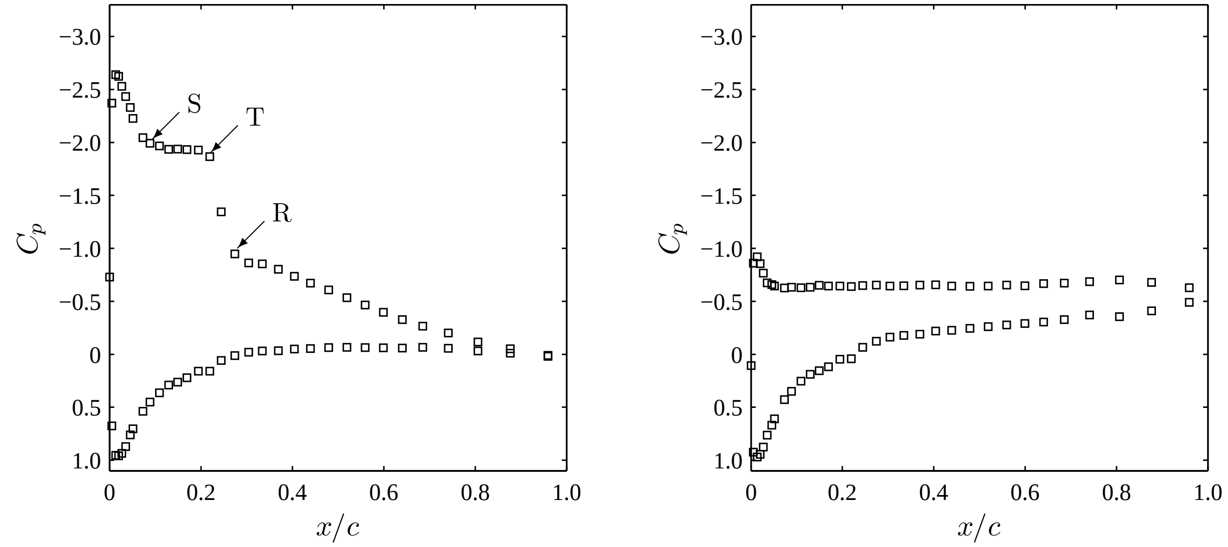

(c) $AOA = 10°$

(d) $AOA = 15°$

Figure 6.10: Model surface pressure distributions with estimated x/c locations of separation (S), transition (T), and reattachment (R) determined from mean surface pressure distributions for conditions at which separation bubbles form. For clarity, in (a), only the upper surface pressure distribution is presented.

the separation point moves upstream, and the separation bubble length decreases. These trends are common for airfoil operation at low Reynolds numbers [8, 50, 53, 138]. The dramatically different flow regime observed in Fig. 6.4 compared to Fig. 6.3, indicates that the separation bubble bursts between $AOA = 10$ and 15°. The resulting upper surface pressure distribution at $AOA = 15°$ shows significantly lower suction pressures than at $AOA = 10°$.

Mean and RMS boundary layer velocity profile measurements are presented in Figs. 6.11-6.14. Figure 6.15 provides a closer view of the boundary layer profiles in and around the relatively small separation bubble for $AOA = 10°$. As discussed in Appendix A, these hot-wire measurements are most accurate in the attached laminar and turbulent boundary layers, and in the higher speed flow outside of the recirculation regions. Velocity measurements from these regions can be used to accurately determine RMS velocity variation along the shear layer core, shear layer energy spectrum development in the streamwise direction, and disturbance amplification rates. In the recirculating flow regions, higher measurement uncertainty results from low speed calibration error [23], hot-wire voltage rectification error [99], error due to enhanced conductive heat loss near the model surface [100–102], and error due to high mean vertical flow speed [99]. Although these sources of error interfere with the accurate determination of the maximum reverse flow speed, the height of the reverse flow region can be confidently determined. By removing measurements obtained at near zero velocity, and rectifying the mean velocity profiles in the reverse flow region, reasonable estimates of boundary layer thickness parameters can also be obtained [38, 53]. Furthermore, it was shown in Chapter 4 that errors in mean velocity profile measurements in the reverse flow region have only a minor effect on LST estimates of disturbance growth rates and streamwise velocity fluctuation profiles.

The boundary layer profiles presented in Figs. 6.11-6.15 show mean velocity field development over the model. These profiles exhibit typical trends for low Reynolds number flows over airfoils [25, 50, 53]. For $AOA = 0$, 5, and 10°, attached laminar boundary layer profile development can be observed upstream of the separation point. For $AOA = 15°$, no attached boundary layer profiles were measured, since separation occurs very close to the leading edge. Downstream of the separation point, separated shear layer profiles are presented for each angle of attack. The mean velocity profiles exhibit reverse flow near the wall and a profile inflection point at the approximate height of the displacement thickness, indicated by the dashed curves in Figs. 6.11-6.14. For $AOA = 0$, 5, and 10°, the height of the inflection point reaches a maximum at approximately the transition location and then decreases to zero. Beyond this point, an attached turbulent boundary layer develops. For $AOA = 15°$, the height of the separated shear layer velocity profile inflection point increases continuously to the trailing edge.

RMS velocity profiles are presented below the mean velocity profiles in Figs. 6.11-

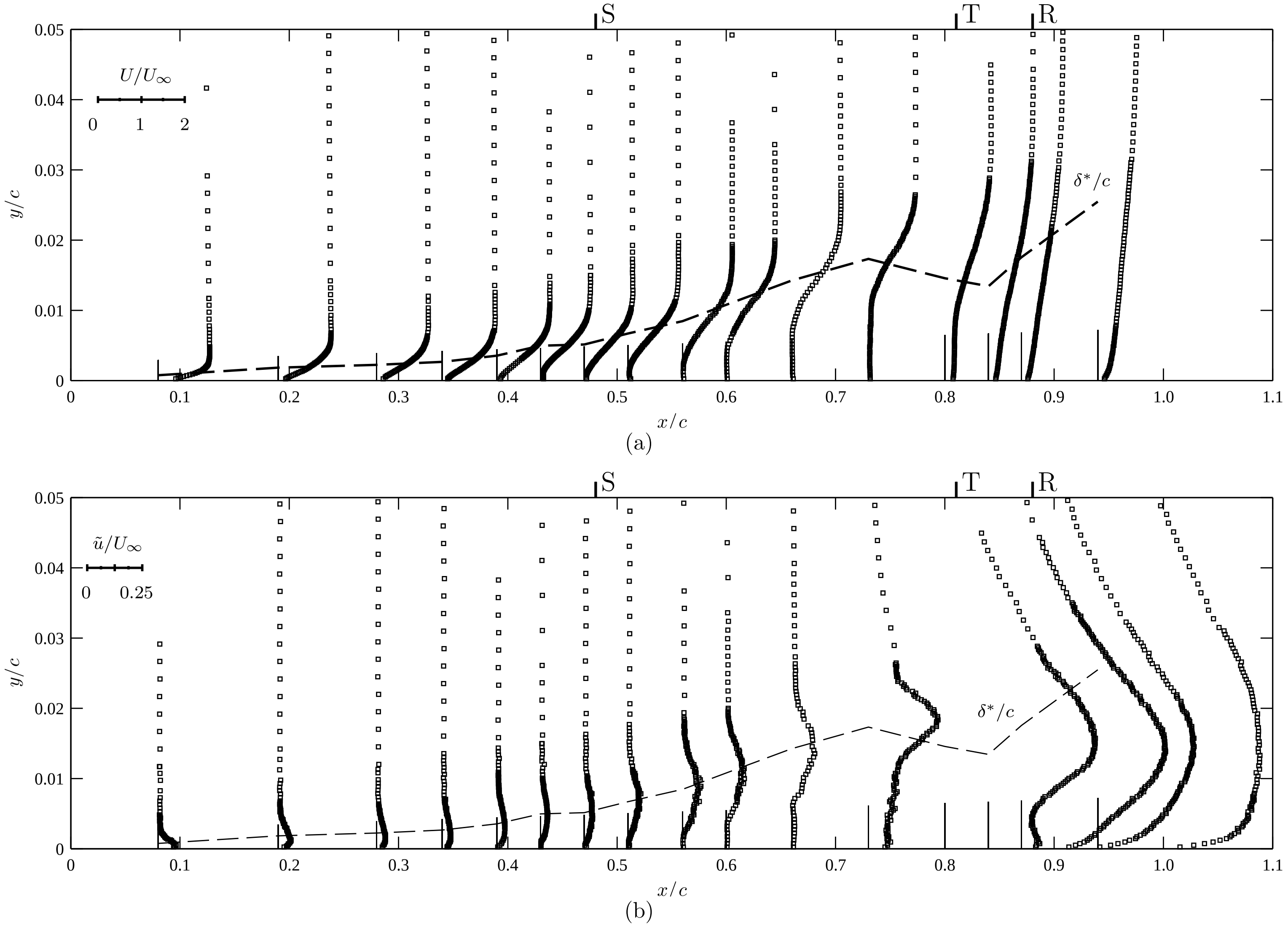

(a)

(b)

Figure 6.11: Boundary layer profiles of (a) mean and (b) RMS velocity for $AOA = 0°$. Estimated x/c locations of separation, transition, and reattachment are indicated by S, T, and R, respectively.

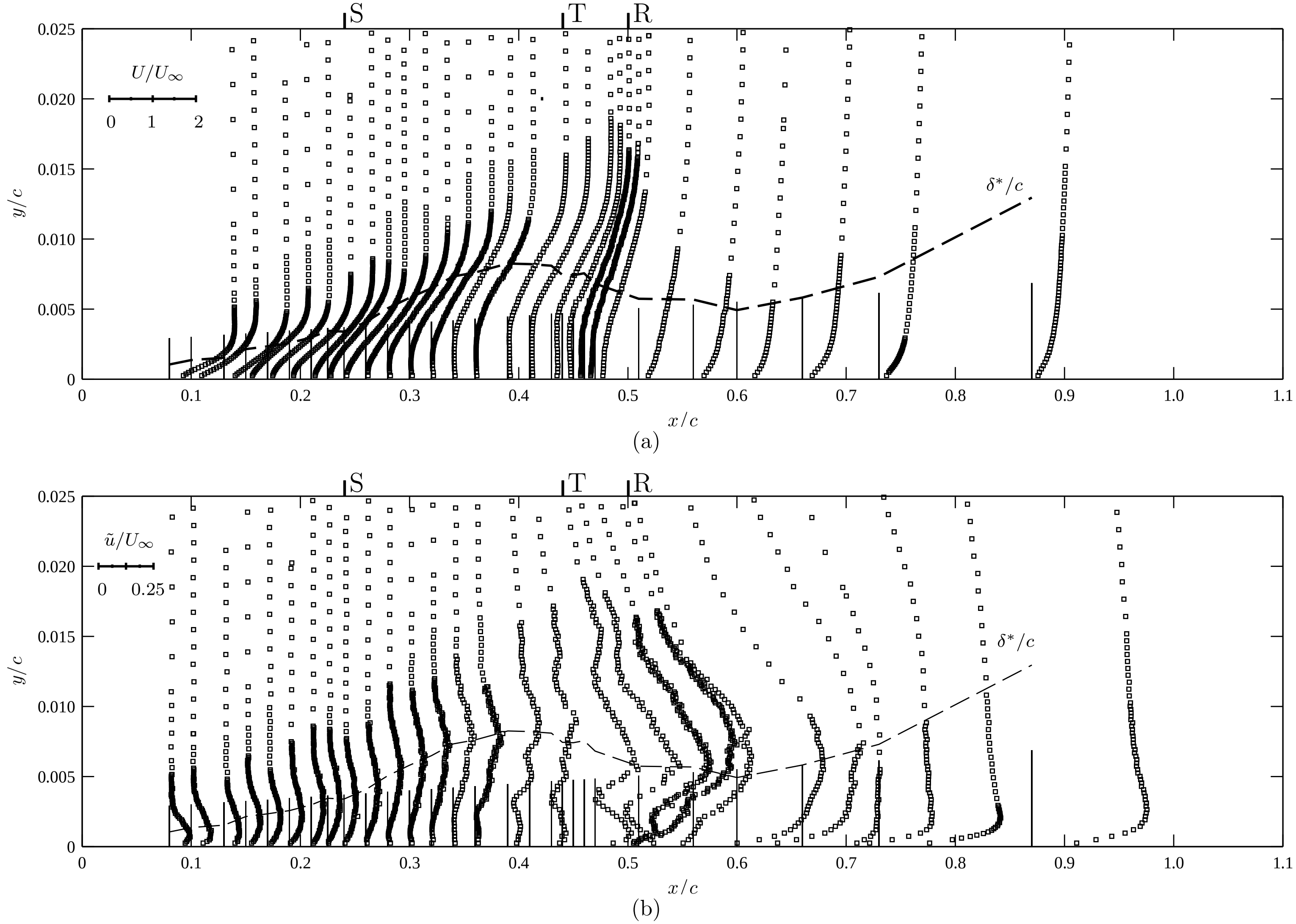

Figure 6.12: Boundary layer profiles of (a) mean and (b) RMS velocity for $AOA = 5°$. Estimated x/c locations of separation, transition, and reattachment are indicated by S, T, and R, respectively.

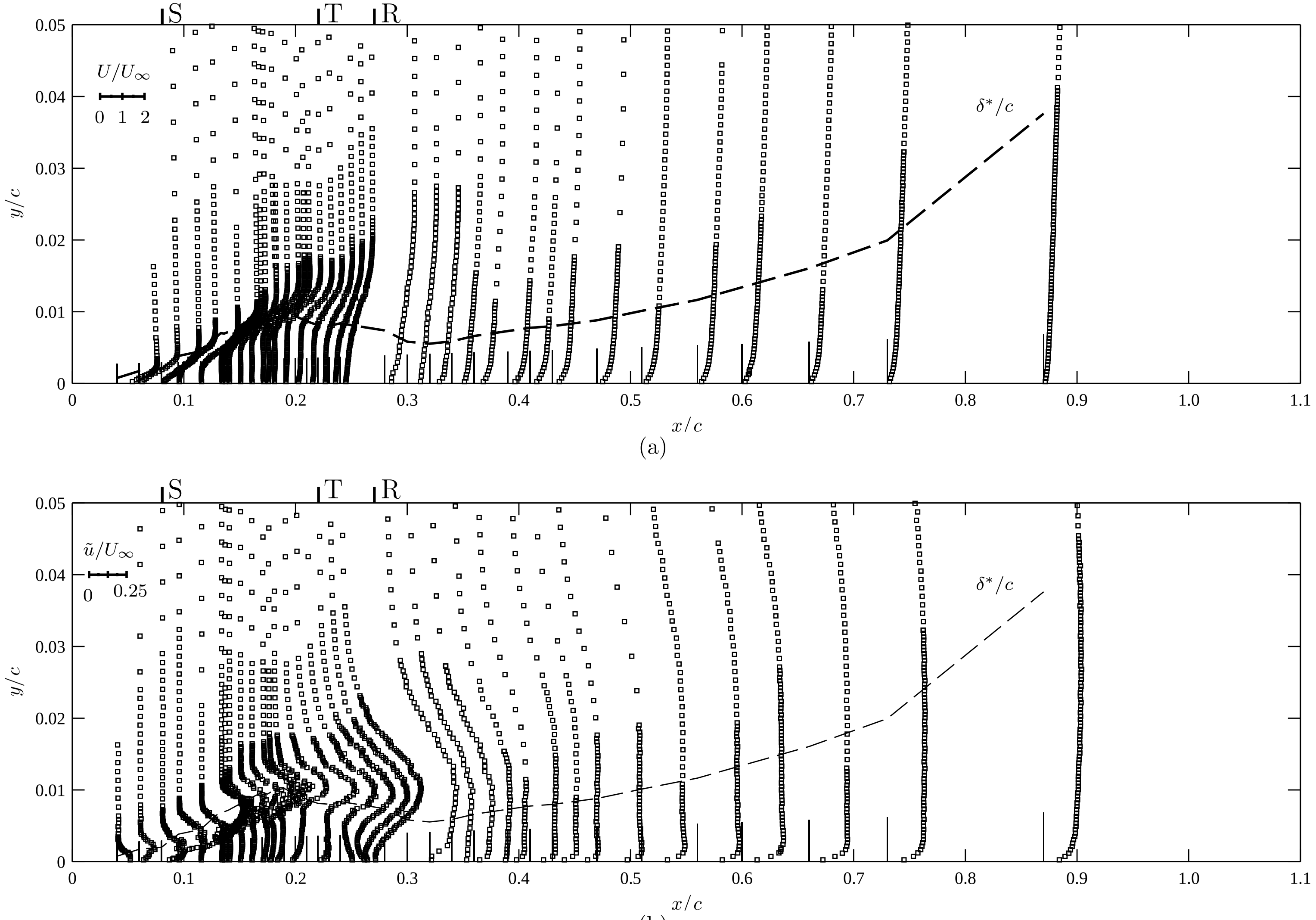

(a)

(b)

Figure 6.13: Boundary layer profiles of (a) mean and (b) RMS velocity for $AOA = 10°$. Estimated x/c locations of separation, transition, and reattachment are indicated by S, T, and R, respectively.

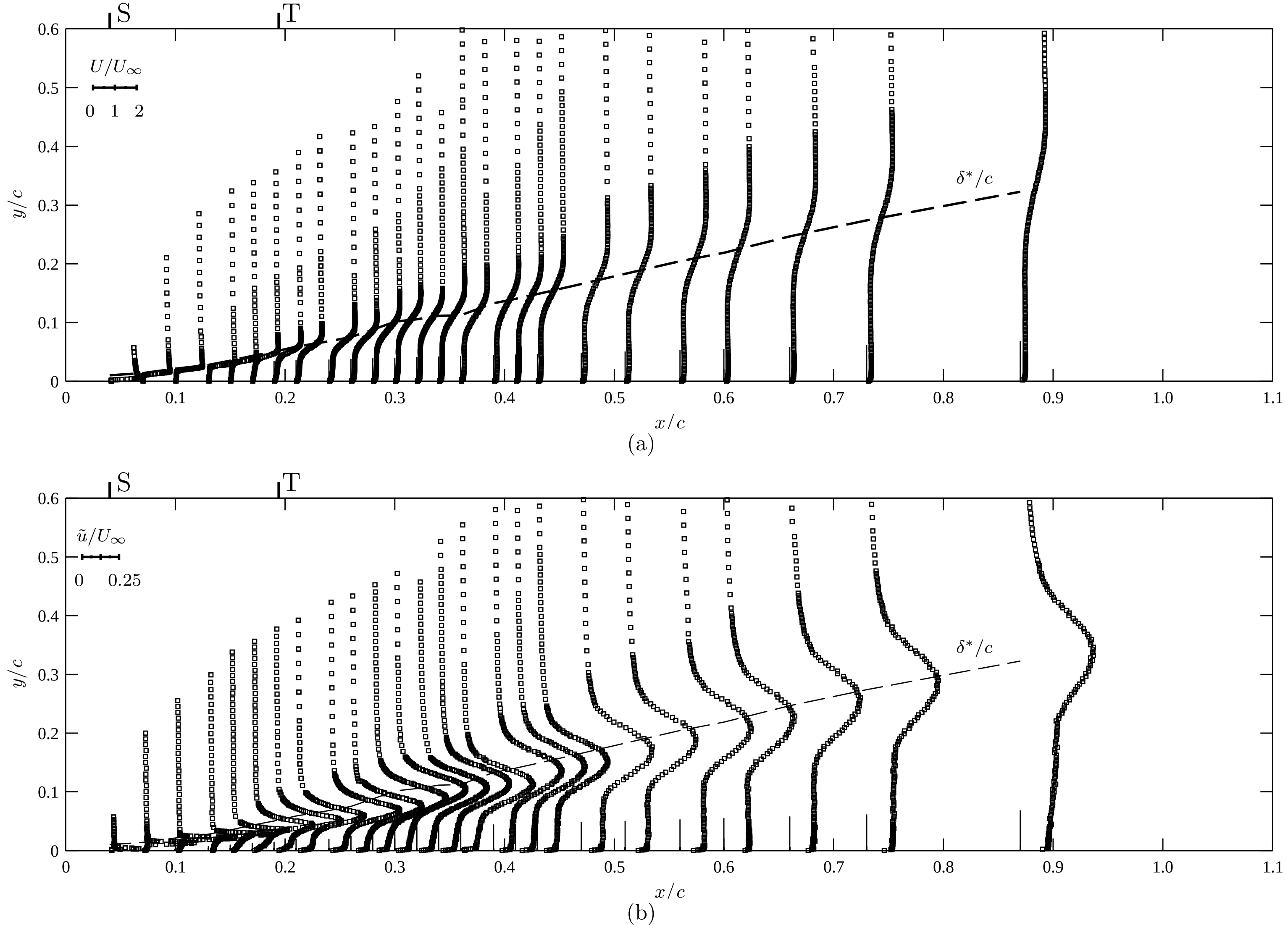

Figure 6.14: Boundary layer profiles of (a) mean and (b) RMS velocity for $AOA = 15°$. Estimated x/c locations of separation and transition are indicated by S and T, respectively.

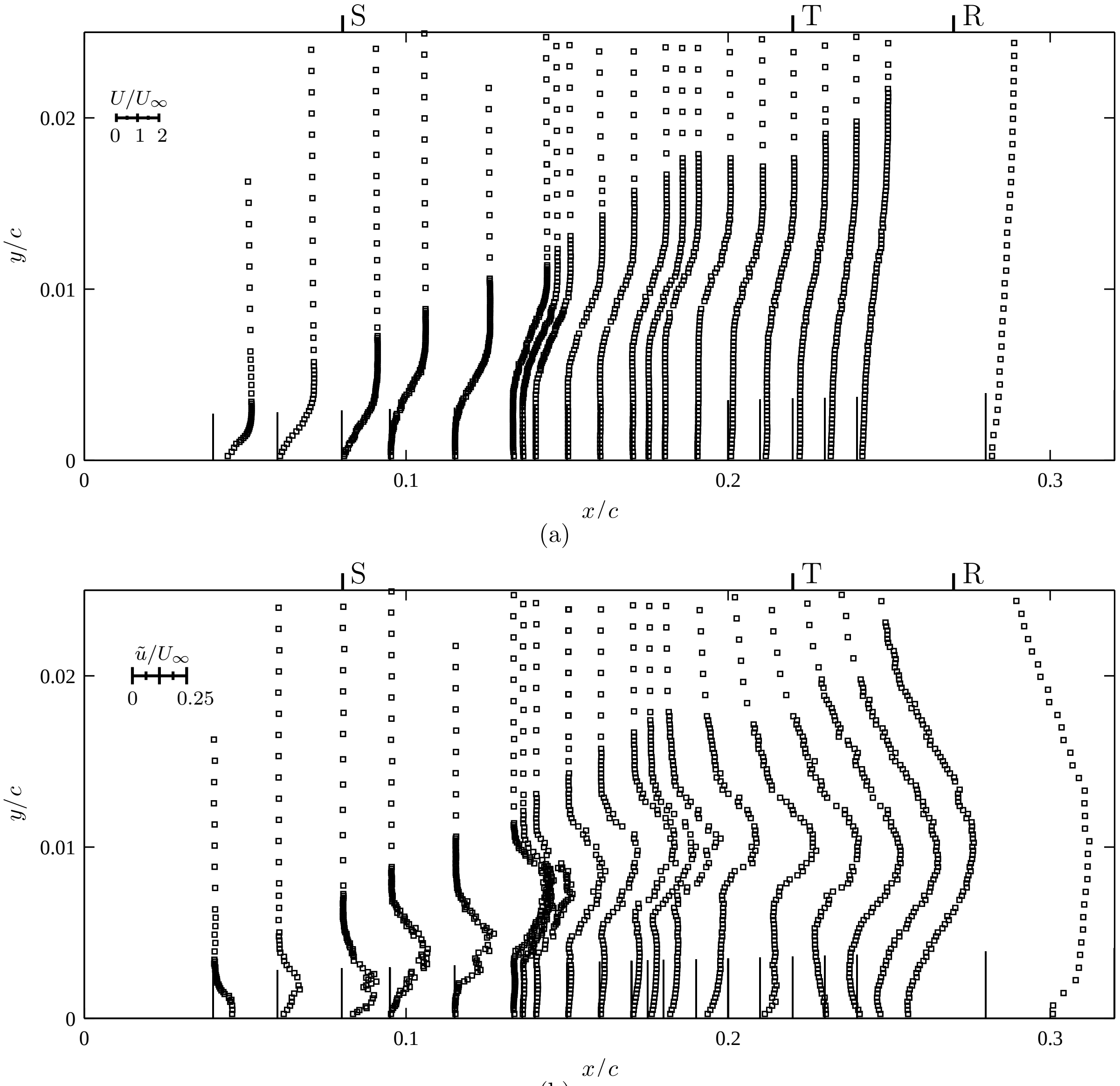

(a)

(b)

Figure 6.15: Boundary layer profiles in and around the separation bubble showing (a) mean and (b) RMS velocity for $AOA = 10°$. Estimated x/c locations of separation, transition, and reattachment are indicated by S, T, and R, respectively.

6.15. In the laminar boundary layer, measured for $AOA = 0$, 5, and 10°, low amplitude fluctuations with a single peak near the wall are observed. These profiles are similar to the Tollmien-Schlichting wave shapes that develop in unstable laminar boundary layers on flat plates [33, 61, 67]. The magnitude of the maximum RMS velocity in each profile changes gradually in the streamwise direction in the attached laminar boundary layer. Downstream, in the laminar separated flow region, the RMS velocity profiles develop additional peaks and the amplitude of fluctuations increase rapidly in the streamwise direction. Such three peak RMS velocity profiles are typical for transitional separated shear layers [24,34,53]. At each streamwise location, the RMS velocity peak with the greatest amplitude is approximately at the height of the displacement thickness, which roughly corresponds to the mean profile inflection point. For $AOA = 0$, 5, and 10°, the RMS velocity profiles in the reattached turbulent boundary layer have a single peak near the wall and decay more gradually into the free stream than in the laminar boundary layer upstream. Sufficiently far downstream, these profiles resemble the RMS velocity profiles commonly measured in the turbulent boundary layers on flat plates [139]. For $AOA = 15°$, over most of the airfoil chord the RMS velocity profiles exhibit a single peak near the mean profile inflection point. This profile is similar to the RMS velocity profiles in turbulent free shear layers (e.g., Ref. [139]), except near the model surface where the profile must satisfy the no-slip condition.

Estimates of the locations of separation, transition, and reattachment can be made based on the mean velocity profiles and energy spectra in the shear layer. The separation location can be estimated as the first profile with zero or negative slope at the model surface. Note that limitations on the closest measurement location, errors associated with low speed and near wall velocity measurements, and probe interference effects identified in Chapter 5 cause uncertainty in this estimate. For conditions at which a separation bubble forms, the transition location can be estimated as the location of maximum displacement thickness [53]. For the case of separation without reattachment, the transition location was estimated from energy spectra of the fluctuating velocity component. The final streamwise location at which a characteristic instability frequency could be identified in the spectrum was used as the estimate of the transition location. This approach was found to provide consistent estimates of the transition location for the separation bubble cases as compared to the estimates based on the model surface pressure distributions. The reattachment location can be estimated as the first location downstream of the transition point at which the mean velocity profile has a positive slope at the wall. Estimates of the separation, transition, and reattachment locations, based on surface pressure distributions for conditions at which boundary layer reattachment occurs and velocity measurements for stalled conditions, are indicated in Figs. 6.11-6.15. Where estimates of these locations can be obtained from both velocity profile measurements and surface pressure measurements, the values agree to within the measurement resolution.

The displacement thickness curves in Figs. 6.11-6.13 exhibit common trends for separation bubbles [53]. The rate of change of displacement thickness in the streamwise direction is low in the attached laminar boundary layer, but increases significantly at the separation point. The displacement thickness continues to increase up to the transition location, and then decreases as enhanced momentum transfer in the turbulent shear layer reduces the height of the reverse flow region near the surface. The minimum displacement thickness downstream of the transition point occurs at approximately the mean reattachment location. Downstream, in the developing turbulent boundary layer, the displacement thickness increases at a much higher rate than in the upstream laminar boundary layer. Under stalled conditions (Fig. 6.14), the displacement thickness increases nearly linearly in the streamwise direction downstream of the separation point.

Figure 6.16 provides an overview of the geometry of the reverse flow region and how it changes with angle of attack. The $U/U_\infty = 0$ contour was estimated from the mean velocity profile measurements in Figs. 6.11-6.14. The observed reverse flow region shapes for $AOA = 0$, 5, and 10° agree qualitatively with previous studies on low Reynolds number airfoils [37,53]. As noted in relation to Fig. 6.10, the separation bubble shifts upstream and decreases in length as the angle of attack increases. However, the height of the reverse flow region does not change monotonically with angle of attack. For a thick airfoil, such as the NACA 0018 airfoil examined in this investigation, the surface geometry in the vicinity of the separation bubble changes significantly with separation bubble location. The effective changes in surface curvature near the separation bubble can be seen in Fig. 6.16, and may contribute to the measured trend in maximum reverse flow height with angle of attack. For conditions at which a separation bubble forms, the distance between the transition and reattachment locations is small compared to the overall bubble length. For $AOA = 15°$, at which boundary layer reattachment does not occur, Fig. 6.16 illustrates how the $U/U_\infty = 0$ contour remains at an approximately constant height in the X-Y coordinate system. For this angle of attack, the flow behaves as that over a bluff body, with laminar separation relatively far upstream and a wide wake forming behind the model.

Boundary layer thickness parameters were computed based on the velocity profile measurements in Figs. 6.11-6.14. The streamwise variation of these parameters is presented in Fig. 6.17, for angles at which a separation bubble forms, and in Fig. 6.18, for the stalled case. The data have been separated in this way because the boundary layer thickness parameters are significantly larger for the stalled case. For conditions at which a separation bubble forms, the zero velocity contours clearly show the trends noted from Fig. 6.16: as the angle of attack increases, the separation bubble shifts upstream and decreases in length, with the maximum height of the reverse flow region at $AOA = 5°$ less than that at 0 and 10°. By comparison with Figs. 6.11-6.13, it can be seen that the transition location approximately corresponds to the streamwise location of maximum separation

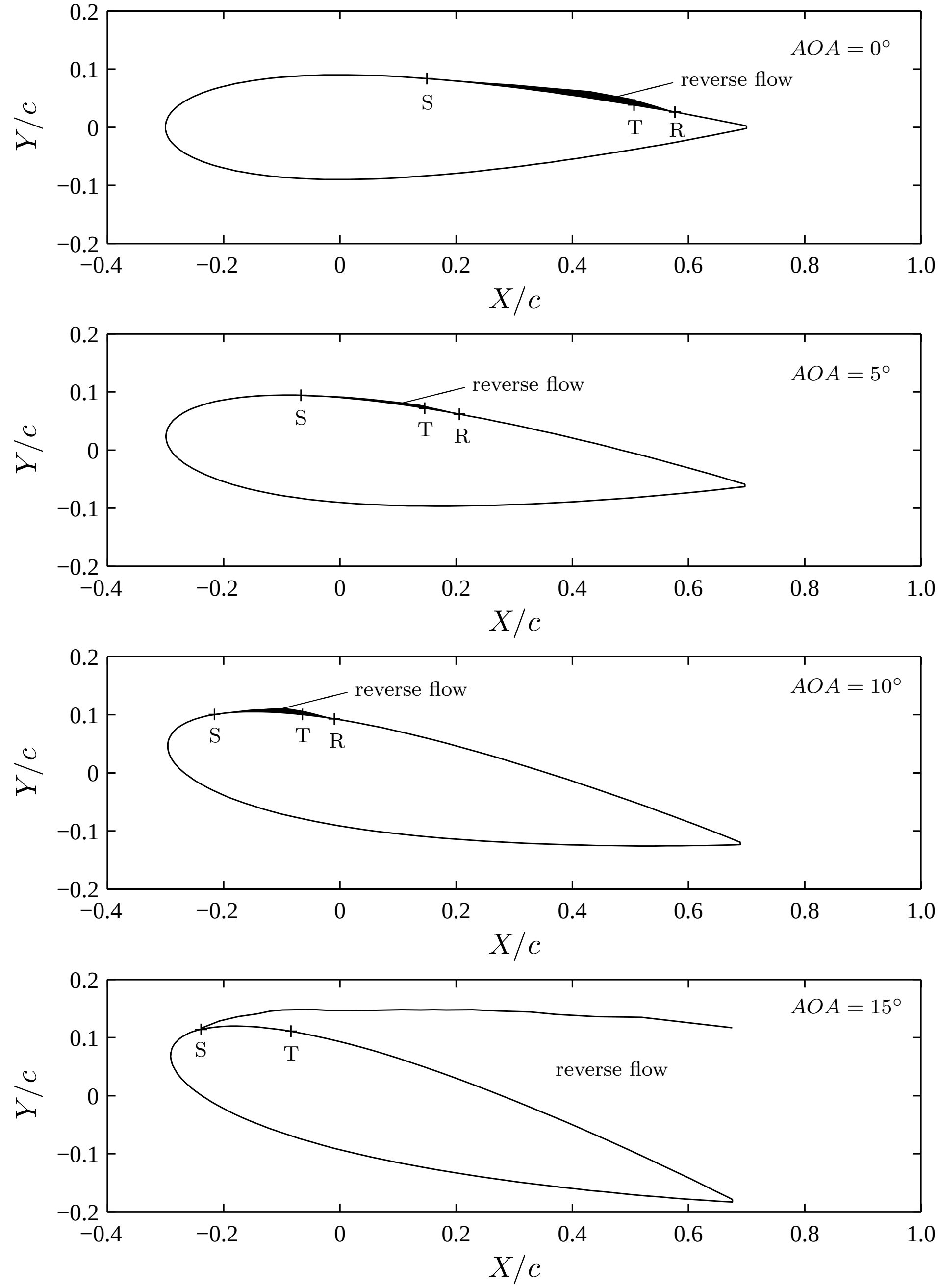

Figure 6.16: Estimated regions of reverse flow on the upper surface of the airfoil. Locations of separation, transition, and reattachment are indicated by S, T, and R, respectively

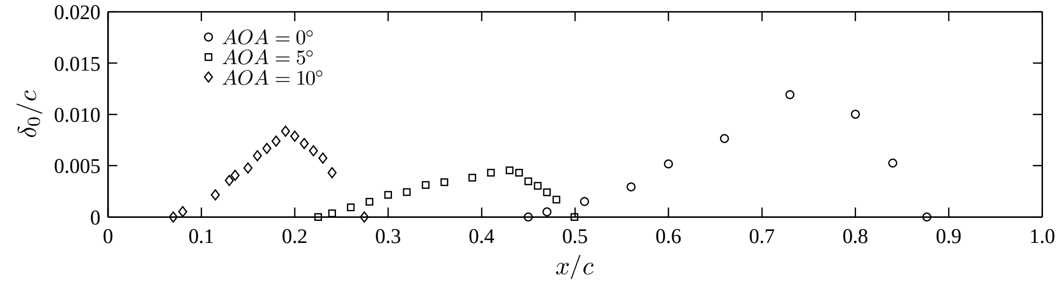

(a) y positions where $U/U_\infty = 0$

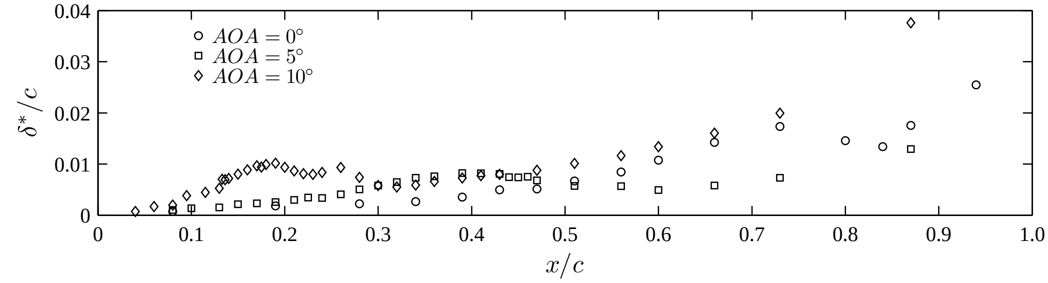

(b) displacement thickness

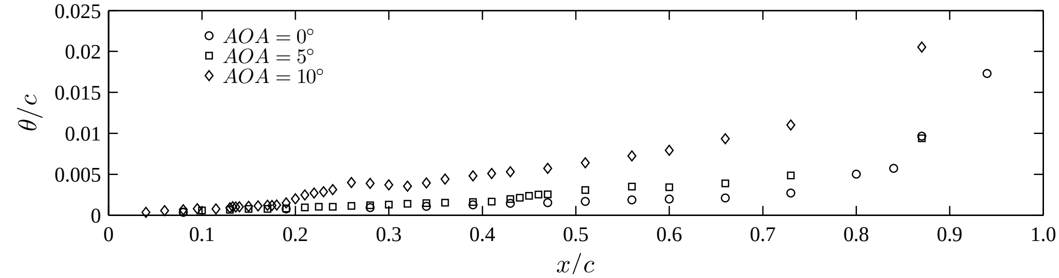

(c) momentum thickness

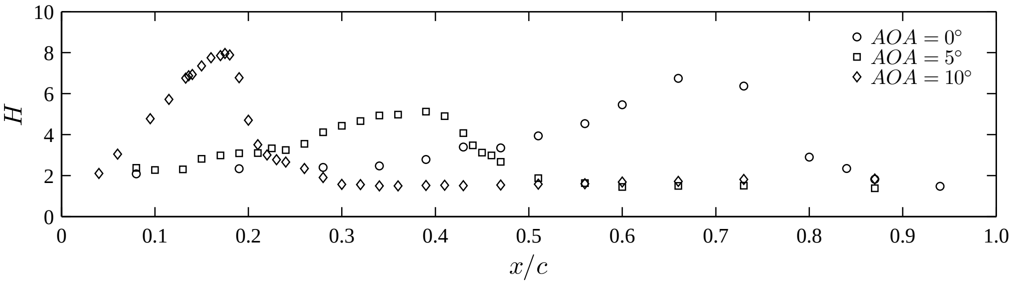

(d) boundary layer thickness shape factor

Figure 6.17: Estimated zero mean velocity contour and boundary layer thickness parameters for $AOA = 0$, 5, and 10°.

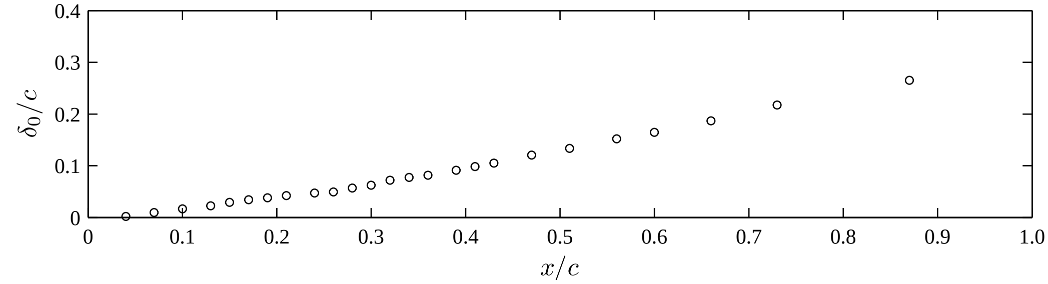

(a) y positions where $U/U_\infty = 0$

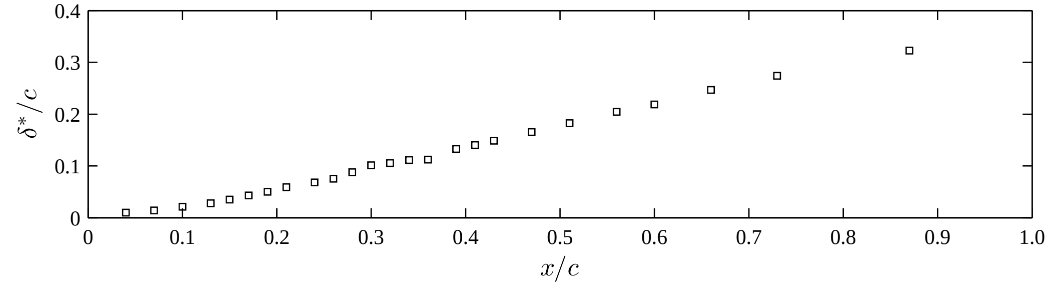

(b) displacement thickness

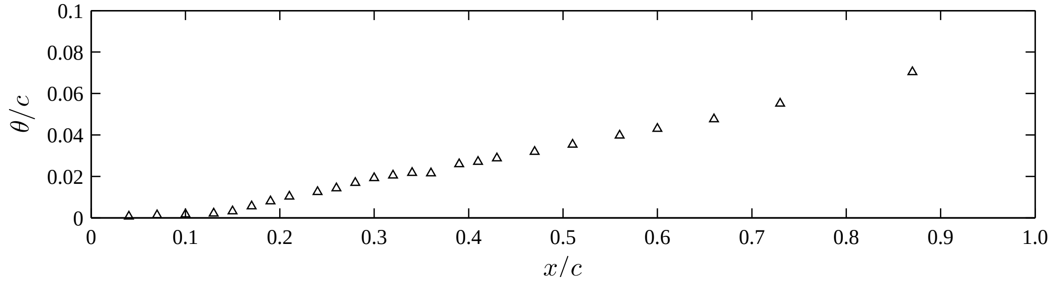

(c) momentum thickness

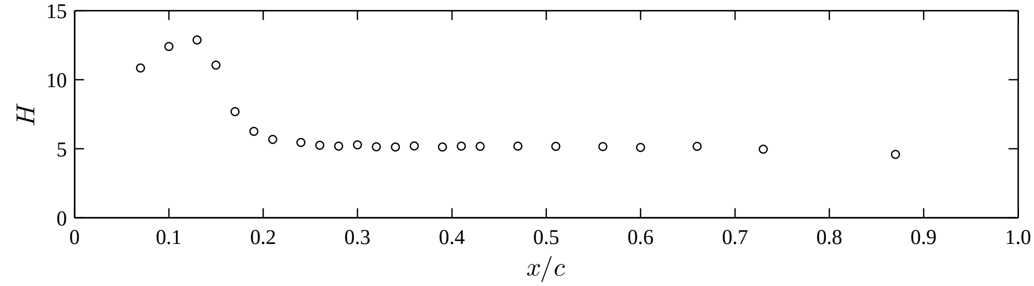

(d) boundary layer thickness shape factor

Figure 6.18: Estimated zero mean velocity contour and boundary layer thickness parameters for $AOA = 15°$.

bubble height, as has been observed in prior low Reynolds number airfoil experiments [53]. Figure 6.17 shows that the maximum displacement thickness is roughly proportional to the maximum height of the reverse flow region in the separation bubble. The momentum thickness plots are consistent with qualitative trends noted by Brendel & Mueller [53] for a Wortmann FX63-137 airfoil at $Re_c = 10^5$; specifically, the momentum thickness has a small, nearly constant value upstream of the transition point, begins to increase significantly near the transition location, and shows no distinct features at the mean reattachment point. This momentum thickness trend is also observed for the stalled condition in Fig. 6.18. The resulting boundary layer thickness shape factor curves show similar trends between each of the angles of attack, including the stalled case. However, for the stalled case, measurements were only obtained downstream of the separation point, and as a result, trends in the attached boundary layer and just downstream of separation could not be compared. The boundary layer thickness shape factor is relatively constant upstream of the separation point, then gradually increases up to the transition location where it undergoes a steep reduction to a value that remains nearly constant with streamwise position throughout the developing turbulent boundary layer. The nearly constant values of the shape factor upstream and downstream of the transition point are approximately equal. Similar shape factor trends can be observed in the results of Burgmann & Schröder [37]. The maximum value of the shape factor does not follow the same trend with angle of attack as was observed for the height of the reverse flow region.

Figure 6.19 compares the RMS velocity measured along the displacement thickness curve, RMS surface pressure fluctuations, and the locations of separation, transition, and reattachment for each angle of attack investigated. Note that the RMS velocity at the height of the displacement thickness is presented, rather than at the measured RMS velocity maximum, because displacement thickness is obtained through velocity profile integration and is therefore less sensitive to local data scatter around the RMS velocity peak. The RMS velocity trends are in qualitative agreement with separation bubble measurements in previous studies [23,28,50]. Upstream of the separation point, the RMS velocity diminishes in the streamwise direction. This can be observed for both $AOA = 0^\circ$ and $AOA = 5^\circ$. For the other two angles of attack, the separation location is too far upstream for this region to be observed in the measured data. The decay of RMS velocity is attributed to the expansion of the velocity profile in the streamwise direction, the decrease in edge velocity in the pressure recovery region, and the attenuation of certain disturbance components in the boundary layer. Downstream of the separation location the RMS velocity increases at a very high rate and eventually reaches a maximum just upstream of the mean reattachment point. The RMS velocity maximum observed at each of the four angles of attack is in the range $0.2 \lesssim \tilde{u}/U_\infty \lesssim 0.3$, and increases with angle of attack for conditions at which a separation bubble forms. Downstream of the transition location, the RMS velocity

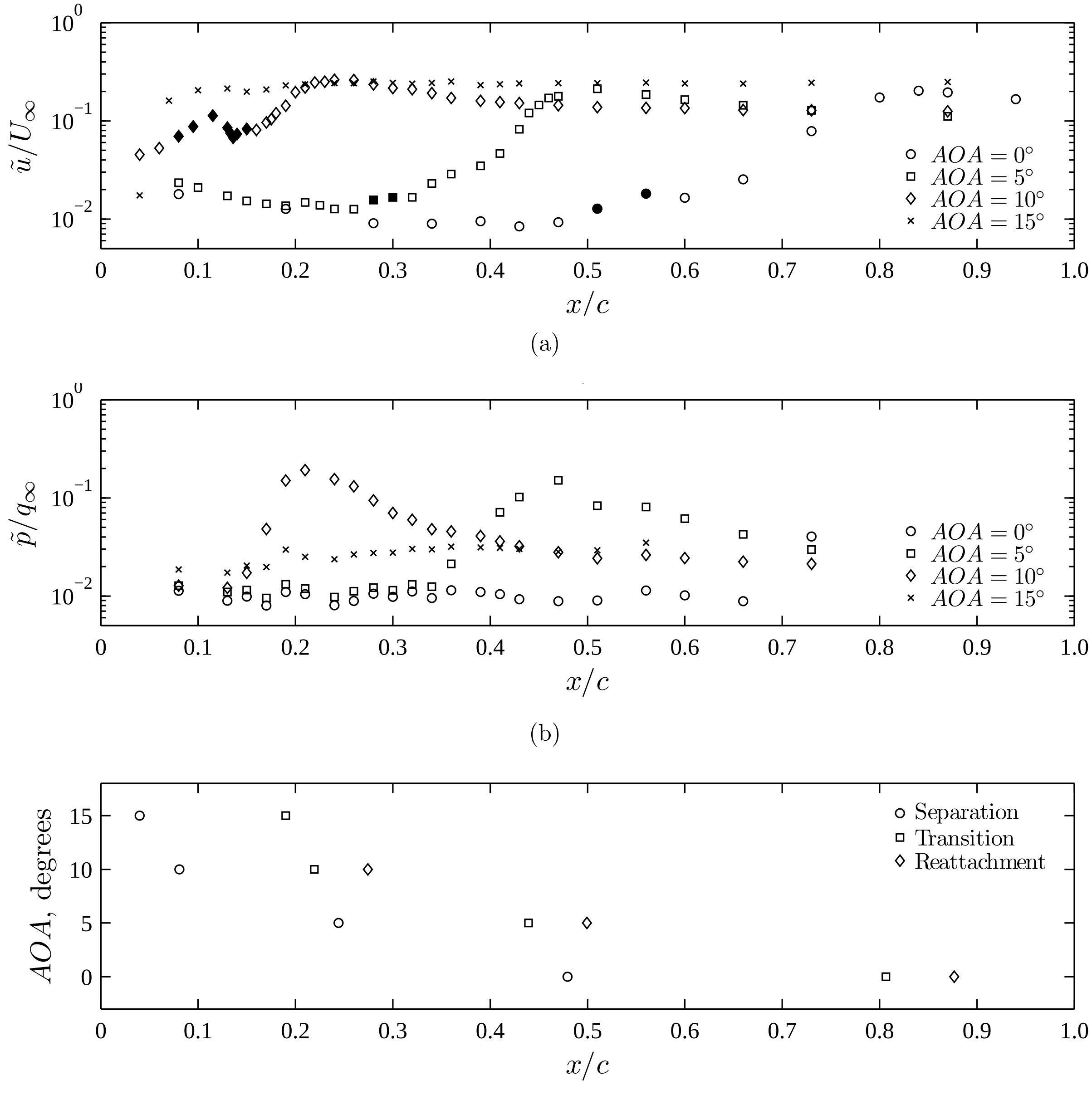

Figure 6.19: Streamwise development of (a) RMS streamwise velocity, at $y = \delta^*$, and (b) RMS surface pressure fluctuations, compared to (c) locations of mean separation, transition, and reattachment. Solid markers indicate measurements for which the hot-wire probe was believed to have changed the location of, or eliminated, separation.

gradually decays. This is similarly observed in turbulent boundary layers on flat plates as a result of the profile expanding into the free stream and absorbing lower turbulence intensity flow [139].

For angles of attack at which a separation bubble forms, the RMS surface pressure development in Fig. 6.19 exhibits qualitatively similar behavior to separation bubbles on blunt splitter plates, splitter plates with fences, forward facing steps, and backward facing steps [106–112]; in the laminar boundary layer upstream of separation, RMS surface pressure is relatively low, increases rapidly downstream of the separation point, reaches a maximum between the transition and reattachment points, and then decays in the attached turbulent boundary layer. The data presented by Mabey [106] for splitter plates with fences, forward facing steps, and backward facing steps show that the maximum value of RMS surface pressure depends on the specific geometry over which the separation bubble forms. The maximum value of $\tilde{p}/q_\infty$, measured to be approximately 0.2 in the present investigation, is higher than the values between 0.04 and 0.1 presented by Mabey [106]. For $AOA = 15°$, low amplitude fluctuations are observed, which increase gradually in the streamwise direction and show no distinctive features. The low amplitude of these fluctuations distinguishes the RMS pressure distribution from that expected for an attached turbulent boundary layer at higher Reynolds numbers, as have been measured by Paterson et al. [105]. These findings indicate that surface pressure measurements can be used to identify whether the airfoil is stalled and to provide reasonable estimates of the location and size of the separation bubble if one exists.

Comparing the RMS velocity and RMS surface pressure distributions in Fig. 6.19, it can be concluded that features that can be identified from RMS velocity measurements along the shear layer core can also be determined from less time consuming surface pressure measurements. Rapid growth of RMS velocity and surface pressure begins at approximately the same location at a given angle of attack, for $AOA = 0$, 5, and 10°. Furthermore, the RMS velocity and surface pressure begin to decay at approximately the same location at a given angle of attack, as observed for $AOA = 5$ and 10°. The RMS surface pressure decays more rapidly than the RMS velocity downstream of the transition location, which may be due to the rapidly increasing turbulent boundary layer thickness reducing the pressure fluctuation magnitudes observed at the surface. Similar behavior could not be verified for the $AOA = 0°$ case, because the transition location at this angle of attack was downstream of the microphone array. For the stalled condition ($AOA = 15°$), the increase in RMS velocity between the separation and transition locations is not reflected in the RMS surface pressure distribution. Furthermore, the RMS velocity decay downstream of the transition location is not seen in the RMS surface pressure distribution. These observations suggest that for a taller shear layer, as exists at $AOA = 15°$, the distance between the shear layer core and the surface causes differences between the trends of pressure fluctuations at the surface and velocity fluctuations at the shear layer core.

It should be noted that the solid markers in Fig. 6.19a identify those measurements for which the hot-wire probe is believed to have caused the mean separation location to shift upstream or to have forced transition without separation. Such an influence when the hot-wire probe is positioned near the separation point was inferred from mean surface pressure distributions in Chapter 5, and is further supported by comparing the location where RMS velocity and RMS surface pressure begin to increase in Figs. 6.19a and b. The $AOA = 10°$ data show a particularly strong influence of the hot-wire probe, consistent with the relatively significant effect of the hot-wire probe on separation, as suggested by Fig. 5.12c. The RMS velocity data show the onset of disturbance growth, followed by a sudden decay, before the smooth and continuous growth leading to turbulent transition. The earlier onset of growth observed in the velocity RMS plots explains the upstream movement of the transition location inferred from Fig. 5.12c.

Energy spectra of the fluctuating streamwise velocity and surface pressure are presented in Figs. 6.20-6.23. Upstream of the mean separation point, the velocity spectra are flat, indicating that the free-stream disturbances are of relatively low magnitude and that no appreciable disturbance growth has occurred in the attached boundary layer. Just downstream of the separation point, the energy content grows and extends to a broader range of frequencies around a central value. The central instability frequency increases with increasing angle of attack for angles at which a separation bubble forms. Harmonics of the central frequency are seen to develop upstream of the transition location. Harmonics of the fundamental frequency may be observed as a result of the contribution of vertical velocity fluctuations to the measurements of streamwise velocity fluctuations and static surface pressure fluctuations. Vertical velocity fluctuations are expected to have a similar spectral distribution to those of streamwise velocity and static surface pressure, however, these three signals will be out of phase. As a result, if two of these quantities contribute to the response of one sensor, the resulting energy spectrum may contain lower energy value harmonics of the fundamental frequency. The magnitude of the spectral peak decreases significantly between the transition point and the subsequent measurement station, which for $AOA = 10°$ is over a distance of $0.01c$. This change from a dominant frequency in the spectrum to very broadband energy content indicates that the final breakdown to turbulent flow has occurred over a very short length, as is common in separated shear layer transition [53]. For the post-stall angle of attack, the location of this abrupt change from frequency centered energy content to wide spread energy content was used to identify the transition location. For each of the angles of attack, well downstream of the transition point a typical broadband turbulent energy spectrum is observed (see, e.g., Ref. [139]).

Energy spectra of the fluctuating surface pressure show the same trends as for the

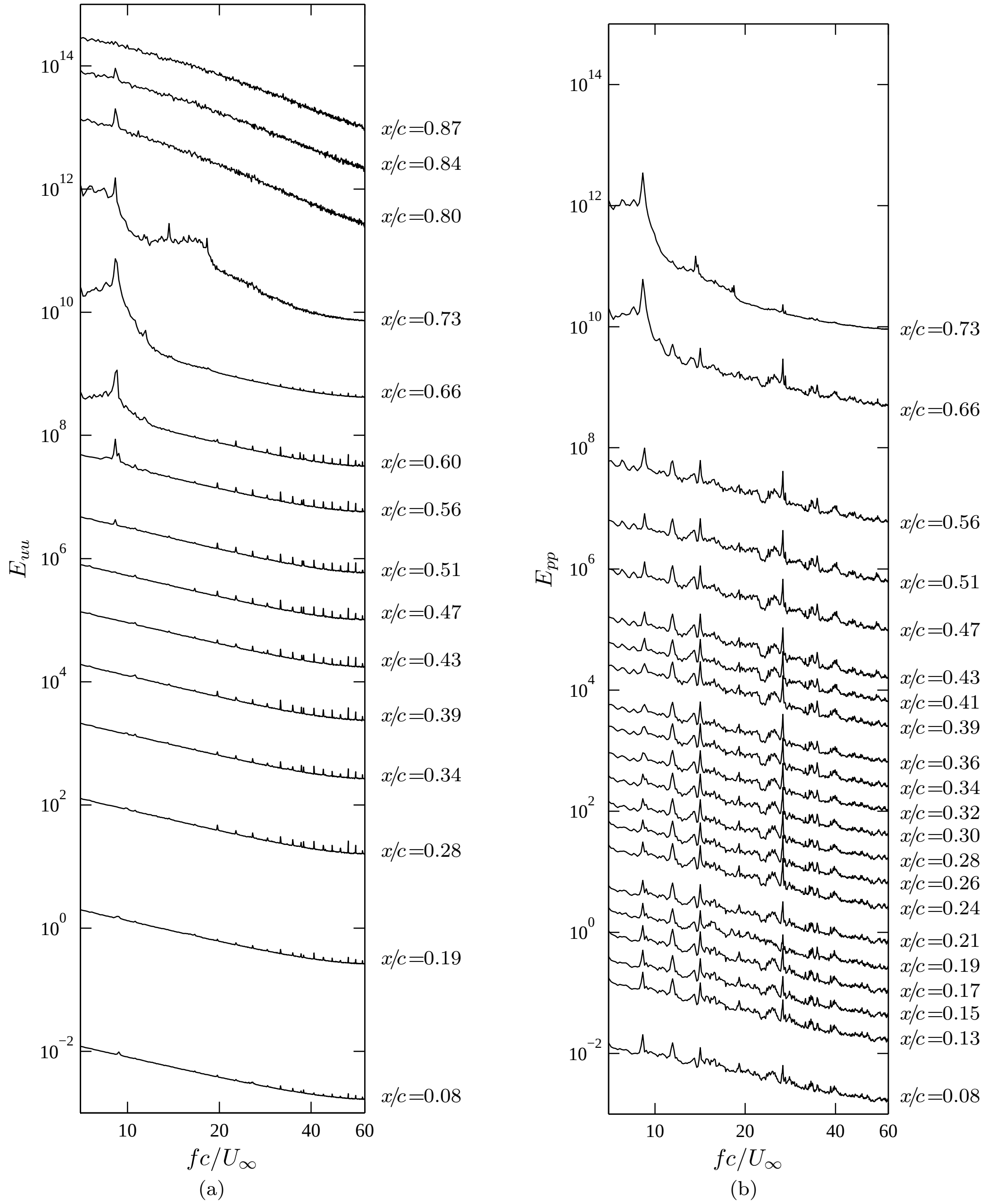

(a) (b)

Figure 6.20: Spectra of (a) streamwise velocity fluctuations and (b) surface pressure fluctuations for $AOA = 0°$. For clarity, spectra are normalized by the total energy content and scaled by a factor proportional to $10^{x/c}$.

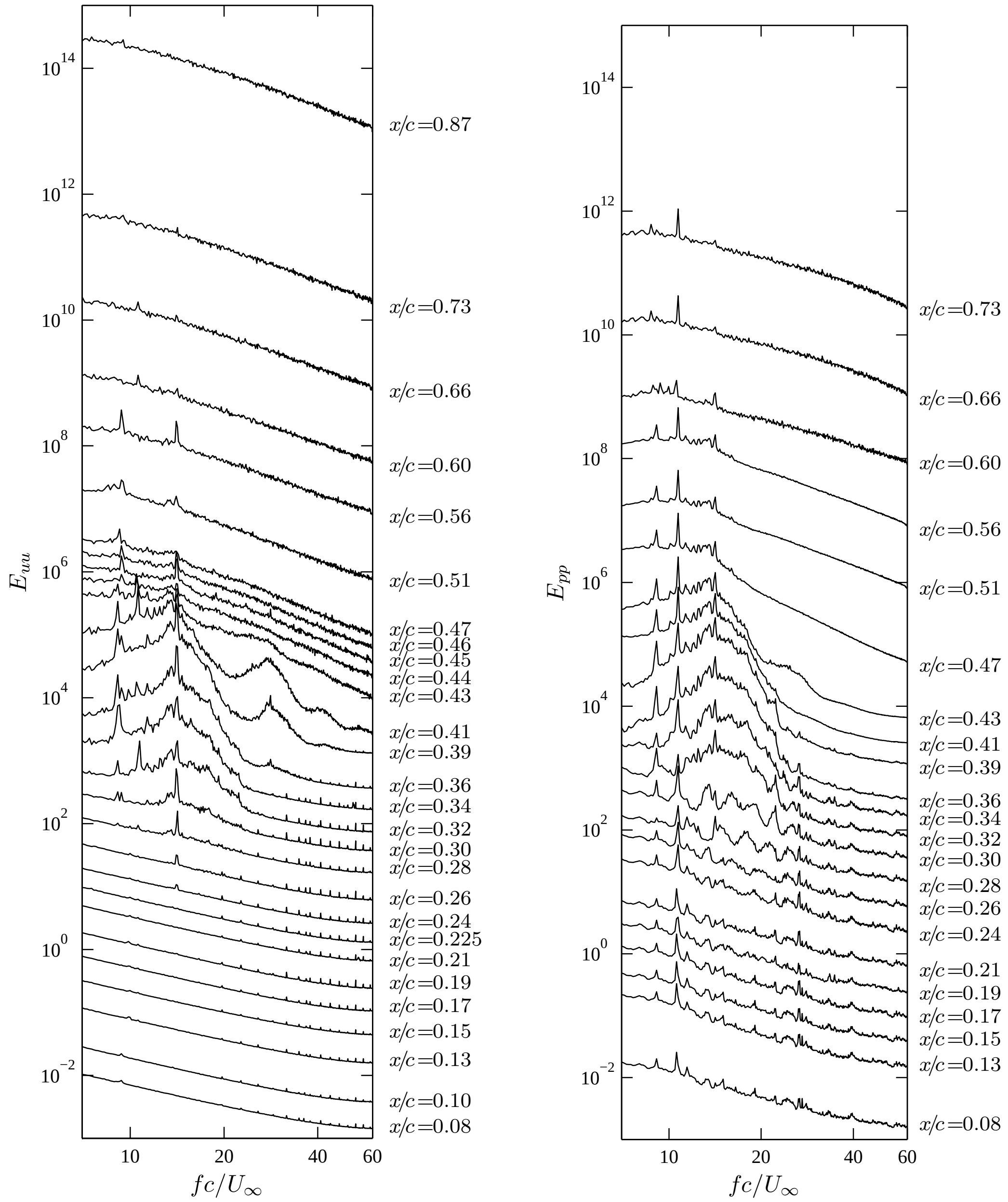

(a) (b)

Figure 6.21: Spectra of (a) streamwise velocity fluctuations and (b) surface pressure fluctuations for $AOA = 5°$. For clarity, spectra are normalized by the total energy content and scaled by a factor proportional to $10^{x/c}$.

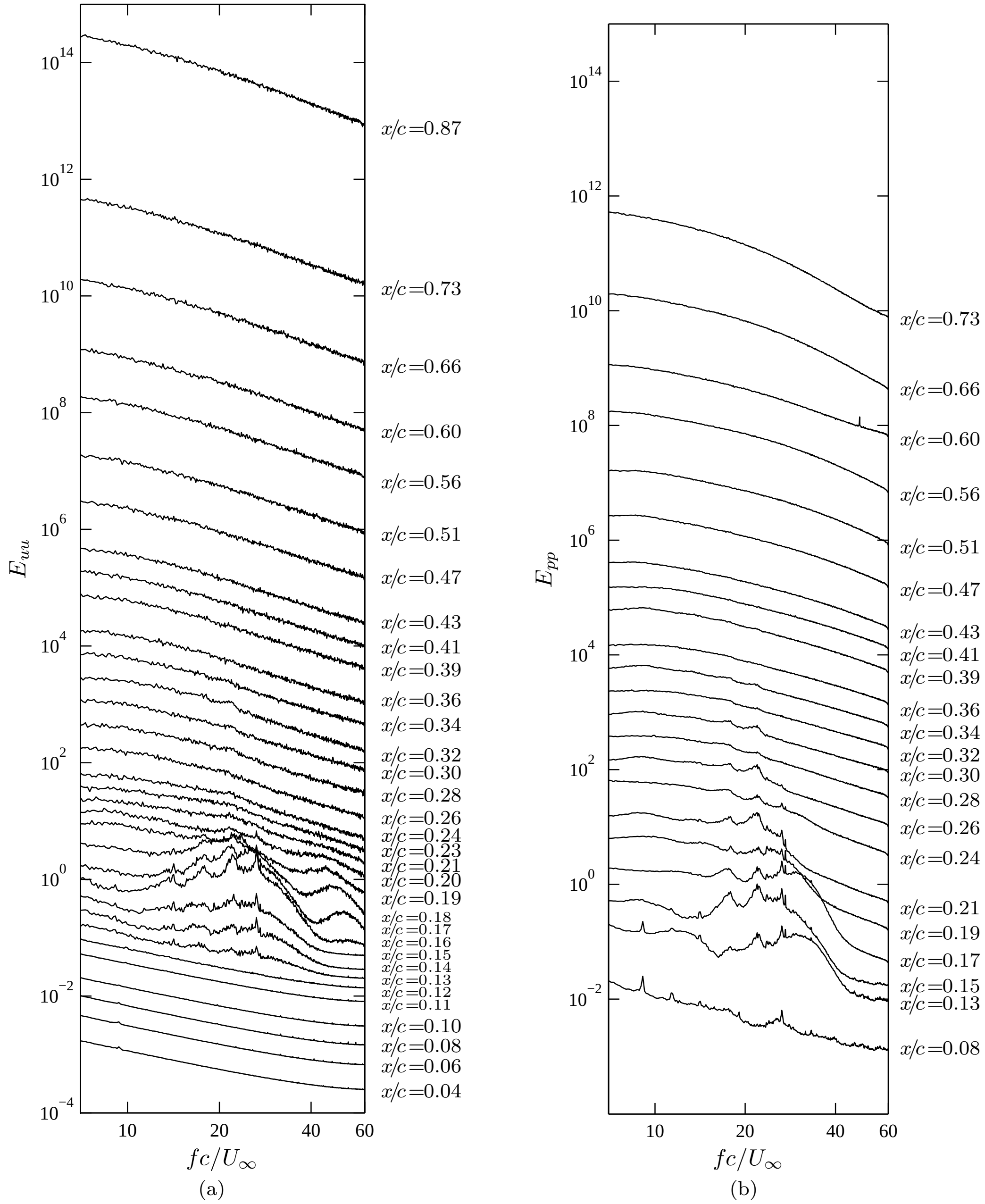

(a) (b)

Figure 6.22: Spectra of (a) streamwise velocity fluctuations and (b) surface pressure fluctuations for $AOA = 10^\circ$. For clarity, spectra are normalized by the total energy content and scaled by a factor proportional to $10^{x/c}$.

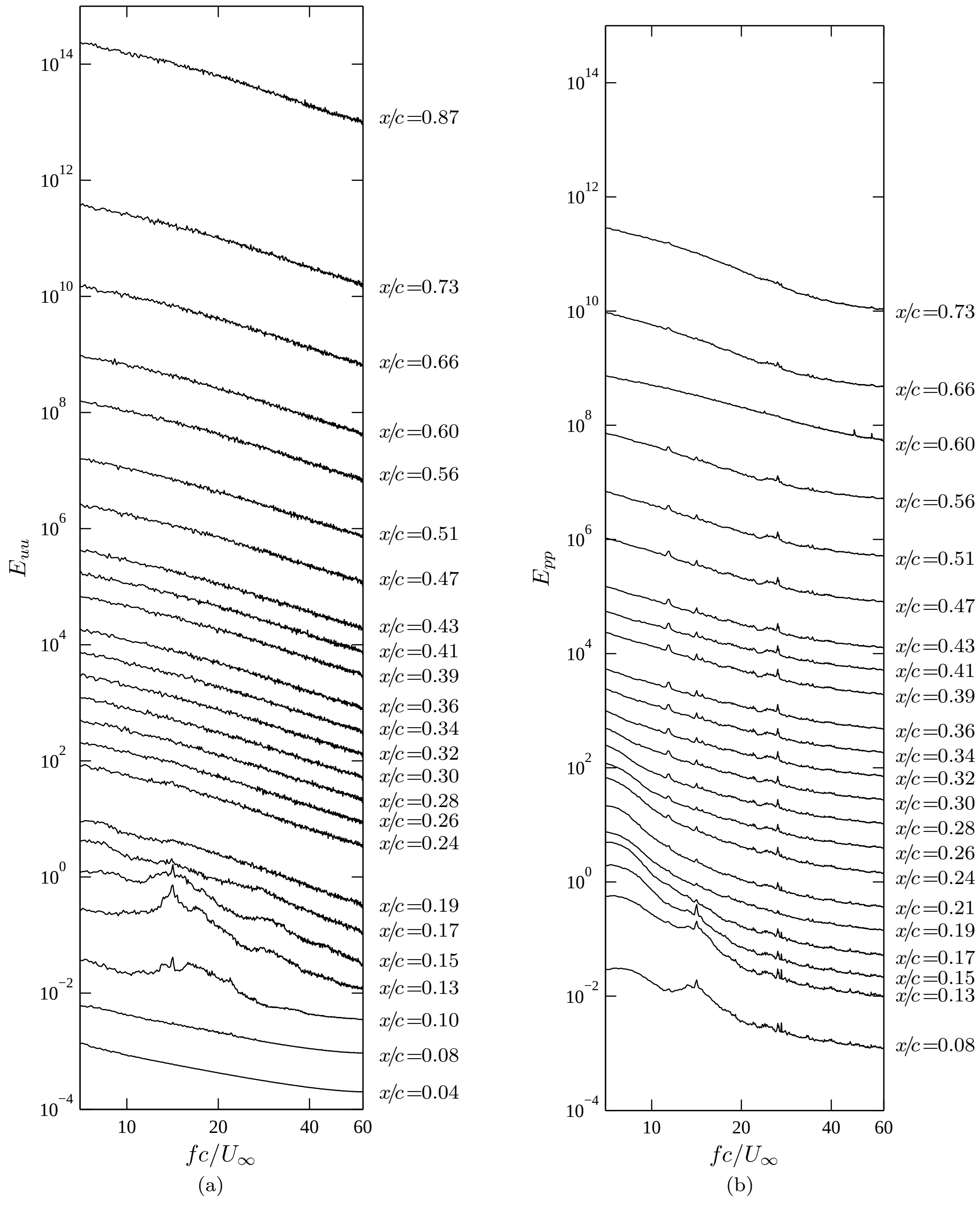

Figure 6.23: Spectra of (a) streamwise velocity fluctuations and (b) surface pressure fluctuations for $AOA = 15^\circ$. For clarity, spectra are normalized by the total energy content and scaled by a factor proportional to $10^{x/c}$.

velocity fluctuations. Locations where dominant disturbance growth begins and transition occurs agree to within the spatial resolution of the measurements. Energy spectra of surface pressure fluctuations in the laminar boundary layer contain significant signal noise related to the very low magnitude of pressure fluctuations at the surface in this region. The contribution of signal noise is less significant in the separation bubble, where higher energy fluctuations develop through the transition process. It should be noted that the background disturbances observed in laminar boundary layer measurements had very low magnitude and were not centered at any specific frequency. Therefore, if acoustic noise has contributed to this signal, it is unlikely to have influenced the dominant instability frequency controlling separation bubble transition.

Multiple narrow spectral peaks are observed within the band of unstable frequencies in Figs. 6.20-6.23, particularly in the energy spectra for $AOA = 10°$ (Fig. 6.22). Some studies on transitional separation bubbles have attributed lower frequency secondary peaks to bubble flapping [24]. In the present investigation, the cause of the distinct peaks within the unstable band of frequencies was not confirmed. Flow visualization experiments employing high frame rate imaging may reveal the physical reason for these peaks, and are recommended as future work.

Many features of flow development over the airfoil were identified through measurements with embedded microphones. Based on the measurements in this section, a few areas for improvement can be noted for consideration in future experiments. As mentioned in relation to Fig. 6.19, the microphone array does not extend sufficiently far upstream to fully resolve the details of disturbance growth and transition for $AOA = 15°$, nor does it extend sufficiently far downstream to resolve these details at $AOA = 0°$. Furthermore, greater microphone resolution would enhance the capabilities of this system for smaller separation bubbles, such as that at $AOA = 10°$. At certain angles of attack, higher resolution would improve the accuracy of disturbance growth rate and instability wave length measurements. The benefits of a larger microphone array with higher spatial resolution are illustrated by the greater details available from the velocity spectra in Figs. 6.20-6.23, than from the corresponding pressure spectra.

6.3 Instability of the Laminar Separated Shear Layers

Linear stability analysis was performed on the measured separated shear layer profiles presented in Section 6.2. The results are compared to measured growth rates, phase speeds, and streamwise velocity fluctuation profiles in this section to gain insight into flow development in transitioning separated shear layers. Disturbance growth rate estimates based on hot-wire and surface pressure measurements are compared to evaluate the capabilities of an embedded surface pressure sensor array for measurements of disturbance development. Such measurements are significantly less time consuming than hot-wire measurements, and would therefore be valuable in parametric studies.

In Fig. 6.19, disturbance growth is evident in the laminar portion of the separation bubble in both the RMS velocity and RMS surface pressure plots. These data are presented on a logarithmic scale in order to emphasize the agreement and disagreement from exponential disturbance growth, assumed by LST for component disturbances. For each angle of attack, a region of relatively constant growth rate can be identified. However, even in these regions the trend is not perfectly linear. This deviation does not necessarily invalidate the linear growth assumption, as it may be an effect of the combined disturbance components in the RMS velocity measurement. Non-parallel flow effects may also contribute to the discrepancy. LST is based on the assumption that the mean vertical velocity is negligible, implying that the flow is parallel, and that the growth rate spectrum does not vary in the streamwise direction. However, as is clearly seen in Figs. 6.11-6.14, the displacement thickness changes significantly in the separated flow region, indicating that the flow is not parallel. Linear stability theory may still provide a reasonable model for disturbance growth at each individual measurement location, assuming quasi-parallel flow; however, the frequency band of amplified disturbances or the growth rate magnitudes may change in the streamwise direction. Thus, even if the RMS velocity and pressure plots do not show perfectly exponential growth, this does not mean that non-linear terms are influencing disturbance development. Near the transition location, significant deviation from exponential disturbance growth is observed. This is likely a result of non-linear interactions, which dominate the transition process over a very short section of the chord and which have been identified in numerical simulations of separation bubble development [25, 54].

In this section, linear stability predictions are presented for the velocity profiles characterized in Table 6.1. The profiles for each angle of attack were selected from profiles at three to five x/c locations in the linear growth portion of the laminar separated shear

Table 6.1: Characteristic parameters of profiles used in linear stability calculations.

AOA	x/c	γ	δ^*	θ	H	U_e/U_∞	Re_{δ^*}
0°	0.73	31.7°	0.0173	0.0027	6.4	1.15	2.0×10^3
5°	0.34	41.5°	0.0073	0.0015	4.9	1.46	1.0×10^3
10°	0.18	23.5°	0.0099	0.0013	7.9	1.79	1.7×10^3
15°	0.10	13.5°	0.0212	0.0017	12.4	1.25	2.8×10^3

layer. Results for one profile at each angle of attack are presented. However, the analysis was also performed for the other profiles in the laminar separated shear layer, and the results agreed to within the expected variability due to data scatter, identified in Chapter 4. In Table 6.1, the shear angle, γ, is the mean velocity profile angle at the inflection point, i.e., $\gamma = \arctan(dy/dU)$ at the profile inflection point. For these data, the shear angle decreases with increasing shape factor. This is interesting because the other parameters in Table 6.1 that characterize the profiles show no clear trend connecting values for conditions with and without shear layer reattachment. Since only four profiles are considered, no conclusion can be drawn about the general nature of this trend.

The velocity profiles on which linear stability calculations were performed, were first processed to compensate for mean rectification error in the reverse flow region and to remove extraneous data points where the flow speed was nearly zero. The processed velocity profiles are presented in Fig. 6.24 with the Dini et al. [79] fit (Table 4.2) computed for each profile. The Dini et al. [79] type fit was selected for this analysis over the Falkner-Skan

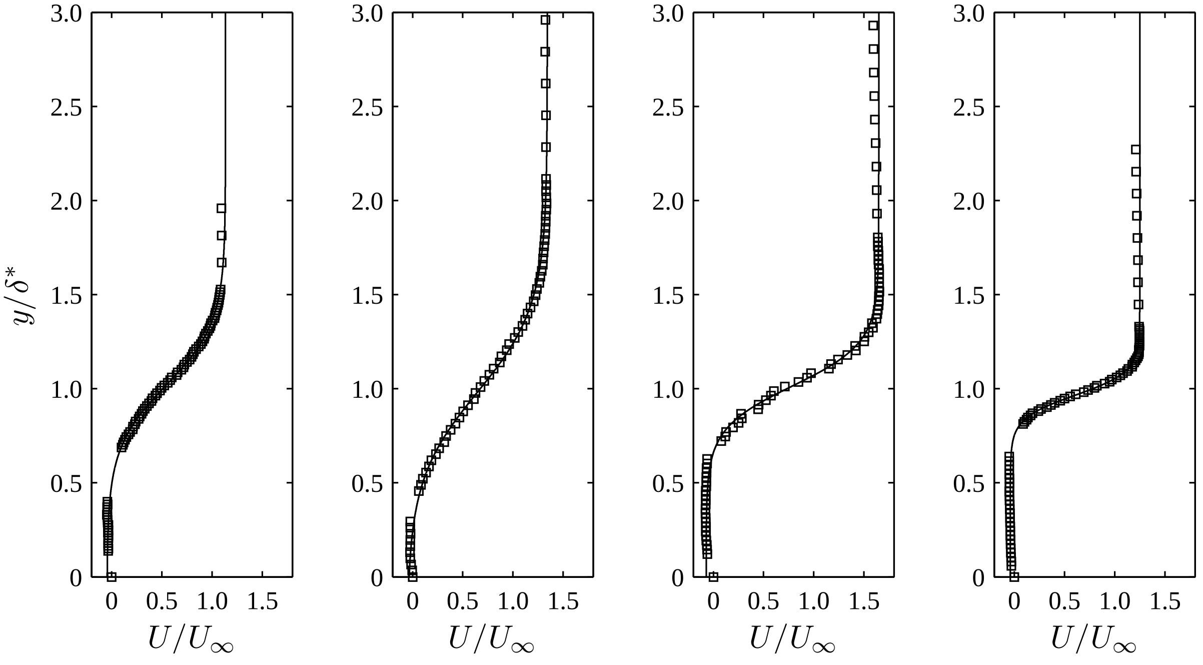

(a) $AOA=0°$ (b) $AOA=5°$ (c) $AOA=10°$ (d) $AOA=15°$

Figure 6.24: Measured velocity profiles (markers) and corresponding Dini et al. [79] fits (solid line) used in linear stability calculations. See Table 6.1 for relevant profile parameters.

and Dovgal et al. [34] fits also recommended in Chapter 4, because this fit has the fewest parameters and does not depend on measured profile curvature in the reverse flow region. Furthermore, this fit showed the lowest variability due to data scatter based on the results in Table 4.5.

Growth rate spectra computed from both the Rayleigh and Orr-Sommerfeld equations, for the profiles in Fig. 6.24, are compared to measured disturbance growth rates in Fig. 6.25. Measured growth rates were obtained by calculating the spatial growth exponent from RMS values of band-pass filtered hot-wire measurements at $y = \delta^*$ and from RMS surface pressure measurements. For the stalled case, growth rates could only be determined from the hot-wire measurements because the microphone array did not extend far enough upstream or have sufficient spatial resolution to provide reasonable estimates of the growth rate. For each angle of attack, the computed spectra predict spatial amplification over a band of frequencies, as was observed to occur from the energy spectra in Figs. 6.20-6.23. Disturbance amplification is predicted over a wider range of frequencies than is observed in Figs. 6.20-6.23, because small growth rates at very high and very low frequencies do not result in detectable amplification in the laminar separated shear layer. In Fig. 6.25, the maximum disturbance growth rate increases with increasing angle of attack for angles at which a separation bubble forms. The higher spatial growth rates at higher angles of attack explains why the separation bubble length decreases with increasing angle of attack, as noted in relation to Fig. 6.10.

The measured and computed growth rate spectra in Fig. 6.25 agree to within the combined uncertainty in growth rate measurements and in the LST predictions due to the choice of curve fit and to mean profile data scatter (Chapter 4). The frequency of maximum disturbance growth rate is accurately predicted, and agrees with the central frequencies observed in the energy spectra in Figs. 6.20-6.23. The frequency band of amplified disturbances can be more easily identified from the measured growth rates than from the energy spectra of Figs. 6.20-6.23.

The effect of viscosity on the growth rate predictions from LST in Fig. 6.25 is similar to that observed in Section 4.4; specifically, the spectrum retains its general shape and dominant frequency but viscosity has a damping effect on the disturbance growth rate. Figure 6.26 shows the percentage difference in maximum growth rate predictions between the viscous and inviscid solutions, computed from Dini et al. [79] fits to profiles measured in this study and previous experimental studies on transition in separated shear layers. The data have a strong dependence on the displacement thickness Reynolds number. This dependence is indicated by the solid line curve fit, which quantifies the rate at which the error between viscous and inviscid LST predictions for measured separated shear layers on low Reynolds number airfoils decreases with increasing Reynolds number. The fit provides a method of estimating the effect of viscosity or adjusting inviscid growth rate calculations.

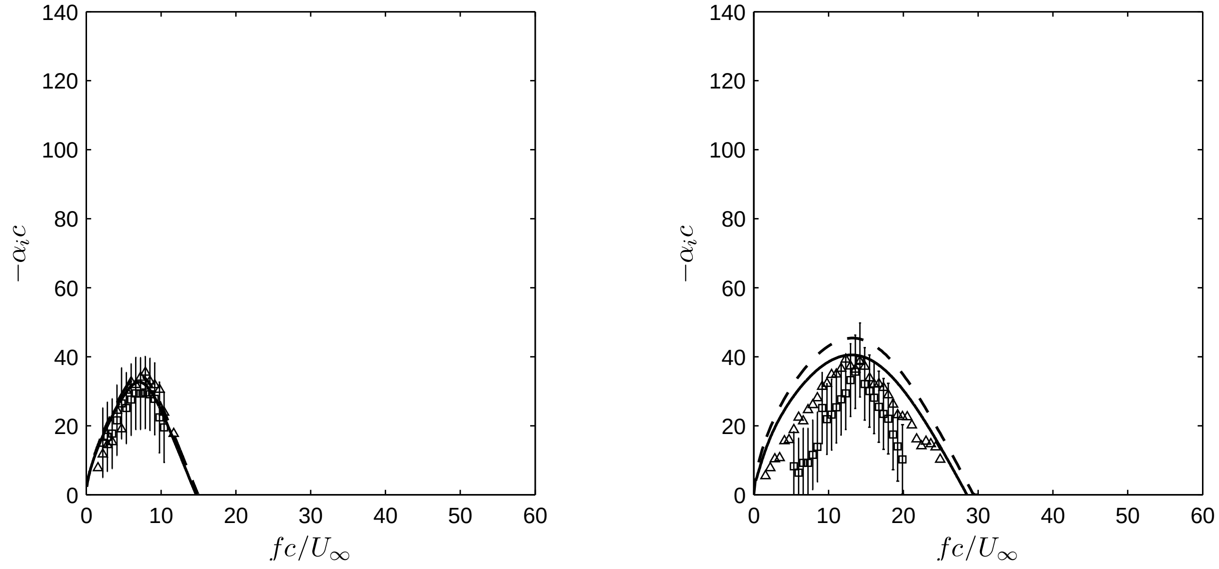

(a) $AOA = 0°$ (b) $AOA = 5°$

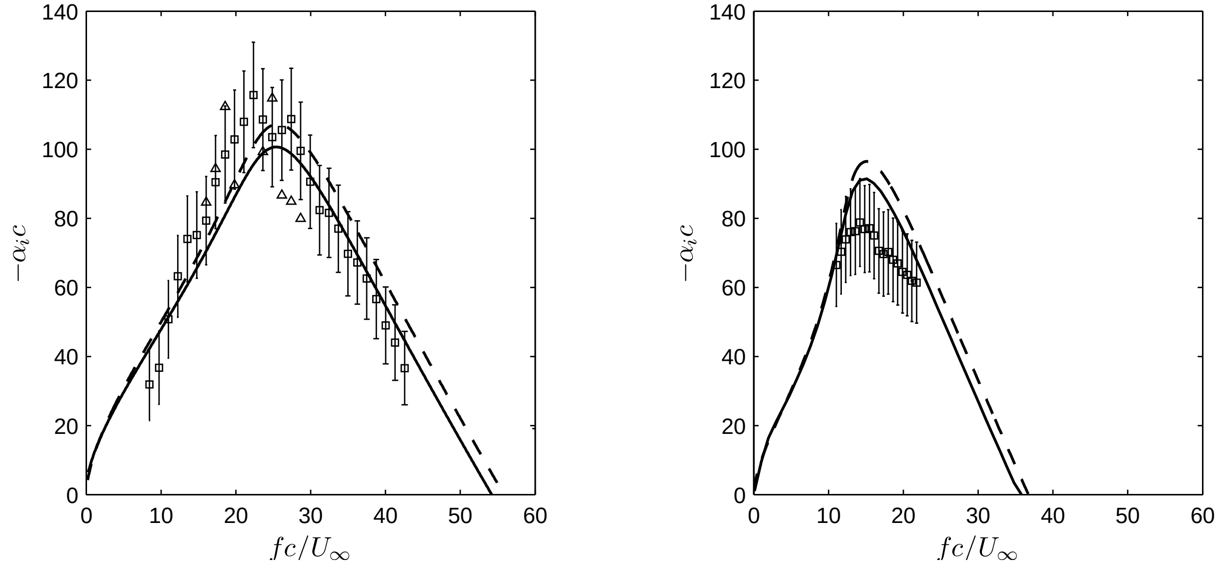

(c) $AOA = 10°$ (d) $AOA = 15°$

Figure 6.25: Growth rate spectra from hot-wire measurements (□ markers) and surface pressure measurements (△ markers) compared to predictions of the Rayleigh equation (dashed line) and the Orr-Sommerfeld equation (solid line). Uncertainty bars are shown for hot-wire data only; the estimated uncertainty in $\alpha_i c$ based on surface pressure measurements is quantified in Appendix A.

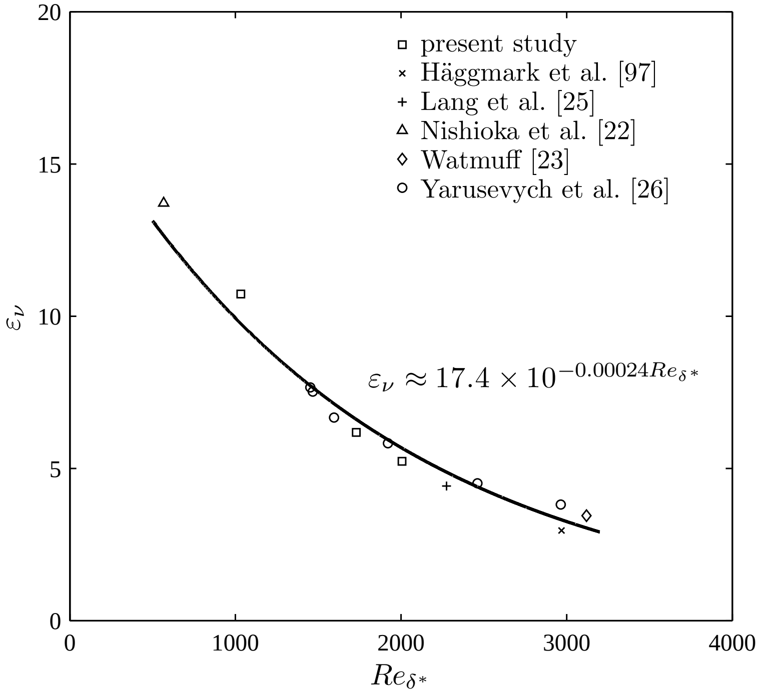

Figure 6.26: Percentage difference in the maximum disturbance growth rate prediction between viscous and inviscid linear stability analyses from several separated shear layer experiments.

The difference between growth rate predictions from viscous and inviscid analysis for these experiments does not exceed 15%, which is less than the variability due to the choice of curve fit (Chapter 4) and the uncertainty in the measured growth rate (Appendix A). It is concluded that, for this type of flow, the inviscid instability approximation does not limit the value of LST predictions of disturbance amplification rates based on measured mean velocity profiles.

Computed and measured real wave number spectra are presented in Fig. 6.27. Wave number was determined from the phase speed of spatial instability waves, measured as the ratio of the streamwise distance between successive microphones and the time delay between the measured pressure fluctuation signals at each frequency. The time delay was estimated from the cross-correlation sequence of the band-pass filtered microphone data. As noted for the growth rate spectra, measurements can only be obtained over the band of frequencies for which pressure fluctuations are of sufficient magnitude relative

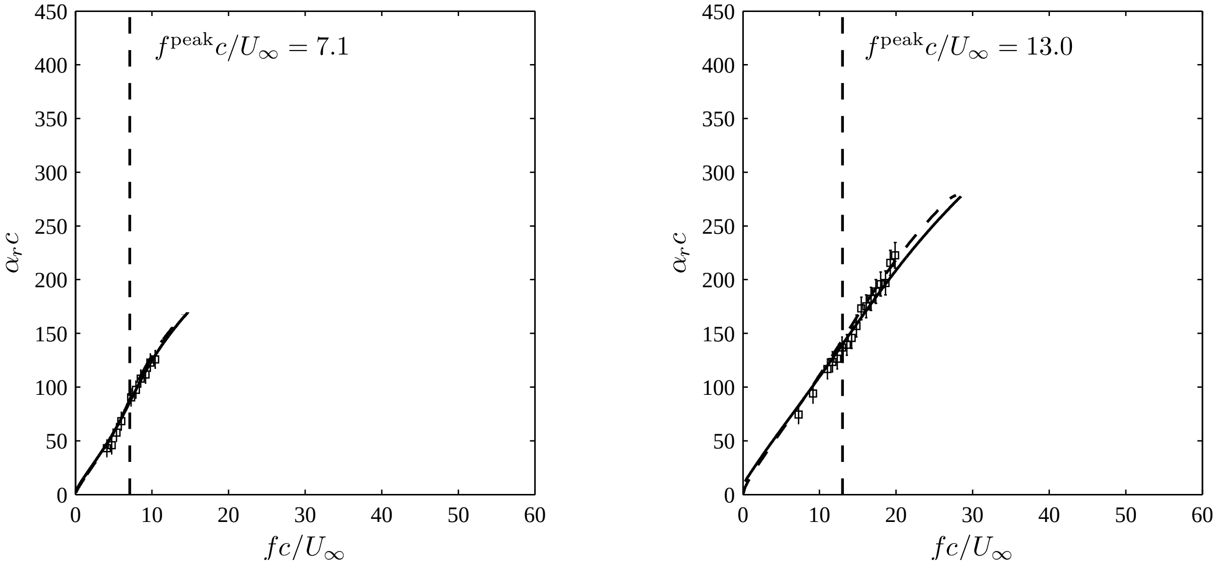

(a) $AOA = 0°$ (b) $AOA = 5°$

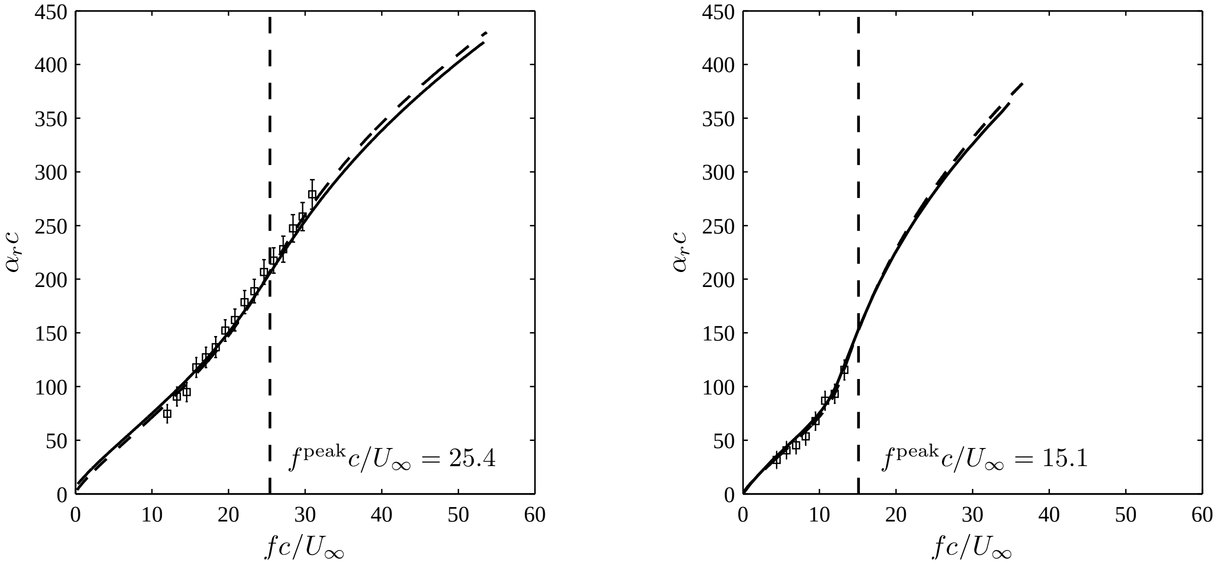

(c) $AOA = 10°$ (d) $AOA = 15°$

Figure 6.27: Wave number spectra measured (markers) and computed from the Rayleigh equation (dashed curve) and the Orr-Sommerfeld equation (solid curve). Dashed vertical lines identify the computed frequency of maximum disturbance growth rate from the Orr-Sommerfeld equation solution.

to the background disturbance environment. Furthermore, for the $AOA = 15°$ case, the spatial resolution of the microphone array is not sufficient to estimate the wave number of disturbances near or above the frequency of maximum disturbance amplification. As a result, only the longer wavelength disturbances at lower frequencies could be measured for this case. The measurements agree with the computed wave number spectra to within the combined uncertainty in the measurements and the variability due to data scatter and analysis approach in linear stability calculations. The wave number spectra show smaller differences between the Rayleigh and Orr-Sommerfeld equation solutions than were observed in the growth rate spectra. Thus, using the inviscid approximation when the wave number spectrum is of interest should have only a minor effect on the predictions.

The results in Figs. 6.25 and 6.27 demonstrate that surface pressure measurements can be used to obtain estimates of disturbance growth rate and wave number for conditions at which a separation bubble forms on the airfoil surface. Because the disturbance wavelength and microphone spacing were of the same order of magnitude, adjustments had to be made to compensate for wave number aliasing in some of the measurements. Greater spatial resolution of the microphone array could eliminate this source of error and enable measurements over a wider range of conditions. It should also be noted that, for the measurements presented in Fig. 6.27, the time delay between measurement locations was on the order of one millisecond. In light of this, a high measurement sample rate of 40 kHz was used to reduce discretization error in phase speed estimates, which would have increased the uncertainty in wave number measurements. The difficulties associated with high frequency and small wavelength disturbance measurements mentioned here should be considered in the design of embedded sensor arrays for aerodynamic applications or experimental measurements.

Table 6.2 provides a summary of the Orr-Sommerfeld equation solutions, measured convection speeds, as well as the separation, transition, and reattachment locations for each angle of attack. These data reiterate the trends noted previously: for angles of attack at which a separation bubble forms, the separation bubble decreases in length as the angle of attack increases due to higher disturbance growth rates in the separated shear layer. This change is accompanied by an increase of the phase speed and a reduction of the wavelength of disturbances.

The surface pressure fluctuation convection speeds in Table 6.2 were measured in the same way as phase speeds, without band-pass filtering the surface pressure data obtained from the embedded microphones. The convection speed represents the average speed at which pressure fluctuations are convected downstream in the separated shear layer. This quantity is different from phase speed, in that it describes the speed of the total pressure fluctuation signal, not the speed of disturbances at a particular frequency. If the pressure fluctuations in the separated shear layer can be attributed to linear disturbance growth, the

Table 6.2: Summary of flow development in the separation bubble.

	measured				Orr-Sommerfeld equation solution				
AOA	x_S/c	x_T/c	x_R/c	U_c/U_∞	$f^{\text{peak}}c/U_\infty$	$-\alpha_i^{\text{peak}}c$	$\alpha_r^{\text{peak}}c$	λ/c	c_r/U_∞
0°	0.48	0.81	0.88	0.42	7.1	32.7	85.9	0.073	0.45
5°	0.24	0.44	0.50	0.53	13.0	40.5	140.2	0.045	0.54
10°	0.08	0.22	0.27	0.61	25.4	100.7	205.1	0.031	0.63
15°	0.04	0.19	–	–	15.1	91.6	153.5	0.041	0.46

phase speed at the frequency of maximum disturbance amplification should be similar to the convection speed. This is expected because the phase speed does not vary significantly over the band of measurable unstable frequencies and because pressure fluctuations near the dominant instability frequency will provide the most significant contribution to the overall pressure fluctuation field. The computed phase speeds at the frequency of maximum disturbance growth rate are graphically compared to the measured convection speeds in Fig. 6.28. The computed phase speed accurately predicts the measured convection speed for angles at which a separation bubble forms, further supporting the claim of Gerakopulos [35] that the measured convection speeds in separation bubbles over low Reynolds number airfoils are associated with growing disturbance wave packets propagating through the shear layer. Note that the convection speed was not measured for $AOA = 15°$, due to limitations on the spatial resolution of surface pressure measurements.

Convection and phase speeds obtained in the present investigation and those reported in previous experimental studies on flow development over airfoils at low Reynolds numbers are presented in Fig. 6.29. In this plot, phase speeds were computed from LST, whereas convection speeds were measured experimentally. In Fig. 6.29a, the free-stream velocity is used to non-dimensionalize the data, whereas in Fig. 6.29b, scaling is in terms of the edge velocity. For clarity, uncertainty bands are not presented in Fig. 6.29, but are of similar magnitude to those in Fig. 6.28. Consistent with the data in Fig. 6.28, Fig. 6.29 indicates that when scaling is in terms of free-stream velocity, the convection speed increases with angle of attack for angles at which a separation bubble forms. Normalizing by the edge velocity reduces the range of non-dimensional phase speeds and convection speeds to between approximately 0.3 and 0.5. Yarusevych et al. [136] found a narrower range of values, between approximately 0.45 and 0.5 from a smaller data set. They reasoned that this range of speeds corresponds to the average of the edge velocity and the maximum reverse flow speed, because that is the approximate speed of the fluctuation vorticity core at the mean velocity profile inflection point. The wider range of values observed in Fig. 6.29

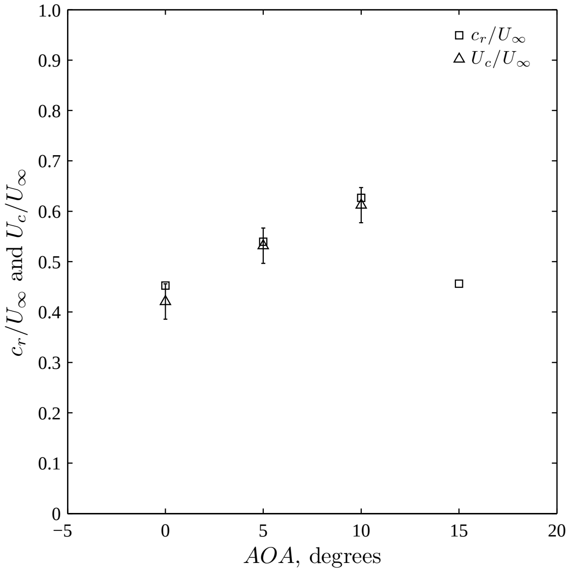

Figure 6.28: Comparison of measured convection speeds and computed phase speeds at the dominant frequencies of disturbance amplification.

may partially be due to measurement uncertainty, which is as high as ±0.05 for some of the data points. Another factor may be the variation in phase speed at the dominant instability frequency due to differences in the separated shear layer velocity profile. By applying LST to analytical separated shear layer profiles, Dovgal et al. [34] computed phase speeds at the frequency of maximum disturbance growth rate between approximately 0.3 and 0.5. These values were obtained by analyzing profiles with different maximum reverse flow speeds, distances of the inflection point from the wall, and Reynolds numbers based on shear layer thickness. The phase speeds they computed are between the value of approximately 0.5, predicted from inviscid analysis of a free shear layer which approaches zero velocity in one direction [140], and values of less than 0.3 predicted for the Blasius boundary layer profile for $Re_{\delta^*} \gtrsim 3 \times 10^3$ (Ref. [63]). The results presented here indicate that the convection speed of disturbances in the separated shear layer over a low Reynolds number airfoil are dependent on more factors than just the edge velocity and maximum reverse flow speed. The similar range of values in Fig. 6.29 compared to the phase speed range in predictions of Dovgal et al. [34] suggest that the convection speed of disturbances also have a strong dependence on the velocity profile Reynolds number and the distance of the shear layer core from the airfoil surface.

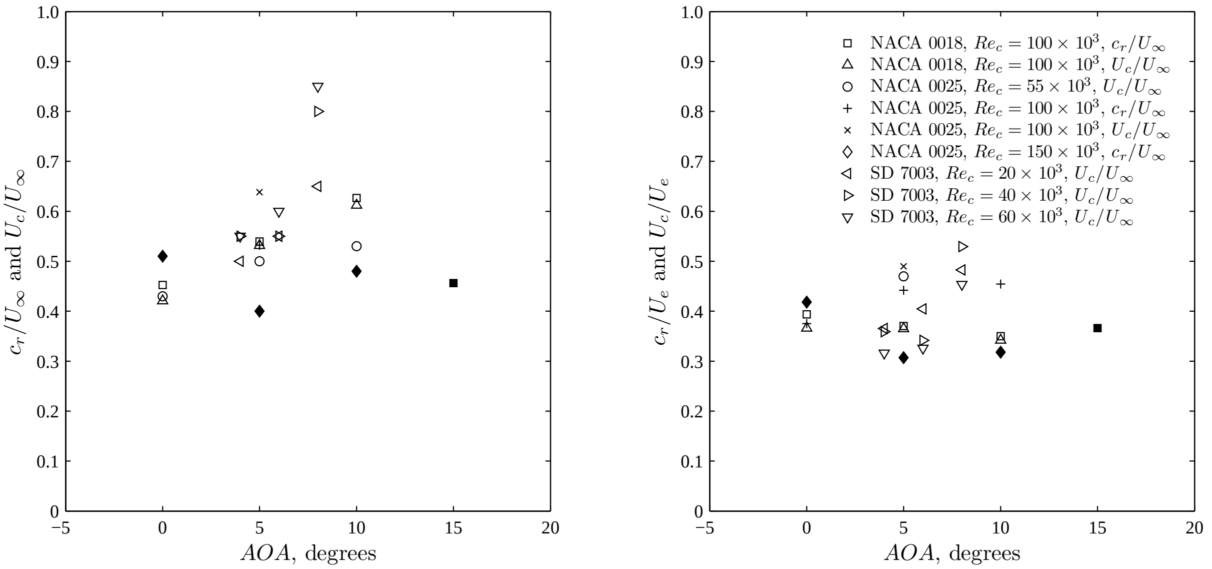

(a) (b)

Figure 6.29: Comparison of convection speed and phase speed measurements from various studies. Filled markers (i.e., the ♦ and ■ markers) indicate conditions at which separation occurred without reattachment. All other markers are for conditions at which a separation bubble formed. Data for the NACA 0018 airfoil were measured in the present study, phase speeds for the NACA 0025 airfoil are from Yarusevych et al. [26], convection speeds for the NACA 0025 airfoil are from Yarusevych et al. [136], and data for the SD 7003 airfoil are from Burgmann & Schröder [37].

Streamwise velocity fluctuation amplitude profiles are presented in Figs. 6.30-6.33. The measured profiles are of RMS velocity at particular frequencies, and were computed after band-pass filtering velocity data on intervals of $fc/U_\infty \pm 0.6$. For each angle of attack, four profiles are presented, which span the range of unstable disturbances that could be resolved. The results are normalized by the maximum RMS velocity at the frequency of maximum disturbance growth rate. Measurements are compared to computed streamwise velocity fluctuation profiles from both the Rayleigh and Orr-Sommerfeld equations.

The measured RMS streamwise velocity fluctuation amplitude profiles in Figs. 6.30-6.33 show commonly observed trends for velocity fluctuation amplitude profiles in laminar separated shear layers [22, 25] and those predicted from LST [34]. Specifically, the profiles have three maxima for $y/\delta^* \gtrsim 0.5$, the largest coinciding with the mean velocity profile

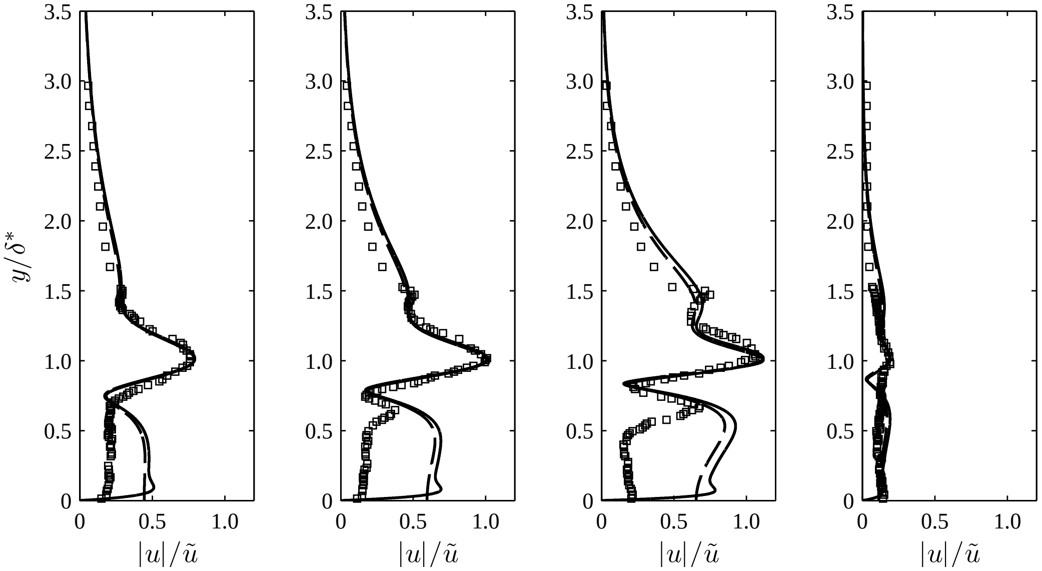

(a) $fc/U_\infty = 5.4$ (b) $fc/U_\infty = 7.3$ (c) $fc/U_\infty = 9.2$ (d) $fc/U_\infty = 10.4$

Figure 6.30: Streamwise velocity fluctuation amplitude profiles measured (markers) and computed from the Rayleigh (dashed line) and Orr-Sommerfeld (solid line) equations for $AOA = 0°$.

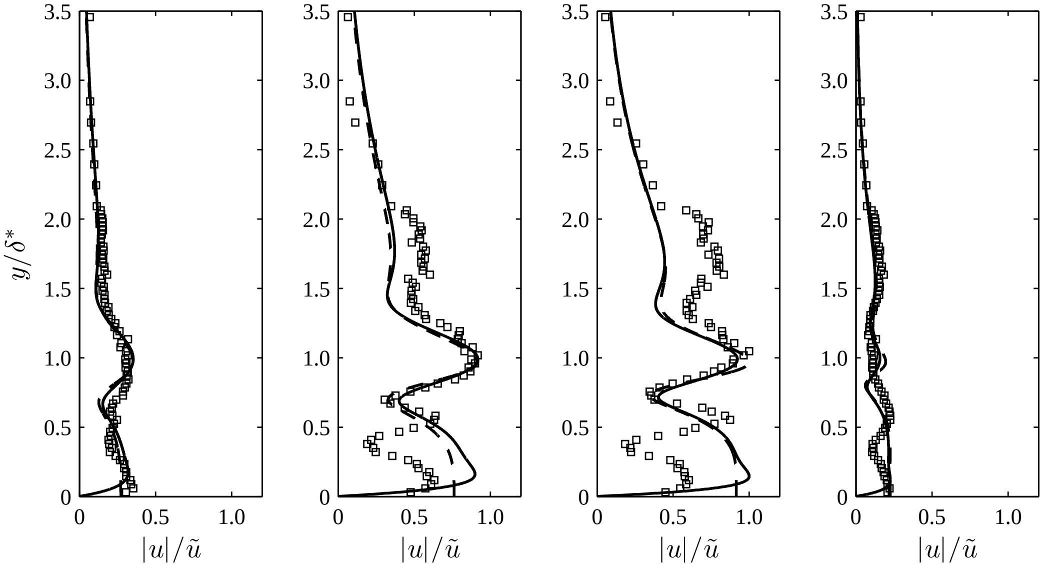

(a) $fc/U_\infty = 8.5$ (b) $fc/U_\infty = 10.4$ (c) $fc/U_\infty = 12.9$ (d) $fc/U_\infty = 19.3$

Figure 6.31: Streamwise velocity fluctuation amplitude profiles measured (markers) and computed from the Rayleigh (dashed line) and Orr-Sommerfeld (solid line) equations for $AOA = 5°$.

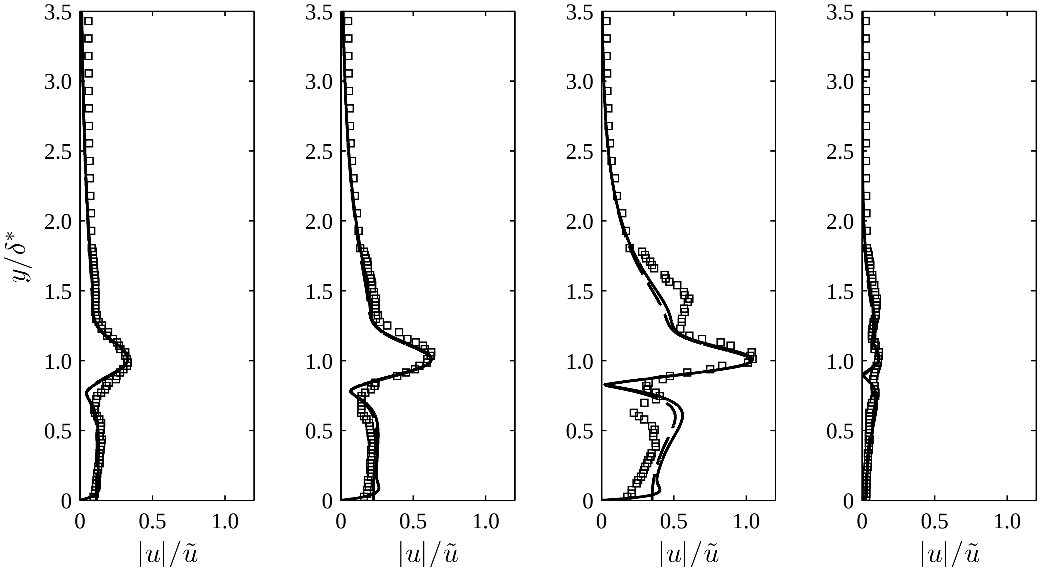

(a) $fc/U_\infty = 14.8$ (b) $fc/U_\infty = 18.6$ (c) $fc/U_\infty = 26.1$ (d) $fc/U_\infty = 31.2$

Figure 6.32: Streamwise velocity fluctuation amplitude profiles measured (markers) and computed from the Rayleigh (dashed line) and Orr-Sommerfeld (solid line) equations for $AOA = 10°$.

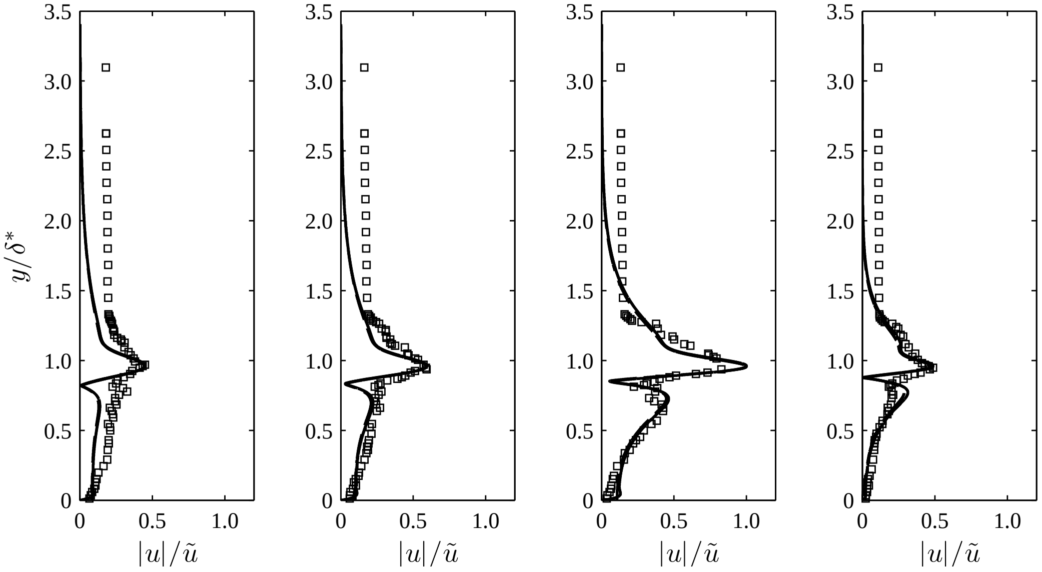

(a) $fc/U_\infty = 14.8$ (b) $fc/U_\infty = 12.9$ (c) $fc/U_\infty = 16.1$ (d) $fc/U_\infty = 19.9$

Figure 6.33: Streamwise velocity fluctuation amplitude profiles measured (markers) and computed from the Rayleigh (dashed line) and Orr-Sommerfeld (solid line) equations for $AOA = 15°$.

inflection point and the other two near the locations of maximum and minimum curvature in the mean profile. The correspondence between the location of this dominant peak and the mean profile inflection point indicates that an inviscid instability mechanism is driving the initial stages of transition in the separated shear layers forming at each angle of attack. The modal RMS velocity profiles decay into the laminar free stream and also approach the no-slip condition at the model surface. The amplitude of fluctuations diminish at higher and lower frequencies. In this way, the contribution of velocity fluctuations at a particular frequency to the overall velocity signal decreases as $|f - f^{\text{peak}}|$ increases.

The computed streamwise velocity fluctuation profiles from the Rayleigh and Orr-Sommerfeld equations show a similar three peak structure to that which was measured experimentally. Figures 6.30-6.33 shows that both the inviscid and viscous analyses provide accurate predictions of the location of the dominant peak at $y/\delta^* \approx 1$. The location of the peak at $y/\delta^* \approx 1.5$ is also accurately predicted; however, the relative magnitude of this peak compared to that at $y/\delta^* \approx 1$ is not well predicted for $AOA = 5°$ at $fc/U_\infty = 10.4$ and 12.9, or for $AOA = 10°$ at $fc/U_\infty = 26.1$. The relative magnitude of the peak at $y/\delta^* \approx 1.5$ was similarly under-predicted in the linear stability analysis of Lang et al. [25] of the measured transitional separation bubble on a flat plate. In Chapter 4, it was observed that the magnitude of this peak can be affected by the choice of curve fit (Fig. 4.12), with the solution for the Dini et al. [79] fit predicting a lower magnitude peak than the solution for the Falkner-Skan fit. The decay of the streamwise velocity fluctuation amplitude into the free stream is reasonably predicted for $AOA = 0$, 5, and 10° (Figs. 6.30-6.32). However, for $AOA = 15°$ (Fig. 6.33), the measured velocity fluctuation amplitudes in the free stream are higher than those predicted from LST. For this angle of attack, separation occurs close to the leading edge. This causes low absolute magnitudes of fluctuations in the free stream, and results in higher relative error in the measurements for this case. The largest discrepancies between the measured and computed streamwise velocity fluctuation profiles are observed at $AOA = 5°$, the angle for which the maximum height of the separation streamline is closest to the surface. Some of the discrepancies for this angle of attack may be a result of greater hot-wire measurement error near the surface. Discrepancies between the measured and computed profiles at each angle of attack for $y/\delta^* \lesssim 0.5$ are attributed to low speed and rectification error in hot-wire measurements over this region. Similar discrepancies for $y/\delta^* \lesssim 0.5$ are apparent in the computed and measured streamwise velocity fluctuation profiles in Fig. 4.8 from the results of Nishioka et al. [22].

Figures 6.30-6.33 show similar agreement between the Rayleigh and Orr-Sommerfeld equation predictions of the streamwise velocity fluctuation profiles as was observed for the simulated mean velocity profile in Section 4.4. The solutions agree well on the location and relative magnitudes of the three profile peaks. However, discrepancies between the two solutions are observed for $y/\delta^* \lesssim 0.5$. The inviscid solution does not satisfy the no-slip condition at the wall, whereas the viscous solution does. The Orr-Sommerfeld equation solution also contains a small amplitude peak at $y/\delta^* \approx 0.15$, possibly resulting from a viscous instability mechanism providing a minor contribution to disturbance development.

Phase shift profiles for the computed streamwise velocity fluctuation amplitude profiles in Figs. 6.30-6.33 are plotted in Fig. 6.34. These profiles, combined with the fluctuation amplitude profiles in Figs. 6.30-6.33, define predicted instantaneous modal velocity fluctuation profiles. The phase difference between two points at a particular angle of attack and frequency in Fig. 6.34 is the predicted phase difference between the component velocity fluctuations at that frequency between those two points. The phase shift profiles show that, at each streamwise location, component velocity fluctuations near the wall ($y/\delta^* \lesssim 0.5$) are out of phase with those in the free-stream ($y/\delta^* \gtrsim 1.5$). The extent of the phase change across the profile is greatest near the central instability frequency, with lower phase differences observed at higher and lower frequencies. This suggests that the amplitude of modal vorticity fluctuations at the mean profile inflection point are greatest near the

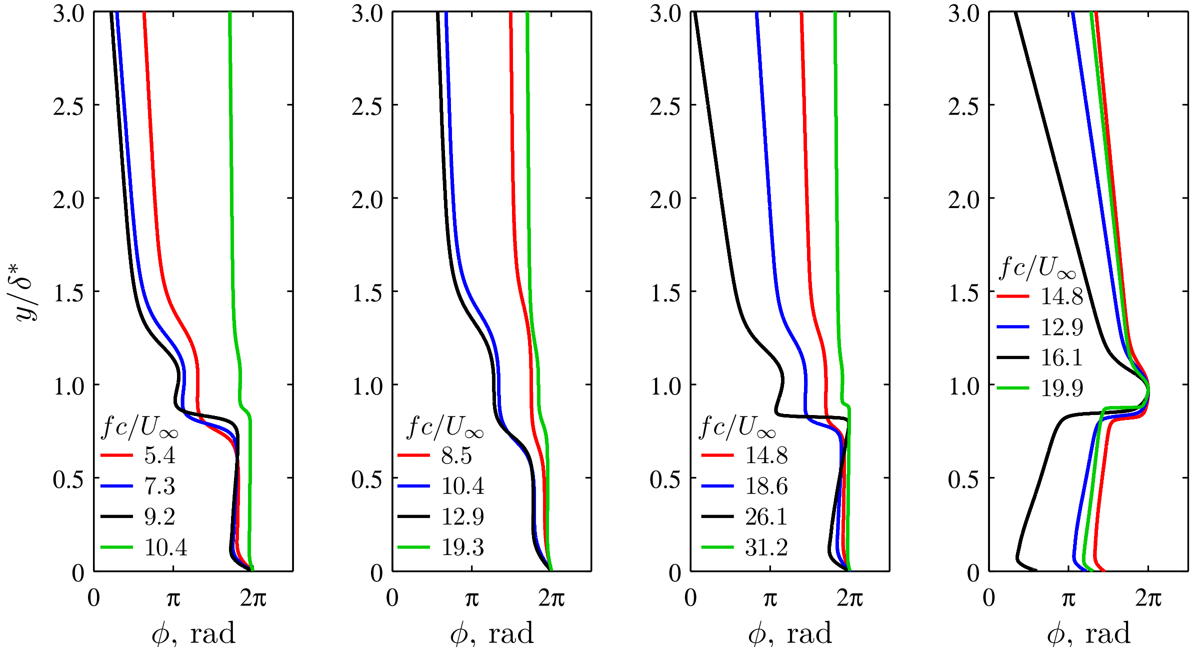

(a) $AOA = 0°$ (b) $AOA = 5°$ (c) $AOA = 10°$ (d) $AOA = 15°$

Figure 6.34: Streamwise velocity fluctuation phase shift profiles computed for the measured velocity profiles from the Orr-Sommerfeld equation. Profiles are shifted in phase to have a maximum phase of 2π rad.

central instability frequency. The general shape of the phase shift profile does not change significantly with frequency for the cases considered. In each of the phase shift profiles, a local maximum exists near the mean profile inflection point ($y/\delta^* \approx 1$). Just below this point, a relatively steep phase reversal is observed. The rate of phase reversal changes with both frequency and angle of attack.

Chapter 7

Conclusions

Boundary layer development over a NACA 0018 airfoil model at a Reynolds number of $Re_c = 10^5$ and angles of attack of $AOA = 0$, 5, 10, and 15° was investigated experimentally. Two flow regimes common to airfoil operation at low Reynolds numbers were observed in this range of flow conditions; for $AOA = 0$, 5, and 10°, a separation bubble formed on the airfoil surface, whereas for $AOA = 15°$, laminar boundary layer separation occurred without reattachment of the turbulent shear layer. This investigation had three main objectives: (1) quantify the sensitivity of linear stability predictions for measured separated shear layers to both the analysis approach and experimental data scatter, (2) assess the influence of end plates, test section blockage, and intrusive equipment on the low Reynolds number airfoil experiments, and (3) investigate flow development over the model with particular attention to laminar-to-turbulent transition characteristics that can be measured with embedded surface pressure sensors.

7.1 Sensitivity of Linear Stability Analysis

The sensitivity of spatial linear stability analysis of measured separated shear layers was evaluated. It was found that, for measured velocity profiles of low data scatter and high spatial resolution, the finite difference method, piecewise linear velocity profile approximation method, and Runge-Kutta method, applied directly to measured data, can each provide accurate stability predictions. However, when these solution methods were applied directly to measured separated shear layer profiles, extraneous growth rate spectrum behavior was observed for profiles with moderate levels of data scatter. On this basis, it was concluded that for the level of data scatter typical of hot-wire measurements in separated shear layers over low Reynolds number airfoils, a direct analysis of the discrete profile may produce unreliable results.

Performing stability analysis on curve fits to measured velocity profiles is an alternative to directly analyzing experimental data. This approach can provide realistic stability predictions over a wider range of spatial resolutions and levels of data scatter. Ten curve fits were examined in this study. Differences in the predictions of the Rayleigh equation due to the choice of curve fit were evaluated by applying stability analysis to curve fits of a simulated discrete velocity profile without data scatter. Despite the accuracy with which each curve fit matched the discrete velocity data, the predicted frequency of maximum disturbance growth rate was found to vary by up to 25% between fits. The ten fits were further evaluated based on the sensitivity of Rayleigh equation predictions, obtained using these fits, to base velocity profile data scatter. The lowest variability due to data scatter was observed in the results obtained using the reverse flow Falkner-Skan, Dini et al. [79], Dovgal et al. [34], Green [77], and LeBlanc et al. [27] fits. These five fits were further compared based on Rayleigh equation predictions for ten experimental separated shear layer profiles. No one fit consistently provided the most accurate prediction of the frequency of maximum disturbance growth rate compared to that measured in the experiment. Base profile fits with discontinuous derivatives, such as the Green [77] and LeBlanc et al. [27] fits, were shown to produce streamwise velocity fluctuation profile predictions with non-physical discontinuities.

A similar approach was employed to examine the sensitivity of the Orr-Sommerfeld equation to data scatter and the choice of a separated shear layer velocity profile fit. For the experiments considered, including viscosity in the analysis reduced the predicted growth rates by less than 15%. The variability in the maximum disturbance growth rate and corresponding frequency due to the choice of curve fit was similar to that observed for the Rayleigh equation. Further comparison of the variability due to data scatter for the Falkner-Skan, Dini et al. [79], and Dovgal et al. [34] fits revealed that Orr-Sommerfeld equation solutions are marginally less sensitive than Rayleigh equation solutions. The results show that the variation in the growth rate spectrum due to the choice of curve fit is greater than that due to mean profile data scatter. The maximum disturbance growth rate and corresponding frequency were found to vary by as much as 35% between fits. The apparent sensitivity of spatial linear stability analysis of measured separated shear layer profiles to experimental data scatter and the velocity profile processing approach should be considered when drawing conclusions from such an analysis.

7.2 Effect of Experimental Setup

The effects of end plates, blockage, and intrusive equipment on low Reynolds number airfoil experiments were investigated through experiments on a NACA 0018 airfoil model at $Re_c = 100 \times 10^3$ and $AOA = 0$, 5, 10, and 15°. From measurements on the model with various end plate configurations, it was shown that end plates significantly improve the mean spanwise uniformity of the flow compared to experiments conducted on a model with free ends or with only end caps installed. The extent of this improvement in mean spanwise uniformity was quantified using mean static pressure measurements across the span at three streamwise locations. The surface pressure distributions and lift coefficient curves were least sensitive to end plate spacing for end plate spacings of $b/c \gtrsim 2.0$ ($b/d \gtrsim 6.6$). It was shown that the added solid blockage with end plates installed can affect measured lift coefficients, and should be taken into account. The transition location and stall angles were shown to have only a minor dependence on end plate configuration. However, it was found that installing end plates reduces noise in energy spectra of surface pressure fluctuations in the separation bubble and that the end plate configuration affects disturbance amplification during separated shear layer transition. Measurements in the wake of the model showed that positioning the end plates at $b/c \lesssim 1.5$ reduces the coherence of wake vortices compared to measurements on the model with $b/c \gtrsim 1.5$. The end plate spacing did not affect the frequency of vortex shedding; however, the vortex shedding frequency measured for a free ends model and for a model with only end caps installed were both lower than the value with end plates installed.

Blockage effects were assessed through measurements in the GSW, ASW, and SLW configurations. The angles of attack and end plate configurations considered provided blockage ratios of between 4 and 8%. The locations of separation, transition, and reattachment did not change with wall configuration by more than the spatial resolution of the static pressure taps. However, changes in the values of mean pressure between the transition and reattachment points suggests that blockage has a small effect on the locations of transition and reattachment. Blockage was found to cause errors in the measured lift coefficients as high as 9% of the maximum lift coefficient at this Reynolds number. Applying the blockage correction method described by Barlow et al. [15] for two-dimensional bodies spanning the test section accurately adjusted sectional lift coefficient data for test section blockage when a separation bubble formed on the airfoil surface. However, this correction method performed poorly for data at $AOA = 15°$ due to limitations of simple blockage correction formulas for bluff bodies of solid blockage ratios greater than approximately 6%. For $AOA = 15°$, test section blockage was found to increase the wake vortex shedding frequency by 3.5%, indicating that blockage may be an important consideration if detailed measurements are to be performed in the wake of the model at post-stall angles of attack. SLW contours were determined from the WAS using both the original method of Judd et al. [96] for estimating the imaginary velocity field and a potential flow method to estimate the imaginary velocity field. The resulting wall shapes and flow measurements agreed to within their respective uncertainties, verifying the newly developed WAS program for the University of Waterloo adaptive-wall wind tunnel. Although the results from the two methods agreed for the flow conditions tested, in experiments with higher blockage ratios the potential flow method is expected to reduce experimental error.

The effect of the hot-wire probe and traverse on flow development was assessed using mean and RMS surface pressure measurements with the hot-wire probe positioned at various locations. It was found that, when the traverse is moved to the streamwise position where measurements will be acquired but with the probe well above the surface, the added blockage of the traverse causes a measurable shift in the magnitude of the mean surface pressure distribution. Positioning the probe near the separation point can shift the separation point upstream. For angles of attack approaching the stall angle, positioning the hot-wire probe near the measured separation point can force transition to occur in the attached boundary layer without separation. A comparison of RMS surface pressure development to RMS velocity in the shear layer indicated that this change in separation location shifts the location of measurable disturbance amplification upstream. No changes in surface pressure distributions or energy spectra were observed when the probe was positioned near the surface in the downstream turbulent flow.

The extent to which the flow is disturbed by opening the wind tunnel door to apply smoke-wire fluid for flow visualization experiments was investigated. It was concluded that, for each angle of attack tested, the mean pressure at the suction peak and the surface pressure energy spectra return to their prior states within thirty seconds of closing the test section door.

7.3 Separated Shear Layer Development

Smoke-wire flow visualization images provided qualitative insight into flow development over the model and in the near wake. The images show significantly different wake development when a separation bubble forms than at post-stall angles of attack. Specifically, bubble bursting dramatically increases the wake width and the length scale of spanwise vortical structures shed from the model. These images confirmed that wake vortex shedding was responsible for the observed peak in energy spectra of velocity fluctuations in the wake of the model. Furthermore, the images for $AOA = 5$ and 10° showed a greater degree of roll-up in the vortical structures forming below the wake centerline than in those forming above it, providing a physical interpretation for the observed asymmetry in mean and RMS wake velocity profiles and an explanation for why stronger spectral peaks were measured along the shear layer core below the wake centerline. The smoke-wire flow visualization images also indicate that the assumption of irrotational flow sufficiently removed from the model, inherent in the wall adaptation algorithm, was satisfied in these experiments. Furthermore, the images showed that the model wake vortex formation length was less than the distance that the end plates extended into the wake, satisfying the end plate design requirement proposed by Kubo et al. [14].

Detailed hot-wire measurements of shear layer development over the model were obtained. Consistent with previous studies (e.g., Ref. [8]), the results show that the separation bubble moves upstream, decreased in length, and exhibits higher disturbance growth rates as the angle of attack is increased. However, the separation bubble height did not show a monotonic trend with angle of attack. In agreement with the findings of Brendel & Mueller [53] for a Wortmann FX63-137 airfoil at $Re_c = 10^5$, it was found that the displacement thickness increases significantly between the locations of separation and transition, and reaches a maximum at the location of maximum bubble height, i.e., at the transition location. Furthermore, the momentum thickness remained nearly constant up to the transition location, where it began to increase rapidly. The boundary layer thickness shape factor followed similar trends for the cases of separation with and without reattachment, and was in qualitative agreement with the measured shape factors of Burgmann & Schröder [37]. The shape factor had a low, nearly constant value upstream of the separation point and well downstream of the transition point, increased substantially between the separation and transition locations, and decreased downstream of the transition point. The displacement thickness was shown to provide a reasonable estimate for the location of the maximum RMS velocity and the mean velocity profile inflection point in the separated shear layer.

Surface pressure spectra and velocity spectra along the separated shear layer core showed similar trends. The location of separation was marked by a noticeable increase in the disturbance amplification rate, which remained nearly constant until just upstream of the transition location. The RMS surface pressure continued to rise to a maximum just upstream of the reattachment location and then decayed gradually downstream as the turbulent profile expanded. This is consistent with trends observed in separation bubbles formed on other geometries [106, 107]. The results of Mabey [106] show that the maximum RMS surface pressure in a separation bubble depends on the specific geometry inducing separation [106]. The maximum values of $\tilde{p}/q_\infty$ on the order of 0.2 measured in the present investigation are higher than the values between 0.04 and 0.1 reported by Mabey [106] for splitter plates with fences, forward facing steps, and backward facing steps. The streamwise development of the maximum RMS velocity showed a more gradual decay downstream of the reattachment location than observed in the RMS surface pressures and a maximum value in the range $0.2 \lesssim \tilde{u}/U_\infty \lesssim 0.3$ for each angle of attack. The trends observed in the energy spectra of surface pressure and velocity fluctuations were also in agreement; just downstream of the separation point the energy content increased within a band of frequencies, developed harmonics near the transition point, and spread to produce broadband spectral content downstream.

Linear stability analysis revealed a correspondence between the measured central frequency of disturbance growth and that predicted from theory. Viscosity was found to influence the predicted dominant frequency by less than 5% as compared to the inviscid spectrum. Furthermore, measured frequency component RMS velocity fluctuation profiles matched the inviscid linear stability predictions well for $y/\delta^* \gtrsim 0.5$. Including viscosity in the analysis mainly affected the predicted velocity fluctuation profiles in a region very close to the airfoil surface ($y/\delta^* \lesssim 0.15$). These findings suggest that disturbance development over the majority of the laminar separated shear layer is primarily governed by a linear inviscid mechanism. Linear stability predictions were further compared to measured amplification rates, wave numbers, and phase speeds determined from the embedded pressure sensors. Linear stability predictions agreed with measurements to within the measurement uncertainty. The agreement of phase speed predictions with convection speed measurements further supports the claim of Gerakopulos [35] that the convection speeds measured in separation bubbles over low Reynolds number airfoils are associated with wave packets of growing disturbances propagating through the shear layer. Measured growth rate spectra computed from hot-wire measurements along the shear layer core and from embedded surface pressure sensor measurements agreed to within the measurement uncertainty. This demonstrates that embedded surface pressure sensors can be used to measure disturbance growth rates in separation bubbles on low Reynolds number airfoils in significantly less time than is required for similar measurements using hot-wire anemometry. Such measurements could also be completed on the wing of an aircraft, to compare separation bubble development under experimental conditions to actual operating conditions, and may find application in active flow control systems. Measured convection speeds from this investigation and prior low Reynolds number airfoil experiments were also compared. Convection speeds in the range $0.3 \lesssim U_c/U_e \lesssim 0.5$ were observed, consistent with the range of phase speeds computed by Dovgal et al. [34] from linear stability analysis on representative separated shear layer profiles. This suggests that the convection speed of pressure fluctuations in the separated shear layer over a low Reynolds number airfoil depends on the reverse flow speed, the distance of the shear layer core from the surface, and the characteristic Reynolds number.

Chapter 8

Recommendations

The following recommendations are made based on the findings of this thesis:

1. Linear stability analysis on hot-wire measurements of the separated shear layer over a low Reynolds number airfoil should be performed using a Falkner-Skan, Dini et al. [79], or Dovgal et al. [34] fit to the experimental data. The results of this investigation indicate that the reliability of stability predictions for measured velocity profiles depends on the spatial resolution and level of data scatter in the measurements. For high spatial resolution profiles with low data scatter, performing stability analysis directly on the discrete velocity profile, using a finite difference method, piecewise linear velocity profile approximation method, or a Runge-Kutta method, can remove the dependence of the predictions on the choice of curve fit. However, for data typical of hot-wire measurements over low Reynolds number airfoils, such an approach can produce unreliable results, and thus, curve fitting will be required. Reverse flow Falkner-Skan, Dini et al. [79], and Dovgal et al. [34] fits to the measured velocity profile were found to provide realistic growth rate spectrum and streamwise velocity fluctuation profile predictions with relatively low sensitivity to profile data scatter.

2. End plates should be installed for low Reynolds number airfoil experiments following the general recommendations for circular cylinders. The results of this investigation indicate that the general guidelines that end plates be positioned outside of the side wall boundary layers and at $b/d \gtrsim 7$, also apply to low Reynolds number airfoil experiments. End plates were found to have a particularly strong effect on the frequency of vortex shedding behind a stalled airfoil. It was also shown that although end plates improve mean spanwise uniformity, the added blockage they produce should be taken into account.

3. Investigate the effect of wall streamlining on drag and wake development behind this model. It was shown that wall streamlining can affect the vortex shedding frequency in the wake of the model. The results also show significant wall deflections behind the airfoil, particularly for the stalled case, indicating that blockage is affecting wake development. Furthermore, wall streamlining may have a more significant effect on drag than lift. Therefore, measurements of wake profiles with the walls in the GSW, ASW, and SLW configurations are recommended and should be used to assess the effect of blockage on measured drag forces and on wake development.

4. Hot-wire measurements near the separation point at angles of attack approaching bubble bursting conditions should be carefully scrutinized. It was found that the hot-wire probe can change the location of, or eliminate, separation, and can affect velocity fluctuation amplitudes. It was shown that changes in flow development caused by the presence of the hot-wire probe can be detected in mean surface pressure and RMS velocity data.

5. Obtain high frame rate flow visualization images of the separation bubble. Energy spectra of the velocity and surface pressure fluctuations revealed secondary spectral peaks at lower frequencies than that of the dominant shear layer instability. Furthermore, smoke-wire flow visualization images revealed oscillations in the streaklines near the model surface, indicative of shear layer unsteadiness. Bubble flapping or the development of vortical structures in the shear layer could explain these observations, however, further investigation is required. Flow visualization experiments employing high frame rate imaging are recommended to help identify the physical reason for the observed unsteadiness.

6. Compare LST predictions to PSE solutions for two-component velocity data in the separation bubble. It is expected that a particle image velocimetry system will soon be available for measurements on this model. PSE solutions for two-component velocity data, which can be obtained from this system, may provide insight into flow development. This tool may help determine the influence of non-parallel flow over thick airfoils and help in describing non-linear interactions.

7. Investigate the potential for using more sensitive pressure sensors, extending closer to the leading edge, for measurements when leading edge stall occurs. Similar to the findings of Gerakopulos [35], it was observed that the magnitudes of surface pressure fluctuations are significantly smaller for cases of separation without subsequent reattachment than for conditions at which a separation bubble forms. Since a major advantage of flow control on low Reynolds number airfoils is the potential to prevent or recover from stall, being able to accurately measure separated shear layer development with embedded

pressure sensors after the bubble bursts may be of interest. An array of more sensitive microphones extending closer to the leading edge may be difficult to implement, but could provide more detailed information about flow development when separation occurs without subsequent reattachment.

8. Explore the possibility of increasing the spatial resolution of the microphone array. For the flow conditions in these experiments, the spatial resolution of the microphone array imposed limitations on the measurements. These limitations include the inability to resolve details of disturbance development for short separation bubbles, inadequate spatial resolution for disturbance wave number measurements at some conditions, and an inability to detect the transition and reattachment trends for bubbles near the trailing edge. Increasing the number of microphones to improve spatial resolution and extending the array closer to the trailing edge could provide more details on flow development. Operating this array by scanning through the various sensors, instead of acquiring actual simultaneous data, would improve the resolution of wave number decompositions and could allow for frequency wave number energy spectrum analysis. These results could be used to determine whether absolute instability waves are propagating upstream, as have been detected in the separation bubble on a splitter plate with a fence by Hudy et al. [107], and predicted in the direct numerical simulation of the separation bubble on a NACA 0012 airfoil by Jones et al. [30].

9. Measure phase shift profiles of modal velocity fluctuations in the separation bubble. By acquiring simultaneous hot-wire profiles and surface pressure measurements in the laminar portion of the separation bubble, it may be possible to determine phase shift profiles for the disturbance components. These measurements will likely require a high sample rate in order to adequately resolve the phase shifts. Such measurements could verify the trends observed in computed phase shift profiles from LST.

PERMISSIONS

UNIVERSITY OF
WATERLOO

200 University Avenue West, Waterloo, ON, Canada N2L 3G1
519-888-4567 | uwaterloo.ca

July 25, 2011

Michael S. H. Boutilier
Department of Mechanical & Mechatronics Engineering
University of Waterloo
200 University Avenue West
Waterloo, ON, Canada, N2L 3G1

Hello Michael,

In response to your request, I grant you permission to publish content from the following two papers, in full or in part, in your MASc thesis:

1) Boutilier, M. S. H. and Yarusevych, S. Inviscid Spatial Linear Stability Analysis of Separated Shear Layers based on Experimental Data. In Proceedings of the AIAA 40th Fluid Dynamics Conference and Exhibit, 28 June - 1 July 2010, Chicago, Illinois. AIAA Paper No. 2010-4293.

2) Boutilier, M. S. H. and Yarusevych, S. Effects of End Plates and Blockage on a Low Reynolds Number Airfoil Experiment. In Proceedings of the AIAA 41st Fluid Dynamics Conference and Exhibit, 27 - 30 June 2011, Honolulu, Hawaii. AIAA Paper No. 2011-3723.

Also, I grant you permission to present in your MASc thesis the data from Figs. 2f and 3f in

3) Yarusevych, S. and Boutilier, M. S. H. Vortex Shedding Characteristics of a NACA 0018 Airfoil at Low Reynolds Numbers. In Proceedings of the AIAA 40th Fluid Dynamics Conference and Exhibit, 28 June - 1 July 2010, Chicago, Illinois. AIAA Paper No. 2010-4628.

Best regards,

Serhiy Yarusevych, Ph.D., P.Eng.,

Assistant Professor
Department of Mechanical & Mechatronics Engineering
University of Waterloo
200 University Avenue West
Waterloo, ON, Canada, N2L 3G1
Phone: (519) 888-4567 x35442
Fax: (519) 885-5862
E-mail: syarus@uwaterloo.ca
Web: www.fmrl.uwaterloo.ca

REFERENCES

[1] B. H. Carmichael. Low Reynolds number airfoil survey Vol. I. NASA, CR 165803, 1981.

[2] P. B. S. Lissaman. Low-Reynolds-number airfoils. *Annual Review of Fluid Mechanics*, 15:223–239, 1983.

[3] T. J. Mueller. Low Reynolds number vehicles. AGARDograph 288, 1985.

[4] T. J. Mueller and J. D. DeLaurier. Aerodynamics of small vehicles. *Annual Review of Fluid Mechanics*, 35:89–111, 2003.

[5] M. Gad-el-Hak. Control of low-speed airfoil aerodynamics. *AIAA Journal*, 28(9):1537–1552, 1990.

[6] M. Gad-el-Hak. Flow control: the future. *Journal of Aircraft*, 38(3):402–418, 2001.

[7] E. J. Fitzgerald and T. J. Mueller. Measurements in a separation bubble on an airfoil using laser velocimetry. *AIAA Journal*, 28(4):584–592, 1990.

[8] M. M. O'Meara and T. J. Mueller. Laminar separation bubble characteristics on an airfoil at low Reynolds numbers. *AIAA Journal*, 25(8):1033–1041, 1987.

[9] T. J. Mueller, L. J. Pohlen, P. E. Conigliaro, and B. J. Jansen. The influence of free-stream disturbances on low Reynolds number airfoil experiments. *Experiments in Fluids*, 1(1):3–14, 1983.

[10] J. F. Marchman. Aerodynamic testing at low Reynolds numbers. *Journal of Aircraft*, 24(2):107–114, 1987.

[11] P. K. Stansby. The effects of end plates on the base pressure coefficient of a circular cylinder. *Aeronautical Journal*, 78:36–37, 1974.

[12] W. A. Mair and P. K. Stansby. Vortex wakes of bluff cylinders in shear flow. *Journal of Applied Mathematics*, 28(2):519–540, 1975.

[13] T. A. Fox and G. S. West. On the use of end plates with circular cylinders. *Experiments in Fluids*, 9(4):237–239, 1990.

[14] Y. Kubo, M. Miyazaki, and K. Kato. Effect of end plates and blockage of structural members on drag forces. *Journal of Wind Engineering and Industrial Aerodynamics*, 32(3):329–342, 1989.

[15] J. B. Barlow, W. H. Rae Jr., and A. Pope. *Low-Speed Wind Tunnel Testing, third edition.* John Wiley & Sons, 1999.

[16] S. W. D. Wolf. Adaptive wall technology for improved wind tunnel testing techniques – a review. *Progress in Aerospace Sciences*, 31(2):85–136, 1995.

[17] H. C. Garner, E. W. E. Rogers, W. E. A. Acum, and E. C. Maskell. Subsonic wind tunnel wall corrections. AGARDograph 109, 1966.

[18] B. F. R. Ewald. Wind tunnel wall correction. AGARDograph 336, 1998.

[19] U. Ganzer. A review of adaptive wall wind tunnels. *Progress in Aerospace Sciences*, 22(2):81–111, 1985.

[20] O. Meyer and W. Nitsche. Update on progress in adaptive wind tunnel wall technology. *Progress in Aerospace Sciences*, 40(3):119–141, 2004.

[21] U. Hartmann. Wall interference effects on hot-wire probes in a nominally two-dimensional highly curved wall jet. *Journal of Physics E: Scientific Instruments*, 15:725–730, 1982.

[22] M. Nishioka, M. Asai, and S. Yoshida. Control of flow separation by acoustic excitation. *AIAA Journal*, 28(11):1909–1915, 1990.

[23] J. H. Watmuff. Evolution of a wave packet into vortex loops in a laminar separation bubble. *Journal of Fluid Mechanics*, 397:119–169, 1999.

[24] A. V. Boiko, G. R. Grek, A. V. Dovgal, and V. V. Kozlov. *The Origin of Turbulence in Near-Wall Flows.* Springer, 2002.

[25] M. Lang, U. Rist, and S. Wagner. Investigations on controlled transition development in a laminar separation bubble by means of LDA and PIV. *Experiments in Fluids*, 36(1):43–52, 2004.

[26] S. Yarusevych, J. G. Kawall, and P. E. Sullivan. Separated-shear-layer development on an airfoil at low Reynolds numbers. *AIAA Journal*, 46(12):3060–3069, 2008.

[27] P. LeBlanc, R. Blackwelder, and R. Liebeck. A comparison between boundary layer measurements in a laminar separation bubble flow and linear stability theory calculations. In *Proceedings of the Low Reynolds Number Aerodynamics Conference*, pages 189–205, Notre-Dame, Indiana, 5-7 June 1989.

[28] C. P. Häggmark, C. Hildings, and D. S. Henningson. A numerical and experimental study of a transitional separation bubble. *Aerospace Science and Technology*, 5(5):317–328, 2001.

[29] S. Yarusevych, P. E. Sullivan, and J. G. Kawall. Coherent structures in an airfoil boundary layer and wake at low Reynolds numbers. *Physics of Fluids*, 18(4):1–11, 2006.

[30] L. E. Jones, R. D. Sandberg, and N. D. Sandham. Direct numerical simulations of forced and unforced separation bubbles on an airfoil at incidence. *Journal of Fluid Mechanics*, 602:175–207, 2008.

[31] L. E. Jones, R. D. Sandberg, and N. D. Sandham. Stability and receptivity characteristics of a laminar separation bubble on an aerofoil. *Journal of Fluid Mechanics*, 648:257–296, 2010.

[32] W. Balzer and H. F. Fasel. Direct numerical simulation of laminar boundary-layer separation and separation control on the suction side of an airfoil at low Reynolds number conditions. In *Proceedings of the AIAA* 40th *Fluid Dynamics Conference and Exhibit*, Chicago, Illinois, 28 June - 1 July 2010, AIAA Paper No. 2010-4866.

[33] P. G. Drazin and W. H. Reid. *Hydrodynamic Stability, second edition.* Cambridge University Press, 2004.

[34] A. V. Dovgal, V. V. Kozlov, and A. Michalke. Laminar boundary layer separation: Instability and associated phenomena. *Progress in Aerospace Sciences*, 30(1):61–94, 1994.

[35] R. J. Gerakopulos. Investigating flow over an airfoil at low Reynolds numbers using novel time-resolved surface pressure measurements. University of Waterloo, MASc thesis, 2011.

[36] H. Horton. Laminar separation bubbles in two and three dimensional incompressible flow. Queen Mary College, PhD thesis, 1968.

[37] S. Burgmann and W. Schröder. Investigation of the vortex induced unsteadiness of a separation bubble via time-resolved and scanning PIV measurements. *Experiments in Fluids*, 45(4):675–691, 2008.

[38] G. S. Schmidt and T. J. Mueller. Analysis of low Reynolds number separation bubbles using semiempirical methods. *AIAA Journal*, 27(8):993–1001, 1989.

[39] R. Gerakopulos, M. S. H. Boutilier, and S. Yarusevych. Aerodynamic characterization of a NACA 0018 airfoil at low Reynolds numbers. In *Proceedings of the* 40^{th} *Fluid Dynamics Conference and Exhibit*, Chicago, Illinois, 28 June - 1 July 2010, AIAA Paper No. 2010-4629.

[40] M. Gaster. The structure and behaviour of laminar separation bubbles. Aeronautical Research Council, RM 3595, 1969.

[41] T. J. Mueller. The influence of laminar separation and transition on low Reynolds number airfoil hysteresis. *Journal of Aircraft*, 22(9):763–770, 1985.

[42] A. Pelletier and T. J. Mueller. Low Reynolds number aerodynamics of low-aspect-ratio thin/flat/cambered-plate wings. *Journal of Aircraft*, 37(5):825–832, 2000.

[43] S. Watkins, J. Milbank, B. J. Loxton, and W. H. Melbourne. Atmospheric winds and their implications for microair vehicles. *AIAA Journal*, 44(11):2591–2600, 2006.

[44] S. Watkins, S. Ravi, and B. Loxton. The effect of turbulence on the aerodynamics of low Reynolds number wings. *Engineering Letters*, 18(3), 2010.

[45] R. H. Ellsworth and T. J. Mueller. Airfoil boundary layer measurements at low Re in an accelerating flow from a nonzero velocity. *Experiments in Fluids*, 11(6):368–374, 1991.

[46] U. Rist, K. Augustin, and S. Wagner. Numerical simulation of laminar separation-bubble control. In *Proceedings of the* 12^{th} *STAB/DGLR Symposium*, Stuttgart, Germany, 2002.

[47] T. C. Corke, C. L. Enloe, and S. P. Wilkinson. Dielectric barrier discharge plasma actuators for flow control. *Annual Review of Fluid Mechanics*, 42:505–529, 2010.

[48] R. Hain, C. J. Kähler, and R. Radespiel. Dynamics of laminar separation bubbles at low-Reynolds-number aerofoils. *Journal of Fluid Mechanics*, 630:129–153, 2009.

[49] S. Yarusevych, P. E. Sullivan, and J. G. Kawall. Airfoil boundary layer separation and control at low Reynolds numbers. *Experiments in Fluids*, 38(4):545–547, 2005.

[50] S. Yarusevych. Investigation of airfoil boundary layer and turbulent wake development at low Reynolds numbers. University of Toronto, PhD thesis, 2006.

[51] U. Rist and U. Maucher. Investigations of time-growing instabilities in laminar separation bubbles. *European Journal of Mechanics – B/Fluids*, 21(5):495–509, 2002.

[52] I. Tani. Low-speed flows involving bubble separations. *Progress in Aerospace Sciences*, 5:70–103, 1964.

[53] M. Brendel and T. J. Mueller. Boundary-layer measurements on an airfoil at low Reynolds numbers. *Journal of Aircraft*, 26(7):612–617, 1988.

[54] U. Rist, U. Maucher, and S. Wagner. Direct numerical simulation of some fundamental problems related to transition in laminar separation bubbles. In *Proceedings of the ECCOMAS Computational Fluid Dynamics Conference*, pages 319–325, 1996.

[55] L. L. Pauley, P. Moin, and W. C. Reynolds. The structure of two-dimensional separation. *Journal of Fluid Mechanics*, 220:397–411, 1990.

[56] O. Marxen and U. Rist. Mean flow deformation in a laminar separation bubble: Separation and stability characteristics. *Journal of Fluid Mechanics*, 660:37–54, 2010.

[57] J. C. M. Lin and L. L. Pauley. Low-Reynolds-number separation on an airfoil. *AIAA Journal*, 34(8):1570–1577, 1996.

[58] S. Burgmann, C. Brücker, and W. Schröder. Scanning PIV measurements of a laminar separation bubble. *Experiments in Fluids*, 41(2):319–326, 2006.

[59] S. Burgmann, W. Schröder, and C. Brücker. Volumetric measurement of vortical structures in the reattachment region of a laminar separation bubble using stereo scanning PIV. In *Proceedings of the* 13th *International Symposium on Applications of Laser Techniques to Fluid Mechanics*, Lisbon, Portugal, 26-29 June 2006, Paper No. 1228.

[60] C. M. Ho and P. Huerre. Perturbed free shear layers. *Annual Review of Fluid Mechanics*, 16:365–422, 1984.

[61] H. Schlichting and K. Gersten. *Boundary-layer theory,* 8th *revised and enlarged edition.* Springer-Verlag, 2000.

[62] H. L. Reed. Gallery of fluid motion. *The Physics of Fluids*, 29(9):2769–2780, 1986.

[63] F. M. White. *Viscous Fluid Flow, third edition.* McGraw-Hill, 2003.

[64] V. Theofilis, S. Hein, and U. Dallmann. On the origins of unsteadiness and three-dimensionality in a laminar separation bubble. *Philosophical Transactions of the Royal Society of London A*, 358(1777):3229–3246, 2000.

[65] R. Betchov and W. O. Criminale. *Stability of Parallel Flows*, volume 10 of *Applied Mathematics and Mechanics*. Academic Press, 1967.

[66] P. J. Schmid and D. S. Henningson. *Stability and Transition in Shear Flows*, volume 142 of *Applied Mathematical Sciences*. Springer, 2001.

[67] W. O. Criminale, T. L. Jackson, and R. D. Joslin. *Theory and Computation in Hydrodynamic Stability*. Cambridge University Press, 2003.

[68] W. Tollmien. The production of turbulence. National Advisory Committee for Aeronautics, TM 609, 1931.

[69] T. Allen and N. Riley. Absolute and convective instabilities in separation bubbles. *Aeronautical Journal*, 99(990):439–448, 1995.

[70] D. A. Hammond and L. G. Redekopp. Local and global instability properties of separation bubbles. *European Journal of Mechanics – B/Fluids*, 17(2):145–164, 1998.

[71] M. Alam and N. D. Sandham. Direct numerical simulation of 'short' laminar separation bubbles with turbulent reattachment. *Journal of Fluid Mechanics*, 410:1–28, 2000.

[72] P. R. Spalart and M. Strelets. Mechanisms of transition and heat transfer in a separation bubble. *Journal of Fluid Mechanics*, 403:329–349, 2000.

[73] H. L. Reed, W. S. Saric, and D. Arnal. Linear stability theory applied to boundary layers. *Annual Review of Fluid Mechanics*, 28:389–428, 1996.

[74] T. Herbert. Secondary instability of boundary layers. *Annual Review of Fluid Mechanics*, 20:487–526, 1988.

[75] T. Herbert. Parabolized stability equations. *Annual Review of Fluid Mechanics*, 29:245–283, 1997.

[76] T. Cebeci. *Stability and Transition: Theory and Application*. Springer, 2004.

[77] J. E. Green. Two-dimensional turbulent reattachment as a boundary-layer problem. AGARD, 1966.

[78] J. L. van Ingen and L. M. M. Boermans. Aerodynamics at low Reynolds numbers: a review of theoretical and experimental research at Delft University of Technology. In *Proceedings of the International Conference on Aerodynamics at Low Reynolds Numbers* $10^4 < Re < 10^6$, pages 1.1–1.40, 1986.

[79] P. Dini, M. S. Selig, and M. D. Maughmer. Simplified linear stability transition prediction method for separated boundary layers. *AIAA Journal*, 30(8):1953–1961, 1992.

[80] M. Drela. Viscous-inviscid analysis of transonic and low Reynolds number airfoils. *AIAA Journal*, 25(10):1347–1355, 1987.

[81] U. Maucher, U. Rist, and S. Wagner. Direct numerical simulation of airfoil separation bubbles. In *Proceedings of the ECCOMAS Computational Fluid Dynamics Conference*, pages 471–477, 1994.

[82] E. D. Obasaju. On the effects of end plates on the mean forces on square sectioned cylinders. *Journal of Wind Engineering and Industrial Aerodynamics*, 5(1-2):179–186, 1979.

[83] G. S. West and C. J. Apelt. The effects of tunnel blockage and aspect ratio on the mean flow past a circular cylinder with Reynolds numbers between 10^4 and 10^5. *Journal of Fluid Mechanics*, 114:361–377, 1982.

[84] S. Szepessy and P. W. Bearman. Aspect ratio and end plate effects on vortex shedding from a circular cylinder. *Journal of Fluid Mechanics*, 234:191–217, 1992.

[85] P. W. Bearman. Investigation of the flow behind a two-dimensional model with a blunt trailing edge and fitted with splitter plates. *Journal of Fluid Mechanics*, 21:241–256, 1965.

[86] A. Pelletier and T. J. Mueller. Effect of endplates on two-dimensional airfoil testing at low Reynolds numbers. *Journal of Aircraft*, 38(6):1056–1059, 2001.

[87] M. M. Alam, Y. Zhou, and H. X. Yang. The ultra-low Reynolds number airfoil wake. *Experiments in Fluids*, 48(1):81–103, 2010.

[88] T. Lee and P. Gerontakos. Investigation of flow over an oscillating airfoil. *Journal of Fluid Mechanics*, 512:313–341, 2004.

[89] P. Kankainen, E. Brundrett, and J. A. Kaiser. A small wind tunnel significantly improved by a multi-purpose, two-flexible-wall test section. *Journal of Fluids Engineering*, 116:419–423, 1994.

[90] G. P. Russo, G. Zuppardi, and M. Basciani. An experimental comparison of two adaptation strategies in an adaptive-walls wind-tunnel. *Experiments in Fluids*, 19(4):274–279, 1995.

[91] M. J. Goodyer and M. Saquib. Blockage limits in a two-dimensional self-streamlining wind tunnel. In *Proceedings of the* 25^{th} *AIAA Applied Aerodynamics Conference*, Miami, Florida, 25-28 June 2007.

[92] M. J. Bishop. Experimental investigation of the effect of wall adaptation on flow over a cylinder in a modernized adaptive-wall wind tunnel. University of Waterloo, MASc thesis, 2010.

[93] E. J. Saltzman and T. G. Ayers. Review of flight-to-wind-tunnel drag correlation. *Journal of Aircraft*, 19(10):801–811, 1982.

[94] S. W. D. Wolf and M. J. Goodyer. Predictive wall adjustment strategy for two-dimensional flexible walled adaptive wind tunnel – a detailed description of the first one-step method. NASA, CR 181635, 1988.

[95] J. L. Everhart. A method for modifying two-dimensional adaptive wind-tunnel walls including analytical and experimental verification. NASA, TP 2081, 1983.

[96] M. Judd, M. J. Goodyer, and S. W. D. Wolf. Application of the computer for on-site definition and control of wind tunnel shape for minimum boundary interference. In *Proceedings of the AGARD Conference on Numerical Methods and Wind-tunnel Testing, AGARD CP-210*, 1976.

[97] C. P. Häggmark, A. A. Bakchinov, and P. H. Alfredsson. Experiments on a two-dimensional laminar separation bubble. *Philosophical Transactions of the Royal Society of London A*, 358(1777):3193–3205, 2000.

[98] C. Tropea, J. Foss, and A. Yarin. *Springer Handbook of Experimental Fluid Mechanics*. Springer-Verlag, 2007.

[99] H. H. Brunn. *Hot-Wire Anemometry: Principles and Signal Analysis.* Oxford University Press, 1995.

[100] C. F. Lange, F. Durst, and M. Breuer. Wall effects on heat losses from hot-wires. *International Journal of Heat and Fluid Flow*, 20(1):34–47, 1999.

[101] F. Durst, E.-S. Zanoun, and M. Pashtrapanska. In situ calibration of hot wires close to highly heat-conducting walls. *Experiments in Fluids*, 31(1):103–110, 2001.

[102] F. Durst and E. Zanoun. Experimental investigation of near-wall effects on hot-wire measurements. *Experiments in Fluids*, 33(1):210–218, 2002.

[103] Y. T. Chew, S. X. Shi, and B. C. Khoo. On the numerical near-wall corrections of single hot-wire measurements. *International Journal of Heat and Fluid Flow*, 16(6):461–476, 1995.

[104] W. W. Willmarth. Pressure fluctuations beneath turbulent boundary layers. *Annual Review of Fluid Mechanics*, 7:13–38, 1975.

[105] R. W. Paterson, P. G. Vogt, M. R. Fink, and C. L. Munch. Vortex noise of isolated airfoils. *Journal of Aircraft*, 10(5):296–302, 1973.

[106] D. G. Mabey. Analysis and correlation of data on pressure fluctuations in separated flow. *Journal of Aircraft*, 9(9):642–645, 1972.

[107] L. M. Hudy, A. M. Naguib, and W. M. Humphreys Jr. Wall-pressure-array measurements beneath a separating/reattaching flow region. *Physics of Fluids*, 15(3):706–717, 2003.

[108] T. M. Farabee and M. J. Casarella. Measurements of fluctuating wall pressure for separated/reattached boundary layer flows. *Journal of Vibration, Acoustics, Stress, and Reliability in Design*, 108(3):301–307, 1986.

[109] D. M. Driver, H. L. Seegmiller, and J. G. Marvin. Time-dependent behavior of a reattaching shear layer. *AIAA Journal*, 25(7):914–919, 1987.

[110] I. Lee and H. J. Sung. Characteristics of wall pressure fluctuations in separated and reattaching flows over a backward-facing step: Part I. time-mean statistics and cross-spectral analysis. *Experiments in Fluids*, 30(3):262–272, 2001.

[111] N. J. Cherry, R. Hillier, and M. E. M. P. Latour. Unsteady measurements in a separated and reattaching flow. *Journal of Fluid Mechanics*, 144:13–46, 1984.

[112] E. Weibust, A. Bertelrud, and S. O. Ridder. Experimental investigation of laminar separation bubbles and comparison with theory. *Journal of Aircraft*, 24(5):291–297, 1987.

[113] D. Sumner. An experimental investigation of 3-D models in a 2-D adaptive wall test section. University of Waterloo, MASc thesis, 1994.

[114] S. W. D. Wolf. The design and operational development of self-streamlining two-dimensional flexible walled test sections. NASA, CR 172328, 1984.

[115] H. H. Brunn, M. A. Khan, H. H. Al-Kayiem, and A. A. Fardad. Velocity calibration relationships for hot-wire anemometry. *Journal of Physics E: Scientific Instruments*, 21(2):225–232, 1988.

[116] R. Gerakopulos. Wind tunnel traversing mechanism integration and flow quality assessment. University of Waterloo report, 2008.

[117] A. McPhee. The development of a research technique for low speed aeroacoustics. University of Waterloo, MASc thesis, 2009.

[118] P. K. Kundu and I. R. Cohen. *Fluid Mechanics, fourth edition.* Academic Press, 2008.

[119] S. Yarusevych, P. E. Sullivan, and J. G. Kawall. Smoke-wire flow visualization in separated flows at relatively high velocities. *AIAA Journal*, 47(6):1592–1595, 2009.

[120] W. W. W. Liou and P. J. Morris. The eigenvalue spectrum of the Rayleigh equation for a plane shear layer. *International Journal for Numerical Methods in Fluids*, 15(12):1407–1415, 1992.

[121] T. J. Bridges and P. J. Morris. Differential eigenvalue problems in which the parameter appears nonlinearly. *Journal of Computational Physics*, 55(3):437–460, 1984.

[122] R. Blockley and W. Shyy. *Encyclopedia of Aerospace Engineering.* John Wiley & Sons, 2010.

[123] A. Tumin. Multimode decomposition of spatially growing perturbations in a two-dimensional boundary layer. *Physics of Fluid*, 15(9):2525–2540, 2003.

[124] S. A. Orszag. Accuate solution of the Orr-Sommerfeld stability equation. *Journal of Fluid Mechanics*, 50:689–703, 1971.

[125] T. J. Bridges and P. J. Morris. Spectral calculations of the spatial stability of non-parallel boundary layers. In *Proceedings of the AIAA* 22^{nd} *Aerospace Sciences Meeting*, Reno, Nevada, 9-12 January 1984, AIAA Paper No. 84-0437.

[126] G. Danabasoglu and S. Biringen. A Chebyshev matrix method for spatial modes of the Orr-Sommerfeld equation. NASA, CR 4247, 1989.

[127] J. J. Dongarra, B. Straughan, and D. W. Walker. Chebyshev tau - QZ algorithm methods for calculating spectra of hydrodynamic stability problems. *Applied Numerical Mathematics*, 22(4):399–434, 1996.

[128] G. B. McFadden, B. T. Murray, and R. F. Boisvert. Elimination of spurious eigenvalues in the Chebyshev tau spectral method. *Journal of Computational Physics*, 91:228–239, 1990.

[129] S. S. Motsa and P. Sibanda. On the Chebyshev spectral collocation method in channel and jet flows. *Journal of Pure and Applied Mathematics*, 1(1):36–47, 2001.

[130] A. Boguslawski. Inviscid instability of the hyperbolic-tangent velocity proifle – spectral "tau" solution. *Task Quarterly*, 5(2):155–164, 2001.

[131] D. Bourne. Hydrodynamic stability, the Chebyshev tau method and spurious eigenvalues. *Continuum Mechanics and Thermodynamics*, 15(6):571–579, 2003.

[132] C. Canuto, M. Y. Hussaini, A. Quarteroni, and T. A. Zang. *Spectral Methods in Fluid Dynamics*. Springer-Verlag, 1988.

[133] Math Works. *MATLAB Curve Fitting ToolboxTM 2: Users Guide*, 2010.

[134] E. C. Maskell. A theory of the blockage effects on bluff bodies and stalled wings in a closed wind tunnel. Aeronautical Research Council, RM 3400, 1965.

[135] J. E. Hackett and K. R. Cooper. Extensions to Maskell's theory for blockage effects on bluff bodies in a closed wind tunnel. *Aeronautical Journal*, 105(5):409–418, 2001.

[136] S. Yarusevych, P. E. Sullivan, and J. G. Kawall. On vortex shedding from an airfoil in low-Reynolds-number flows. *Journal of Fluid Mechanics*, 632:245–271, 2009.

[137] S. Yarusevych and M. S. H. Boutilier. Vortex shedding characteristics of a NACA 0018 airfoil at low Reynolds numbers. In *Proceedings of the AIAA* 40^{th} *Fluid Dynamics Conference and Exhibit*, Chicago, Illinois, 28 June - 1 July 2010, AIAA Paper No. 2010-4628.

[138] T. J. Mueller and S. M. Batill. Experimental studies of separation on a two-dimensional airfoil at low Reynolds numbers. *AIAA Journal*, 20(4):457–463, 1982.

[139] S. B. Pope. *Turbulent Flows*. Cambridge University Press, 2000.

[140] A. Michalke. On spatially growing disturbances in an inviscid shear layer. *Journal of Fluid Mechanics*, 23(3):521–544, 1965.

[141] R. J. Moffat. Describing the uncertainties in experimental results. *Experimental Thermal and Fluid Sciences*, 1(1):3–17, 1988.

[142] J. G. Kawall, M. Shokr, and J. F. Keffer. A digital technique for the simultaneous measurement of streamwise and lateral velocities in turbulent flows. *Journal of Fluid Mechanics*, 133:83–112, 1983.

[143] S. H. Chue. Pressure probes for fluid measurement. *Progress in Aerospace Sciences*, 16(2):147–223, 1975.

[144] F. M. White. *Fluid Mechanics, sixth edition.* McGraw-Hill, 2008.

[145] M. Drela. XFOIL - an analysis and design system for low Reynolds number airfoils. In *Proceedings of the Low Reynolds Number Aerodynamics Conference*, Notre Dame, Indiana, 5-7 June 1989, pages 1-12.

[146] R. K. Nagle, E. B. Saff, and A. D. Snider. *Fundamentals of Differential Equations and Boundary Value Problems, fourth edition.* Pearson, 2004.

[147] B. S. Ng and W. H. Reid. An initial value method for eigenvalue problems using compound matricies. *Journal of Computational Physics*, 30(1):125–136, 1979.

[148] M. Y. Hussaini and T. A. Zang. Spectral methods in fluid dynamics. *Annual Review of Fluid Mechanics*, 19:339–367, 1987.

APPENDICES

Appendix A

Experimental Uncertainty

Table A.1 summarizes the uncertainty estimates for measured quantities presented in this thesis. Figures and tables are identified that contain measurements to which these uncertainty estimates apply. Subsequent sections of this appendix describe how the estimates in Table A.1 were obtained. Throughout this appendix, the uncertainty is stated as a 95% confidence interval on the reported measurement. Estimates were based on the approach to uncertainty analysis presented by Moffat [141]. The uncertainties due to each significant source of error are estimated and combined under the assumption of mutually exclusive contributions to the overall uncertainty. Note that the uncertainties due to the end plate configuration and test section wall interference are not included in the estimates. These factors are addressed in Chapter 5, where the uncertainty estimates from this appendix are used to determine how significant a change due to end plate configuration or wall adaptation is required to conclude that the flow has changed.

A.1 Uncertainty in Experimental Setup

Specified experimental conditions each have a degree of uncertainty associated with them, which determines the range of possible flow conditions to which the measurements correspond. This section provides estimates of the uncertainty in free-stream speed, angle of attack, and end plate spacing.

Chord Reynolds number was determined from the measured pressure difference across the wind tunnel inlet contraction. The pressure difference was correlated to the free-stream speed by measurements with a Pitot-static tube. The main sources of uncertainty in the measured free-stream speed are due to the manometer resolution used to measure the pressure difference, the calibration procedure, and the accepted variation in free-

Table A.1: Summary of measurement uncertainty estimates.

quantity	conditions	uncertainty	applicable tables & figures
AOA		$\pm 0.22°$	
b/c		± 0.025	Figs. 5.1, 5.2, 5.3, 5.6, & 5.9
C_L		± 0.024	Figs. 5.2 & 5.10
C_p		± 0.016	Figs. 5.1, 5.3, 5.12, & 6.10
$C_{p,w}$		± 0.016	Figs. 5.6b & 5.8
$f^{peak}c/U_\infty$		± 0.63	Table 6.2
H		$\pm 0.105H$	Figs. 6.17d, 6.18d, & Table 6.1
Re_c		± 2800	
St		± 0.002	Table 5.2
U/U_∞	for $U/U_\infty \gtrsim 0.25$	± 0.05	Figs. 6.6a, 6.7a, 6.8a, 6.9a, 6.11a, 6.12a, 6.13a, 6.14a, 6.15a, & 6.24
U_c/U_∞		± 0.035	Figs. 6.28, 6.29, & Table 6.2
$\tilde{u}/U_\infty$	for $U/U_\infty \gtrsim 0.25$	± 0.05	Figs. 6.6b, 6.7b, 6.8b, 6.9b, 6.11b, 6.12b, 6.13b, 6.14b, 6.15b, 6.19a, 6.30, 6.31, 6.32, & 6.33
$\lvert u\rvert/U_\infty$	for $U/U_\infty \gtrsim 0.25$	± 0.10	Figs. 6.30, 6.31, 6.32, & 6.33
$\tilde{v}/U_\infty$	for $U/U_\infty \gtrsim 0.25$	± 0.05	Fig. 5.5
$\tilde{p}/q_\infty$		$\pm\sqrt{(0.02)^2+(0.20\tilde{p}/q_\infty)^2}$	Fig. 6.19b
x_R/c		± 0.01	Figs. 6.10, 6.11, 6.12, 6.13, 6.15, 6.16, 6.19c, & Table 6.2
x_S/c		± 0.02	Figs. 6.10, 6.11, 6.12, 6.13, 6.14, 6.15, 6.16, 6.19c, & Table 6.2
x_T/c	based on C_p	± 0.01	Figs. 6.10, 6.11, 6.12, 6.13, 6.15, 6.16, 6.19c, & Table 6.2
x_T/c	based on E_{vv}	± 0.02	Figs. 6.14, 6.16, 6.19c, & Table 6.2
$\Delta Y/c$	for the ASW configuration	± 0.005	Fig. 5.7
$\Delta Y/c$	for the SLW configuration	± 0.010	Fig. 5.7
y/c		± 0.00025	Figs. 6.6, 6.7, 6.8, 6.9, 6.11, 6.12, 6.13, 6.14, 6.15, 6.16, 6.24, 6.30, 6.31, 6.32, 6.33, & 6.34
$-\alpha_i c$	based on $\tilde{u}/U_\infty$	$\pm\sqrt{(10)^2+(0.1\alpha_i c)^2}$	Fig. 6.25
$-\alpha_i c$	based on $\tilde{p}/q_\infty$	$\pm\sqrt{(10)^2+(0.3\alpha_i c)^2}$	Fig. 6.25
$\alpha_r c$		$\pm\sqrt{(8)^2+(0.04\alpha_r c)^2}$	Fig. 6.27
δ^*/c		$\pm 0.05\delta^*/c$	Figs. 6.17b, 6.18b, 6.24, 6.30, 6.31, 6.32, 6.33, 6.34, & Table 6.1
δ_0/c	for $AOA = 0, 5,$ and $10°$	± 0.001	Figs. 6.17a & 6.16a-c
δ_0/c	for $AOA = 15°$	± 0.01	Figs. 6.18a & 6.16d
θ/c		$\pm 0.05\theta/c$	Figs. 6.17c, 6.18c, & Table 6.1

stream speed during an experiment. The inclined manometer used for free-stream speed measurements had 0.25 Pa minor divisions. The uncertainty in the inclined manometer reading was estimated to be less than 0.50 Pa, roughly 1.5% of the pressure difference corresponding to $Re_c = 10^5$. Manometer measurements of the pressure difference across the contraction and across the Pitot-static tube during calibration each had the same uncertainty as that associated with manometer measurements. During experiments, the free-stream speed was allowed to vary to within 1% of the specified value. Combining these estimated values yields a total uncertainty of 2.8%.

The angle of attack was set with a digital protractor with an angular resolution of 0.1°. The uncertainty in the angle of attack setting is also influenced by a bias error introduced in determining the aerodynamic zero angle of attack. The aerodynamic zero angle of attack was determined by measuring model pressure distributions over a wide range of angles and finding the zero angle that provided the best symmetry between pressure distributions at positive and negative angles [35]. Small imperfections in the model can make an accurate determination of the zero-lift angle of attack difficult, particularly at low Reynolds numbers, for which the flow is very sensitive to experimental conditions [3]. Based on measured pressure distributions over various Reynolds numbers and angles of attack, it was estimated that the uncertainty in the aerodynamic zero angle of attack is less than 0.2°. The combined uncertainty due to the protractor setting and the aerodynamic zero angle determination is 0.22°.

End plate spacing was set as close to the stated values as was reasonable. The uncertainty in this setting was assessed by measurements of the end plate spacing at four locations on the circumferences of the end plates, each time the end plates were installed. Based on these measurements, the b/c spacing was set to within ± 0.025, with the end plates having a maximum tilt of less than 0.5°.

A.2 Hot-Wire Uncertainty

Hot-wire measurement uncertainty has been examined in several studies [98–103, 115, 142]. The accuracy of such measurements depends on factors including probe geometry, calibration method, flow incidence angle, turbulence intensity, flow speed, and proximity to solid surfaces [99]. Error caused by flow obstruction by the probe and incidence angle have been limited by using a boundary-layer type normal hot-wire probe angled at 7° to the surface, based on the recommendations of Brendel & Mueller [53]. The uncertainty in mean and RMS velocity measurements with the normal hot-wire probe was estimated to be less than 5% of the free-stream speed for flow speeds greater than about 2 m/s, based on an extensive study on hot-wire error completed by Kawall et al. [142]. Lower speed measurements presented in this thesis were influenced by more significant sources of error, including those due to mean surface normal flow, hot-wire signal rectification, and enhanced conductive heat transfer to the airfoil model, each of which are discussed below.

As discussed in Section 2.3.3, there is no generally accepted correction method for near wall conductive heat transfer errors in hot-wire measurements acquired in separation bubbles. No corrections have been made in this thesis for near wall conductive losses in hot-wire measurements. The thickness of the layer affected by enhanced conductive heat transfer to the model was estimated to be $0.0015c$ from hot-wire measurements with zero free-stream speed. The thickness of the affected region is expected to be smaller with a non-zero free-stream speed, due to more dominant convective losses from the wire. However, the zero flow condition is used to estimate an upper bound on the error due to convective losses of $0.06U_\infty$ near the wall.

Hot-wire rectification error can significantly affect the mean and RMS velocity measurements in a separated shear layer. Based on the measured velocity at the location of $y = \delta_0$, the uncertainty due to rectification error, after negating the mean reverse flow speed measurement, is estimated to be less than 25% of the free-stream speed.

Particularly between the transition and reattachment points, directional unsteadiness and high vertical velocities contribute to significant hot-wire errors [53, 99]. In the experiments discussed in this thesis, separated shear layer measurements below the separation streamline and between the transition and reattachment locations were exposed to strong vertical velocity fluctuations, and as a result the hot-wire measurement error is high in this region. Based on the separated shear layer measurements presented in Chapter 6, it is estimated that the uncertainty in normal hot-wire measurements between the transition and reattachment locations and between the airfoil surface and the mean separation streamline, due to high mean vertical flow speed, is less than 25% of the free-stream speed.

It should be noted that the high uncertainty in the reverse flow hot-wire measurements have a less significant effect on post-processed results, including LST predictions, boundary layer thickness estimates, and disturbance growth rate measurements. Although the uncertainty is very limiting in the study of flow below the separation streamline, it was not limiting for most of the analysis presented in this thesis. The uncertainty cited here does not include those profiles identified in Chapter 6 as having separation induced by the presence of the hot-wire probe.

A cross-wire probe was used to measure the vertical velocity fluctuations in the airfoil wake for the purpose of estimating the vortex shedding frequency and other features of the spectral energy distribution. Based on the study by Kawall et al. [142], the uncertainty in the RMS vertical velocity is estimated to be less than 5% of the free-stream speed.

Uncertainty in the measured distance of the hot-wire probe from the airfoil surface also affects the shear layer profile measurements presented in Chapter 6. This uncertainty was assessed in two ways, one based on optical resolution and the other based on measurement repeatability. The position measurement requires determining four points on digital photographs, two calibration grid locations, the tip of the hot-wire prong, and the surface location directly below the hot-wire probe. From these images, the operator could be confident in the location of each of these points to within ±1.5 pixels. Since each distance measurement is based on the locations of four points, the uncertainty in the measurement is the combined uncertainty in determining the coordinates of each point. Based on the optical resolution of the system, the uncertainty in the measured hot-wire probe position was estimated to be less than 0.05 mm. The number of traverse motor steps from the initial probe location, after traverse lead screw backlash was removed, was used to determine all other positions away from the model surface. As such, the uncertainty in traverse movements had to be assessed. This was done by moving the probe to thirty arbitrary locations and using the optical measurement device to measure the distance traveled. Furthermore, each image was processed five times to determine the variability in measured distance with the optical system. By this approach, the total uncertainty due to the operator of the optical measurement device, variability in the traverse movement, and error in the optical measurement procedure was estimated to be less than 0.05 mm. It was also found that the uncertainty in traverse movement over fifty 1 mm movements was purely due to variability; error stack-up over long traverses was less than the measurement uncertainty.

Disturbance growth rate measurements are affected by several sources of error. A main source of uncertainty is the combined error in hot-wire measurements resulting from computing the slope of the RMS velocity in the streamwise direction. This contribution to the uncertainty is estimated to be less than $10/c$ based on an uncertainty in RMS velocity measurements of $0.05U_\infty$. As can be seen in Fig. 6.19, the measured RMS growth in the separated flow region is not perfectly exponential. As a result, the estimated growth rate can be affected by the measurement points included in the calculation. Similarly, the streamwise spatial resolution of measurements contributes to the error in computed growth rate by affecting the number of points over which the growth rate is averaged and the confidence that the points used in the estimate are in the linear growth region. Based on a sensitivity analysis of the computed growth rate magnitudes to the points included in the calculation, the uncertainty in reported growth rate measurements due to the calculation procedure and the spatial resolution is estimated to be less than 10% of the computed growth rate at each point. Finally, error is introduced into the growth rate measurements through band-pass filtering the hot-wire signals to decompose the growth rate into frequency components. This has the effect of averaging the modal growth rate over a narrow band of frequencies and also introduces errors due to imperfect filter design.

Since this error is difficult to quantify, and is likely small in comparison to the 10% errors introduced by other sources, this component is neglected. The combined uncertainty reported in the growth rates obtained from hot-wire measurements is estimated to be less than $\sqrt{(10/c)^2 + (0.1\alpha_i)^2}$.

Disturbance amplitude profiles for particular frequencies were computed from the RMS velocity measurements after band-pass filtering. The uncertainty in this type of measurement is difficult to quantify, but results from uncertainty in the RMS velocity measurements and due to the filtering operation. It is conservatively estimated to be less than 10% of the free-stream speed, outside of the low speed and reverse flow regions near the wall.

Boundary layer thickness parameters were computed from hot-wire measurements. These estimates are susceptible to hot-wire errors and uncertainty due to the estimation method. Displacement thickness and momentum thickness estimates are insensitive to the estimate of δ_e, because the integrand in their definitions is nearly zero for $U/U_e \approx 1$. The main contribution to uncertainty in these estimates are those due to hot-wire error at low speeds, in the reverse flow region and near the wall. The uncertainties in the measured displacement and momentum thicknesses were estimated based on a bias in the reverse flow velocity of 10% of the free-stream velocity and over a vertical distance of roughly $0.5\delta^*$. By this method, the uncertainty in the reported displacement and momentum thicknesses is estimated to be less than 5%. Boundary layer shape factor is determined as the ratio of these two parameters. The maximum uncertainty in the boundary layer thickness shape factor is estimated to be less than $0.105H$. Estimates of the zero velocity locations are also affected by hot-wire rectification error and mean vertical flow. The uncertainty in this location is estimated from the separated shear layer profiles presented in Chapter 6. It can be seen that as the wall is approached from the free stream, at a certain location the nearly linear velocity profile curves to have zero slope. It is physically expected that this roughly linear trend will continue into the start of the reverse flow region. Therefore, the uncertainty in the determined zero velocity location can be estimated as the distance between the location where the velocity profile begins to deviate significantly from the linear trend and the intersection of the extrapolated linear shear region to the zero velocity axis. Based on this approach, the worst case uncertainty in the reported zero velocity location is estimated to be less than $0.001c$ for cases of boundary layer reattachment and $0.01c$ for cases without boundary layer reattachment.

Locations of separation and transition were determined from hot-wire measurements for $AOA = 15^\circ$, i.e., for the stalled case. From the profiles and energy spectra presented in Chapter 6, the locations of separation and transition could be identified with confidence to within one profile location on either side. This was used as the uncertainty estimate for x_S/c and x_T/c for the stalled case.

The wake vortex shedding frequency was estimated as the central frequency of the peak in the energy spectrum of vertical velocity fluctuations. The sample rate and the number of averages used in the discrete Fourier transform were set to values that ensured that the frequency resolution in the computed energy spectrum produced a negligible contribution to the uncertainty in the identified vortex shedding frequency. The main contribution to the uncertainty was in identifying the central frequency of the spectral peak, which has width and contains noise from the hot-wire signal. For $AOA = 15°$, the central frequency could be determined with confidence to within ±0.25 Hz. Uncertainty in the central instability frequency was similarly estimated to be within ±25 Hz.

A.3 Uncertainty in Static Pressure Measurements

In this section, the uncertainty of mean static pressure measurements and the uncertainty in values obtained from these measurements are estimated. The estimates in this section apply to both model surface pressure and test section wall pressure measurements.

The most significant source of uncertainty in the mean static pressure measurements reported in this thesis were introduced through the calibration method. A constant pressure was applied to an inclined manometer with 0.25 Pa minor divisions and to the pressure transducer. This was repeated for ten pressure levels over the operating range for the experiment. A linear fit over these data was then used to interpolate mean static pressure from transducer voltage measurements. The uncertainty in the inclined manometer measurement was estimated to be less than 0.50 Pa. Error in the measured voltage was estimated as the discretization error of the data acquisition system to be less than 0.05 Pa. Deviation in the pressure-voltage response from the linear fit was estimated to be less than 0.005 Pa, as the maximum deviation from the average which could be estimated from any two calibration points.

Pressure transducer calibration curves are sensitive to temperature. The most significant effect is removed by measuring the zero pressure voltage offset before each experiment, and shifting the measured voltage data by the change in this quantity from the calibration data. However, temperature changes during the experiment can still cause a time dependent error in the measurements. Furthermore, changes in the linear calibration fit slope with temperature can have an effect on the measurements. Based on zero pressure voltage offset measurements, acquired before and after each of twenty pressure distribution measurements, it was estimated that the uncertainty due to zero pressure voltage offset drift during an experiment is less than 0.1 Pa. The manufacturer specified pressure-voltage response slope variation with temperature for the Lucas Schaevitz P3061-2WD pressure transducer is 0.02%/°C. During all of the measurements reported in this thesis, the ambient temperature was recorded to deviate by less than 1°C from the calibration value. This variation contributes to the uncertainty, because no adjustment was made for changes in the calibration fit slope. The uncertainty due to variation in the pressure-voltage response slope was estimated to be less than 0.1 Pa. The time required to calibrate the system was short enough that no measured temperature variation was recorded. Thus, the uncertainty due to temperature drift during calibration was neglected. Furthermore, temperature variation in the resistance of the cables connecting the transducer to the data acquisition card was neglected.

Static pressure tap geometry can affect mean static pressure measurements [143]. The static pressure tap geometry can cause a small local change in streamline curvature above the tap, inducing a small centrifugal force, which increases the measured pressure, or can produce a small separated flow region, decreasing the measured pressure [143]. Based on a number of experiments summarized by Chue [143], the maximum error due to pressure tap geometry in this study is estimated to be less than 0.14 Pa.

Rise time for pressure in the static lines was estimated by continuously sampling each pressure tap for 200 s after setting the Scanivalve mechanical multiplexer system to measure that tap. These data were used to determine the delay time between incrementing the Scanivalve mechanical multiplexer setting and beginning to acquire the measurement. In a similar way, the sample time required to obtain a stable ensemble average was determined from subsets of these data. Since the static pressure lines are relatively long, pressure fluctuations of the time scale observed in this experiment are expected to have a negligible influence on instantaneous measurements. Longer time scale fluctuations, resulting from variation in the fan speed, may still be observed. As a result, the mean static pressure can vary slowly with time. This introduces uncertainty in the pressure measurement due to both the selected rise time and sample duration. Based on the variability in one second averages of mean static pressure over two minutes for each pressure tap, it was estimated that the uncertainty due to long time variations in the mean static pressure are less than 0.13 Pa.

Prior to acquiring mean static pressure measurements, the zero pressure voltage offset was measured to compensate for temperature drift in this quantity. Thus, each static pressure measurement is based on the voltage from the transducer when exposed to the pressure differential that is to be measured, and a voltage measurement with zero pressure differential across the transducer. As a result, the uncertainty in the measured voltage at zero pressure contributes to the uncertainty in the mean static surface pressure measurement. A discretization error of less than 0.05 Pa and due to long time variation in the ensemble average of less than 0.13 Pa contribute to this uncertainty. The measurement of static surface pressure is also subject to a discretization error of less than 0.05 Pa.

The repeatability of an experiment is another source of uncertainty. This includes uncertainty in the measured surface pressure distribution due to error in setting the angle of attack and free-stream speed as well as any changes between experiments that were not realized or could not be controlled. This component of uncertainty was estimated based on three model surface pressure distributions, measured on different days over a one month period. The second standard deviation of the difference between each set of measurements was estimated to be less than 0.03 Pa.

Combining the uncertainties described above based on the procedure described by Moffat [141] leads to an estimated total uncertainty in the static pressure measurements of less than 0.56 Pa, or equivalently, less than 1.6% of the free-stream dynamic pressure.

Aerodynamic forces on the airfoil model were computed from mean surface pressure measurements. In this calculation, more than 95% of the lift force resulted from the pressure difference between the upper and lower surface at each location along the chord, multiplied by the area over which those pressures acted. On this basis, the uncertainty in the pressure difference used in the integration was estimated to be the combined uncertainty of two pressure measurements, i.e., 2.3% of the free-stream dynamic pressure. The static pressure taps have a finite size, and an uncertainty in their location on the model, contributing to uncertainty in the computed lift coefficient through uncertainty in the distance between taps used in the numerical integration. Based on the specified model manufacturing tolerances (see Ref. [35]), the uncertainty in the location of each pressure tap is estimated to be less than $0.0002c$. The pressure across the finite size pressure tap is expected to be a central value over the tap. Therefore, the contribution of the finite pressure tap size to uncertainty in the lift coefficient is neglected. Based on these estimates, the combined uncertainty in the lift coefficient due to uncertainty in mean static pressure measurements and pressure tap locations is expected to be less than 2.4% of the free-stream dynamic pressure per unit span.

For angles of attack at which flow reattachment occurs, locations of separation, transition, and reattachment were estimated from model surface pressure distributions. Thus, the uncertainties in these estimates are based on the spatial resolution of model surface pressure taps. The laminar portion of the separation bubble can be estimated from mean static pressure measurements as the region of nearly constant surface pressure downstream of the suction peak, and followed by a region of steep pressure recovery [52]. The separation location can be estimated as the start of the region of constant pressure. Since this pressure plateau can make a small angle to the inviscid flow pressure distribution, it is estimated that this location can be determined to within three static pressure taps, i.e., ±4 mm. The transition location can be identified as the start of the steep pressure recovery region [8]. Since in the present investigation, the pressure recovery region in the separation bubble was always very distinct, it was estimated that the transition location could be determined to within one static pressure tap, i.e., ±2 mm. The reattachment location can be determined as the location where a marked decrease in the rate of surface pressure recovery is observed [8]. This location is also very distinct, and can be estimated to within one static pressure tap, i.e., ±2 mm.

A.4 Microphone Measurement Uncertainty

Microphone measurement uncertainty results from the calibration approximations and the background noise level. During calibration, it was assumed that the pressure voltage response of the microphone was linear with amplitude. Furthermore, the microphone sensitivity was assumed to be independent of frequency in the operating range. For the microphone array used in experiments discussed in this thesis, the validity of these assumptions were demonstrated by Gerakopulos [35]. Based on the calibration data presented by Gerakopulos [35], the uncertainty due to the measured sensitivity coefficient and the calibration procedure is estimated to be less than 20%. Ambient noise in the laboratory as well as electrical noise resulting from signal amplification and interference with other equipment also contribute to the measurement uncertainty. Gerakopulos [35] presents the RMS surface pressure measured by each microphone with the wind tunnel off. Wind tunnel generator and fan noise are also expected to contribute to this uncertainty. The uncertainty in $\tilde{p}/q_\infty$ due to background noise was estimated from the minimum value of RMS surface pressure measured in the experiments to be approximately 0.02. Therefore, the total uncertainty in $\tilde{p}/q_\infty$ is estimated to be less than $\sqrt{(0.02)^2 + (0.20\tilde{p}/q_\infty)^2}$.

Disturbance growth rate estimates from microphone measurements have similar sources of uncertainty as those estimates obtained from hot-wire measurements. Specifically, the uncertainty in the RMS surface pressure measurements, the sensitivity of the estimated exponential growth coefficient to the spatial locations included in the average, and the spatial resolution of the measurements all contribute to the overall uncertainty in the growth rate measurement. For hot-wire data, measurement locations could be selected to limit the error due to spatial resolution in growth rate estimates. This was not possible with the microphone array. As a result, the uncertainty in the growth rate estimate for small separation bubble cases is relatively high. Employing the same method as for growth rate measurements from hot-wire data, the uncertainty in growth rate measurements from microphone data was estimated to be less than $\sqrt{(10/c)^2 + (0.3\alpha_i)^2}$.

Convection speed was determined as the ratio of the distance between two microphones in the separated shear layer to the time lag between the two microphone signals. The time lag was determined from the cross-correlation function of the two microphone signals. The uncertainty in the time lag is estimated to be less than 4% from the ratio of the dominant disturbance frequency to the sample rate. The uncertainty in the computed convection speed is then estimated to be less than 3.5% of the free-stream speed. This estimate is also used for the uncertainty in the phase speed estimates, which are computed in a similar way. Measured phase speeds are not directly reported in this thesis, but are used in computing the real wave number spectrum. The frequency component is also used in the wave number calculation, and therefore, the uncertainty resulting from averaging over a frequency band also affects the result. Combining these sources of uncertainty, the total uncertainty in measured $\alpha_r c$ values is estimated to be less than $\sqrt{(8)^2 + (0.04\alpha_r c)^2}$.

A.5 Uncertainty in SLW Configuration

Sumner [113] estimated the uncertainty in setting the wall contours of the University of Waterloo adaptive-wall wind tunnel to be less than 1 mm. Uncertainty in the calculated wall configuration results from uncertainty in wall contour settings, uncertainty in wall pressure measurements, and variation in the wall boundary layer thickness due to the presence of the model. The repeatability of the SLW coordinates was estimated by computing these contours based on pressure measurements in the final SLW configuration on two separate days. The SLW coordinates for each angle of attack were repeatable to within 1.5 mm. Employing a model for boundary layer thickness on a flat plate with an imposed pressure gradient, it was estimated that the uncertainty in the SLW configuration due to pressure gradient induced displacement thickness variation is less than 1 mm. Combining these factors, the total uncertainty in the SLW coordinates is estimated to be less than 2.1 mm. Uncertainty in the ASW contours results from error in setting the walls and in the $1/7^{\mathrm{th}}$ power law turbulent boundary layer growth approximation, including error in the measured virtual origin and in the side wall boundary layer growth multiplying factor. The $1/7^{\mathrm{th}}$ power law estimate was determined to be accurate through measurements of the side wall boundary layer thickness, and was found to be insensitive to the uncertainty in the measured input parameters.

Appendix B

End Plate Design

As discussed in Section 3.1.2, the design of end plates has been studied in several prior investigations [11–14,82]. The end plate design used in the present investigation is described here, and technical drawings of the final assembly are provided.

The end plates were to be designed based on those employed in similar low Reynolds number airfoil investigations. The end plate spacing needed to be adjustable, and the end plates had to fit on an existing NACA 0018 model. Furthermore, for the purpose of flow visualization, it was desirable for the end plates to produce minimal optical obstruction of the center-span plane and to limit the reflection of light from the off-camera flash.

The end plates used on the airfoil are illustrated in Fig. 3.2. The end plates clamp on to the model as opposed to the axle, which allows for changes of the end plate spacing without changing the model blockage ratio [83, 84]. Weather striping was used to seal the interface between the end plates and the airfoil, as reported for the low Reynolds number airfoil experiments in Ref. [10].

The end plate on the acrylic wall side was machined from transparent Lexan to allow for photographs of the center-span plane. The end plate on the particle board wall side was machined from aluminum and painted a matte black to limit the reflection of light from this end plate in flow visualization images. Such a configuration, in which one end plate is made of aluminum and the other of a transparent material, was also employed in the low Reynolds number airfoil experiments in Ref. [9] to facilitate flow visualization photographs. Lexan was selected as the transparent end plate material for ease of machining.

Circular end plates were chosen to limit changes in the effective end plate configuration with changes in the angle of attack. Despite the finding for a circular cylinder that rectangular end plates produce a flow most representative of that over a wide-span model [11], circular end plates have been used in this investigation because studies on square cylinders indicate that the flow is affected when rectangular end plates are rotated with the model [82]. Furthermore, circular end plates are common in low Reynolds number airfoil experiments [86, 88].

Dimensions for the end plates were selected based on those used in other low Reynolds number airfoil experiments, and to follow the general guidelines developed for other geometries [11, 13, 14]. An end plate diameter of 45 cm, greater than twice the chord length, was selected based on the dimensions used by Lee & Gerontakos [88] for a low Reynolds number airfoil experiment. This diameter also allowed the end plates to extend 9 cm upstream of the model and 16 cm downstream of the model. For $AOA \lesssim 15°$, the end plates extend more than 2.5 model heights upstream of the model axle and 4.5 model heights downstream, as recommended for circular cylinder models [11, 14]. The end plate thickness was chosen to be 6.35 mm based on rigidity tests on end plates of various thicknesses in the wind tunnel at typical operating speeds for this model.

As seen in the technical drawings in Section B.1, the end plates were designed to slide on to the model from the trailing edge. This limited optical obstruction in flow visualization images from the seams in the end plates. The end plates were secured by clamping pieces that screwed into the side of the main plate, on the test section wall side. The through holes in one clamp were over sized so that the end plates could be secured by compression from the top and bottom connector pieces.

B.1 End Plate Drawings

The following pages provide technical drawings for the aluminum end plate components. The Lexan end plate is a mirror image of this design, across the center-span plane. Other than the material, the only difference between the end plates is that the type of holes used in the top connector and the bottom connector are interchanged.

UNLESS OTHERWISE SPECIFIED:

DIMENSIONS ARE IN MILLIMETERS
TOLERANCES:
FRACTIONAL± 0.001 in
ANGULAR: MACH± BEND ±
TWO PLACE DECIMAL ±
THREE PLACE DECIMAL ±

ITEM NO.	DESCRIPTION	QTY.
1	PLATE	1
2	LEADING EDGE INSERT	1
3	TOP CONNECTOR	1
4	BOTTOM CONNECTOR	1
N/A	10-24 UNC 1/2 IN HEX SOCKET FLAT HEAD SS CAP SCREW (P/N: 370-308)	4
N/A	10-24 UNC 1/2 IN HEX SOCKET BUTTON HEAD SS CAP SCREW (P/N: 370-408)	6

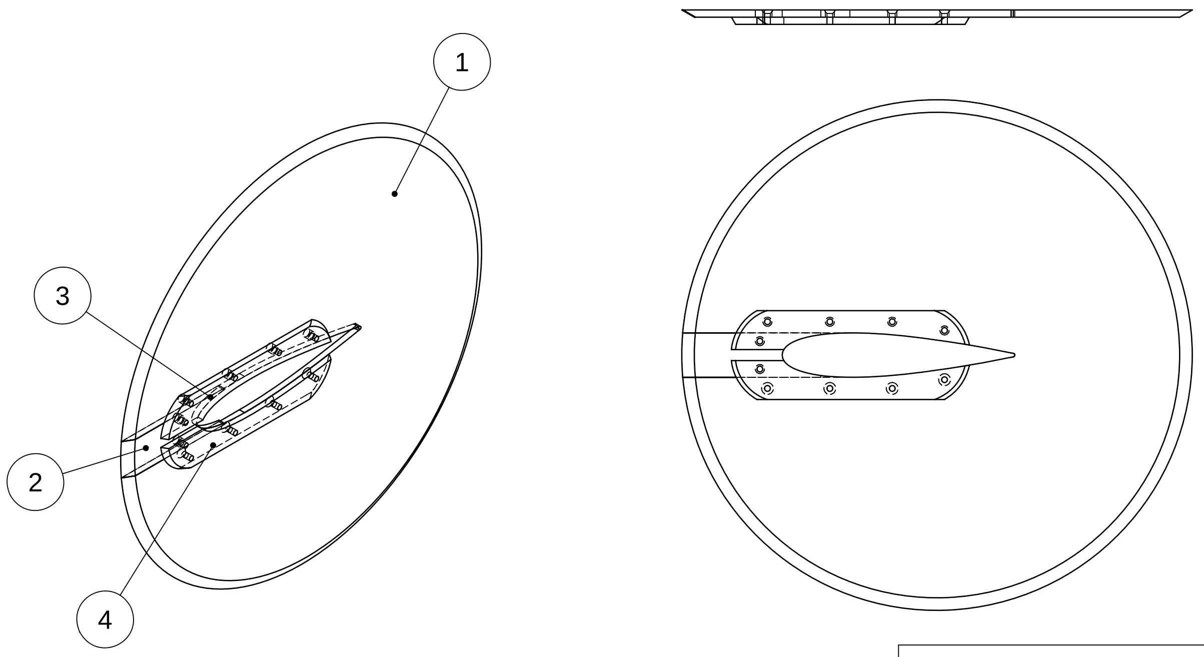

PROPRIETARY AND CONFIDENTIAL

THE INFORMATION CONTAINED IN THIS DRAWING IS THE SOLE PROPERTY OF UW FWWT GROUP. ANY REPRODUCTION IN PART OR AS A WHOLE WITHOUT THE WRITTEN PERMISSION OF UW FWWT GROUP IS PROHIBITED.

			NAME	DATE
MATERIAL	ALUMINIUM 6061			
FINISH	N/A	DRAWN	MSHB	
DO NOT SCALE DRAWING		CHECKED		

END PLATE ASSEMBLY

SIZE A
ASSEMBLY: END PLATE
REV
SCALE: 1:5
QTY: 1
SHEET 1 OF 5

5 4 3 2 1

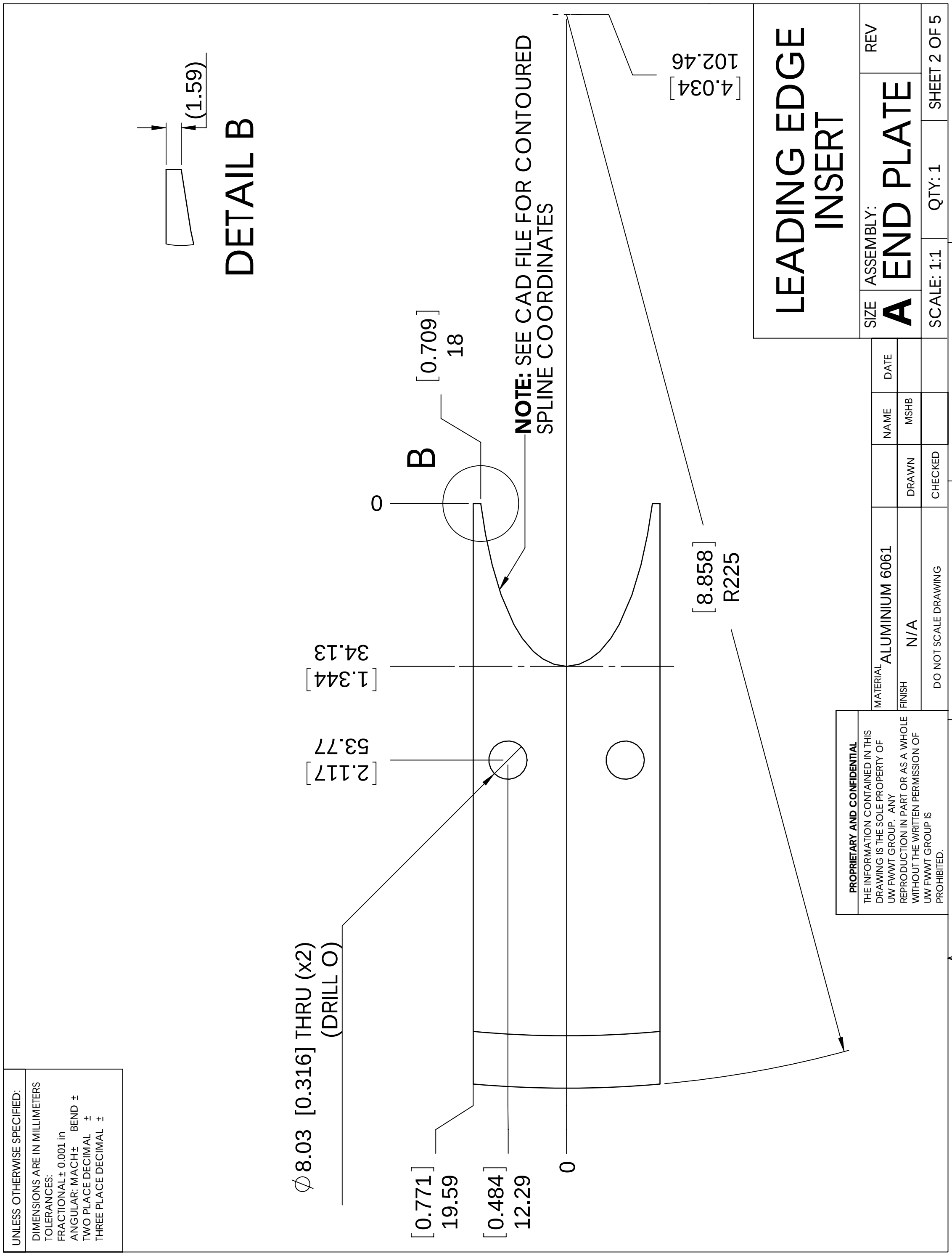
UNLESS OTHERWISE SPECIFIED:
DIMENSIONS ARE IN MILLIMETERS
TOLERANCES:
FRACTIONAL± 0.001 in
ANGULAR: MACH ± BEND ±
TWO PLACE DECIMAL ±
THREE PLACE DECIMAL ±
(1.59)
DETAIL B
[0.709] 18
B
0
NOTE: SEE CAD FILE FOR CONTOURED SPLINE COORDINATES
102.46 [4.034]
[8.858] R225
34.13 [1.344]
53.77 [2.117]
⌀8.03 [0.316] THRU (x2) (DRILL O)
[0.771] 19.59
[0.484] 12.29
0
PROPRIETARY AND CONFIDENTIAL
THE INFORMATION CONTAINED IN THIS DRAWING IS THE SOLE PROPERTY OF UW FWWT GROUP. ANY REPRODUCTION IN PART OR AS A WHOLE WITHOUT THE WRITTEN PERMISSION OF UW FWWT GROUP IS PROHIBITED.
MATERIAL ALUMINIUM 6061
FINISH N/A
DO NOT SCALE DRAWING
NAME
DATE
DRAWN
MSHB
CHECKED
LEADING EDGE INSERT
SIZE
A
ASSEMBLY:
END PLATE
REV
SCALE: 1:1
QTY: 1
SHEET 2 OF 5
1
2
3
4
5

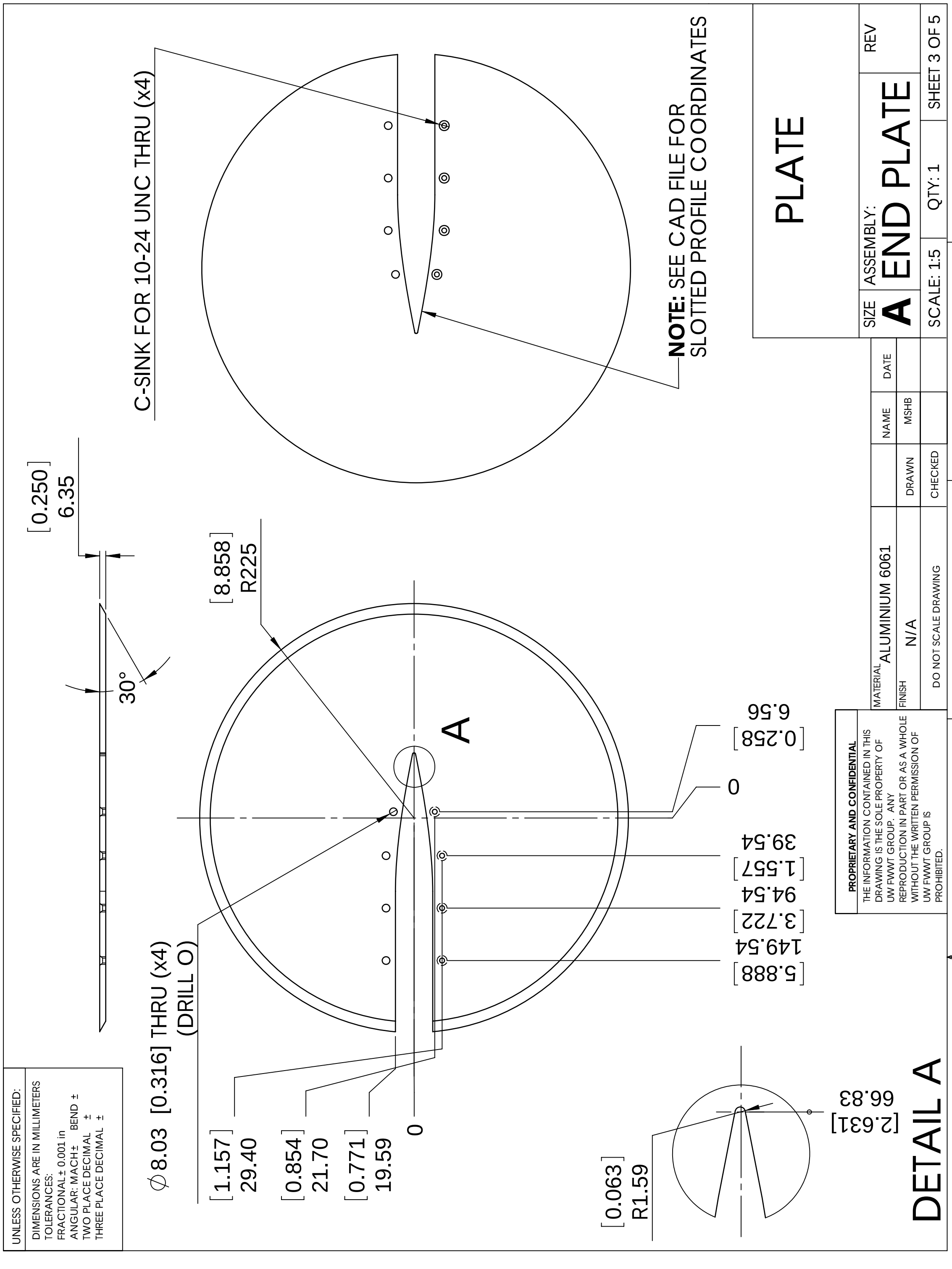
UNLESS OTHERWISE SPECIFIED:
DIMENSIONS ARE IN MILLIMETERS
TOLERANCES:
FRACTIONAL± 0.001 in
ANGULAR: MACH ± BEND ±
TWO PLACE DECIMAL ±
THREE PLACE DECIMAL ±
C-SINK FOR 10-24 UNC THRU (x4)
NOTE: SEE CAD FILE FOR SLOTTED PROFILE COORDINATES
[0.250] 6.35
[8.858] R225
30°
A
Ø8.03 [0.316] THRU (x4) (DRILL O)
[1.157] 29.40
[0.854] 21.70
[0.771] 19.59
0
[0.258] 6.56
0
39.54 [1.557]
94.54 [3.722]
149.54 [5.888]
[0.063] R1.59
66.83 [2.631]
DETAIL A
PROPRIETARY AND CONFIDENTIAL
THE INFORMATION CONTAINED IN THIS DRAWING IS THE SOLE PROPERTY OF UW FWWT GROUP. ANY REPRODUCTION IN PART OR AS A WHOLE WITHOUT THE WRITTEN PERMISSION OF UW FWWT GROUP IS PROHIBITED.
MATERIAL ALUMINIUM 6061
FINISH N/A
DO NOT SCALE DRAWING
NAME
DATE
DRAWN MSHB
CHECKED
PLATE
SIZE A
ASSEMBLY: END PLATE
REV
SCALE: 1:5
QTY: 1
SHEET 3 OF 5
1
2
3
4
5

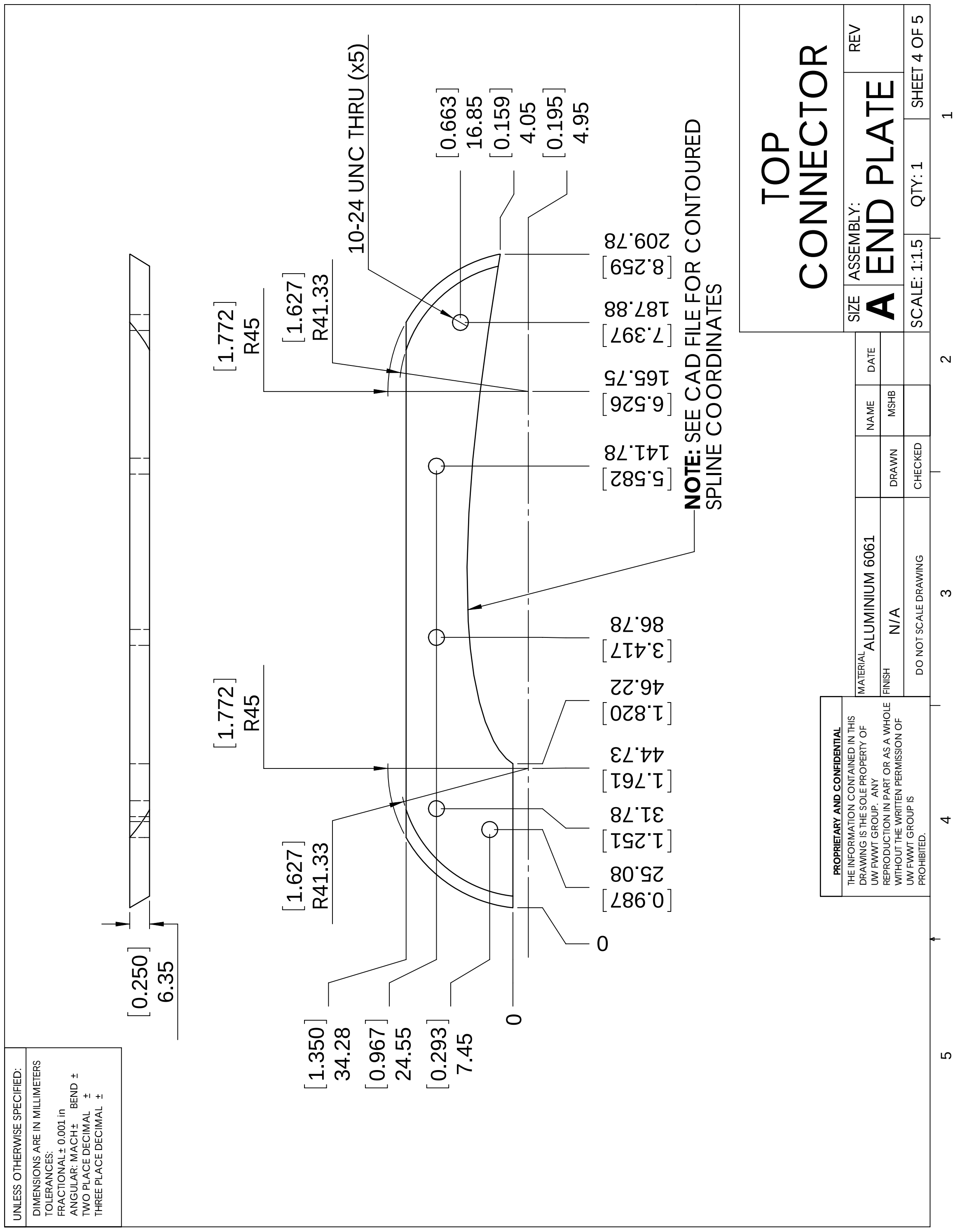
TOP CONNECTOR
SIZE A
ASSEMBLY: END PLATE
REV
SCALE: 1:1.5
QTY: 1
SHEET 4 OF 5
MATERIAL ALUMINIUM 6061
FINISH N/A
DO NOT SCALE DRAWING
NAME
DATE
DRAWN MSHB
CHECKED
PROPRIETARY AND CONFIDENTIAL
THE INFORMATION CONTAINED IN THIS DRAWING IS THE SOLE PROPERTY OF UW FWWT GROUP. ANY REPRODUCTION IN PART OR AS A WHOLE WITHOUT THE WRITTEN PERMISSION OF UW FWWT GROUP IS PROHIBITED.
UNLESS OTHERWISE SPECIFIED:
DIMENSIONS ARE IN MILLIMETERS
TOLERANCES:
FRACTIONAL ± 0.001 in
ANGULAR: MACH ± BEND ±
TWO PLACE DECIMAL ±
THREE PLACE DECIMAL ±
10-24 UNC THRU (x5)
NOTE: SEE CAD FILE FOR CONTOURED SPLINE COORDINATES
[0.250] 6.35
[1.772] R45
[1.627] R41.33
[1.772] R45
[1.627] R41.33
[0.663] 16.85
[0.159] 4.05
[0.195] 4.95
[1.350] 34.28
[0.967] 24.55
[0.293] 7.45
0
0
[0.987] 25.08
[1.251] 31.78
[1.761] 44.73
[1.820] 46.22
[3.417] 86.78
[5.582] 141.78
[6.526] 165.75
[7.397] 187.88
[8.259] 209.78
1
2
3
4
5

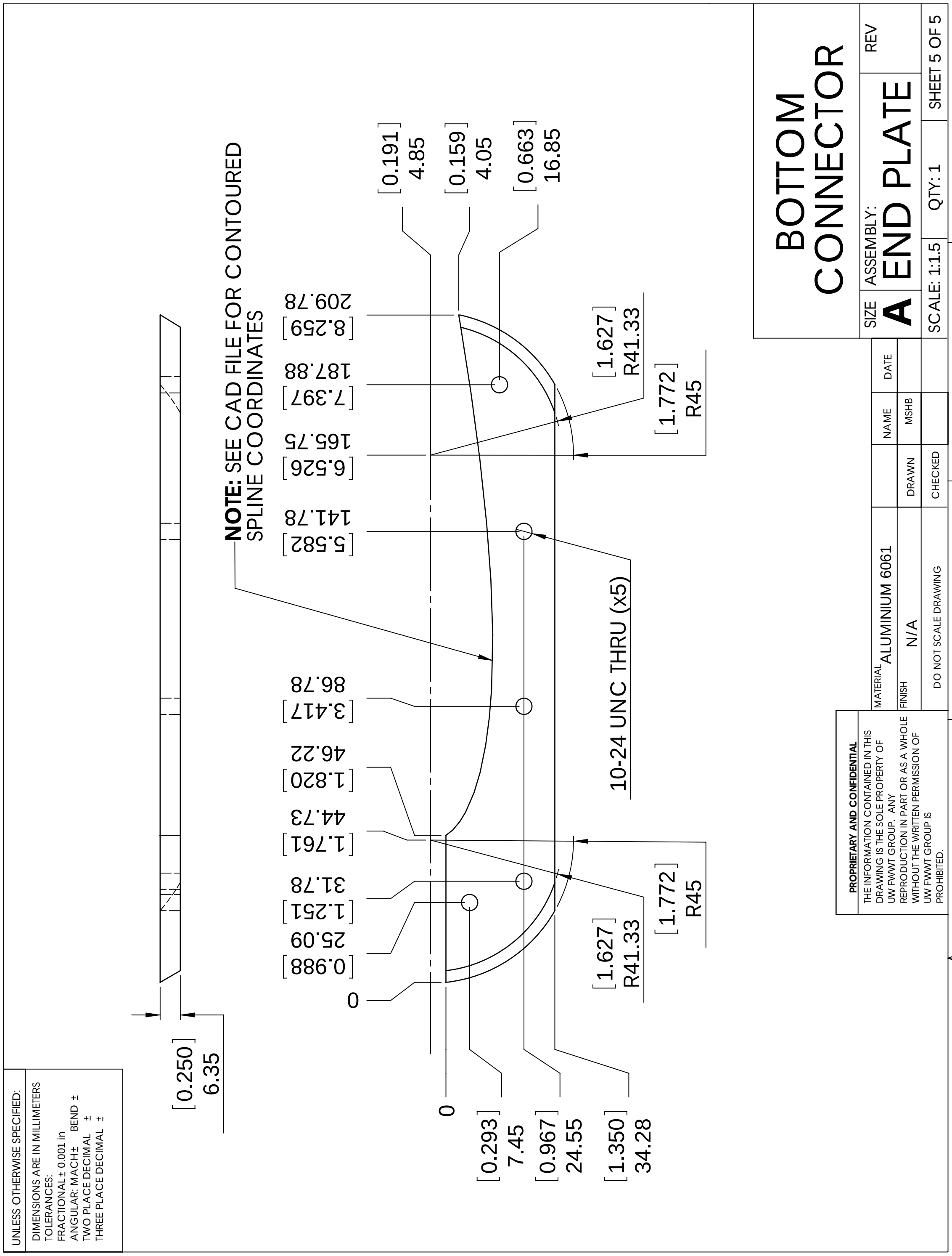
BOTTOM CONNECTOR
SIZE A
ASSEMBLY: END PLATE
REV
SCALE: 1:1.5
QTY: 1
SHEET 5 OF 5
MATERIAL ALUMINIUM 6061
FINISH N/A
DO NOT SCALE DRAWING
NAME
DATE
DRAWN MSHB
CHECKED
PROPRIETARY AND CONFIDENTIAL
THE INFORMATION CONTAINED IN THIS DRAWING IS THE SOLE PROPERTY OF UW FWWT GROUP. ANY REPRODUCTION IN PART OR AS A WHOLE WITHOUT THE WRITTEN PERMISSION OF UW FWWT GROUP IS PROHIBITED.
UNLESS OTHERWISE SPECIFIED:
DIMENSIONS ARE IN MILLIMETERS
TOLERANCES:
FRACTIONAL± 0.001 in
ANGULAR: MACH± BEND ±
TWO PLACE DECIMAL ±
THREE PLACE DECIMAL ±
NOTE: SEE CAD FILE FOR CONTOURED SPLINE COORDINATES
10-24 UNC THRU (x5)
[0.191] 4.85
[0.159] 4.05
[0.663] 16.85
[1.627] R41.33
[1.772] R45
[1.627] R41.33
[1.772] R45
[8.259] 209.78
[7.397] 187.88
[6.526] 165.75
[5.582] 141.78
[3.417] 86.78
[1.820] 46.22
[1.761] 44.73
[1.251] 31.78
[0.988] 25.09
0
[0.250] 6.35
0
[0.293] 7.45
[0.967] 24.55
[1.350] 34.28
1
2
3
4
5

Appendix C

Scanivalve Control System

In order to reduce the uncertainty in wall and model surface pressure measurements for the low pressures to be measured in this investigation, the digital pressure scanners used in recent experiments in this facility [35, 92] were replaced with Scanivalve mechanical multiplexers. The main advantage of this system is that a pressure transducer with a narrower operating range than those in the existing digital pressure scanner system, described in Ref. [92], could be used. A schematic of the wiring and pneumatic connections of the Scanivalve mechanical multiplexer system is presented in Fig. C.1, with descriptions of components and cables provided in Table C.1. Figure C.2 presents the control circuit developed to relay the data acquisition system commands to the Scanivalve mechanical multiplexer solenoids and to signal when each multiplexer is in the home position. The main control circuit was deigned and built by Neil Griffett and was later modified to switch between active solenoids, so that the same circuit could be used to control multiple pairs of solenoids.

Control logic for the system was programmed in LabVIEW. At the start of operation, the Scanivalve units are returned to the home position, i.e., the zero pressure voltage offset measurement location. This is accomplished by sending a square wave signal to the control circuit, instructing the Scanivalve units to step through measurement positions until the home position signal is returned. At this first measurement location, the pressure transducer is connected on both sides to a constant reference pressure, allowing the zero pressure voltage offset to be measured. Following this measurement, the system steps through each of the measurement positions and samples the voltage response of the pressure transducer for a set period. Because there are a total of 235 static pressure taps along the walls and on the model, whereas single multiplexer wafers only contain twenty-four inputs, the SV1 unit is used to change the wafers on the SV2, SV3, and SV4 units that are

Table C.1: Description of labels in Fig. C.1.

label	description
module	
Ctrl Box	control circuit detailed in Fig. C.2
DAQ	data acquisition system
PS	power supply
PT	pressure transducer
SV1	Scanivalve mechanical multiplexer 1
SV2	Scanivalve mechanical multiplexer 2
SV3	Scanivalve mechanical multiplexer 3
SV4	Scanivalve mechanical multiplexer 4
electrical cables	
❶	24 VDC power from PS to Ctrl Box
❷	Ctrl Box Scanivalve 2 terminal block to solenoid and home position indicator of SV2
❸	Ctrl Box Scanivalve 3 terminal block to solenoid and home position indicator of SV3
❹	Ctrl Box Scanivalve 4 terminal block to solenoid and home position indicator of SV4
❺	Ctrl Box Scanivalve 1 terminal block to solenoid and home position indicator of SV1
❻	Ctrl Box DAQ terminal block to 5 VDC supply, ground, digital input 1-2, and digital output 1-2 of DAQ
❼	PT output to analog input 1 of DAQ
pneumatic lines	
①	from upper wall pressure taps to SV2; taps 1-24 connect to disk 1, 2-48 to disk 2, and 48-70 to disk 3
②	from airfoil pressure taps to SV3; taps 1-24 connect to disk 1, 2-48 to disk 2, 48-72 to disk 3, and 73-95 to disk 4
③	from lower wall pressure taps to SV3; taps 1-24 connect to disk 1, 2-48 to disk 2, and 48-70 to disk 3
④	from SV2 to SV1; outputs of SV2 disks 1-3 connect to inputs 6-8 of SV1 disk 1
⑤	from SV3 to SV1; outputs of SV3 disks 1-4 connect to inputs 2-5 of SV1 disk 1
⑥	from SV4 to SV1; outputs of SV4 disks 1-3 connect to inputs 9-11 of SV1 disk 1
⑦	from the reference static pressure taps to SV1 disk 1 input 1 and PT
⑧	SV2 disk 1 output to PT

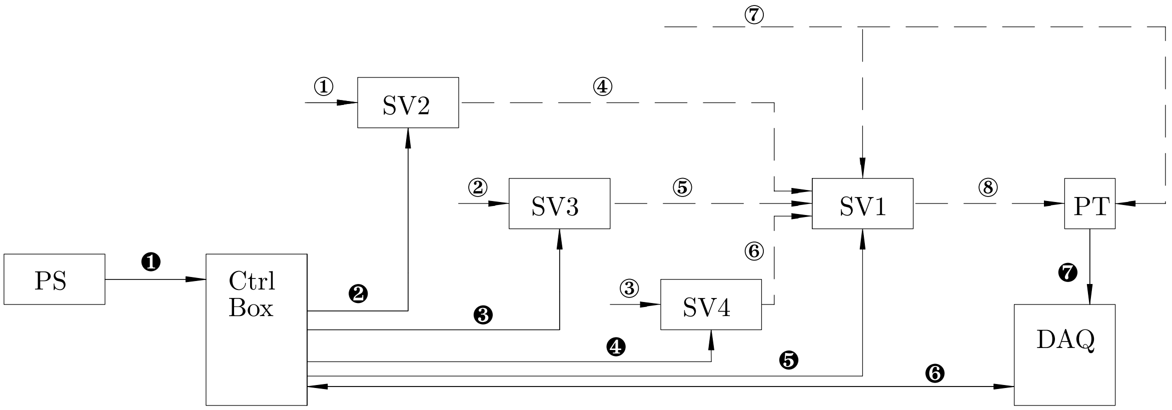

Figure C.1: Scanivalve mechanical multiplexer system pneumatic and electrical connection routing diagram.

Table C.2: Description of terminal wires in Fig. C.2.

terminal	description
power	
1	+24 VDC from power supply
2	power supply ground
DAQ terminal block	
3	DAQ +5 VDC power
4	DAQ ground
5	DAQ digital output 1
6	DAQ digital output 2
7	DAQ digital input 1
8	DAQ digital input 2
Scanivalve terminal blocks	
9, 13, 17, 21	solenoid power
10, 14, 18, 22	solenoid power return
11, 15, 19, 23	home position indicator
12, 16, 20, 24	home position indicator return

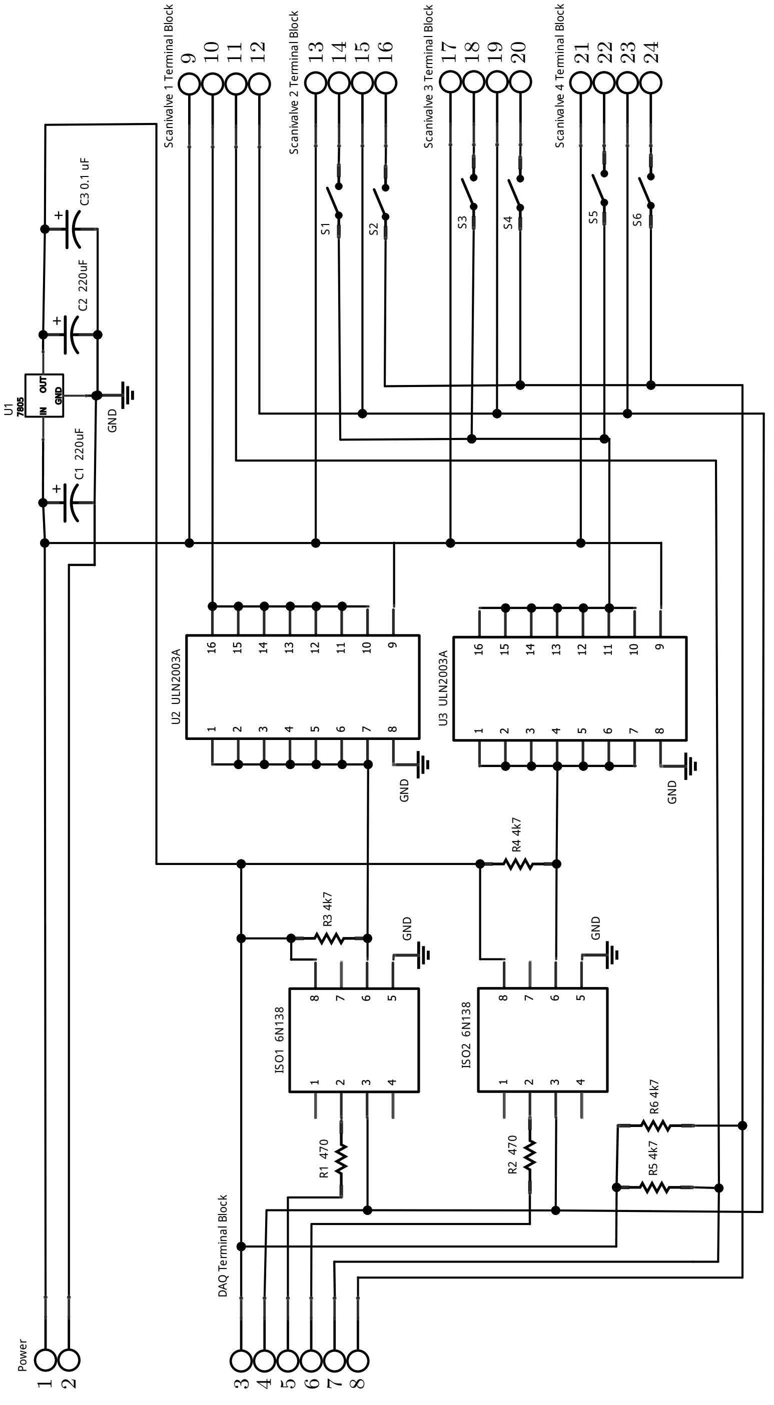
Scanivalve 1 Terminal Block
9
10
11
12
Scanivalve 2 Terminal Block
13
14
15
16
Scanivalve 3 Terminal Block
17
18
19
20
Scanivalve 4 Terminal Block
21
22
23
24
S1
S2
S3
S4
S5
S6
C3 0.1 uF
C2 220uF
C1 220uF
U1
7805
IN
OUT
GND
GND
U2 ULN2003A
U3 ULN2003A
R4 4k7
R3 4k7
ISO1 6N138
ISO2 6N138
R1 470
R2 470
R6 4k7
R5 4k7
DAQ Terminal Block
Power
1
2
3
4
5
6
7
8

Figure C.2: Scanivalve mechanical multiplexer system control circuit.

connected to the pressure transducer. In this way, the pressure in each of the pneumatic lines can be measured by the same pressure transducer.

Appendix D

Wall Adaptation Strategy

In this appendix, the WAS developed by Judd et al. [96], as detailed by Wolf & Goodyer [94], is described. An approach for implementing subsequent recommendations by the authors of Ref. [94] for estimating the imaginary velocity field is also discussed [16]. The WAS algorithm was coded in MATLAB to compute new wall contours for the University of Waterloo adaptive-wall wind tunnel from arbitrary input wall contours and pressure distributions.

Figure 3.5 provides a sketch of the WAS concept. The boundary contour is the wall contour offset by the difference between the GSW and ASW displacements at each location along the test section. Initial wall contours must be selected that provide a known imaginary flow field over the boundary contour. Traditionally, the ASW configuration has been used [94]. In this configuration, the wall shapes are adjusted to remove the streamwise pressure gradient in the empty test section. This is equivalent to displacing the walls from the GSW configuration by the wall boundary layer displacement thickness, multiplied by an experimentally determined factor to account for the side wall boundary layer thickness. A $1/7^{\text{th}}$ power law turbulent velocity profile approximation can be used to estimate the displacement thickness [63],

$$\delta_w^*(X) = 0.02\,(X - X_{vo})^{6/7}\left(\frac{c}{Re_c}\right)^{1/7}. \tag{D.1}$$

Sumner [113] determined the side wall boundary layer thickness compensation factor for displacement thickness in the University of Waterloo adaptive-wall wind tunnel to be 2.72 based on measurements at various free-stream speeds. It was further determined that the virtual origin for the power law displacement thickness calculation was $X_{vo}/c \approx 10$ (Ref. [113]). These values were verified more recently by Bishop [92] and the accuracy of the displacement thickness model was established with point measurements in the present investigation.

In the ASW configuration, the boundary contours are straight and parallel. This results in an inviscid flow field solution over these contours of a constant velocity parallel to the walls. Alternatively, any other reasonable wall contour can be selected and used, and the imaginary flow field over the boundary contour determined by potential flow calculations. To reduce the number of wall movements to convergence, potential flow streamlines over the model are commonly selected as the initial state [91].

With the model installed and the walls in the initial configuration, test section wall pressure distributions are measured and converted to velocities through the definition of the pressure coefficient. The imaginary and measured flow fields are then joined at the boundary contour. At the boundary between the two flow fields, there is a discontinuity in velocity, which can be represented by a distributed vorticity source, as illustrated in Fig. 3.5. The strength distribution of the notational vorticity, $\Gamma(X)$, at the wall pressure measurement locations, is proportional to the difference between the measured and imaginary velocity fields at these location, i.e., $\Gamma(X) = U_R(X) - U_I(X)$. As a result of the velocity discontinuity along the boundary, a vertical component of velocity is induced at each location, $v_w(X)$. Since the wall slope is generally small, the induced velocity can be estimated by approximating the contribution of each elemental vorticity as being entirely in the vertical direction, i.e.,

$$v_w(X) = \frac{1}{2\pi} \int_{-\infty}^{\infty} \frac{\Gamma(\check{x})}{X - \check{x}} d\check{x}. \tag{D.2}$$

In implementing the wall streamlining algorithm, Eq. D.2 is integrated analytically, using a third order polynomial fit for $\Gamma(X)$ based on the values computed at the two upstream and two downstream measurement locations on each interval. Upstream and downstream of the test section the integrand is assumed to be zero. In the objective SLW configuration, there is zero induced vertical velocity. For small wall slopes, the amount of wall movement required to eliminate the induced velocity on an interval can be approximated as,

$$\Delta\left(\frac{dY}{dX}\right) \approx -\frac{v_w}{U_\infty}. \tag{D.3}$$

The predicted change in slope does not account for changes in the flow field around the model due to changes in the wall contours, nor does it account for changes in the pressure distribution along one wall due to movements of the other wall [94]. As a result, wall streamlining is an iterative process. The main problem is that by moving both walls, the free-stream velocity in the wind tunnel is changed due to a one-dimensional continuity effect. In order to ensure convergence to the SLW configuration, the wall movements are reduced by a scaling factor (SF), and a coupling factor ($CPLF$) is applied to transfer a portion of the computed wall movement from each wall onto the opposite wall. The choice of these factors can affect the number of WAS iterations required. Typical values of $SF = 0.8$ and $CPLF = 0.35$ have been reported by Wolf & Goodyer [94], and were adopted in the present investigation.

Based on the new wall configuration, the imaginary velocity field over the boundary contour is estimated by one of the two approaches outlined in Section D.1. The walls are then moved to the new configuration and the process of measuring the wall pressure distributions and completing wall adaptation calculations is repeated. This continues until the wall movements or pressure distribution changes are within a specified tolerance [16].

D.1 Estimating the Imaginary Velocity Field

In the original WAS algorithm, the imaginary flow field pressure distribution was determined iteratively based on wall pressure measurements from the previous iterations [94]. This method required the ASW configuration to be used to initiate the wall streamlining procedure. For a single adaptive-wall in a semi-infinite flow field on one side of a two-dimensional model, and for which the effect of the wall movement on the flow over the model has no significant effect on the pressure distribution on the wall, the imaginary and real velocity fields must be equal. Thus, the velocity field after a wall displacement change would be $U_I^{new}(X) = U_I^{old}(X) + \frac{1}{2}\left[U_R^{old}(X) - U_I^{old}(X)\right]$. With two adaptive walls, this approximation is still employed. In order to incorporate the scaling factors, it is assumed that scaling the wall movement equivalently scales the imaginary velocity field adjustment, i.e.,

$$U_I^{new,s}(X) = U_I^{old}(X) + \frac{SF}{2}\left[U_R^{old}(X) - U_I^{old}(X)\right]. \tag{D.4}$$

The coupling factor is incorporated by approximating the change in imaginary velocity field due to the transfered wall movement, as that which would occur over the opposite wall due to the movement:

$$U_I^{new,c}(X) = U_I^{new,s}(X) + CPLF\left[U_I^{new,s}(X)_o - U_R^{old}(X)_o\right], \tag{D.5}$$

where the o subscript indicates that the quantities correspond to the opposite wall.

D.1.1 Potential Flow Estimate

Iterative adjustment of the imaginary velocity field, as described above, improved the efficiency of the WAS algorithm when computer resources for calculating the imaginary flow field by potential flow theory were limiting the speed of wall adaptation studies [96]. In general, the approximations and compounded uncertainty introduced by iterative calculations using experimental data are undesirable [16]. Modern implementations of the WAS need not invoke these approximations, because the alternative potential flow calculations no longer require significant computing time. This type of calculation is outlined here.

The inviscid flow field over a body can be determined from the superposition of a uniform velocity and a set of potential flow sources [118]. For the purpose of efficient potential flow calculations in the WAS algorithm, each wall's boundary contour can be modeled as one side of a symmetric two-dimensional body [91]. This model is depicted in Fig. D.1. Note that because the adaptive walls can have positive or negative displacements relative to the GSW configuration, the boundary contour known from the experiment, and extending over the length L_{TS} in Fig. D.1, is displaced from the centerline a distance h.

The coordinates of the boundary contour can be determined from the known wall coordinates by adjusting for the scaled displacement thickness, i.e., the displacements from the GSW contours to the ASW contours. The boundary contour coordinates determined from the wall shape extend over the test section length, L_{TS}. Upstream and downstream of the test section, distances of L_{US} and L_{DS}, respectively, the streamline is assumed to be flat, as is expected sufficiently far from the model. Points p_1 to p_N on the streamline are determined by a cubic spline interpolation to provide sufficient resolution for grid

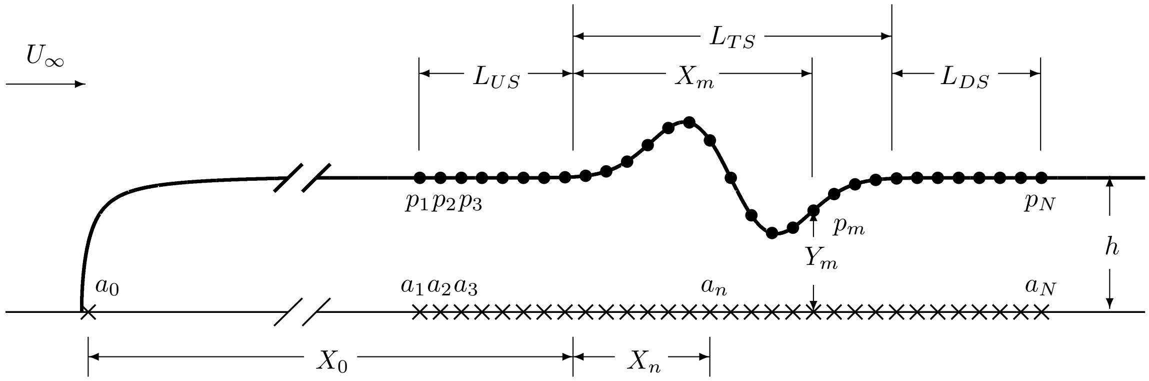

Figure D.1: Sketch of sources and sinks approximation for potential flow calculation.

independent potential flow solutions. Potential flow sources of strength a_1 to a_N are distributed along the centerline to produce the boundary contour. In order to displace the boundary contour a distance h, a source of strength a_0 is placed far upstream of the test section, so that the free-stream velocity has recovered by the point p_1. This effectively imposes the boundary contour shape on a Rankine half body [144].

To obtain the streamline offset of h, the source far upstream is assigned a strength of $a_0 = -h/\pi$, based on the properties of a Rankine half body [144]. The value of the streamfunction corresponding to the modeled boundary streamline is then $\Psi/U_\infty = h$. The value of the sources a_1 to a_N are assigned such that the value of the streamfunction is constant along the boundary contour. Applying superposition of potential flow sources, the equation for the streamfunction at each p_m point is then,

$$\frac{\Psi_m}{U_\infty} = h = Y_m + \sum_{n=0}^{N} a_n \arctan\left[\frac{Y_m}{X_m - X_n}\right]. \tag{D.6}$$

This provides a linear system of equations for the sources a_n, which can be directly solved. From this solution, the velocity at each p_m location can then be computed as,

$$\frac{U_m}{U_\infty} = 1 + \sum_{n=0}^{N} a_n \arctan\left[\frac{X_m - X_n}{(X_m - X_n)^2 + Y_m}\right]. \tag{D.7}$$

The vertical component of velocity can be similarly computed; however, because the wall displacements are small relative to the length of the test section, this component was found to be negligible in WAS calculations.

The above solution method was programmed in MATLAB. Grid independence from the choice of h, L_{US}, L_{DS}, X_0, and N was verified for representative cases. The efficiency of this calculation was not found to be an issue, even with $N \approx 1.5 \times 10^4$. Because the value of X_0 does not affect the number of calculations, this parameter could be set higher than necessary, to 10^4 m. The accuracy of the solution method was verified against XFOIL [145] predictions for symmetric airfoils formed from boundary contour coordinates.

D.2 Determining Wall Contours

Computed slope changes are used to determine wall contours in the next iteration by integrating the slope changes in the streamwise direction from the upstream anchor point, fixed at zero slope. The integration is computed for a cubic spline to the slope increments, available at each wall pressure tap. This integral is evaluated up to each jack location, yielding the displacement of each jack.

Since the entrance and exit to the test section have fixed cross sections, it is necessary to blend the wall contours to the height at the exit of the test section. The blending algorithm applied in previous WAS calculations for the University of Waterloo adaptive-wall wind tunnel has been adopted here [92, 113]. A 0.8 m portion of the adaptive-wall section was used to implement the blending shape. The coordinates of two jacks upstream of this section, computed using the WAS, and two jacks downstream of this section with coordinates for the ASW configuration, were used to define a cubic polynomial interpolation for the blended wall shape. This approach has been shown to provide accurate SLW results for a circular cylinder in this facility [92].

Differences between the flow field in the test section and an infinite flow field are still expected after wall streamlining due to several limitations. Despite design efforts to ensure a long adaptive section [89], finite test section length prevents boundary contours from exactly following infinite flow field streamlines upstream of the model and can limit the length into the wake that can be adapted. Side wall boundary layer growth leads to streamline displacement towards the center-span plane. Although the acceleration of the flow due to this growth is accounted for in the top and bottom wall displacements, the change in streamline shape near the side walls cannot be eliminated in two adaptive-wall test sections. Finally, the calculated displacement thickness of the boundary layers on the test section walls does not account for pressure gradients in the streamwise direction due to the presence of the model. Although in some investigation efforts have been taken to account for this variation, e.g., Ref. [91], it is difficult to do so because the gradients along the side walls also vary with distance from the model. In the present investigation, the variation in wall boundary layer thickness due to model induced pressure gradients was estimated using a Kármán integral relation for turbulent boundary layers with imposed pressure gradients and simple Kármán-type closure with an approximate correlation between Coles' wake parameter and the Clauser parameter (see, e.g., Ref. [63], pages 454-457). It was found that, for the flow conditions in these experiments, the variation in estimated wall contours caused by the influence of model induced pressure gradients on the test section wall boundary layer thickness, was within the uncertainty in setting the wall displacements. Furthermore, the uncertainty in the refined displacement thickness estimate, due mainly to approximating the streamwise pressure gradient from low pressure measurements, was on the order of the uncertainty in setting the wall contours.

Appendix E

Additional WAS Results

Measurements of wall and model surface pressure distributions, as well as predicted wall shapes, obtained with and without end plates installed and using both the potential flow imaginary velocity field WAS calculation method and the original iterative method, are presented in this appendix. Figure E.1 provides SLW configuration model surface pressure distributions measured with only end caps installed on the model. These data were used to compute lift coefficients in Fig. 5.10a. Similar SLW configuration wall displacements and wall pressure distributions were obtained with only end caps installed as with end plates installed, and are presented in Figs. E.2 and E.3. These data show that only minor differences result from using end plates. The wall movements are consistently of greater magnitude when end plates are installed, as a result of the higher solid blockage ratio with end plates installed.

Figures E.2 and E.3 compare SLW configuration results obtained using both the original iterative imaginary velocity field estimation method in the WAS algorithm, and the potential flow calculation method. The difference in wall coordinates between the two methods was on the order of the uncertainty in setting the wall positions. This verified the potential flow calculation modification to the program and showed that, in the University of Waterloo adaptive-wall wind tunnel, at blockage ratios on the order of less than 8% and for free-stream speeds providing a chord Reynolds number on this model of approximately 10^5, using the potential flow calculation instead of the original method is unnecessary. However, at higher blockage ratios, for which more than three iterations of the WAS algorithm are required to determine the SLW coordinates, the accumulated error from using the original method may be significant. Furthermore, since the potential flow calculation does not noticeably increase the calculation time for wall movements, this method should be used for future studies in this facility, to reduce accumulated error in wall displacements.

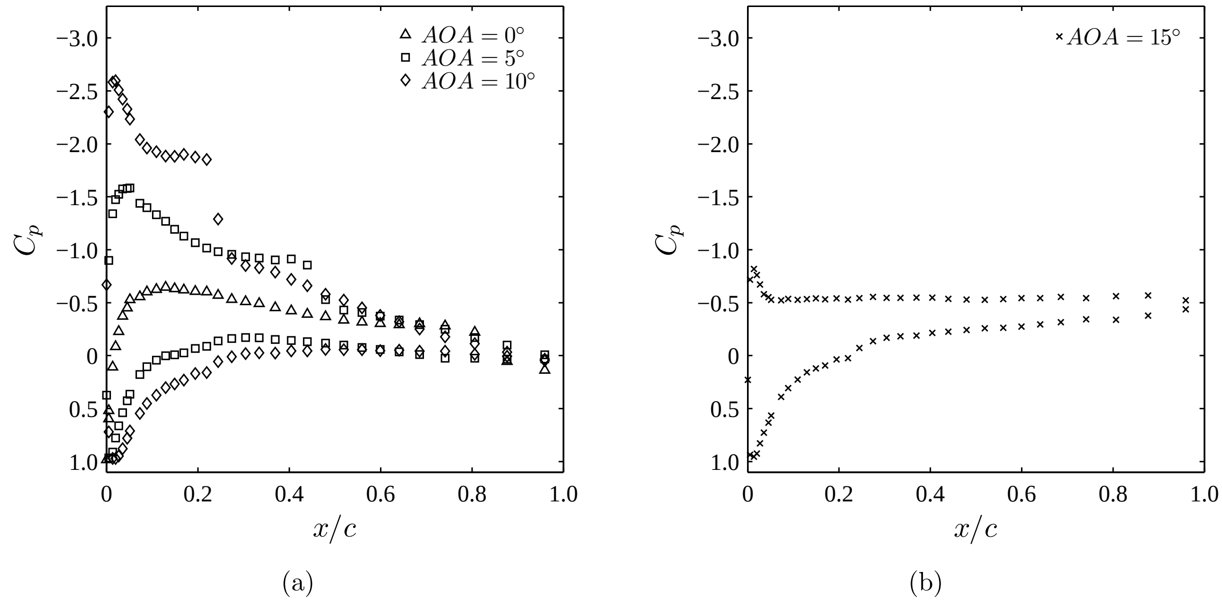

Figure E.1: Streamwise distributions of model surface pressure in the SLW configuration with only end caps installed. Data for angles of attack at which a separation bubble formed are presented in (a) and data for the stalled condition are presented in (b).

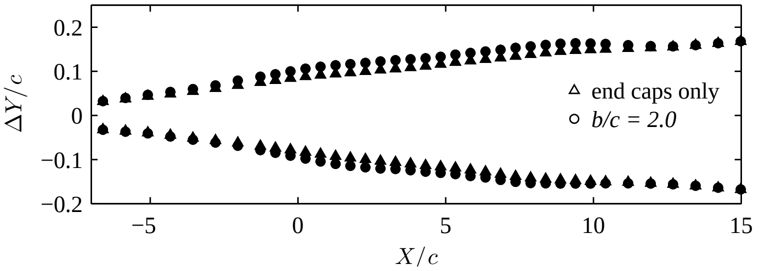

(a) $AOA = 0°$

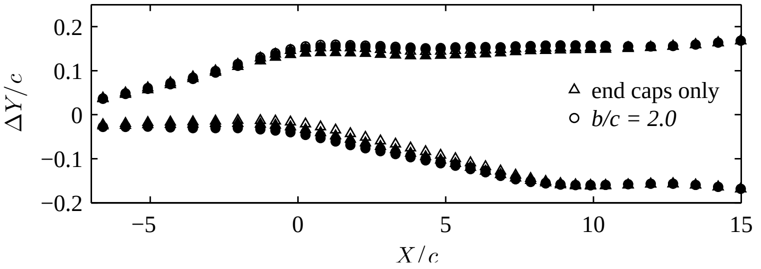

(b) $AOA = 5°$

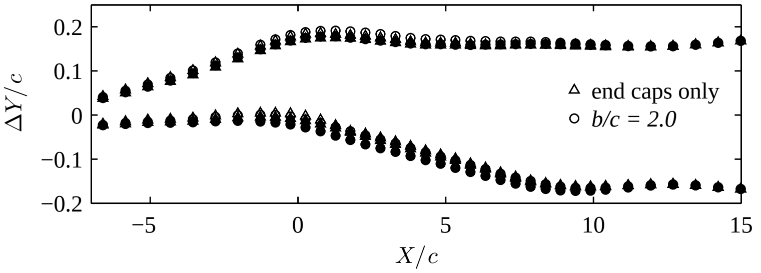

(c) $AOA = 10°$

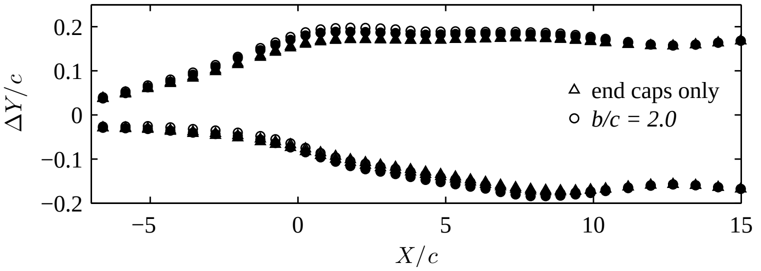

(d) $AOA = 15°$

Figure E.2: SLW contours with and without end plates installed and using the original (filled markers) and potential flow (unfilled markers) imaginary velocity field estimation methods.

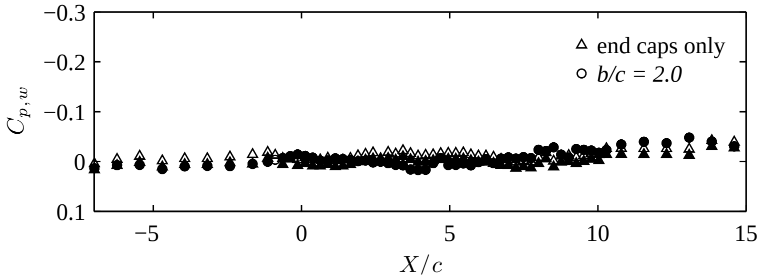

(a) $AOA = 0°$

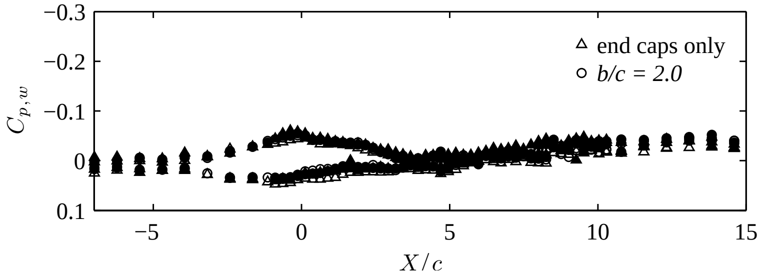

(b) $AOA = 5°$

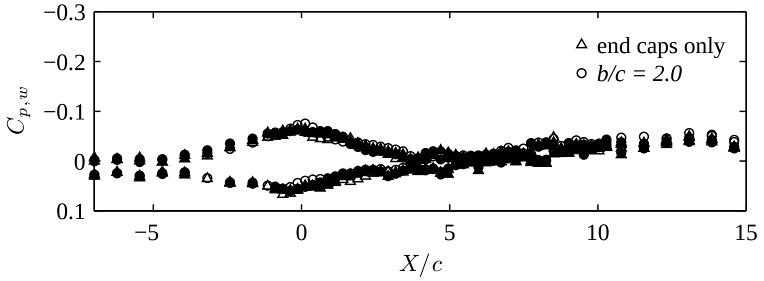

(c) $AOA = 10°$

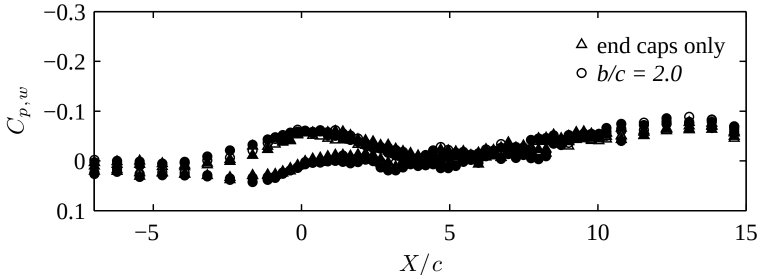

(d) $AOA = 15°$

Figure E.3: Wall pressure distributions with and without end plates installed and using the original (filled markers) and potential flow (unfilled markers) imaginary velocity field estimation methods.

Appendix F

LST Solvers

This appendix provides details on the numerical methods used to solve the Rayleigh and Orr-Sommerfeld equations in this investigation. MATLAB programs were developed to apply each of the solution methods to arbitrary separated shear layer profiles.

F.1 PWL Method

Approximating the mean streamwise velocity profile as a set of linear segments reduces the Rayleigh equation (Eq. 2.3) to a second order homogeneous ordinary differential equation with constant coefficients [66]:

$$v'' - \alpha^2 v = 0. \tag{F.1}$$

The constants of integration for each linear segment are determined by applying the two boundary conditions in Eq. 2.4 to the first and last segments and by enforcing continuity of pressure and wall normal velocity at the connection points between linear segments [66]:

$$[[(U - \omega/\alpha)\, v' - U'v]] = 0, \tag{F.2}$$

$$\left[\left[\frac{v}{U - \omega/\alpha}\right]\right] = 0, \tag{F.3}$$

where, $[[\cdot]]$ indicates the difference between the quantity evaluated on the upper and lower curve segment, at the connection point. Substituting the general solution into the matching conditions at each connection point leads to the following relations:

$$a_{2n-1} - a_{2n+1} = (a_{2n+2} - a_{2n})\, e^{2\alpha y_n}, \tag{F.4}$$

$$\begin{aligned}\alpha\left(U_n-\omega/\alpha\right)&\left[\left(a_{2n+2}-a_{2n}\right)e^{\alpha y_n}-\left(a_{2n+1}-a_{2n-1}\right)e^{-\alpha y_n}\right]\\&=\left(U'_{n+1}a_{2n+1}-U'_na_{2n-1}\right)e^{-\alpha y_n}+\left(U'_{n+1}a_{2n+2}-U'_na_{2n}\right)e^{\alpha y_n},\end{aligned}\tag{F.5}$$

where $\boldsymbol{a}$ is the vector of integration constants for each interval. Applying the boundary conditions, $a_1 = -a_2$ and $a_{2N} = 0$, closes the algebraic system. Thus, the problem takes the form,

$$C_0\boldsymbol{a} = \mathbf{0},\tag{F.6}$$

where the coefficient, C_0, is determined by evaluating Eqs. F.4 and F.5. Since this is a homogeneous linear system, the solution can be found by determining the eigenvalue such that $\det(C_0) = 0$ (Ref. [67]).

In theory, the algebraic system can be solved directly for all of the eigenvalues for a particular piecewise linear profile approximation. However, due to the non-linear appearance of the eigenvalue in the system for spatial stability analysis, such an approach becomes inefficient for large numbers of profile segments. Instead, an iterative procedure to determine one mode at a time is employed. For a particular disturbance frequency, an initial approximation for the eigenvalue is used to evaluate $\det(C_0)$. The eigenvalue is iteratively refined using a secant method until $\det(C_0)$ is within a specified tolerance of zero. For each disturbance frequency, the initial approximation for the eigenvalue is determined by extrapolating converged values from solutions obtained for other frequencies.

F.2 RK Integration

Runge-Kutta integration can be used to solve the Rayleigh and Orr-Sommerfeld equations for velocity profiles with non-zero values of U''. For the purpose of numerical integration, the Rayleigh equation is rearranged into a system of first order equations as follows:

$$\frac{dv}{dy} = u,\tag{F.7}$$

$$\frac{du}{dy} = \left(\frac{U''}{U-\omega/\alpha}+\alpha^2\right)v.\tag{F.8}$$

Noting that the separated shear layer profile approaches a constant value in the free stream, the free-stream boundary condition of Eq. 2.4 can be rewritten as [65],

$$\lim_{y\to\infty}\frac{u}{v} = -\alpha,\tag{F.9}$$

in order to obtain a grid independent solution with a smaller integration domain. The U'' term in Eq. F.8 can be computed by a second order central difference approximation for the interior points, and first order forward and backward difference formulas at the lower and upper domain boundaries, respectively. The Rayleigh equation can then be solved numerically for a given disturbance frequency by a Runge-Kutta method (see, e.g., Ref. [146]) to integrate Eqs. F.7 and F.8 from the free stream to the wall, using a guessed value of α, the boundary value $u(y_{\max}) = -\alpha v(y_{\max})$, and an arbitrarily chosen $v(y_{\max})$. The secant method is used to iteratively adjust the value of α, computed from the new value of $v(0)$ in each iteration until the wall boundary condition is satisfied to within a specified tolerance. This procedure is completed for each disturbance frequency for which a solution is desired, with a secant method employed to extrapolate initial eigenvalue guesses from those computed at other frequencies.

F.2.1 An Alternative to the Rayleigh Equation for Inviscid LST

The first order system formulation of the Rayleigh equation, given by Eqs. F.7 and F.8, contains a term with the second derivative of the mean streamwise velocity, the computed value of which is very sensitive to experimental data scatter. It has been suggested that more reliable results can be obtained by formulating the linear stability problem in a form without the U'' term [122]. To explore this option, the linear stability equations are formulated in terms of the pressure fluctuation and vertical velocity fluctuation profiles instead of the streamwise and vertical velocity fluctuation profiles [123].

Simplifying the Navier-Stokes equations by assuming parallel mean flow, neglecting higher order fluctuation terms, assuming that disturbances can be decomposed into normal modes, and taking the inviscid limit, results in a system of three first order inviscid linear stability equations for fluctuating pressure and velocity components [61]. Instead of uncoupling the system from the pressure fluctuation equation and invoking the disturbance streamfunction to arrive at a single second order equation, i.e., the Rayleigh equation, the streamwise velocity fluctuation equation is uncoupled, resulting in an equivalent system of two first order equations [123]:

$$\frac{dp}{dy} = -i\rho\left(\alpha U - \omega\right)v, \tag{F.10}$$

$$\frac{dv}{dy} = \left(i\alpha\frac{p}{\rho} + v\frac{dU}{dy}\right)\left(U - \frac{\omega}{\alpha}\right). \tag{F.11}$$

Similar boundary conditions are used as for the Rayleigh equation. A value for the vertical velocity fluctuation at $y_{\max}$ is selected, and the equation,

$$\lim_{y\to\infty} \frac{p/\rho}{v} = i\left(U_e - \frac{\omega}{\alpha}\right)^{-1}, \tag{F.12}$$

is used to define numerical boundary condition for the free-stream pressure fluctuation as, $p(y_{\max}) = i\rho\,(U_e - \omega/\alpha)\,v(y_{\max})$.

The above system of equations can be solved by Runge-Kutta integration employing a secant method to iteratively determine the eigenvalues such that the zero fluctuation conditions are satisfied at the wall. Note that, whereas Eqs. F.7 and F.8 contain a U'' term, Eqs. F.10 and F.11 do not. For a velocity profile with sufficiently high profile spatial resolution, as would be available from a curve fit to the measured velocity profile, these two systems will provide the same solution. However, it is possible that their solutions will

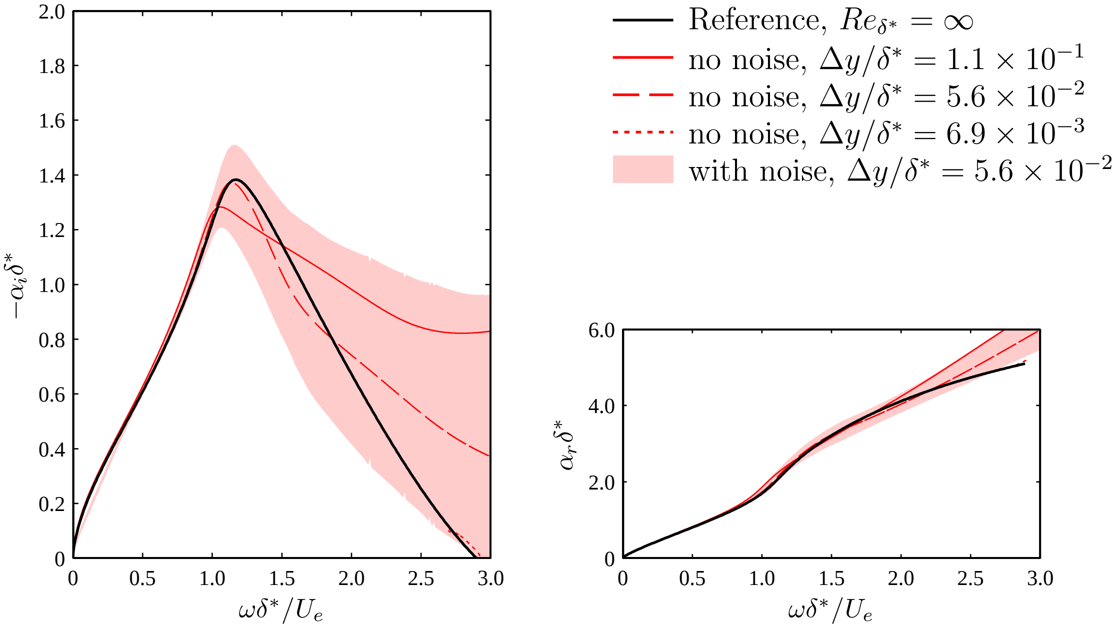

Figure F.1: Convergence rate and variability due to data scatter for the alternative RK method applied directly to discrete velocity profile data. Curves show solutions for the simulated profile without data scatter and the shaded band indicates the second standard deviation of solutions for one hundred simulated profiles with $\Delta y/\delta^* = 5.6 \times 10^{-2}$ and imposed data scatter.

differ for the relatively low profile spatial resolution available from experimental data, due to the amplification of experimental data scatter in computing U''.

Figure F.1 illustrates the convergence and variability due to data scatter for this solution method. Figures 4.1 and 4.3 are similar plots for the other solution methods applied directly to discrete velocity profiles. The alternative RK method (Fig. F.1) performs poorly for low spatial resolutions as compared to the other methods (Fig. 4.1); however, the variability due to data scatter for this formulation is on the same order as the other methods (Fig. 4.3).

F.2.2 Compound Matrix Method

Directly solving the Orr-Sommerfeld equation by a shooting method can be difficult because the equation is numerically stiff [147]. The compound matrix method establishes an equivalent system of equations for which numerical solutions are more easily determined [147]. Detailed mathematical formulations of this method are presented in Refs. [67] and [147]. Through these manipulations, a system of equations is developed that is equivalent to the Orr-Sommerfeld equation [67]:

$$\Theta_1' = \Theta_2, \tag{F.13}$$

$$\Theta_2' = \Theta_3 + \Theta_4, \tag{F.14}$$

$$\Theta_3' = \left\{ 2\alpha^2 + \frac{i\alpha Re_{\delta^*}}{U_e \delta^*} \left(U - \frac{\omega}{\alpha} \right) \right\} \Theta_2 + \Theta_5, \tag{F.15}$$

$$\Theta_4' = \Theta_5, \tag{F.16}$$

$$\Theta_5' = \left\{ \alpha^4 + \frac{i\alpha Re_{\delta^*}}{U_e \delta^*} \left[\alpha^2 \left(U - \frac{\omega}{\alpha} \right) + U'' \right] \right\} \Theta_1 + \left\{ 2\alpha^2 + \frac{i\alpha Re_{\delta^*}}{U_e \delta^*} \left(U - \frac{\omega}{\alpha} \right) \right\} \Theta_4 + \Theta_6, \tag{F.17}$$

$$\Theta_6' = \left\{ \alpha^4 + \frac{i\alpha Re_{\delta^*}}{U_e \delta^*} \left[\alpha^2 \left(U - \frac{\omega}{\alpha} \right) + U'' \right] \right\} \Theta_2. \tag{F.18}$$

The boundary conditions are then,

$$\Theta_1(y_{\max}) = 1, \tag{F.19}$$

$$\Theta_2(y_{\max}) = -(\alpha + \chi), \tag{F.20}$$

$$\Theta_3(y_{\max}) = \alpha^2 + \alpha\chi + \chi^2, \tag{F.21}$$

$$\Theta_4(y_{\max}) = \alpha\chi, \tag{F.22}$$

$$\Theta_5(y_{\max}) = -\alpha\chi(\alpha + \chi), \tag{F.23}$$

$$\Theta_6(y_{\max}) = \alpha^2\chi^2, \tag{F.24}$$

where $\chi = \sqrt{\alpha^2 + i\alpha Re_{\delta^*}(1-\omega/\alpha)/(U_e\delta^*)}$. Runge-Kutta integration can then be applied to these equations for each disturbance frequency, using a secant method to determine the eigenvalue such that the wall boundary condition, $\Theta_1(0) = 0$, is satisfied. Once the eigenvalue is determined, the eigenfunction can be computed by numerically integrating the equation [67],

$$\Theta_1 v'' - \Theta_2 v' + \Theta_4 v = 0, \tag{F.25}$$

towards the wall from an arbitrarily selected value of the free-stream vertical velocity fluctuation.

F.3 FD Formulation

Finite difference approximations to the Rayleigh equation have been shown to provide accurate results in comparison with Runge-Kutta integration and spectral methods [120]. In this investigation, finite difference solutions have only been applied for discrete data points, and for this reason the formulation accommodates uneven profile point spacing. Substitution of second order central difference formulas into the Rayleigh equation (Eq. 2.3) leads to,

$$\frac{v_{m+1} - \left(1 + \frac{y_{m+1}-y_m}{y_m - y_{m-1}}\right) v_m + \left(\frac{y_{m+1}-y_m}{y_m-y_{m-1}}\right) v_{m-1}}{\frac{1}{2}\left(y_{m+1}-y_m\right)\left(y_{m+1}-y_{m-1}\right)} - \left(\frac{U_m''}{U_m - \omega/\alpha} + \alpha^2\right) v_m = 0, \tag{F.26}$$

for $m \in [1, N]$. Similarly, the boundary condition of Eq. 2.4 and the impermeability condition become $\left[1 + \alpha\left(y_{N+1} - y_N\right)\right] v_{N+1} = v_N$ and $v_0 = 0$. This system of equations can be rearranged into a polynomial eigenvalue problem with matrix coefficients of the form,

$$\left(C_0\alpha^3 + C_1\alpha^2 + C_2\alpha + C_3\right)\boldsymbol{v} = \boldsymbol{0}, \tag{F.27}$$

and solved using the companion matrix method, described in Section F.5.

F.4 Chebyshev Collocation Formulation

Spectral methods have a number of advantages over local methods when solving stiff differential eigenvalue problems such as the Orr-Sommerfeld equation [132, 148]. Most notably, spectral methods allow for the direct solution of multiple modes simultaneous and do not require an iterative procedure to determine the eigenvalues. An appropriate choice of trial functions can provide moderate solution accuracy with very few terms in the assumed solution [132], making such methods ideal for determining approximate eigenvalues to initiate the shooting procedures in local methods when high accuracy or fine spectral resolution is required [67].

Spectral methods employ a series of orthogonal trial functions to approximate the solution to a differential equation [132]. Test functions are selected so that the properties of orthogonal functions can be exploited to develop an algebraic system of equations for the coefficients of the series solution. Spectral methods are categorized based on the choice of trial and test functions. Chebyshev polynomials are commonly used as trial functions in Orr-Sommerfeld equation solutions [66,120,121,124–131] because they provide infinite convergence, i.e., the solution converges faster than the number of trial functions used in the expansion to any finite power [132]. A number of studies have verified that Chebyshev collocation and Chebyshev tau schemes can both be used in linear stability analysis to accurately calculate eigenvalues [120,124,127,130]. In the present investigation, a Chebyshev collocation method, similar to that described in Ref. [66], is employed with appropriate modifications to accommodate a spatial stability formulation for a semi-infinite domain problem. It should be noted that the Chebyshev collocation approach was only used to identify less dominant modes induced by data scatter in measured mean velocity profiles and to find a sufficient approximation for the eigenvalue at one location to initiate the shooting procedure in local methods. Thus, the convergence of this method was not important, provided that the computed eigenvalue provided convergence of the shooting procedure in the Runge-Kutta integration. For this purpose, 200 terms in the Chebyshev polynomial series expansion was found to be more than sufficient.

The n^{th} Chebyshev polynomial is given as $T_n(\hat{y}) = \cos[(n-1)\arccos(\hat{y})]$ (Ref. [132]). The domain of these functions is $\hat{y} \in [-1, 1]$, whereas the domain of a separated shear layer profile is $y \in [0, \infty)$. In order to approximate the solution to the Orr-Sommerfeld equation with Chebyshev polynomials, it is necessary to map the problem domain onto that of the trial functions. Various transforms have been used for this purpose, and have been found to affect the number of polynomial terms required for convergence [148]. the choice of domain mapping was not a concern in the present investigation because spectral calculations were only needed for approximate solutions. The following simple coordinate transformation was selected to map the physical coordinate system, $y \in [0, \infty)$, onto the Chebyshev polynomial domain, $\hat{y} \in [-1, 1]$: $\hat{y} = 2y/y_{\max} - 1$. Substitution into the Orr-Sommerfeld equation (Eq. 2.1) yields,

$$(U - \omega/\alpha)\left(\xi^2 \frac{d^2v}{d\hat{y}^2} - \alpha^2 v\right) - U''v = -\frac{iU_e\delta^*}{\alpha Re_{\delta^*}}\left(\xi^4 \frac{d^4v}{d\hat{y}^4} - 2\alpha^2\xi^2 \frac{d^2v}{d\hat{y}^2} + \alpha^4 v\right), \tag{F.28}$$

where $\xi = 2/y_{\max}$. Similarly, the boundary conditions of Eq. 2.2 become,

$$v\left(\pm 1\right) = v'\left(\pm 1\right) = 0. \tag{F.29}$$

In spectral collocation formulations, Dirac delta functions with singularities coinciding with the collocation points are used as the test functions [132]. For numerical accuracy, the N collocation points, $\hat{y}_m$, are selected as locations of the minima and maxima of the highest order Chebyshev polynomial used in the expansion, i.e., $\hat{y}_m = \cos(m\pi/N) + 1$. Thus, a series expansion of the eigenfunction that exactly satisfies the differential equation at these locations is to be determined. Expanding the vertical velocity fluctuation profile in Eqs. F.28 and F.29 into a Chebyshev polynomial series,

$$v = \sum_{n=1}^{N} a_n T_n(\hat{y}), \tag{F.30}$$

and evaluating the equation at the collocation points, reduces the Orr-Sommerfeld equation to a system of algebraic equations in the form,

$$\left(C_0\alpha^4 + C_1\alpha^3 + C_2\alpha^2 + C_3\alpha + C_4\right)\boldsymbol{a} = \boldsymbol{0}, \tag{F.31}$$

where, for $n \in [1, N]$ and $m \in [3, N-2]$,

$$C_{0_{m,n}} = -\frac{U_e\delta^*}{iRe_{\delta^*}} T_n(\hat{y}_m), \tag{F.32}$$

$$C_{1_{m,n}} = -U_m T_n(\hat{y}_m), \tag{F.33}$$

$$C_{2_{m,n}} = \frac{2\xi^2 U_e\delta^*}{iRe_{\delta^*}} \frac{d^2T_n}{d\hat{y}^2}(\hat{y}_m) + \omega T_n(\hat{y}_m), \tag{F.34}$$

$$C_{3_{m,n}} = -U''_m T_n(\hat{y}_m) + U_m\xi^2 \frac{d^2T_n}{d\hat{y}^2}(\hat{y}_m), \tag{F.35}$$

$$C_{4_{m,n}} = -\frac{\xi^4 U_e\delta^*}{iRe_{\delta^*}} \frac{d^4T_n}{d\hat{y}^4}(\hat{y}_m) - \omega\xi^2 \frac{d^2T_n}{d\hat{y}^2}(\hat{y}_m). \tag{F.36}$$

The boundary conditions are $C_{4_{1,n}} = T_n(-1)$, $C_{4_{2,n}} = T'_n(-1)$, $C_{4_{N-1,n}} = T_n(1)$, $C_{4_{N,n}} = T'_n(1)$, and $C_{0_{m,n}} = C_{1_{m,n}} = C_{2_{m,n}} = C_{3_{m,n}} = 0$ for $m = 1$, 2, $N-1$, and N. Equation F.31 can then be solved directly by the companion matrix method described in Section F.5.

F.5 Companion Matrix Method

As seen in Sections F.3 and F.4, finite difference and Chebyshev collocation formulations for spatial linear stability analysis lead to polynomial eigenvalue problems with matrix coefficients (e.g., Eq. F.31). Such equations can be recast into linear generalized eigenvalue problems through the companion matrix method, and then solved efficiently. To illustrate this method, consider Eq. F.31. This equation can be rearranged into the following linear generalized eigenvalue problem [121]:

$$\left\{ \begin{bmatrix} -C_1 & -C_2 & -C_3 & -C_4 \\ I & 0 & 0 & 0 \\ 0 & I & 0 & 0 \\ 0 & 0 & I & 0 \end{bmatrix} - \alpha \begin{bmatrix} C_0 & 0 & 0 & 0 \\ 0 & I & 0 & 0 \\ 0 & 0 & I & 0 \\ 0 & 0 & 0 & I \end{bmatrix} \right\} \begin{Bmatrix} \alpha^3 \boldsymbol{a} \\ \alpha^2 \boldsymbol{a} \\ \alpha \boldsymbol{a} \\ \boldsymbol{a} \end{Bmatrix} = \mathbf{0}. \tag{F.37}$$

Equations of this form can be solved using the QR algorithm [132], pre-programmed into scientific computing software such as MATLAB.

Appendix G

Intrusiveness of Flow Visualization

This appendix examines the effect of opening and closing the wind tunnel door while the tunnel is running. Such intrusion is sometimes necessary to apply smoke-wire fluid for flow visualization experiments. It is important to know whether the flow returns to its previous state after the door is closed, and how long it takes for the flow to settle, in order to have confidence that flow visualization images are of the same flow development that was measured. These effects were assessed by measuring mean and fluctuating surface pressure over a time interval in which the wind tunnel door was opened for fifteen seconds and then closed.

The response of mean static pressure at the suction peak for each angle of attack is presented in Fig. G.1. For each angle of attack, it took less than thirty seconds for the measured pressure to return to the initial value. Note that this is not a precise measurement because, due to the static pressure tube length, the rise time for static pressure measurements from this system is approximately twenty seconds. However, the fact that the magnitude of the suction peak returns to the value before the door was opened suggests that the mean flow returns to its previous state less than thirty seconds after the door is closed, for each set of flow conditions considered.

Simultaneous microphone measurements were acquired during and following opening and closing the wind tunnel door to assess whether quasi-periodic flow behavior returned to the same state following the intrusion. The results are summarized using spectrogram plots in Fig. G.2. For each of the angles of attack and microphone locations, the energy spectra appear to return to the prior state within ten seconds of closing the door. The energy spectra acquired before and after the door was opened and closed further suggest that the same flow state is re-established once the wind tunnel door is closed. Based on these measurements, it is concluded that acquiring flow visualization images thirty seconds after closing the wind tunnel door is sufficient to ensure that the flow being photographed is the same as that which was measured without opening the door.

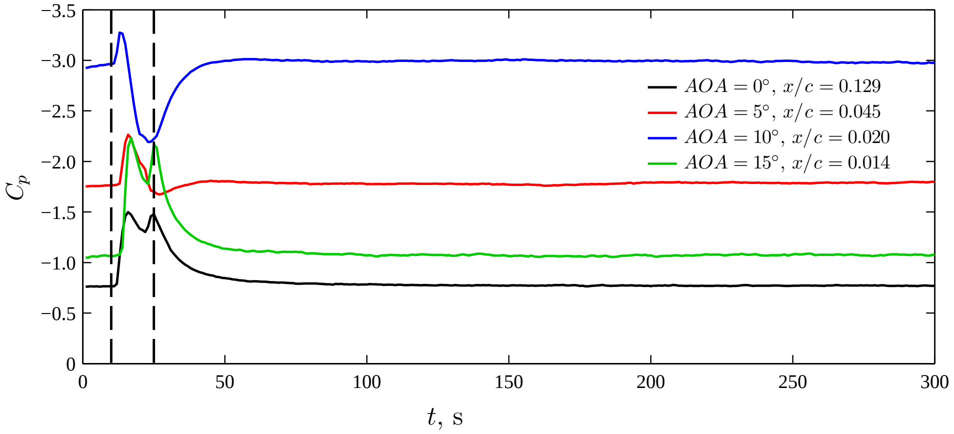

Figure G.1: Response of mean surface pressure near the suction peak to opening the wind tunnel door for fifteen seconds. The test section door was open for the time between the dashed lines.

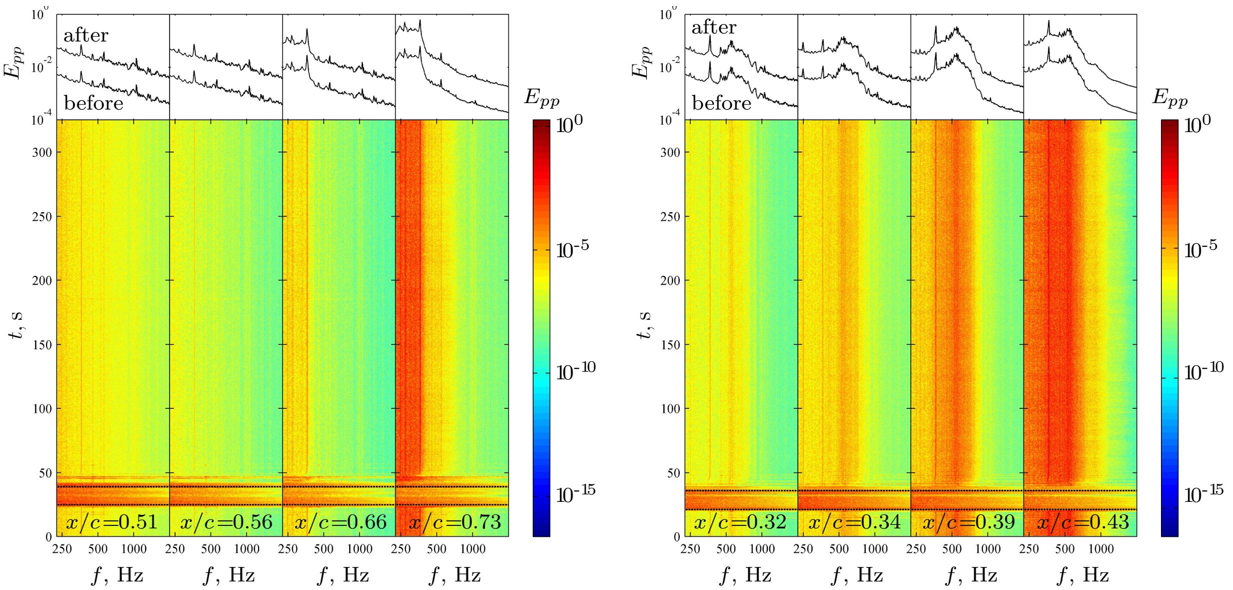

(a) $AOA = 0°$

(b) $AOA = 5°$

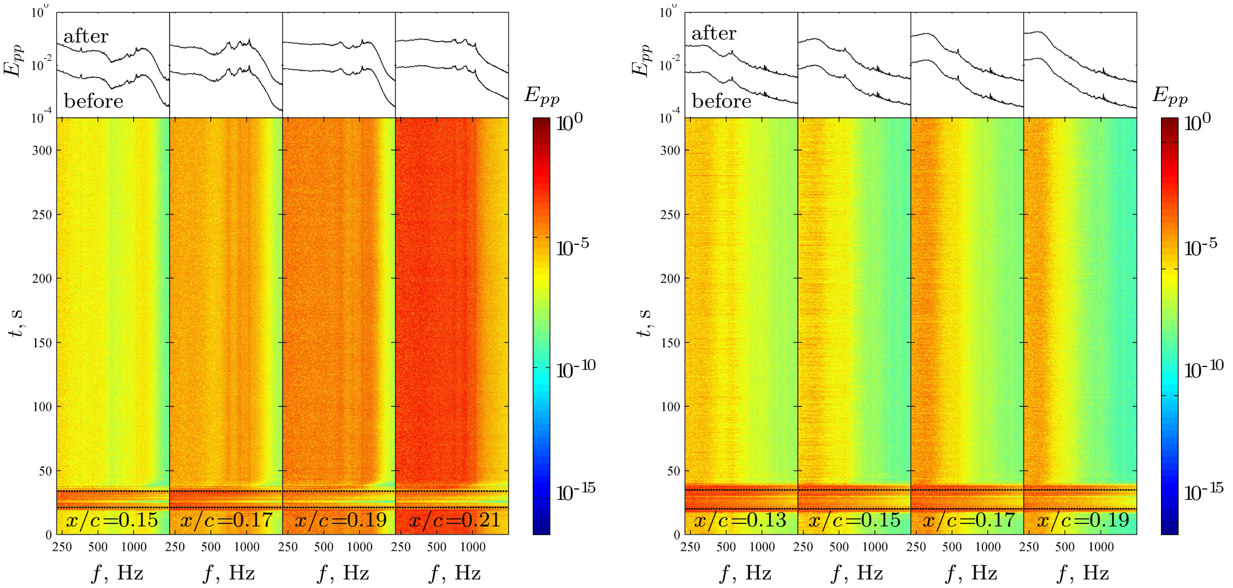

(c) $AOA = 10°$

(d) $AOA = 15°$

Figure G.2: Time evolution of energy spectra of pressure fluctuations measured with embedded microphones, with the wind tunnel door open for the time between the dashed lines. Average spectra were taken before opening the door and over a period of 105 s, beginning thirty seconds after closing the door. Spectra obtained before and after the intrusion are normalized and shifted in magnitude for clarity.